

(6)

Spin-dependent deep inelastic positron scattering from a polarized helium-3 internal gas target

by

Dirk De Schepper

B.A., Electrotechnical Engineer with specialization in Physics
Universiteit Gent
June 1991

Submitted to the Department of Physics
in partial fulfillment of the requirements for the degree of

Doctor of Philosophy

at the

MASSACHUSETTS INSTITUTE OF TECHNOLOGY

June 1997

© Massachusetts Institute of Technology 1997

Signature of Author.....

Handwritten signature

Department of Physics
April 25, 1997

Certified by.....

Professor Robert P. Redwine
Professor of Physics
Thesis Supervisor

Certified by.....

Professor Richard Milner
Associate Professor of Physics
Thesis Supervisor

Accepted by.....

Professor George F. Koster
Chairman of the Graduate Committee

MASSACHUSETTS INSTITUTE OF TECHNOLOGY

JUN 09 1997 **Science**

LIBRARIES

Spin-dependent deep inelastic positron scattering from a polarized helium-3 internal gas target

by

Dirk De Schepper

Submitted to the Department of Physics
on May 21, 1997, in partial fulfillment of the
requirements for the degree of
Doctor of Philosophy

Abstract

This thesis presents the first results from the HERMES experiment, using the data taken in 1995. In this year the HERMES experiment was successfully commissioned and data were taken on the deep inelastic scattering asymmetry of positrons from polarized ^3He . The author's main involvement was with the design and construction of the metastability exchange optically pumped ^3He gas target and the analysis of the inclusive as well as the semi-inclusive asymmetries.

The thesis is divided into five chapters. The first chapter presents an overview of the physics goals pursued by the HERMES experiment. In the second chapter the HERA accelerator facility and the HERMES detector are described. The third chapter goes into the details of the target construction and operation. The fourth chapter explains particular aspects of the analysis of the data, especially the data quality criteria. In the last chapter the results of the analysis of the inclusive scattering data are presented.

Thesis Supervisor: Professor Robert P. Redwine
Title: Professor of Physics

Thesis Supervisor: Professor Richard Milner
Title: Associate Professor of Physics

Biography

Full name: Dirk Margaretha Edmond De Schepper

Place of Birth: Leuven, Belgium

Date of Birth: November, 28, 1968

Email: dirk@marie.mit.edu

Office: room B-241, building 203
Argonne National Laboratory
9700 South Cass Ave.
Argonne, IL 60439

Office phone: (630) 252-4012

Home page: <http://marie.mit.edu/~dirk>

Home address: 1343 Branchwood Circle (apt. 202)
Naperville, IL 60563, U.S.A.

Home phone: (630) 428-9244

Education

Burgerlijk Ingenieur in Computer Wetenschap en Numerieke Analyse, Katholieke Universiteit Leuven, Leuven, Belgium, spring 1992.

Equivalent degree: M.S. in Computer Science and Numerical Analysis (without thesis)

Burgerlijk Electrotechnisch Ingenieur met specialisatie Natuurkunde, Universiteit Gent, Gent, Belgium, spring 1991.

Equivalent degree: M.S.E.E. with specialisation in physics.

Thesis: *“Study of the delta resonance by means of pion electroproduction ”*

*Tomorrow I will seven eagles see, a great comet will appear,
and voices will speak from whirlwinds foretelling monstrous and fearful things -
This Universe never did make sense; I suspect it was built on government contract.
- R.A. Heinlein “The number of the beast”*

Acknowledgments

When I arrived at MIT in 1992, I found myself in an almost perfect situation. After a year of courses, exams and gradual familiarization with the HERMES experiment (still in its final design stage), I had the chance to work on a running experiment (CE-25), using the target that would be the basis for the HERMES internal target. A great way to become familiar with the target, and an excellent introduction to the practical aspects of experimental physics. I had the chance to work closely with Kevin Lee on this project. I owe him many thanks for his patient explanations and quiet expertise.

At that point MIT was designing the HERMES vacuum system. A nice project in which I got very involved, culminating in the installation of the HERMES test experiment in the fall of 1993. During this project I had the chance to freshen up my mechanical engineering courses, which were of very limited use. I learned much more from working with Jim Kelsey and Ron Filosa. The design of the cryogenic system for the internal target was another project that MIT was working on at that time. I learned a lot from the discussions with Steve Pate, Laird Kramer, Jim Kelsey, Geoff Court and Jim Stewart.

Shortly thereafter I had the opportunity to help set up the 88-25 experiment at BATES, again using an optically polarized ^3He target. Again I had the chance to learn from an expert on the helium target, in this case Haiyan Gao. Ole Hansen and I spent several nights ambling through the BATES control room hooking up wires and checking control software. Thanks to Ole I no longer go into "shell"-shock when I find myself on a VMS system - and I know what Q is ...

In the mean time we worked on the many aspects of the HERMES target, resulting in the test experiment at the Caltech Pelletron accelerator. Many people made that hectic time bearable - through enthusiasm and long, long hours in the lab: Mark Pitt, Andrea Dvoredsky, Bob Carr, Bob McKeown and Brad Filippone - thanks guys.

I can't even begin to name the people that built the HERMES detector just so I could get my thesis done - after all there are 250+ physicists in the collaboration. Working in a collaboration this size has the advantage that one meets a lot of interesting people. I came to respect many of them, and I hope I will get the chance to work with them again. I would just like to mention the people that I learned the most from. My thesis advisor Richard Milner started me on this great project and was always very supportive. I learned a lot about physics from him, and even more about the way experiments are done. When thesis time came around, he read and corrected at an incredible speed. He 'ld read the corrections to me over the phone, while holding on to a son or two. Sorry for calling at such inconvenient times... I 'ld like to thank Steve Pate and Laird Kramer for many discussions over the years - about everything

from World War I to lemo connectors and yes, even physics. Arthur Mateos was there for this most interesting and daunting part of the experiment: the tedious and often exasperating analysis. Working with him was a pleasure. Thanks to him Q is now available for unix... During that time I also learned a lot from Brad Filippone, our NAPA coordinator. He showed me that you can actually use common sense in this business - a novel technique. Bob Redwine acted as my advisor during much of the analysis. I don't know how he does it, being the lab director and all, but he was always there for a chat, some advice or even to comb (with a very, very fine comb) through my thesis. If this thesis is readable, it is due to him. During the final analysis and the thesis writing I had the pleasure of calling Ralf Kaiser at midnight to talk about the data, the state of the universe and in general to blow off some steam. It made things so much easier.

I would not have survived 1994 and 1995 if it weren't for the ESSO - für Essen und Trinken at 3 am -, the Paloma - for a viable alternative to Halle Ost at 6 am and the DESY kantine - for cheap food that didn't kill if taken in moderation.

But most of all I thank my wife, Jacqueline, for putting up with being a HERMES widow for the best part of two years and supporting me through the entire ordeal. I 've loved her since the day I met her, and things have only gotten better.

Contents

1	Introduction	13
1.1	The basic framework	14
1.1.1	The one-photon approximation	15
1.1.2	The quark parton model	16
1.1.2.1	Relationship to constituent quarks	17
1.1.2.2	Global fits to the existing data	19
1.1.3	The elementary cross section for the inclusive process	19
1.1.4	The interpretation of g_1	22
1.1.4.1	The quark parton model	22
1.1.4.2	QCD	24
1.1.5	The sum rules	26
1.1.5.1	Flavor decomposition of the nucleon spin	32
1.2	Experimental considerations	32
1.2.1	The depolarization factor	32
1.2.2	Radiative corrections	33
1.2.3	Nuclear corrections	35
1.2.4	Evolution to a common Q^2	36
1.2.5	Extrapolation of g_1 outside the measured region	37
1.3	The semi-inclusive process	38
1.3.1	The hadronization process	39
1.3.2	Some applications of the semi-inclusive process at HERMES	40
1.3.2.1	The contribution to the spin of the valence quarks	40
1.3.2.2	The polarization of the strange sea	40
1.3.2.3	Physics from the Λ production	43
1.4	Other polarized lepton-quark scattering experiments	44
1.4.1	The SLAC experiments	44
1.4.2	The CERN experiments	44

2	The HERMES experiment	46
2.1	The HERA accelerator facility	46
2.1.1	The Sokolov-Ternov effect	47
2.1.2	The beam polarimeter	50
2.2	The HERMES spectrometer	52
2.2.1	The spectrometer magnet	55
2.2.2	The tracking detectors	55
2.2.2.1	The vertex chambers	58
2.2.2.2	The forward chambers	58
2.2.2.3	The back chambers	59
2.2.2.4	The magnet chambers	59
2.2.3	The particle identification detectors	59
2.2.3.1	The calorimeter	60
2.2.3.2	The preshower detector	62
2.2.3.3	The Čerenkov detector	62
2.2.3.4	The hodoscope H1	64
2.2.3.5	The transition radiation detector	64
2.2.4	The luminosity monitor	66
2.2.5	The trigger	66
3	The polarized ^3He internal target	68
3.1	Principles of the optically pumped metastability exchange polarized target	68
3.1.1	The optical pumping mechanism	68
3.1.1.1	The atomic level structure of ^3He	69
3.1.1.2	The metastability exchange process	71
3.1.2	The flow-through pumping cell	73
3.1.3	Previous experiments with the MIT target	75
3.2	Design parameters for the HERMES target	75
3.3	The target region	77
3.3.1	The storage cell and vacuum chamber	78
3.3.2	The differential pumping system	80
3.3.3	The cryogenic cooling system	82
3.3.3.1	Thermal properties of the target cell and its support system	83
3.3.3.2	The cryogenic cooling circuit	83
3.3.3.3	Target temperature measurement and control	84
3.3.3.4	Heat load on the storage cell	84
3.3.4	The collimator system	85

3.3.5	The wakefield suppressors	85
3.4	The helium target	88
3.4.1	The pumping cell	88
3.4.1.1	Calibrations	91
3.4.1.2	Cleaning	92
3.4.2	The gasfeedsystem	92
3.4.3	The laser system	96
3.4.4	The target holding field	99
3.4.5	The RF system	104
3.4.6	Target polarimetry	104
3.4.6.1	The principle of optical polarimetry for ^3He	104
3.4.6.2	The pumping cell polarimeter (PCP)	107
3.4.6.3	Systematic error of the target polarization measurement	107
3.4.6.4	The target optical polarimeter (TOM)	111
3.4.6.5	Depolarization studies	113
3.5	Target performance	115
4	The data analysis	118
4.1	The data flow	118
4.1.1	The data acquisition system	118
4.1.2	The analysis chain	119
4.1.2.1	The track reconstruction algorithm	120
4.1.2.2	The particle identification procedure	121
4.2	The data quality selection criteria	124
4.2.1	Run Selection	124
4.2.2	Burst Selection	125
4.2.2.1	Target Polarization	125
4.2.2.2	Beam Polarization	128
4.2.2.3	DAQ	128
4.2.2.4	Luminosity	128
4.2.2.5	Tracking Efficiency	129
4.2.2.6	PID and Trigger Quality:	129
4.2.2.7	Overall Stability	131
4.2.3	Track Selection	132
4.3	Extracting the inclusive asymmetries	134
4.3.1	The kinematic plane	135
4.3.2	The raw asymmetries	139

4.4	Corrections to the measured asymmetry	141
4.4.1	Hadron contamination	141
4.4.2	Charge symmetric background	142
4.4.3	The corrected asymmetry	143
4.5	Estimating the systematic error on the result	143
4.5.1	Yield fluctuation studies	144
4.5.2	Asymmetry fluctuation studies	144
4.5.3	Time dependence studies	146
4.5.4	Smearing effects	149
4.5.5	Conclusion	152
5	The physics results	153
5.1	Extraction of A_1^n	153
5.1.1	Nuclear Corrections	154
5.1.2	Radiative Corrections	155
5.2	Extraction of g_1^n	156
5.3	Evaluation of the Ellis-Jaffe Sum of the Neutron	158
5.3.1	Evolution to Constant Q^2	158
5.3.2	Extrapolation	160
5.3.3	Result	165
5.3.3.1	Systematic errors	165
5.3.3.2	Conclusion	167
A	Additional tables	171
A.1	Tables of averaged kinematic functions per bin	172
A.2	Convergence of the radiative corrections	173
A.3	Helpful factors for Q^2 evolution	174
A.4	Evolved g_1^n and integral for “both together” data set	174
A.5	Extrapolations for “both together” data set	175
B	The influence of the lower Q^2 limit on the result	176

Chapter 1

Introduction

Electromagnetic scattering of high-energy leptons is a powerful tool in the study of the substructure of the nucleon. The point-like character of the leptons reduces the complexity of the problem, while the relative weakness of the electromagnetic interaction allows a rapidly converging perturbative approach. Electromagnetic scattering was instrumental in the discovery of the atomic nucleus and the nucleons in the nucleus. With the advent of higher energy accelerators in the 60's it was also discovered that the unpolarized structure functions of the nucleon are in first approximation independent of the momentum transfer Q^2 . This scaling behavior indicates that the nucleons consist of sub-particles called partons. These particles were found to have a direct relation to the constituent quarks used to classify the observed spectrum of baryons and mesons. The nucleons are made up mainly of u and d quarks, with a small admixture of s quarks. The higher mass flavors c, b and t contribute little to the nucleon wave function and will be neglected in this thesis. The deep inelastic scattering regime in which the leptons can be assumed to scatter off partons has been the object of intense research for the last three decades. It has been shown that only about 50% of the nucleon's momentum is carried by the partons, indicating the presence of charge neutral particles (see chapter 9 in reference [1]). These have been identified with the gluons postulated in Quantum ChromoDynamics (QCD - see also section 1.1.4.2). QCD has been very successful in explaining several characteristics of the nucleons, such as the large gluonic content and small violations of the scaling behavior observed at large Q^2 .

In the 70's a program was started to further study the nucleon substructure by focusing on the spin of the nucleon. The highly successful quark parton model could be used to derive the masses of the hadrons from a simple assignment of masses to the constituent quarks. In a similar fashion magnetic moments were calculated by assigning different anomalous magnetic moments to the constituent quarks. The success of this simple approach led to the belief that the magnetic moment of the nucleons was indeed simply carried by the quarks. The expectation was that the proportion of the total polarization

carried by the quarks, $\Delta\Sigma$, ($\equiv \Delta u + \Delta d + \Delta s$) equaled unity, for all hadrons where u, d and s are the only free flavors. It was also expected that the sea quarks did not carry any spin, since they were dynamically generated. Hence $\Delta s \approx 0$ for all non-strange hadrons. This led to the Ellis-Jaffe sum rule predictions for the integrated polarized distribution functions for the proton and neutron (see section 1.1.5). The first SLAC data seemed to support this sum rule, but the subsequent measurements at EMC showed that the Ellis-Jaffe sum rule was violated. Only about 30% of the spin of the nucleon was carried by the quarks, and the sea quarks were polarized significantly, *opposite* to the nucleon spin. This unexpected result sparked a great interest in the spin structure of the nucleon. Several experiments have been done at SLAC and CERN, and the simple parton models have been replaced by much more sophisticated QCD-inspired ones.

All SLAC and CERN experiments to date have focussed on the inclusive scattering process. HERMES will use the additional information provided by the simultaneous measurement of the hadrons created by the scattering. These semi-inclusive processes have the potential of allowing a full measurement of the quark distribution functions in a consistent way. Although this aspect of the HERMES experiment is not the focus of this thesis, the main issues will be discussed in section 1.3.

1.1 The basic framework

The lepton-hadron scattering process is best analyzed by separating the scattering of the lepton from the subsequent hadronic interaction. This can only be done in the one-photon approximation (OPA), which is in principle the first term in the QED expansion of the electromagnetic scattering process. The elementary Feynman diagram is shown in figure 1-1.

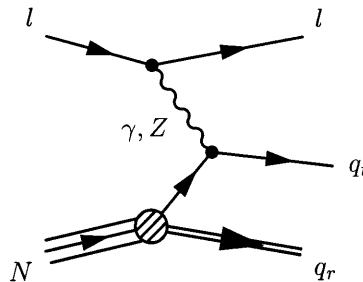


Figure 1-1: The basic deep inelastic scattering diagram

The scattering process is electromagnetic in nature, with the exchanged photon scattering from the constituents of the nucleon. The simple quark parton model (QPM) then allows a straightforward

connection between the scattering cross section and the kinematic distribution of the partons in the nucleon. This is obviously an oversimplification, especially when studying the semi-inclusive interaction. It is a well-known experimental fact that the elementary constituents of the nucleon have never been observed directly, as separate entities. The parton that is *knocked out* of the nucleon (the *current* parton) goes through a process of *hadronization*, giving rise to an observable hadron. The *target fragment* - consisting of the residual part of the struck nucleon - goes through a similar process, and in fact those two processes are necessarily related through the generation of intermediary partons as shown in figure 1-2. Final state interactions can therefore never be negligible, in contrast to nuclear knock-out reactions. This significantly complicates the description of the semi-inclusive processes.

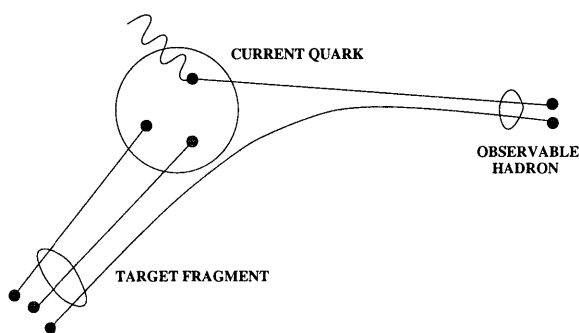


Figure 1-2: Visualising the hadronisation process

1.1.1 The one-photon approximation

The relative weakness of the electromagnetic interaction allows us to study the core aspects of the reaction by only keeping the first term in the expansion of the electromagnetic scattering interaction. Next order terms are in general of the order of $1/\alpha$ smaller. Detailed derivations can be found in references [2], [3] and [1].

This rule of thumb does not apply to the reactions that significantly alter the kinematics of the photon vertex. Indeed, changing the kinematics can change the dominant reaction mechanism. The prime example of this kind of process is radiative scattering (see table 1.1). The corrections coming from this process involve a convolution of the complete elastic and inelastic cross sections with the probability of radiating the corresponding photon. The uncertainty in this cross section becomes a significant source of uncertainty in the final result. A more in-depth analysis of the radiative corrections will be given later (section 1.2.2).

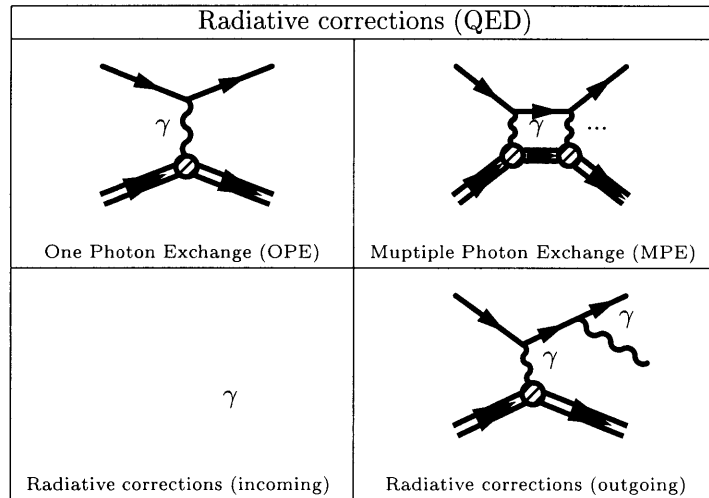


Table 1.1: Feynman diagrams for radiative corrections to the DIS process

1.1.2 The quark parton model

The simplest model for the nucleon is the static quark parton model (QPM). In this model the partons (nucleon constituents) are assumed to have certain momentum distributions (expressed as the portion x of the total nucleon momentum). If we describe the nucleon in the Breit frame (brick wall frame, infinite momentum frame), we can neglect all dynamical issues and just analyze a “snapshot” of the distributions.

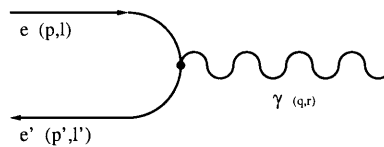


Figure 1-3: The Breit reference frame

The Breit frame is defined as the frame in which the nucleon rebounds with the same 3-momentum as it came in: $\mathbf{p}' = -\mathbf{p}$ (figure 1-3). In this reference frame the nucleon gets infinite momentum, so that the time dilation “freezes” the partons. We can then ignore the interactions that gave rise to the parton momentum distributions. Another aspect of working in this frame is that the mass as well as the transverse momentum of the quarks becomes negligible. These effects reappear when transforming back to the lab frame, but stay small. In the deep inelastic scattering regime the leptons are then assumed to scatter incoherently from the partons. This model was originally developed by Feynman [4] and Bjorken and Paschos [5] to interpret the results from the unpolarized scattering experiments.

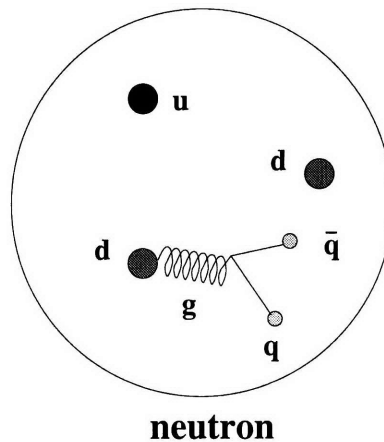


Figure 1-4: Visualising partons

1.1.2.1 Relationship to constituent quarks

The quarks were originally postulated as a classification mechanism ([6],[7]) to bring order to the multitude of hadronic particles that were discovered with the advent of powerful accelerators. Forming the irreducible representation of the symmetry groups, they are just convenient mathematical quantities. As such they can still be assigned quantum numbers, masses and even magnetic moments. These assignments “explained” the observed masses and magnetic moments of the hadrons quite accurately. This is quite impressive considering the simplicity of the assumption.

After the discovery of the parton substructure of the nucleons it seemed logical to identify the constituent quarks with the partons. This would imply that the momentum distribution of the quarks/partons should be peaking around 1/3 of the nucleon momentum ($x=1/3$). The strong force interactions holding the nucleon together are expected to broaden the momentum peak, but it should still peak at 1/3. The

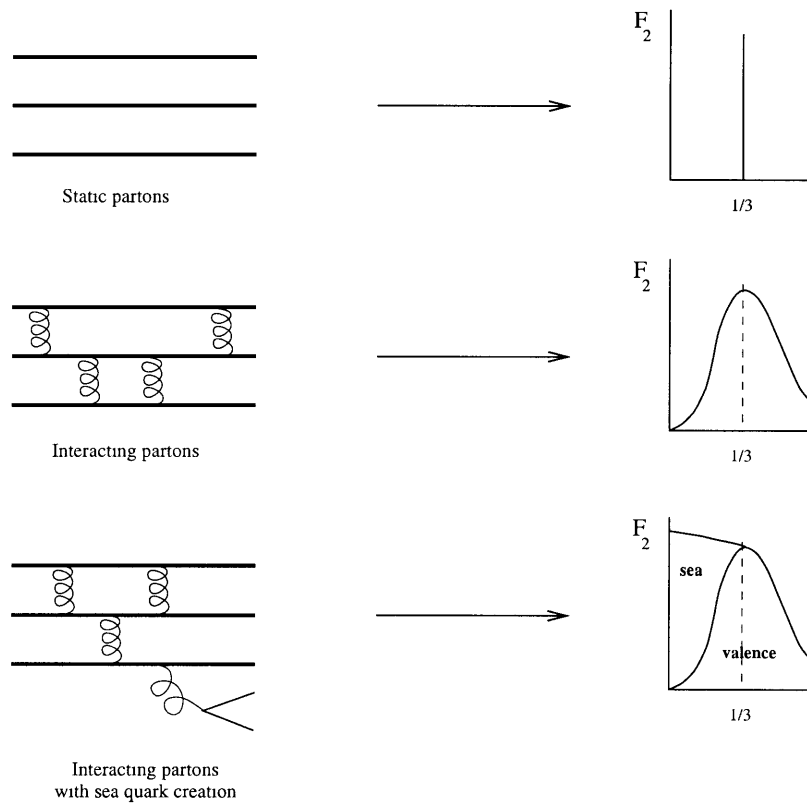


Figure 1-5: The consequences of the simple QPM

carriers of the strong force, the gluons, do not carry an electric charge, and therefore their distribution cannot be directly probed using an electromagnetic probe. It turns out that their contribution to the properties of the nucleon is quite large, both to the total momentum and to the spin. It is also clear from QCD that the charged partons cannot just be identified with the constituent (*valence*) quarks. Other quark-like partons are dynamically generated in the nucleon (figure 1-4). This includes strange and charmed quarks as well as anti-quarks. They are commonly called *sea quarks*. One would assume that the sea quarks don't carry a large fraction of the momentum of the nucleon, and hence they should be most abundant at low momentum fraction. Figure 1-5 summarizes schematically the conclusions of these simple considerations. The experimental evidence for the partons and the qualitative aspects of their momentum distributions is impressive.

1.1.2.2 Global fits to the existing data

The momentum distributions of the quarks have been measured extensively for the case of unpolarized scattering. The results are compiled by the CTEQ collaboration and best fits are made available in the form of software packages and on-line plotting facilities (see for example <http://zebu.uoregon.edu/~parton/partongraph.html>). It is hard to estimate the error on these fits (see for example reference [8]), but in general we can say that these distributions are well known, except at the very lowest x values. The situation for the polarized quark momentum distributions is not so good, but it is rapidly improving. Several “global” data fits are available (a nice compilation with references can be found in reference [9]) and CTEQ [10] now also provides a software package that contains these fits. The low x region is very poorly explored experimentally and theoretically there are many very different possibilities, some of which will be discussed in section 1.2.5. The gluon distribution functions are also not very well known. They cannot be directly probed in electromagnetic processes and global fits usually don't put great constraints on them. Some information has been extracted from the Q^2 -evolution of the structure functions, but it remains one of the least known aspects of the nucleon.

1.1.3 The elementary cross section for the inclusive process

The general OPA Feynman diagram is shown in figure 1-6. We first define the following kinematic quantities:

$$k = (\mathbf{k}, k_0) ; k' = (\mathbf{k}', k'_0) ; q \equiv k - k' \quad (1.1)$$

$$p = (\mathbf{p}, p_0) ; p' = (\mathbf{p}', p'_0) \quad (1.2)$$

$$\nu = \frac{p \cdot q}{M} \stackrel{lab}{=} E - E' \quad (1.3)$$

$$Q^2 \equiv -q^2 \stackrel{lab}{=} 2EE'(1 - \cos\theta) \quad (1.4)$$

$$x \equiv \frac{-q^2}{2pq} \stackrel{lab}{=} \frac{Q^2}{2M\nu} \quad (1.5)$$

$$y \equiv \frac{(pq)}{(pk)} \stackrel{lab}{=} \frac{\nu}{E} \quad (1.6)$$

The amplitude corresponding to figure 1-6 is given by:

$$-i\mathcal{M} = (\bar{u}_f(k', s')) i(-e)\gamma^\mu u_i(k, s) \times \left(\frac{-ig_{\mu\nu}}{Q^2} \right) \times (-iJ^\nu(Q)) \quad (1.7)$$

The relation between this amplitude and the cross section follows from elementary field theory:

$$d\sigma = \frac{d\mathcal{P}|\mathcal{M}|}{\Phi} \quad (1.8)$$

$$d\mathcal{P} = \sum_X \frac{d^3k' d^3p'}{(2\pi)^3 2k'_0} \times (2\pi)^4 \delta^4(k + p - k' - p') \quad (1.9)$$

$$\Phi = 4\sqrt{(p \cdot k)^2 - m^2 M^2} \stackrel{HRL}{\approx} 4(p \cdot k) \stackrel{lab}{=} 4ME \quad (1.10)$$

where HRL stands for Highly Relativistic Limit. One can expect the scattering to occur from quarks

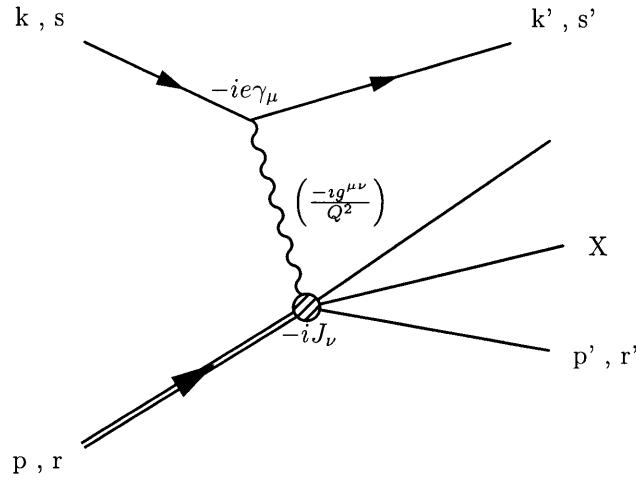


Figure 1-6: General OPA diagram

when the energy of the created state exceeds all strong hadronic resonances ($W^2 > 4$) and the momentum transfer exceeds the hadronic QCD momentum scale, Λ_{QCD} : $Q^2 \gg \Lambda_{QCD}^2$. The hadronic mass scale is typically ≈ 300 MeV. The DIS regime of the scattering process is usually defined by the following requirements:

$$\begin{cases} Q^2 > 1 \\ W^2 > 4 \end{cases} \quad (1.11)$$

One conventionally defines the following tensors:

$$L^{\mu\nu} = \langle k', s' | j^\mu(0) | k, s \rangle \langle k, s | j^\nu(0) | k', s' \rangle \quad (1.12)$$

$$W^{\mu\nu} = \frac{1}{\pi} \sum_X d^3\mathbf{p}' (2\pi)^4 \delta^4(q + p - p') \langle X | J^\mu(0) | p, r \rangle \langle p, r | J^\nu(0) | X \rangle \quad (1.13)$$

This simplifies the cross section expression to:

$$d\sigma = \frac{e^4}{Q^4} \times \frac{d^3\mathbf{k}'}{(2\pi)^3 2E'} \times \frac{4\pi}{4EM} \times L^{\mu\nu} W_{\mu\nu} \quad (1.14)$$

which can be rewritten as follows:

$$\frac{d\sigma}{dx dQ^2} = \frac{e^4}{8\pi Q^4} \times \frac{y^2}{Q^2} \times L^{\mu\nu} W_{\mu\nu} \quad (1.15)$$

The leptonic tensor can be calculated exactly since the leptons are point-like fermions. Under the assumption of minimal coupling we can derive the current operator (shown in figure 1-6) directly from the elementary Dirac equation. After some straightforward algebra (facilitated by the use of the trace theorems) one finds:

$$L^{\mu\nu} = 2 (k^\mu k'^\nu + k^\nu k'^\mu - g^{\mu\nu} (kk' - m^2) - i\epsilon^{\mu\nu\alpha\beta} q_\alpha s_\beta) \quad (1.16)$$

In this formula we used the totally anti-symmetric Levi-Civita tensor. s is the spin vector, defined by the definition of the spin projection operator:

$$\bar{u}(k, s) u(k, s) = (\gamma^\mu p_\mu + m) \frac{1}{2} (1 + \gamma_5 \frac{\gamma^\mu s_\mu}{m}) \quad (1.17)$$

so that it has the dimension of mass. In the highly relativistic limit, the spin vector becomes equal to hk , with k the 4-momentum of the lepton and h its helicity.

Calculating the nuclear tensor from first principles requires a thorough understanding of the structure of the nucleon. One can however easily apply fundamental symmetries to limit the functional form of the nuclear tensor.

$$\begin{aligned} W_{\mu\nu} = & F_1(x, Q^2) \left[-g_{\mu\nu} + \frac{q_\mu q_\nu}{q^2} \right] + F_2(x, Q^2) \left[\frac{\left(p_\mu - \frac{q_\mu (pq)}{q^2} \right) \left(p_\nu - \frac{q_\nu (pq)}{q^2} \right)}{pq} \right] \\ & + i g_1(x, Q^2) \left[\frac{\epsilon_{\mu\nu\gamma\delta} q^\gamma s_n^\delta}{pq} \right] + i g_2(x, Q^2) \left[\frac{(\epsilon_{\mu\nu\gamma\delta} q^\gamma ((pq) s_n^\delta - (s_n q) p^\delta))}{(pq)^2} \right] \end{aligned} \quad (1.18)$$

The nucleon spin vector is defined the same way as for the leptons. In the case that the nucleon mass is negligible with respect to the momentum transfer the nucleon spin vector becomes equal to $h_n p$, with p the 4-momentum of the nucleon and h_n its helicity. This is the DIS limit for s_n .

Using these tensors we obtain the most general *spin-independent* cross section for the OPA process:

$$\frac{d^2\sigma}{dx dQ^2} = \frac{e^4}{4\pi Q^4} \cdot \left[y^2 F_1(x, Q^2) + \left(1 - y - \frac{x^2 y^2 M^2}{Q^2} \right) \frac{F_2(x, Q^2)}{x} \right] \quad (1.19)$$

In the case that beam and target are polarized longitudinally we have the following spin-dependent part of the cross section:

$$\frac{\Delta\sigma}{dx dQ^2} = \frac{e^4 y^2}{2\pi Q^4} \cdot \left[g_1(x, Q^2) \left(\frac{s \cdot s_n}{p \cdot q} + \frac{(q \cdot s)(q \cdot s_n)}{2x(p \cdot q)^2} \right) + g_2(x, Q^2) \left(\frac{s_n \cdot s}{p \cdot q} - \frac{(p \cdot s)(q \cdot s_n)}{(p \cdot q)^2} \right) \right] \quad (1.20)$$

where $\Delta\sigma = \sigma^{\uparrow\downarrow} - \sigma^{\uparrow\uparrow}$.

If we look at this cross section in the HRL for the lepton, and keep only terms of the order M^2/Q^2 in the DIS limit for s_n we obtain the following:

$$\frac{\Delta\sigma}{dx dQ^2} \stackrel{HRL}{\approx} \frac{e^4}{4\pi Q^4} \cdot h \cdot h_n \left[y g_1(x, Q^2) \left(2 - y - \frac{2x^2 y^2 M^2}{Q^2} \right) + g_2(x, Q^2) \left(\frac{4x^2 y^2 M^2}{Q^2} \right) \right] \quad (1.21)$$

It can be seen that the influence of g_2 is small in the limit where $Q^2 \gg M^2$.

1.1.4 The interpretation of g_1

To interpret the structure functions we need some model of the composition of the nucleon. We first discuss the simple quark parton model where we will find a straightforward and intuitive interpretation. Then we will summarize some aspects of the QCD-based description of the nucleon. This description is assumed to be fundamentally correct, although calculating the nucleon properties from first principles is still difficult.

1.1.4.1 The quark parton model

In the QPM DIS is described as an incoherent superposition of quark-virtual photon absorption interactions. The quarks are described as *massless, free* and *pointlike* fermions described by the standard Dirac equation. The only way the confinement enters is through the momentum distributions of the quarks. This description makes sense when the time scale of the scattering interaction is short enough such that the struck quark is not influenced by the nucleonic environment (this neglects the complications caused by hadronization). The asymptotic freedom of the color force makes this possible.

The struck quark has a fraction ξ of the nucleon momentum. In the QPM $\xi \implies x$, as can be seen from momentum conservation at the photon absorption vertex:

$$p'^2 = (\xi p + q)^2 \rightarrow m_q^2 = \xi^2 M^2 + 2(\xi p \cdot q) + q^2 \xrightarrow{m_q \approx 0} \xi = \frac{-q^2}{2(p \cdot q)} \equiv x \quad (1.22)$$

In the QPM we can derive the hadronic tensor based only on the (spin-dependent) momentum distributions of the quarks. Each massless, pointlike quark with charge e_i , momentum ξp and helicity h_q contributes to the structure functions as follows:

$$\begin{aligned} F_1^q(x) &= \frac{e_i^2}{2} \delta(\xi - x) & , & \quad F_2^q(x) = e_i^2 \xi \delta(\xi - x) \\ g_1^q(x) &= \frac{e_i^2}{2} \delta(\xi - x) \left[\delta(h_q + h_\gamma + \frac{1}{2}) + \delta(h_q + h_\gamma - \frac{1}{2}) \right] & , & \quad g_2^q(x) = 0 \end{aligned} \quad (1.23)$$

The helicity δ -functions in $g_1^q(x)$ is the result of the requirement that the quark has to absorb the photon, which has a helicity $h_\gamma = \pm 1$. Consider a longitudinally polarized photon incident on a quark. Since the photon has spin $S=1$, $S_z = \pm 1$, and the quark has spin $S=1/2$, it is obvious that the quark cannot absorb the photon unless its spin is opposite to that of the photon (see figure 1-7). Hence, longitudinally

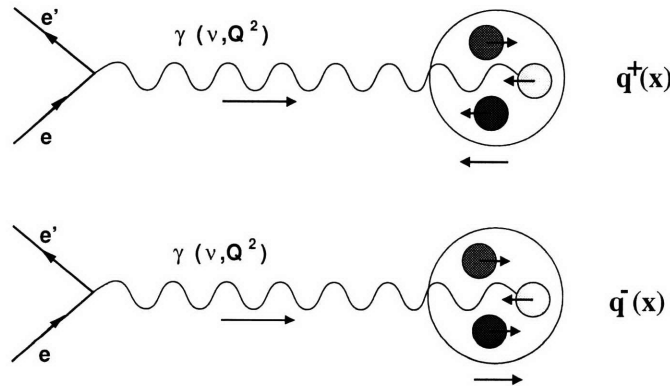


Figure 1-7: A simple QPM explanation of the sensitivity of polarized DIS to the polarized distributions. Polarized photons only scatter from quarks that are polarized opposite to the photon, independent of the polarization of the nucleon. By switching the polarization of the nucleon one can measure the difference in the number of quarks aligned with the spin of the nucleon and those that are anti-aligned.

The nucleon structure function is then obtained by summing over all quark flavors and spins and integrating over all momenta, weighted by the probability of such occurrence in the ground state of the nucleon. Explicitly this means:

$$\begin{aligned}
F_1^q(x) &= \sum_i \frac{e_i^2}{2} (q_+(x) + \bar{q}_+(x) + q_-(x) + \bar{q}_-(x)) \\
F_2^q(x) &= 2xF_1(x) \\
g_1^q(x) &= \sum_i \frac{e_i^2}{2} (q_+(x) + \bar{q}_+(x) - q_-(x) - \bar{q}_-(x)) \equiv \sum_i \frac{e_i^2}{2} \Delta q_i \\
g_2^q(x) &= 0
\end{aligned} \tag{1.24}$$

1.1.4.2 QCD

Quantum chromodynamics is the fundamental non-abelian gauge field theory describing the strong interaction. The gauge bosons mediating the force are vector bosons called gluons. They couple to the color charge of the quarks, binding them into color neutral hadrons. There are three different types of color charge R, G and B, and their anticolors. Contrary to the photons of QED the gluons carry two colors, making for 8 independent combinations. The fact that the force carriers are susceptible to the force themselves makes QCD non-abelian.

The strength of the strong interaction is determined by the strong coupling constant $\alpha_s(Q^2)$. Contrary to the screening of the electric charge by virtual electron-positron pairs, the gluon-gluon coupling causes the force to increase with distance. This is referred to as asymptotic freedom [1], since at zero distance the interaction becomes very small, leaving the partons “free”. This is quantified by the change in the coupling constant. Shorter distances, or increased resolution, correspond to higher Q^2 . This means that α_s decreases as Q^2 increases. The variation can be calculated in QCD, at least relative to a given scale. Usually the reference scale is taken to be the Z_0 -mass, at which the measured value is available. To first order in $\ln(Q^2)$ the running coupling constant varies as:

$$\frac{1}{\alpha_s^1(Q^2)} = \frac{1}{\alpha_s^0(M_Z^2)} + b_0 \cdot \ln\left(\frac{Q^2}{M_Z^2}\right) \tag{1.25}$$

with $b_0 = \frac{(11 - \frac{2}{3}N_f)}{2\pi}$. The second order corrections can then be added using the following:

$$\frac{1}{\alpha_s^2(Q^2)} = \frac{1}{\alpha_s^1(Q^2)} - \frac{b_1}{b_0} \cdot \ln\left(\frac{\alpha_s^1(Q^2)}{\alpha_s^0(M_Z^2)}\right) \tag{1.26}$$

with $b_1 = \frac{(51 - \frac{19}{3}N_f)}{4\pi^2}$. N_f is the number of active flavors. If the number of active flavors is different at Q^2 than at M_Z^2 the continuity of α_s at the flavor thresholds can be used to continue the evolution.

Similarly for the quark distribution functions the evolution between two momentum scales can be calculated, but not the functions themselves. The procedure developed by Altarelli and Parisi [11] describes two ways in which a quark can change its momentum.

1. The quark can radiate a gluon.
2. A gluon can create a pair of quarks

Because of the second process it is impossible to calculate the quark distributions without calculating the gluon momentum distribution $G(x, Q^2)$ as well. The distributions will be linked and need to be solved for simultaneously. The self-interacting nature of QCD allows 3-gluon vertices, so we do need to add the following process to the picture:

3. A gluon can decompose into two other gluons.

The processes are described by the *splitting kernels* $P_{ab}(z)$. They represent the probability that a parton a is generated from a parton b with a momentum fraction z of the parent parton. The partons can be gluons or quarks. Quark masses are neglected and hence the splitting kernels are flavor independent. The coupled evolution equations are

$$\begin{cases} \frac{dq_i(x, Q^2)}{dQ^2} = \frac{\alpha_s(Q^2)}{2\pi Q^2} \int_x^1 \frac{dx'}{x'} (q_i(x', Q^2) P_{qq}(\frac{x}{x'}) + G(x', Q^2) P_{qG}(\frac{x}{x'})) \\ \frac{dG(x, Q^2)}{dQ^2} = \frac{\alpha_s(Q^2)}{2\pi Q^2} \int_x^1 \frac{dx'}{x'} (\sum_{i=1} 2N_f q_i(x', Q^2) P_{Gq}(\frac{x}{x'}) + G(x', Q^2) P_{GG}(\frac{x}{x'})) \end{cases} \quad (1.27)$$

For the spin-dependent distribution functions the kernels need to be replaced by *helicity dependent* splitting kernels $P_{a\pm b\pm}$. Using parity conservation one derives that $P_{a-b\pm} = P_{a+b\mp}$. This then leads to the spin-dependent Altarelli-Parisi (SAP) evolution equations:

$$\begin{cases} \frac{d\Delta q_i(x, Q^2)}{dQ^2} = \frac{\alpha_s(Q^2)}{2\pi Q^2} \int_x^1 \frac{dx'}{x'} (\Delta q_i(x', Q^2) \Delta P_{qq}(\frac{x}{x'}) + \Delta G(x', Q^2) \Delta P_{qG}(\frac{x}{x'})) \\ \frac{d\Delta G(x, Q^2)}{dQ^2} = \frac{\alpha_s(Q^2)}{2\pi Q^2} \int_x^1 \frac{dx'}{x'} (\sum_{i=1} 2N_f \Delta q_i(x', Q^2) \Delta P_{Gq}(\frac{x}{x'}) + \Delta G(x', Q^2) \Delta P_{GG}(\frac{x}{x'})) \end{cases} \quad (1.28)$$

with the definition $\Delta P_{ab}(z) \equiv P_{a+b+}(z) - P_{a+b-}(z)$.

The Altarelli-Parisi equations can be rewritten to determine the Q^2 dependence of g_1 without knowledge of the quark polarization distributions. It does however require that one makes an ansatz for $\Delta G(x, Q^2)$. Using the AP equations and equation 1.24 gives the following

$$\frac{dg_1(x, Q^2)}{dQ^2} = \frac{\alpha_s(Q^2)}{2\pi Q^2} \int_x^1 \frac{dx'}{x'} \left(g_1(x', Q^2) \Delta P_{qq}\left(\frac{x}{x'}\right) + \frac{1}{3} \Delta G(x', Q^2) \Delta P_{qG}\left(\frac{x}{x'}\right) \right) \quad (1.29)$$

Assuming the Q^2 -dependence of g_1 and ΔG is small compared to that of $\frac{\alpha_s(Q^2)}{Q^2}$ allows to integrate this equation to

$$g_1(x, Q^2) - g_1(x, Q_0^2) = \frac{2}{9} \ln \left(\frac{\alpha_s(Q_0^2)}{\alpha_s(Q^2)} \right) \int_x^1 \frac{dx'}{x'} \left(g_1(x', Q_0^2) \Delta P_{qq}\left(\frac{x}{x'}\right) + \frac{1}{3} \Delta G(x', Q_0^2) \Delta P_{qG}\left(\frac{x}{x'}\right) \right) \quad (1.30)$$

Traditionally the experimental data have been evolved to a common Q^2 using the simple experimental observation that the asymmetry A_1 does not depend on Q^2 very strongly. We will return to this in section 1.2.4.

1.1.5 The sum rules

Of great importance to the field of high-energy scattering are the sum rules. Indeed, the complicated dynamics of QCD make it very hard to predict the detailed shape of the distributions that are measured in the experiments. The integrals of the distributions often depend on more general characteristics of the theory and can be calculated. Another benefit is their relationship to interesting quantities like the total spin carried by the quarks. The drawback is that the experimental data cannot cover the entire x -region. To determine the integrals we will need to extrapolate the data outside the measured region. This is further discussed in section 1.2.5.

Limiting ourselves to the active flavors in the nucleon ground state and using isospin symmetry to relate the neutron quark distributions to those in the proton, we can derive from formula 1.23 the integrals of g_1^n and g_1^p :

$$\begin{aligned} \Gamma_1^p &\equiv \int_0^1 g_1^p(x) dx = \frac{1}{2} \left(\frac{4}{9} \Delta u + \frac{1}{9} \Delta d + \frac{1}{9} \Delta s \right) \\ \Gamma_1^n &\equiv \int_0^1 g_1^n(x) dx = \frac{1}{2} \left(\frac{4}{9} \Delta d + \frac{1}{9} \Delta u + \frac{1}{9} \Delta s \right) \end{aligned} \quad (1.31)$$

The quantities Δq_i are defined as:

$$\Delta q_i = \int_0^1 dx \left(q_i^+(x) + \bar{q}_i^+(x) - q_i^-(x) - \bar{q}_i^-(x) \right) \quad (1.32)$$

These quantities occur in several other experimental situations and can be related to the SU(3) reduced matrix elements F and D .

Assuming that the quark fields (u,d,s) form a flavor triplet, we can group some baryons and mesons in octets. The symmetry group applicable to this situation is SU(3). An excellent and thorough description of SU(3) and its application to light quark phenomenology can be found in reference [12]. Some main points are reiterated here.

The axial-vector current matrix elements

$$j_a^{A\mu} = \bar{\Psi} \frac{\gamma^\mu \gamma_5 \lambda_a}{2} \Psi \quad \bar{\Psi} = \begin{bmatrix} \psi_u \\ \psi_d \\ \psi_s \end{bmatrix} \quad (1.33)$$

causing Gamow-Teller transitions in the octet can be related to the polarized quark distributions. Using the standard representation for the generating matrices λ_a we obtain the following explicit expressions for the three crucial currents:

$$\begin{aligned} j_0^{A\mu} &= \frac{1}{2} (\bar{\psi}_u \gamma^\mu \gamma_5 \psi_u + \bar{\psi}_d \gamma^\mu \gamma_5 \psi_d + \bar{\psi}_s \gamma^\mu \gamma_5 \psi_s) \\ j_3^{A\mu} &= \frac{1}{2} (\bar{\psi}_u \gamma^\mu \gamma_5 \psi_u - \bar{\psi}_d \gamma^\mu \gamma_5 \psi_d) \\ j_8^{A\mu} &= \frac{1}{2} (\bar{\psi}_u \gamma^\mu \gamma_5 \psi_u + \bar{\psi}_d \gamma^\mu \gamma_5 \psi_d - 2\bar{\psi}_s \gamma^\mu \gamma_5 \psi_s) \end{aligned} \quad (1.34)$$

Applying the Wigner-Eckart theorem to an expectation value of a general flavor operator under the assumption of SU(3) flavor symmetry gives the following:

$$\langle i | \mathcal{O}^j | k \rangle = f_{ijk} \cdot F + d_{ijk} \cdot D \quad (1.35)$$

Here the factors f_{ijk} and d_{ijk} are the SU(3) structure constants, F is the *symmetric reduced matrix element*, D the *anti-symmetric reduced matrix element*. We can apply this to the three currents:

$$\begin{aligned}
\langle p, s | j_0^{A\mu} | p, s \rangle &= \frac{1}{2} (\langle p, s | \bar{\psi}_u \gamma^\mu \gamma_5 \psi_u | p, s \rangle + \langle p, s | \bar{\psi}_d \gamma^\mu \gamma_5 \psi_d | p, s \rangle + \langle p, s | \bar{\psi}_s \gamma^\mu \gamma_5 \psi_s | p, s \rangle) \\
&\equiv s^\mu A_0 \\
\langle p, s | j_3^{A\mu} | p, s \rangle &= \frac{1}{2} (\langle p, s | \bar{\psi}_u \gamma^\mu \gamma_5 \psi_u | p, s \rangle - \langle p, s | \bar{\psi}_d \gamma^\mu \gamma_5 \psi_d | p, s \rangle) \equiv s^\mu A_3 \\
\langle p, s | j_8^{A\mu} | p, s \rangle &= \frac{1}{2} (\langle p, s | \bar{\psi}_u \gamma^\mu \gamma_5 \psi_u | p, s \rangle + \langle p, s | \bar{\psi}_d \gamma^\mu \gamma_5 \psi_d | p, s \rangle - \langle p, s | 2\bar{\psi}_s \gamma^\mu \gamma_5 \psi_s | p, s \rangle) \\
&\equiv s^\mu A_8
\end{aligned} \tag{1.36}$$

The proportionality constant from the Wigner-Eckart theorem defines the quantities A_i . The relation with the spin carried by the quark flavors follows from:

$$\delta q_i s^\mu = \langle p, s | \bar{\psi}_i \gamma^\mu \gamma_5 \psi_i | p, s \rangle \tag{1.37}$$

Integrating these relations over x we get the following relations:

$$\begin{aligned}
2A_0 \cdot s^\mu &= (\Delta u + \Delta d + \Delta s) s^\mu \equiv (\Delta \Sigma) s^\mu \\
2A_3 \cdot s^\mu &= (\Delta u - \Delta d) s^\mu = (F + D) s^\mu \\
2A_8 \cdot s^\mu &= (\Delta u + \Delta d - 2\Delta s) s^\mu = (3F - D) s^\mu
\end{aligned} \tag{1.38}$$

where $\Delta q = \int_0^1 \delta q(x)$. The first relation can be shown to hold under the weaker assumption of SU(2) isospin symmetry, the second and third relation only hold under the additional assumption of SU(3) flavor symmetry.

Assuming SU(3) flavor symmetry, A_3 is related to the ratio of axial over vector coupling constants and can be measured in the neutron β -decay. A_8 can only be measured in hyperon β -decay.

$$2A_3 \cdot s^\mu = s^\mu \left(\frac{g_a}{g_v} \right) \tag{1.39}$$

$$2A_8 \cdot s^\mu = s^\mu \frac{g_a}{g_v} \left(\frac{3\frac{F}{D} - 1}{\frac{F}{D} + 1} \right) \tag{1.40}$$

This means we can rewrite the formulae 1.31:

$$\Gamma_1^p = \frac{1}{12} \frac{g_a}{g_v} \left(\frac{3 \frac{F}{D} - 1}{\frac{F}{D} + 1} + 1 \right) + \frac{1}{3} \Delta s \quad (1.41)$$

$$\Gamma_1^n = \frac{1}{12} \frac{g_a}{g_v} \left(\frac{3 \frac{F}{D} - 1}{\frac{F}{D} + 1} - 1 \right) + \frac{1}{3} \Delta s \quad (1.42)$$

From this we find the Bjorken sum rule:

$$\Gamma_1^p - \Gamma_1^n = \frac{1}{6} \frac{g_a}{g_v} = 0.209 \quad (1.43)$$

In summary:

$$\begin{cases} F + D & = \Delta u - \Delta d \\ 3F - D & = \Delta u + \Delta d - 2\Delta s \\ \Gamma_1^p & = \frac{1}{2} \left(\frac{4}{9} \Delta u + \frac{1}{9} \Delta d + \frac{1}{9} \Delta s \right) \\ \Gamma_1^n & = \frac{1}{2} \left(\frac{4}{9} \Delta d + \frac{1}{9} \Delta u + \frac{1}{9} \Delta s \right) \\ \Delta \Sigma & = \Delta u + \Delta d + \Delta s \end{cases} \quad (1.44)$$

It is clearly necessary to measure Γ_1^p or Γ_1^n to be able to derive all flavor spin fractions. To predict the values for the integral we can follow Ellis and Jaffe in assuming that Δs is zero and we then predict the following sum rules for the neutron and the proton separately:

$$\Gamma_1^p = \frac{1}{12} \frac{g_a}{g_v} \left(\frac{3 \frac{F}{D} - 1}{\frac{F}{D} + 1} + 1 \right) = 0.199 \quad (1.45)$$

$$\Gamma_1^n = \frac{1}{12} \frac{g_a}{g_v} \left(\frac{3 \frac{F}{D} - 1}{\frac{F}{D} + 1} - 1 \right) = -0.009 \quad (1.46)$$

These sum rules are the Ellis-Jaffe sum rules. The assumption of zero net polarization of the strange quarks seems natural and allows a prediction for the sum rule of the proton and the neutron separately.

One can include QCD-corrections to these sum rules ([13] and references therein) in the following fashion:

$$\Gamma_1^p = \left(\frac{1}{6}A_3 + \frac{1}{18}A_8\right) \cdot C_1 + \frac{2}{9}A_0C_0 \quad (1.47)$$

$$\Gamma_1^n = \left(-\frac{1}{6}A_3 + \frac{1}{18}A_8\right) \cdot C_1 + \frac{2}{9}A_0C_0$$

where the QCD correction factors C_1 and C_0 are given by:

$$C_0 = \left(1 - \frac{\alpha_s}{3\pi} - 0.549\frac{\alpha_s^2}{\pi^2} - \mathcal{O}(2)\frac{\alpha_s^3}{\pi^3}\right) \quad (1.48)$$

$$C_1 = \left(1 - \frac{\alpha_s}{\pi} - \frac{43}{12}\frac{\alpha_s^2}{\pi^2} - 20.215\frac{\alpha_s^3}{\pi^3} - \mathcal{O}(130)\frac{\alpha_s^4}{\pi^4}\right)$$

These correction factors are for the case where there are three degrees of flavor, a reasonable assumption below the charm production threshold.

We can combine equations 1.48 and 1.44 to give:

$$\begin{aligned} \Delta\Sigma &= \frac{9}{C_0} \left[\Gamma_1^p - \left(\frac{F+D}{12} + \frac{3F-D}{36}\right) \cdot C_1 \right] \\ &= \frac{9}{C_0} \left[\Gamma_1^n - \left(-\frac{F+D}{12} + \frac{3F-D}{36}\right) \cdot C_1 \right] \\ \Delta u &= \frac{\Delta\Sigma}{3} + \frac{3F-D}{6} + \frac{F+D}{2} \\ \Delta d &= \frac{\Delta\Sigma}{3} + \frac{3F-D}{6} - \frac{F+D}{2} \\ \Delta s &= \frac{\Delta\Sigma}{3} - \frac{3F-D}{3} \end{aligned} \quad (1.49)$$

which allows easy extraction of quark spin contributions from the measurements.

We can also rewrite the equations 1.47 in the following manner:

$$\Gamma_1^p = \left(\frac{1}{6}\frac{F+D}{2} + \frac{1}{18}\frac{3F-D}{2}\right) \cdot C_1 + \frac{2}{9}(\Delta u + \Delta d + \Delta s) \cdot C_0 \quad (1.50)$$

$$\Gamma_1^n = \left(-\frac{1}{6}\frac{F+D}{2} + \frac{1}{18}\frac{3F-D}{2}\right) \cdot C_1 + \frac{2}{9}(\Delta u + \Delta d + \Delta s) \cdot C_0$$

This allows us to extract the QCD-corrected Ellis-Jaffe sum rule by assuming that the sea quarks are not polarized, and hence $\Delta s = 0$ since all the strange quarks in the nucleon are sea quarks:

$$\Gamma_1^p = \left(\frac{1}{6} \frac{F+D}{2} + \frac{1}{18} \frac{3F-D}{2} \right) \cdot C_1 + \frac{1}{9} (3F - D) \cdot C_0 \quad (1.51)$$

$$\Gamma_1^n = \left(-\frac{1}{6} \frac{F+D}{2} + \frac{1}{18} \frac{3F-D}{2} \right) \cdot C_1 + \frac{1}{9} (3F - D) \cdot C_0$$

This prediction for the integral is plotted in figure 1-8. The error on the prediction is mainly due to the errors in the determination of F and D . We used the following values [13]:

$$\begin{aligned} F &= 0.461 \pm 0.014 \\ D &= 0.798 \pm 0.013 \end{aligned} \quad (1.52)$$

α_s was determined by simple interpolation (power fit) of experimental data (reference [13]).

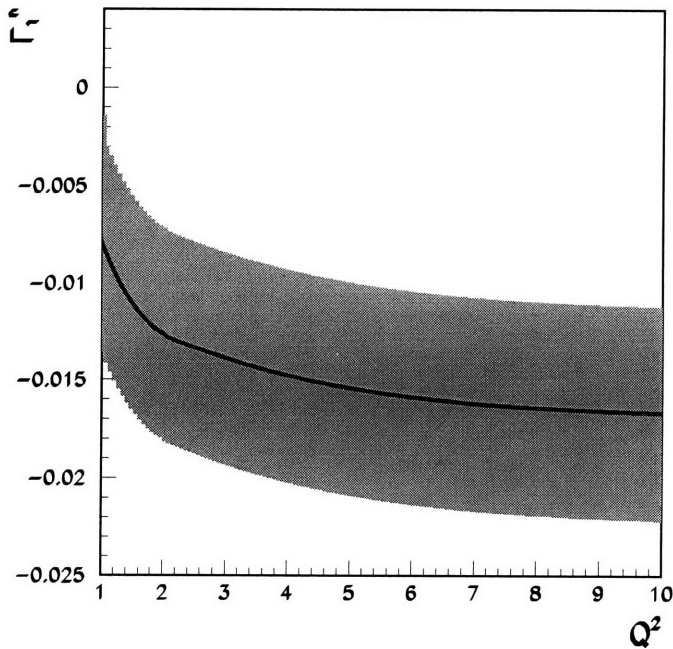


Figure 1-8: Ellis-Jaffe prediction for Γ_1^n versus Q^2

1.1.5.1 Flavor decomposition of the nucleon spin

It is the goal of the HERMES program to determine how the spin of the nucleon is distributed among its constituents. It is “obvious” that the following is true:

$$\frac{1}{2} = \frac{1}{2} \left[\underbrace{\Delta u + \Delta d + \Delta s}_{\Delta\Sigma} \right] + \overbrace{\Delta L_u + \Delta L_d + \Delta L_s}^{\Delta L} + \Delta G + \Delta L_G \quad (1.53)$$

where $\Delta\Sigma$ is the spin carried by the quarks, ΔL is the angular momentum of the quarks, ΔG is the spin carried by the gluons and finally ΔL_G is the angular momentum carried by the gluons. However, the definition of these quantities is open to discussion. For instance, the distinction between quark and gluon field is largely a matter of the gauge one chooses. The focus of the HERMES experiment is the first three terms, the contribution of the intrinsic spin of the quark fields to the nucleon spin. Methods to access the other quantities are being studied.

1.2 Experimental considerations

1.2.1 The depolarization factor

The measured asymmetry A_m is related to the physical asymmetry by correcting for the depolarization of the photon (relative to the polarization of the scattered positron):

$$A_1(x) = \frac{A_m(x)}{D(x,y)} \quad (1.54)$$

The depolarization factor $D(x,y)$ can be calculated exactly for each event since it only depends on the kinematics of the process.

The probability ratio for a polarized lepton to emit a photon polarized longitudinally versus transversely can be calculated (using $\gamma_f = \frac{\sqrt{Q^2}}{\nu}$)

$$\begin{aligned}
\epsilon &= \frac{\Gamma_L}{\Gamma_T} = \frac{4(1-y) - \gamma_f^2 y^2}{4(1-y) + 2y^2 + \gamma_f^2 y^2} \\
&= \left[1 + 2\left(1 + \frac{\nu^2}{Q^2}\right) \tan^2 \frac{\theta}{2} \right]^{-1} \\
&\approx \frac{1-y}{1-y + \frac{y^2}{2}}
\end{aligned} \tag{1.55}$$

The approximation is correct for those kinematics where $\gamma_f^2 y^2 \gg 4 \cdot (1-y)$. The ratio of those quantities for the average kinematics for each HERMES bin (see chapter 4) is less than .002. We can therefore safely use that approximation.

The depolarization factor follows from the previous quantity:

$$\begin{aligned}
D(x, y) &= \frac{E - \epsilon E'}{E(1 + \epsilon R(x, y))} \\
&= \frac{1 - (1-y)\epsilon}{1 + \epsilon R(x, y)} \\
&\approx \frac{y(2-y)}{2(1-y)(1 + R(x, y)) + y^2}
\end{aligned} \tag{1.56}$$

where $R(x, y)$ is the ratio of longitudinal to vertical cross section.

1.2.2 Radiative corrections

In principle radiative corrections are a straightforward effect, one that can be calculated exactly and corrected for. In practice the calculation requires a detailed knowledge of the cross section at kinematic points outside the experimental range. This is easily seen from the Feynman diagrams in table 1.1. The emission of the photon changes the kinematics at the vertex, hence allowing the contribution of non-DIS reactions between the virtual photon and the nucleus to appear in the kinematic region under study. Elastic, quasi-elastic and non-DIS inelastic nucleon scattering can now contribute to the scattering cross sections.

$$\sigma = \sigma_{DIS} + \sigma_{elastic} + \sigma_{quasi-elastic} + \sigma_{inelastic-DIS} + \sigma_v \tag{1.57}$$

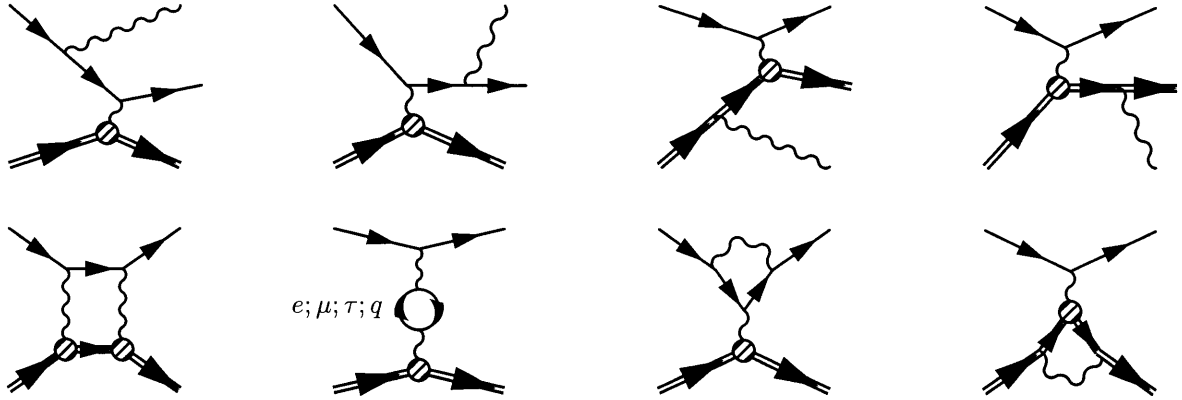


Table 1.2: Simple contributions to the radiative corrections

The last term is the cross section due to virtual photon emission and vacuum terms. Aside from changing the yields due to contributions from different reaction channels, the radiation of a photon can also deflect a lepton into the detector that would have otherwise gone undetected. The opposite is also true. For the HERMES detector this is a minor consideration because of its large acceptance. We will further ignore this effect.

Since we are only interested in the asymmetry of the DIS reaction, we only need to correct for the admixture of the asymmetries of all other reaction mechanisms. Even if its asymmetry is zero, the mere presence of a reaction channel dilutes the DIS asymmetry. To calculate these contributions we need to know the polarized cross section over the entire kinematic region accessible through the radiation of a photon before or after the vertex. The elastic and quasi-elastic processes have been studied in great detail, which allows us to calculate their tails very accurately using QED. The inelastic processes are a different matter altogether, and some approximations and parameterizations are necessary, in particular for the spin-dependent scattering in the resonance region.

The FORTRAN program POLRAD [14] calculates the radiative corrections through an iterative procedure in which the measured asymmetry is fit and radiated. The radiative correction is applied to the data, after which the procedure is repeated with the corrected asymmetry taking the place of the data. The process converges quickly. The asymmetry is fit using the Schäfer [15] parameterization.

1.2.3 Nuclear corrections

One has to correct for the fact that the target contains a small amount of polarized protons, which contribute to the asymmetry of the cross section. The asymmetry due to the neutron is given by:

$$A_1^n(x) = \frac{A_1^{3\text{He}}(x) - P_p^{3\text{He}} \times \frac{2 \times F_2^p(x)}{F_2^n(x) + 2 \times F_2^p(x)} \times A_1^p(x)}{P_n^{3\text{He}} \times \frac{F_2^n(x)}{F_2^n(x) + 2 \times F_2^p(x)}} \quad (1.58)$$

where $P_p^{3\text{He}}$ is the net polarization of the proton in ^3He and $P_n^{3\text{He}}$ is the net polarization of the neutron. The correctness of the formula can be checked by inspection. The unpolarized structure functions $F_2^{n/p}$ are used to correct for the difference in the scattering cross sections off neutrons and protons. One can similarly use $F_2^{d/p}$, which have both been measured. The formula then becomes (after some simplification):

$$A_1^n = \frac{A_1^{3\text{He}} (2F_2^d + F_2^p)}{P_n^{3\text{He}} (2F_2^d - F_2^p)} - 2 \frac{F_2^p}{(2F_2^d - F_2^p)} \frac{P_p^{3\text{He}}}{P_n^{3\text{He}}} A_1^p \quad (1.59)$$

where it is useful to remember that the deuteron structure function is the average of the proton and neutron structure functions: $2F_2^d = F_2^n + F_2^p$.

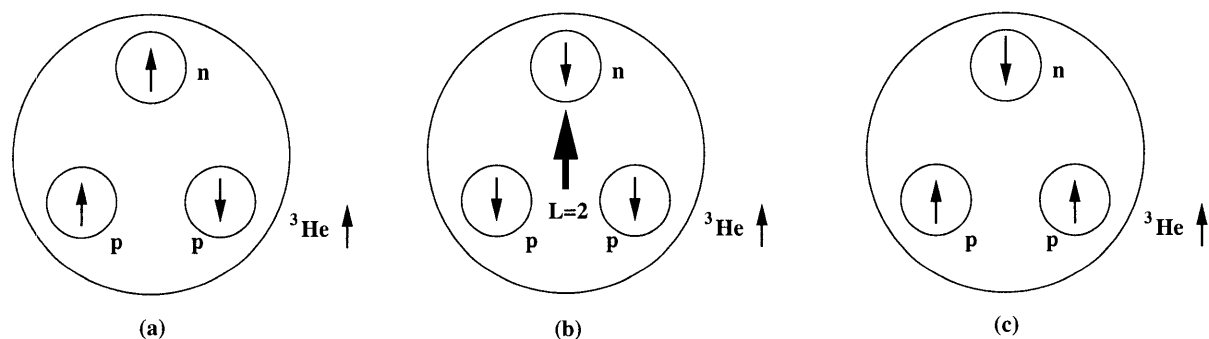


Figure 1-9: Components of the ground state wave function of ^3He . (a) S-wave, protons paired off. (b) D-wave. (c) S'-wave, neutron pairs with one of the protons.

The use of polarized ^3He as an effective polarized neutron target is caused by the dominance of the S-wave in the ground state ([16], [17]). The possible configurations for the ground state are sketched in figure 1-9. The spatially symmetric S-wave accounts for about 90% of the ground state wave function. In this state all nucleons are in their lowest energy orbit and the two protons are paired off in an asymmetric spin combination, so they do not contribute to the nuclear spin. In this state the neutron

carries the nuclear spin, and we have an almost perfect polarized neutron target, apart from some dilution coming from the protons. There is a D-state contribution due to the presence of the tensor force. This amounts to about 8% of the ground state. In this state all nucleons are polarized opposite to the nuclear spin. The S'-state is a mixed symmetry state. It accounts for about 1.5% of the ground state wave function, and arises from the spin-orbit interaction. In this state the polarization is distributed over protons and neutrons. The total net polarization of a proton in helium 3 has been calculated to be 2.8% ([18],[19]). The neutron polarization was calculated to be 86%. These numbers allow us to make a fairly accurate correction for the nuclear effects in the scattering process. More sophisticated corrections are not necessary.

1.2.4 Evolution to a common Q^2

Finally g_1 is calculated from A_1^n using the following formula (neglecting the contribution of g_2):

$$g_1^n(x, Q^2) = \frac{A_1^n \times F_2^n(x, Q^2)}{2x(1 + R(x, Q^2))} \quad (1.60)$$

This gives the value of the measured $g_1^n(x, Q^2)$ at the kinematics of the bin. To extract the physics, one will need to bring these quantities to a common Q^2 scale.

To “evolve” $g_1^n(x, Q^2)$ from the average Q^2 of the measurement (which in general depends on x) to a common Q_0^2 one usually makes the assumption that the asymmetry does not depend on Q^2 . Then one simply substitutes the desired Q_0^2 for Q^2 in formula 1.60. As described in a recent review article on the subject of NLO kernels for the Q^2 -evolution (reference [20]) this is no longer the only option available. Higher order kernels have been computed. A short overview of the method will be presented here.

The AP equations for the parton distributions (section 1.1.4.2) only depend on the parton distributions for higher x and the same Q^2 . This requires a fit to the data at all x , naturally leading to an iterative procedure similar to the one used to calculate the radiative corrections. The search for a set of self-consistent parton distributions obeying the correct evolution equations has been the subject of several papers (references [21] and [22]). It is necessary to choose an ansatz for the functional form of the distributions. Some dependence of the results on this ansatz can be expected and this introduces an error in the computed evolutions. However, the low- x behavior of the ansatz functions is not very important since the evolution depends mainly on the high- x values. The behavior at low x is however extremely important for the extrapolation needed to determine the first moment of the distributions from the data. This is clear from the recent results on unpolarized distributions functions. They indicate a much steeper than expected rise at low x for the distributions. This has been explained by the effects

of the perturbative QCD evolution. These effects increase with Q^2 . In section 1.2.5 the extrapolation issue is further discussed. For the calculation of Γ_1^p it seems premature to use the NLO calculations, as they do not give a significant different answer than the simple assumption that A_1^p does not depend on Q^2 . The scatter in the NLO result caused by using different ansatz functions is too large. This is not the case for Γ_1^p .

1.2.5 Extrapolation of g_1 outside the measured region

In a recent review article [20] the low-x functional form has been derived under the following assumptions:

- Regge theory holds at low Q^2 . This is reasonable considering the success of Regge theory in soft hadronic physics.
- The steepness of the response is due to the accumulation of perturbative QCD evolution (see section 1.2.4).

The polarized densities are of course limited by the corresponding unpolarized densities. The unpolarized singlet quark and gluon distributions from the QCD evolution equations lead to the following asymptotic behavior at small x :

$$\begin{aligned} xg(x) &\propto \sigma^{-1/2} e^{2\gamma\sigma - \delta\zeta} (1 + \sum_{i=1}^n \epsilon^i \rho^{i+1} \alpha_s^i) \\ x\Sigma(x) &\propto \rho^{-1} \sigma^{-1/2} e^{2\gamma\sigma - \delta\zeta} (1 + \sum_{i=1}^n \epsilon_f^i \rho^{i+1} \alpha_s^i) \end{aligned} \quad (1.61)$$

where $\xi = \log\left(\frac{x_0}{x}\right)$, $\zeta = \log\left(\frac{\alpha_s(Q_0^2)}{\alpha_s(Q^2)}\right)$, $\sigma = \sqrt{\xi\zeta}$ and $\rho = \sqrt{\frac{\xi}{\zeta}}$. The ϵ^n terms are corrections of the n^{th} perturbative order (NLO corresponds to $n=1$). The separate parton distributions ($f = q_{NS}, \Delta q_{NS}, \Delta\Sigma, \Delta g$) similarly behave as following:

$$f(x) \propto \sigma^{-1/2} e^{2\gamma_f\sigma - \delta_f\zeta} (1 + \sum_{i=1}^n \epsilon_f^i \rho^{2i+1} \alpha_s^i) \quad (1.62)$$

These functions are less singular by a factor x than the singlet unpolarized distributions, but the higher order corrections are more important since the exponent $i+1$ is replaced by $2i+1$. The order to which the summation has to be carried is the topic of serious controversy. High order summations could lead to behavior as a power of x , spoiling the “leading” terms which are only logarithmic. No indication of such behavior is shown in the current experimental data.

The starting distributions need to be relatively nonsingular, such that the singularity generated by the evolution is the only one present. This is required by self-consistency with the derivation. We start

in the soft region of $Q_0^2 \approx 1 \text{ GeV}^2$, where Regge theory has been successful in describing unpolarized behavior. We then predict a flat trajectory with $\alpha_1 \in [-0.5, 0.0]$ for the unpolarized distributions. The polarized distributions are then limited in their divergence to less than $x^{-0.5}$. This does not, however, pose a strong limit on the singlet divergence, and one needs to rely on the accuracy of the NLO approximation and the Regge behavior at low enough momentum scale. The distributions at the reference momentum scale of 1 GeV^2 suggested in reference [20] are:

$$\Delta f(x, Q_0^2) = \mathcal{N}_f \eta_f x^{\alpha_f} (1-x)^{\beta_f} (1 + \gamma_f x^{\delta_f}) \quad (1.63)$$

with $\Delta f = \Delta q_{NS}$, $\Delta \Sigma$, Δg and \mathcal{N}_f is a normalization factor chosen such that the first moment of Δf is equal to η_f . The global data fits are done under several additional assumptions for the distributions. The first such set of assumptions is $\delta_\Sigma = \delta_g = 1 = \delta_{NS}$ and $\gamma_\Sigma = \gamma_g$. Distributions of this type are called class A distributions. A second set is $\gamma_\Sigma = \gamma_g = \gamma_{NS} = 0$ and $\beta_g = 15$. This set's distribution functions are class C. The class B distributions are of a total different functional form:

$$\begin{aligned} \Delta \Sigma &= \mathcal{N}_\Sigma \eta_\Sigma x^{\alpha_\Sigma} (\log \frac{1}{x})^{\beta_\Sigma} \\ \Delta q_{NS} &= \mathcal{N}_{NS} \eta_{NS} [(\log \frac{1}{x})^{\alpha_{NS}} + \gamma_{NS} x (\log \frac{1}{x})^{\beta_{NS}}] \\ \Delta g &= \mathcal{N}_g \eta_g [(\log \frac{1}{x})^{\alpha_g} + \gamma_g x (\log \frac{1}{x})^{\beta_g}] \end{aligned} \quad (1.64)$$

The maximal divergence for these functions is logarithmic. This type of distributions can be generated by perturbative evolution.

The results for these fits (and a fourth class, D) have been reported in reference [20]. They all give equally good fits in the measured region, but give very different extrapolations at low x . The low x behavior is always weaker than any power, hence compatible with the Regge prediction.

At high x a fit was done using the form $\beta(1-x)^3$, which can be derived from the QCD counting rules [23]. This is expected to hold for $x > 0.4$.

1.3 The semi-inclusive process

One of the main aims of the HERMES experiment is the study of the semi-inclusive reaction process. The measurement of the hadron produced in the DIS reaction gives valuable information about which type of quark was hit in the process. In the simplest approach one can assume that the quark that was hit would be found in the hadron that was observed. This would allow a direct inference of the quark distributions. In reality the hadronization process complicates things considerably.

	$\frac{\Delta u}{u}$	$\frac{\Delta d}{d}$	$\frac{\Delta s}{s}$	$\frac{\Delta \bar{u}}{\bar{u}}$	$\frac{\Delta \bar{d}}{\bar{d}}$	$\frac{\Delta \bar{s}}{\bar{s}}$
A^{π^+}	0.75	0.10	0.00	0.07	0.08	0.00
A^{π^0}	0.48	0.28	0.00	0.17	0.07	0.00
A^{π^-}	0.27	0.42	0.00	0.27	0.05	0.00
A^{K^+}	0.72	0.14	0.00	0.02	0.01	0.07
A^{K^0}	0.14	0.67	0.00	0.08	0.03	0.08
A^{K^-}	0.18	0.11	0.12	0.48	0.07	0.02

Table 1.3: Quark purity matrix for $x = 0.1$, integrated for $z > 0.4$ as calculated from a PEPSI simulation under fairly simplistic assumptions

1.3.1 The hadronization process

The fact that partons have never been observed as free particles has forced us to rethink the way we look at experimental evidence for a theoretical description of nature. The concept of asymptotic freedom, a consequence of QCD, guarantees that quarks can never be observed as separate entities. Indeed, since all partons are colored quantities, and the color force does not decay with distance (in fact it increases with distance), the potential energy of a bare parton is infinite. So it is clear that figure 1-1 is only the first part of the scattering process. There has to be a final state interaction *dressing* the colored entities. This process is called *hadronization*. One simple but effective model for the hadronization process is described in reference [24].

One can estimate the probability that each type of hadron identified in the detector was the result of the hadronization of particular type of quark struck in the nucleon [25]. One defines this *quark purity* P_f^h of each hadron from the following:

$$A^h = \sum_f P_f \cdot \frac{\Delta q_f}{q_f} \quad (1.65)$$

A very simple model for the hadronization has been used to calculate these purities with the PEPSI [26] monte carlo code. The results are tabulated in table 1.3. They clearly show the u-dominance for those hadrons containing a valence u-quark, and in principle it is clear that the measurement of all 6 asymmetries would allow the extraction of all polarized quark distributions through simple matrix inversion. More detailed studies of these quantities will be undertaken.

1.3.2 Some applications of the semi-inclusive process at HERMES

The natural extension to the study of spin-dependent DIS is the study of the semi-inclusive reaction. Some of the most interesting possibilities are discussed here.

1.3.2.1 The contribution to the spin of the valence quarks

With the inclusive reaction it is not possible to distinguish between valence quarks and sea quarks. It is however possible to isolate the valence quark contribution when we also measure the leading hadron using the *double pion asymmetries*:

$$A^\pi = \frac{\left(N_{\uparrow}^{\pi^+} - N_{\uparrow}^{\pi^-}\right) - \left(N_{\downarrow}^{\pi^+} - N_{\downarrow}^{\pi^-}\right)}{\left(N_{\uparrow}^{\pi^+} - N_{\uparrow}^{\pi^-}\right) + \left(N_{\downarrow}^{\pi^+} - N_{\downarrow}^{\pi^-}\right)} \quad (1.66)$$

where $N_{\uparrow(\downarrow)}^{\pi^{+(-)}}$ is the number of positive (negative) pions detected for a parallel (anti-parallel) target polarization. The counts can be separated into x and y bins.

Measuring this asymmetry on two different targets allows the extraction of the valence quark polarization from the following:

$$\begin{aligned} A_p^\pi(x) &= \frac{4\delta u_v(x) - \delta d_v(x)}{4u_v(x) - d_v(x)} \\ A_d^\pi(x) &= \frac{\delta u_v(x) + d_v(x)}{u_v(x) + d_v(x)} \\ A_{He}^\pi(x) &= \frac{-\delta u_v(x) + 4\delta d_v(x)}{7u_v(x) + 2d_v(x)} \end{aligned} \quad (1.67)$$

HERMES intends to improve upon the existing results from the SMC experiment by increasing the statistics and by providing a clean pion identification.

1.3.2.2 The polarization of the strange sea

The strange sea has been the source of much interest over the past few years. Its large and negative polarization is the central result from the inclusive measurements. To provide more information on the distribution of the polarization in the strange sea one can follow a technique outlined in reference [27].

One can define the following branching ratios:

$$n^{\uparrow\downarrow}(x, z) = \frac{1}{\sigma_{\uparrow\downarrow}^T} \times \frac{d\sigma_{\uparrow\downarrow}^{\pi^+\pi^-}}{dz}$$

$$n^{\uparrow\uparrow}(x, z) = \frac{1}{\sigma_{\uparrow\uparrow}^T} \times \frac{d\sigma_{\uparrow\uparrow}^{\pi^+\pi^-}}{dz}$$
(1.68)

In the quark parton model, neglecting the quark masses, we can write this as:

$$n^{\uparrow\downarrow}(x, z) \equiv \frac{\left[\frac{4}{9}u_+(x) + \frac{1}{9}d_+(x) \right] \times D(z) + \frac{1}{9}s_+(x) \times D_s(z)}{\frac{4}{9}u_+(x) + \frac{1}{9}d_+(x) + \frac{1}{9}s_+(x)}$$

$$n^{\uparrow\uparrow}(x, z) \equiv \frac{\left[\frac{4}{9}u_-(x) + \frac{1}{9}d_-(x) \right] \times D(z) + \frac{1}{9}s_-(x) \times D_s(z)}{\frac{4}{9}u_-(x) + \frac{1}{9}d_-(x) + \frac{1}{9}s_-(x)}$$
(1.69)

where $D(z)$ is the usual light quark fragmentation function in the assumption of isospin and charge conjugation symmetry:

$$q_+(x) \equiv q_+^{3He, val}(x) + q_+^{3He, sea}(x) + \bar{q}_+^{3He, sea}(x)$$

$$D_u^{\pi^+\pi^-}(z) = D_{\bar{u}}^{\pi^+\pi^-}(z) = D_d^{\pi^+\pi^-}(z) = D_{\bar{d}}^{\pi^+\pi^-}(z) \equiv D(z)$$

$$D_s^{\pi^+\pi^-}(z) = D_{\bar{s}}^{\pi^+\pi^-}(z) \equiv D_s(z)$$
(1.70)

Rewriting the equations to eliminate non-strange distributions is easy if we rely on the QPM formula for the inclusive deep inelastic scattering cross section:

$$\frac{4}{9}u_{(+,-)} + \frac{1}{9}d_{(+,-)} + \frac{1}{9}s_{(+,-)} = 2F_1^{3He}(x)(1 \pm A_1^{3He}(x))$$
(1.71)

and it gives:

$$n^{(\uparrow\downarrow),(\uparrow\uparrow)}(x, z) = D(z) + \frac{[D_s(z) - D(z)] \times [s(x) \pm \Delta s(x)]}{18F_1^{3He}[1 \pm A_1^{3He}]}$$
(1.72)

From this expression we determine the sum and difference of the branching ratios:

$$\begin{aligned}
 n^{\uparrow\downarrow}(x, z) + n^{\uparrow\uparrow}(x, z) &= 2D(z) + \frac{[D_s(z) - D(z)]}{9F_1^{3He}} \times \left(\frac{s(x) - A_1^{3He} \Delta s(x)}{1 - [A_1^{3He}]^2} \right) \\
 n^{\uparrow\downarrow}(x, z) - n^{\uparrow\uparrow}(x, z) &= \frac{[D_s(z) - D(z)]}{9F_1^{3He}} \times \left(\frac{\Delta s(x) - A_1^{3He} s(x)}{1 - [A_1^{3He}]^2} \right)
 \end{aligned} \tag{1.73}$$

The unknown strange quark fragmentation function can now be eliminated and we get the following relation:

$$n^{\uparrow\downarrow}(x, z) - n^{\uparrow\uparrow}(x, z) = [n^{\uparrow\downarrow}(x, z) + n^{\uparrow\uparrow}(x, z) - 2D(z)] \times \left(\frac{\Delta s(x) - A_1^{3He} s(x)}{s(x) - A_1^{3He} \Delta s(x)} \right) \tag{1.74}$$

Finally we solve this equation for the strange sea polarization to find:

$$\Delta s(x) = \left(\frac{1 + \frac{\alpha}{\beta} \times A_1^{3He}}{\frac{\alpha}{\beta} + A_1^{3He}} \right) \times s(x) \tag{1.75}$$

where we defined:

$$\begin{aligned}
 \alpha &\equiv n^{\uparrow\downarrow}(x, z) + n^{\uparrow\uparrow}(x, z) - 2D(z) \\
 \beta &\equiv n^{\uparrow\downarrow}(x, z) - n^{\uparrow\uparrow}(x, z)
 \end{aligned} \tag{1.76}$$

The counts are binned in x and z , so we will need to integrate the above formula. This is easily done and the result is the following formula :

$$\begin{aligned}
 \langle \Delta s(x) \rangle_{bin} &= \left(\frac{1 + \langle \frac{\alpha}{\beta} \rangle_{bin} \times \langle A_1^{3He} \rangle_{bin}}{\langle \frac{\alpha}{\beta} \rangle_{bin} + \langle A_1^{3He} \rangle_{bin}} \right) \times \langle s(x) \rangle_{bin} \\
 \langle \frac{\alpha}{\beta} \rangle_{bin} &= \frac{\mathcal{N}^{\uparrow\downarrow} + \mathcal{N}^{\uparrow\uparrow} - \left[2 \int D(z) \cdot \varepsilon(z) \cdot dz \right] \Delta x}{\mathcal{N}^{\uparrow\downarrow} - \mathcal{N}^{\uparrow\uparrow}}
 \end{aligned} \tag{1.77}$$

In this result the unpolarized sea quark distribution is the sum of the distributions in the two protons and the neutron. Similarly Δs is the sum of the sea polarizations in the three nucleons of ^3He .

We will assume that the sea polarizations are the same in proton and neutron. Then:

$$\begin{aligned} s(x) &= s_n(x) + 2s_p(x) \\ \Delta s(x) &= \Delta s_n(x) = \Delta s_p(x) \end{aligned} \quad (1.78)$$

The parameterization of $s(x)$ can be taken from the CTEQ3 FORTRAN subroutines. In essence HERMES measures only the **relative** sea polarization, so that the final result for the strange sea polarization depends on the parameterization of the unpolarized sea only in a trivial way. For the fragmentation function one could use the EMC parameterization for the $\pi^+ \pi^-$ (reference [28]):

$$\begin{aligned} D^{\pi^+} &= 0.7 \times \frac{(1-z)^{1.75}}{z} \\ D^{\pi^-} &= \frac{1-z}{1+z} \times D^{\pi^+} \end{aligned} \quad (1.79)$$

The result is however very sensitive to the fragmentation function, so it will be necessary to determine the fragmentation functions for our exact kinematics. This has been done in dedicated unpolarized runs throughout the running period.

1.3.2.3 Physics from the Λ production

The unique property of the Λ -particles among the light hadrons is that their polarization is easily measured. Its dominant non-leptonic decay $\Lambda \rightarrow p\pi$ is self-analyzing. Under assumption of SU(3)-symmetry one can determine the integrated quark spin contribution for the Λ (reference [29]) :

$$\Delta u_\Lambda \approx -0.12 \quad \Delta d_\Lambda \approx -0.12 \quad \Delta s_\Lambda \approx 0.66 \quad (1.80)$$

The contribution of the u and d quarks has to be equal since the Λ is an isosinglet. Assuming u-quark dominance in Λ production one deduces that the polarization transferred from the beam to the Λ in the production process is given by:

$$P_\Lambda = P_b \frac{y(2-y)}{1+(1-y)^2} \frac{\Delta D_\Lambda^u}{D_\Lambda^u} \quad (1.81)$$

The ΔD_Λ^u and D_Λ^u are the spin-dependent and spin-independent fragmentation functions. With the expected count of 4000 Λ events in the current fragmentation region, HERMES is expected to be sensitive to a relative spin-dependent fragmentation function $\frac{\Delta D_\Lambda^u}{D_\Lambda^u}$ as small as 0.05.

Interestingly the same analysis can be applied when the beam is transversely polarized, allowing a measurement of the *transverse* polarized u-quark distribution in the nucleon.

It has also been shown that Λ 's in the target fragmentation region are sensitive to the polarization of strange quarks in the nucleon. HERMES has detected Λ 's in that kinematical domain.

1.4 Other polarized lepton-quark scattering experiments

1.4.1 The SLAC experiments

A 20 year program of measurements of *inclusive* polarized DIS has been undertaken at SLAC using the A-line electron beam at energies up to 48.6 GeV. All targets are high density liquid and gas targets. This is necessary to obtain sufficiently high count rates. The drawback to these type of targets is that they require containment and high concentrations of non-target atomic species, as for instance in the case of the ammonia or butanol targets. This requires additional corrections to the measured asymmetry. The relevant SLAC experiments have been summarized in the following table.

experiment	beam type	beam energy	target type	x range	Q^2 range	Q^2 average
E80	electrons	16	H-butanol	0.03 - 0.6		2
E130	electrons	19.4/22.7/25.5	H-butanol	0.03 - 0.6		2
E142	electrons	19.4/22.7/25.5	^3He	0.03 - 0.6		2
E143	electrons	9.7/16.2/29.1	NH_3/ND_3	0.029 - 0.8	1.3 - 10	
E154	electrons	48.6 - 82	^3He	0.015 - 0.7	1 - 16	5
E155	electrons	48.55 - 82	NH_3/LiD	0.015 - 0.85	1 - 17	

1.4.2 The CERN experiments

Another extensive program of polarized scattering experiments has been executed at CERN. All experiments used the extracted muon beam from the SPS. The main advantage of this beam is that it is highly energetic and naturally polarized to a high degree. The corresponding disadvantage is that the maximal current achievable is not very high.

experiment	beam type	beam energy	target type	x range	Q^2 range
EMC (1985)	muons	100-200	NH_3	0.005 - 0.75	1 - 200
NMC	muons	90/120/280	H-butanol/D-butanol	0.005 - 0.75	1 - 200
SMC (1992-1996)	muons	100/190	H-butanol/D-butanol/ NH_3	0.003 - 0.7	1 - 60

In figure 1-10 the Ellis-Jaffe prediction for Γ_1^n is shown together with the experimental data. It is clear that the underlying assumption of unpolarized strange quarks is not validated by the experiments. The results for the integrals from the different experiments are also shown in table 1.4.

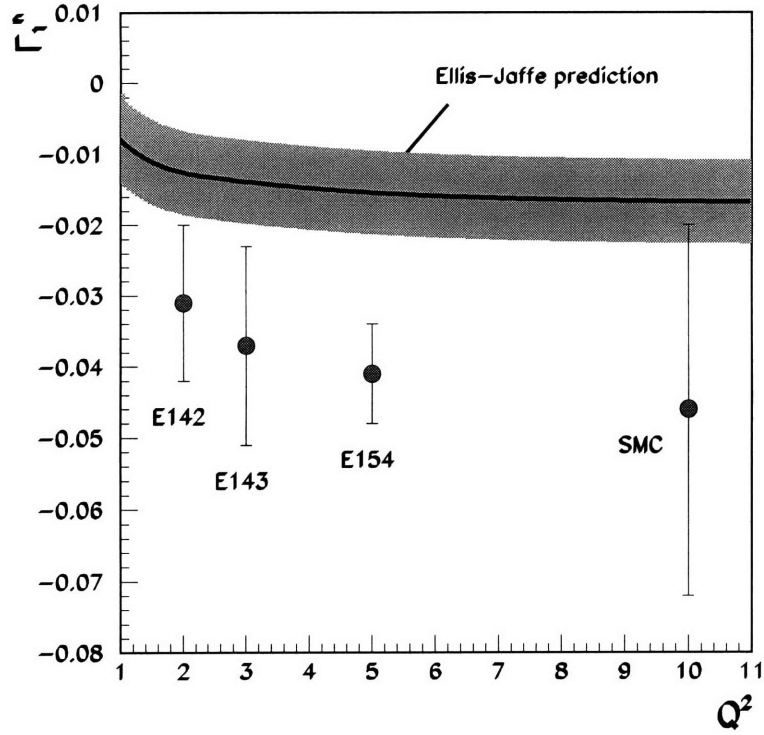


Figure 1-10: Ellis-Jaffe prediction for Γ_1^n versus Q^2 and experimental results.

experiment	Γ_1^n	reference
E142	-0.031 ± 0.011	[30]
E143	-0.037 ± 0.014	[31]
E154	-0.041 ± 0.007	[32]
SMC	-0.046 ± 0.026	[33]

Table 1.4: Experimental data for Γ_1^n

Chapter 2

The HERMES experiment

A unique feature of the HERMES experiment is that it does not use a dense target in an extracted beam, but a thin gas target internal to a storage ring. This allows for a very clean experiment, with different systematic errors from the previous experiments. In this sense the experiment is complementary to other experiments that access the same physical quantities. But the HERMES detector was also designed as a second generation experiment, not only able to study the inclusive process, but also equipped with extensive particle identification to allow the study of semi-inclusive processes.

2.1 The HERA accelerator facility

The choice of the storage ring was mainly determined by the requirement of fast polarization build-up and sufficient beam energy to allow DIS experiments. For this reason the experiment was proposed at the HERA storage ring located at DESY in Hamburg, Germany. HERA is the only operating storage ring providing a polarized lepton beam of sufficient energy for the HERMES experiment. The HERA accelerator was primarily constructed for the collider experiments ZEUS and H1, which are situated in the south and north halls respectively. The proton ring can store typically 60 mA of protons at 820 GeV, the lepton ring 35 mA at 27 GeV. These numbers fall somewhat short of the original design specifications and a major upgrade is planned for the shutdown of 1999-2000. The HERMES experiment was built in the east hall of the ring. This hall (as well as the opposing west hall) was originally foreseen to be used for an additional collider experiment, so both beams crossed each other very closely. The beams were separated by 72 cm and given separate beam lines. This shields the proton ring almost completely from the effects of the internal target. To reduce the background from synchrotron radiation the electron ring lattice was reconfigured within ± 88.5 meters of the target.

2.1.1 The Sokolov-Ternov effect

The polarization of the leptons is accomplished by the Sokolov-Ternov effect [34]. This effect is caused by a small asymmetry in the synchrotron radiation cross section. For electrons moving in a plane perpendicular to a uniform, constant magnetic field, the polarization will build up exponentially:

$$P(t) = P_o(1 - e^{-\frac{t}{\tau_{ST}}}) \quad (2.1)$$

The asymptotic value of the polarization in this ideal “flat” machine is 92.38%. The polarization build-up time depends highly on the beam energy and bending radius ρ of the magnetic field (since they determine the amount of synchrotron radiation being emitted):

$$\tau_{ST} = \left(\frac{5\sqrt{3}c\bar{\lambda}_c r_o \gamma^5}{8\rho^3} \right)^{-1} \quad (2.2)$$

In this formula $\bar{\lambda}_c$ is the reduced Compton wavelength of the electron and r_o is the classical radius of the electron. The polarization achieved in this manner is anti-parallel to the magnetic field for electrons and parallel for positrons.

In a real storage ring the magnetic fields are non-uniform, bending and acceleration are discrete events and imperfections (misalignment, field errors) are unavoidable. The complete description of the polarization process becomes extraordinarily difficult, necessitating the precarious balancing act of applying quantum mechanics to semi-classical orbits. A simpler but insightful approximation is to treat the non-uniform fields in a classical manner by extending the Sokolov-Ternov result. Then the discrete, quantum-mechanical character of the process can be taken into account as a depolarizing effect, called the spin diffusion process.

The extension to non-uniform fields has been studied ([35],[36]) based on the Thomas-BMT equation ([37],[38]) for the precession of the spin.

$$\frac{d\vec{P}}{ds} = \frac{e\vec{P}}{m_e c \gamma} \times \left((1 + a\gamma)\vec{B}_\perp + (1 + a)\vec{B}_\parallel \right) \quad (2.3)$$

The polarization vector \vec{P} is defined in the rest frame of the lepton, $a = \frac{g-2}{2}$ with g the electron anomalous moment factor; s is the longitudinal coordinate. The magnetic field vectors are decomposed in \vec{B}_\perp and \vec{B}_\parallel with respect to the trajectory of the lepton. Closed orbits lead to periodic solutions for the precessing spin. The number of precessions per turn is the so-called spin tune, denoted as ν .

The polarization is in general no longer directed along the local magnetic field. The only change in the build-up time τ_{ST} is a replacement of the bending radius ρ with an effective one ρ_{eff} :

$$\rho_{eff}^{-3} = \frac{1}{C} \int \frac{ds}{|\rho(s)|^3} \quad (2.4)$$

where C is the ring circumference and $\rho(s)$ the local bending radius on the orbit. The spin tune at HERA is 62.5 at 27.5 GeV with a build-up time of 37 minutes. The maximum polarization achievable in the ring is not affected if there are no horizontal magnetic fields on the closed orbits. Under ideal circumstances this is not a problem since the design of a storage ring usually requires the dipole magnets to have only a vertical field. Should the lepton see horizontal field components, the solution for the polarization will acquire a tilt from the magnetic field, making the radiation less effective in polarizing the beam. This “weakening” of the Sokolov-Ternov effect is usually a negligible factor compared to the depolarization arising from the spin diffusion that will occur in such a situation.

The effect of the quantum mechanical nature of the synchrotron radiation process is called spin diffusion. The primary cause of spin diffusion is that the stochastic emission excites oscillations of the leptons around the closed orbit. When fields are not always vertical on the closed orbit, this will lead to small changes in the spin orientation. The stochastic nature of this effect means that it will randomize the spins - hence it depolarizes. This effect is again due to the presence of non-uniform fields, a situation that is in general worst in the quadrupole magnets.

The spin diffusion can be considered to work simultaneously with the Sokolov-Ternov effect. Since the diffusion rate is constant (for a constant orbit), it can be characterized by a diffusion time constant, τ_D . The process will not change the exponential character of the polarization build-up, but it reduces the maximum polarization achievable:

$$P_{max} = P_o \frac{\tau_D}{\tau_{ST} + \tau_D} \quad (2.5)$$

The time constant of the exponential will also change:

$$\tau = \frac{\tau_{ST}\tau_D}{\tau_{ST} + \tau_D} \quad (2.6)$$

From the above it should be obvious that spin diffusion is as unavoidable an effect as the Sokolov-Ternov effect, at least in normal storage rings. Although a minimal diffusion cannot be avoided because of the non-uniform character of the magnets used, it should also be clear that a bad orbit can significantly worsen the situation. Tuning the orbit for maximum polarization will be necessary.

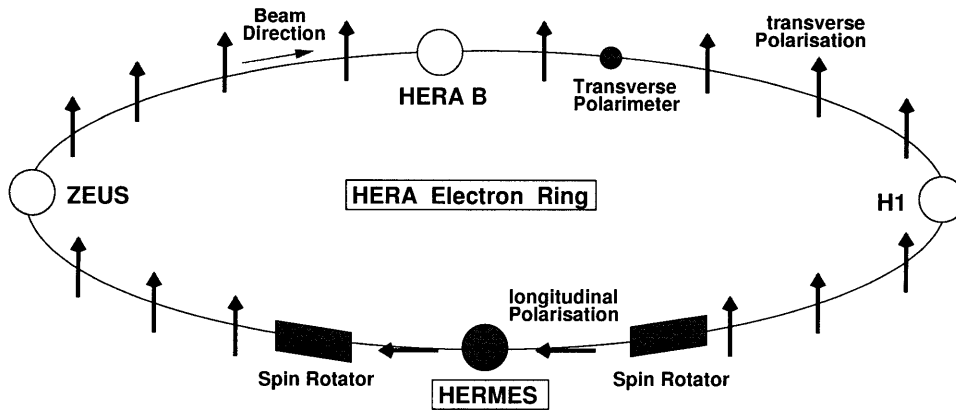


Figure 2-1: The HERA ring with the HERMES spin rotators

Complicating the situation is the fact that one requires longitudinal beam polarization to probe the spin structure of the nucleon. This is accomplished by the insertion of a spin rotator before and after the HERMES experiment (see figure 2-1). These rotators [39], consisted of three horizontal bends interleaved with three vertical bends. The length of the rotator is only 56 meters. The angle of rotation depends on the energy of the beam, so that each beam energy requires a somewhat different positioning of the magnets. The motion range of the HERA rotator magnets allows operation between 27.5 and 35 GeV. The bending of the orbit necessitates the use of horizontal fields, thereby reducing the maximum polarization achievable. The calculated effect of the set of rotators on the HERA ring in terms of weakening the Sokolov-Ternov effect is a reduction of the maximally achievable polarization from 92.38% to 89%, with a small reduction in the build-up time to 36 minutes. As mentioned above, the influence of the presence of horizontal fields on the diffusion process is much larger. This can be calculated by the Monte Carlo program SITROS ([40],[41]). It is of course impossible to take into account the effects of the misalignments in the ring exactly, since they are not known. It is hence impossible to design a tune to correct them (as can be done by the spin-matching technique). Therefore it was decided to use the more flexible technique of “harmonic spin-orbit corrections”. The optimization of these corrections had to be done empirically. The result is shown in figure 2-2. The HERA ring now delivers reproducible, highly polarized lepton beam.

It was not clear at first that this method would yield useful polarizations due to the very *non-ideal* nature of the storage ring. Especially worrisome was the influence of the (unpolarized) proton beam on the electron beam at the collision points at ZEUS and H1. To cover this eventuality it was decided that HERMES would get dedicated beam time if the polarized beam could not coexist with the collider experiments. Fortunately it was shown to be perfectly possible for all three experiments to take data simultaneously.

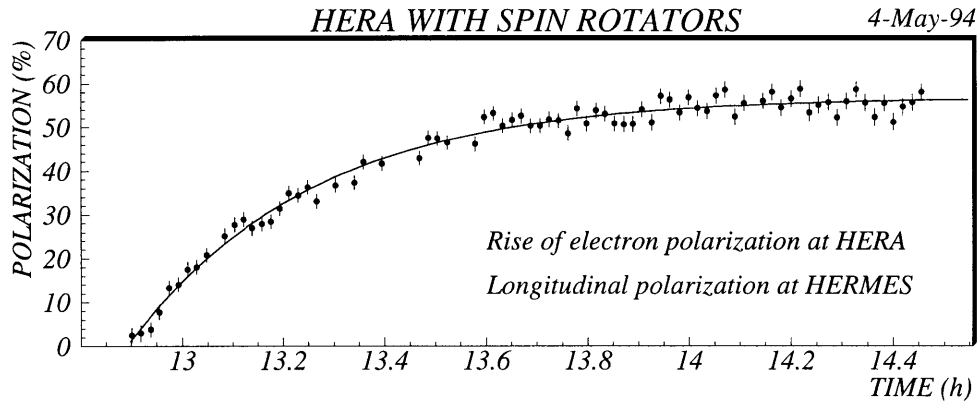


Figure 2-2: The polarization build-up in the HERA positron ring.

2.1.2 The beam polarimeter

The beam polarization is measured using a laser backscattering Compton polarimeter. An Argon-ion laser provides 10 Watts of continuous, polarized laser light, which is transported over more than 200 meter to the interaction point (see figure 2-3). The helicity of the laser light is switched with a frequency of 83.8 Hz using a Pockels cell. The energy and position of the back-scattered photons is measured with a tungsten-scintillator calorimeter (see figure 2-4) 65 meters from the interaction point. The transverse polarization of the positron beam causes a spin-dependent vertical asymmetry in the polarimeter. This asymmetry changes sign when the helicity of the laser light is switched.

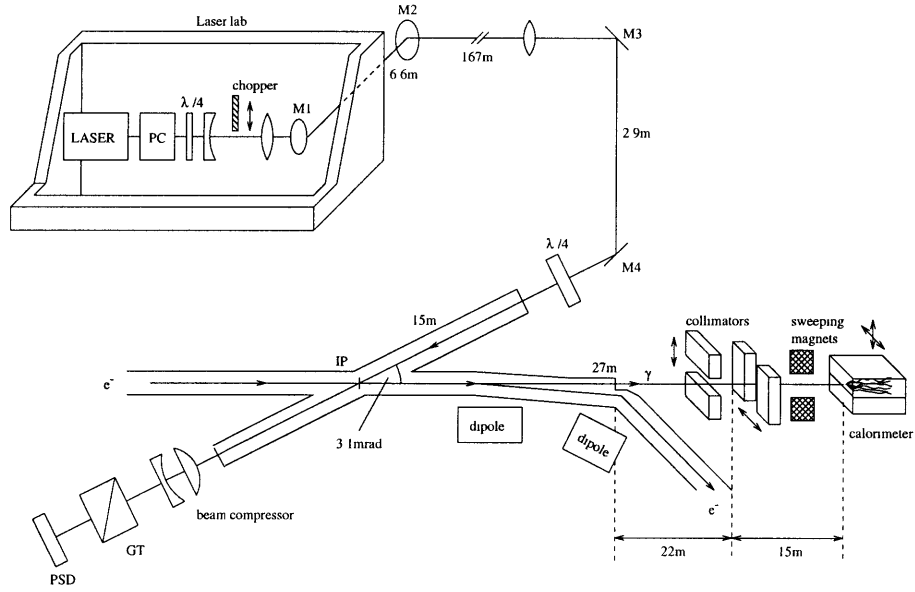


Figure 2-3: Layout of the transverse beam polarimeter

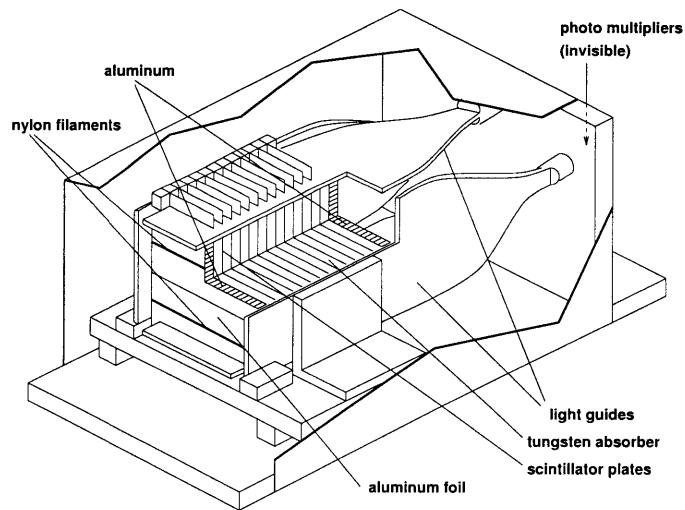


Figure 2-4: Internal structure of the beam polarimeter's calorimeter

2.2 The HERMES spectrometer

The collimators and the storage cell had to be positioned at the beam waist. Since the halls were built to accommodate collider experiments, the detector was foreseen to be heavily asymmetric, and of course biased toward the forward region with respect to the proton ring. Hence the HERA halls were not built symmetrically around the beam waist, allowing only 8.5 meters for the installation of the spectrometer.

The HERMES spectrometer was built on a movable platform. This was done for several reasons. Firstly it allowed the spectrometer to be assembled outside the shielding in the hall during the machine operation. This also meant that major damage to the spectrometer could be repaired after installation of a replacement beam pipe, allowing the machine operation to resume while the repairs are made. Secondly it allowed for a rapid removal of the experiment in case the HERA TRAM needed to be inserted. The TRAM is a versatile transport and installation vehicle designed specifically for the HERA tunnel. In case of a major failure in the accelerator, HERMES must remove its spectrometer within 24 hours to allow the TRAM to access the tunnel.

The combination of fixed target and high energy beam means that the angular distribution of the scattered particles is strongly peaked in the forward direction. To be able to study a large kinematic region the spectrometer was designed with a large angular acceptance. Especially the minimal scattering angle is important since it determines the smallest value of x that the experiment can access. It was limited by the fast increase in the synchrotron radiation background at small angles. The minimal vertical angle was 40 mrad, the maximum 140. The horizontal acceptance is ± 170 mrad. The distributions of several crucial kinematic variables as well as the angular distributions for the DIS positrons are shown in figure 2-6.

The background for the experiment consists mainly of synchrotron radiation, scattering of the beam halo from the collimator system and protons lost in the proton ring. The first two sources of background can be minimized by a good beam tune. The proton background is out of time with the electron bunches and can be eliminated by a simple trigger gate. Only “side-bunches” of protons can therefore cause backgrounds in the spectrometer. A veto detector was set up to monitor this background.

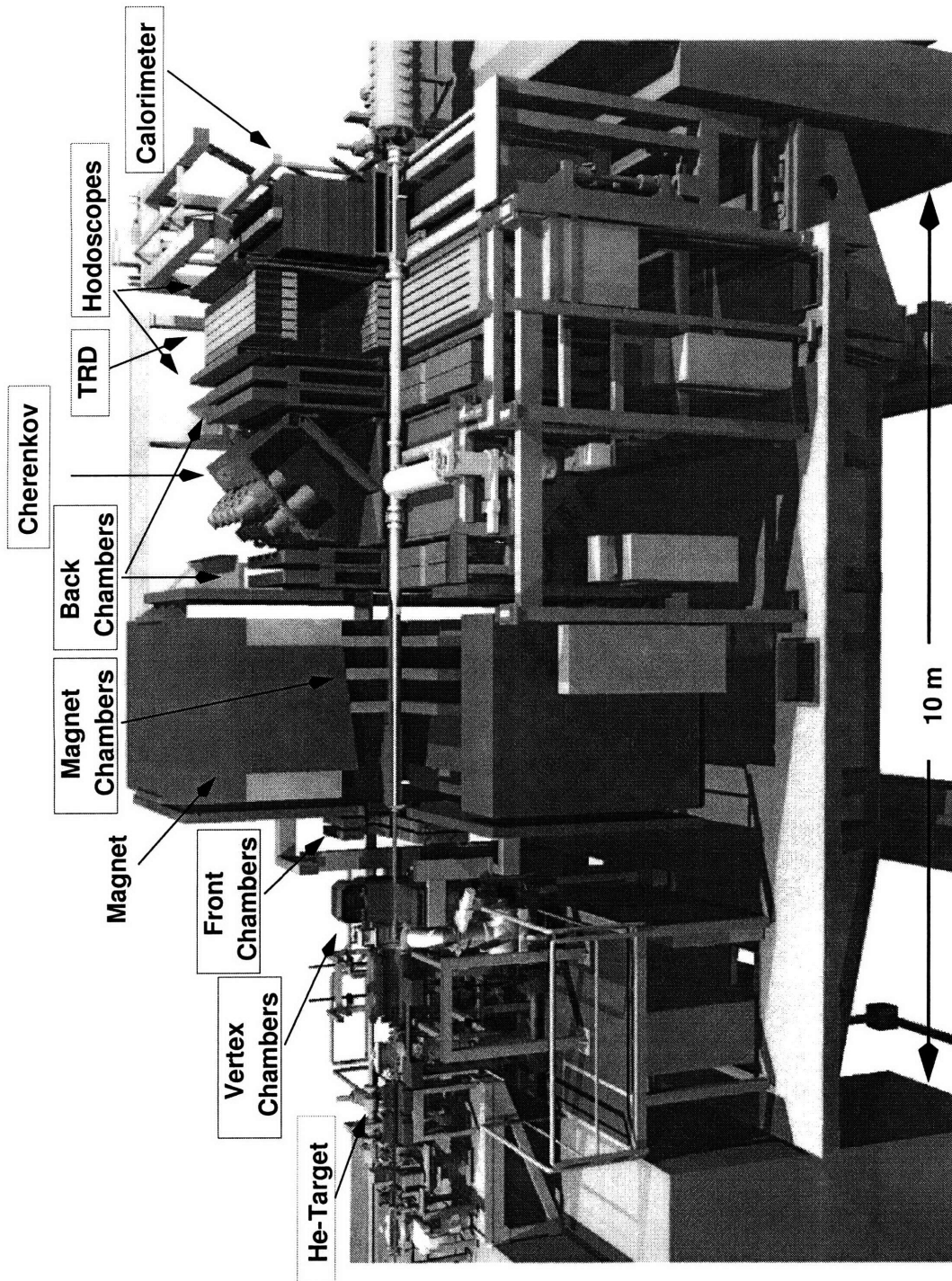


Figure 2-5: An overview of the HERMES detector.

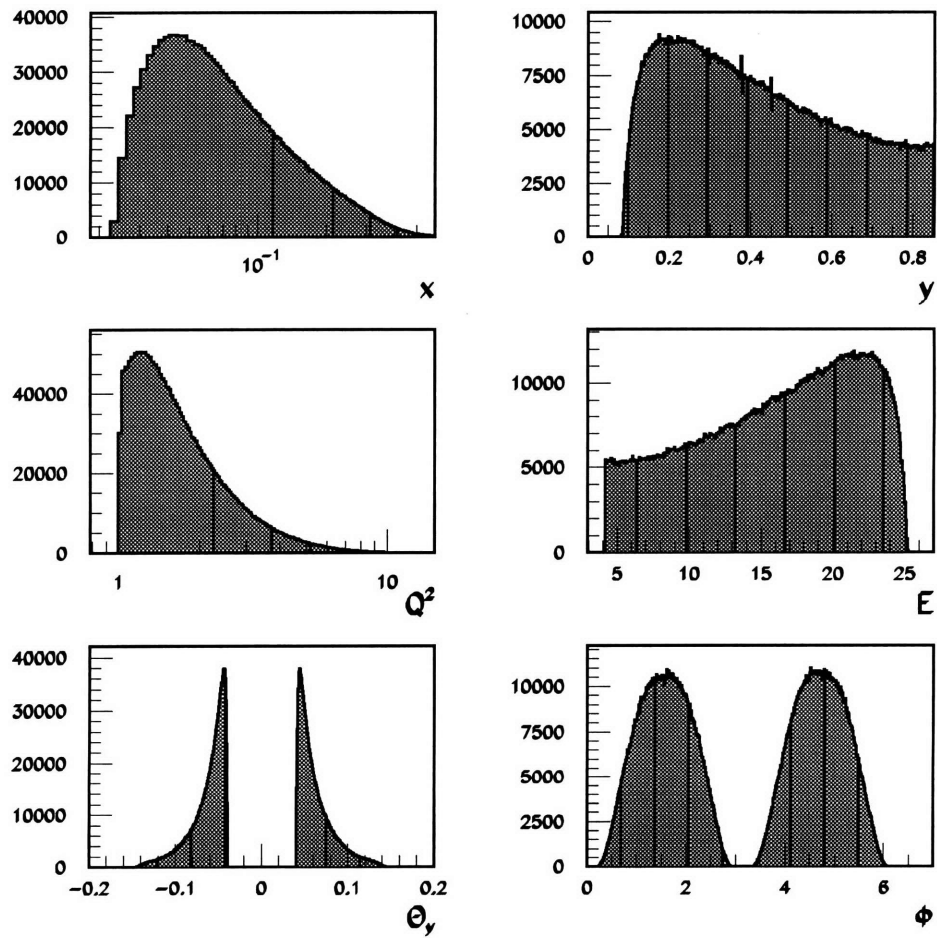


Figure 2-6: Distributions for the DIS positrons in the HERMES detector

2.2.1 The spectrometer magnet

As can be seen in figure 2-5, the core of the HERMES spectrometer is a large conventional spectrometer magnet. The dipole field has an integrated strength of 1.5 T-m, but it was run at only 1.3 T-m for the experiment. The magnet frame is an H-type with the coils internal to the magnet steel. The variation in the integrated field strength for particles within the geometrical acceptance is less than 10%. The power consumption of the magnet is 729 kWatt at the design strength.

The influence of this field on the beams would be unacceptable, so an iron septum plate was mounted in the beam plane. Both beam pipes pass through this plate. To further reduce both dipole and higher order fields several coils were built into the septum plate. Careful field mapping alternated with adjustments in coil current distribution was needed to cancel the stray field effects. To reduce the influence of the stray fields on the spectrometer performance field clamps were mounted on the sides of the magnet. This reduced the stray fields in the tracking detectors from 0.32 T to 0.1 T. In the target region the fields were still in the order of 20 Gauss with a gradient in the order of 220 mGauss/mm. This was enough to warrant serious studies for the helium target, resulting in the addition of a compensating coil to the target assembly to reduce the depolarizing gradient (see section 3.4.4).

2.2.2 The tracking detectors

The tracking detectors consist of several sets of chambers. The distribution of these chambers can be seen in figure 2-7. For tracking purposes we divide the detector into three regions with respect to the spectrometer magnet: *forward*, *back* and *magnet*. The forward region is covered by the vertex chambers (VC) and forward chambers (FC). This region determines the angle of the track and its scattering vertex. The back region is covered by two sets of back chambers (BC). Together with the track in the forward region this determines the angle of deflection of the particle in the spectrometer magnet and hence its momentum. It is of course crucial to match both tracks up correctly. For this reason additional chambers were inserted inside the magnet. These magnet chambers (MC) can also be used to increase the acceptance of the detector for low energetic particles.

All chambers measure three coordinates: u , v and x . The x -coordinate is in the plane of the beams, so the x -detection wires need to be vertical. The u and v coordinates are measured with wires that are mounted at an angle of 30° with respect to the vertical. The use of horizontal wires to measure the y -component of the hits directly would have been preferable, but it was not pursued for practical reasons. The fact that all chambers measure the same coordinates makes it possible to reconstruct the tracks in

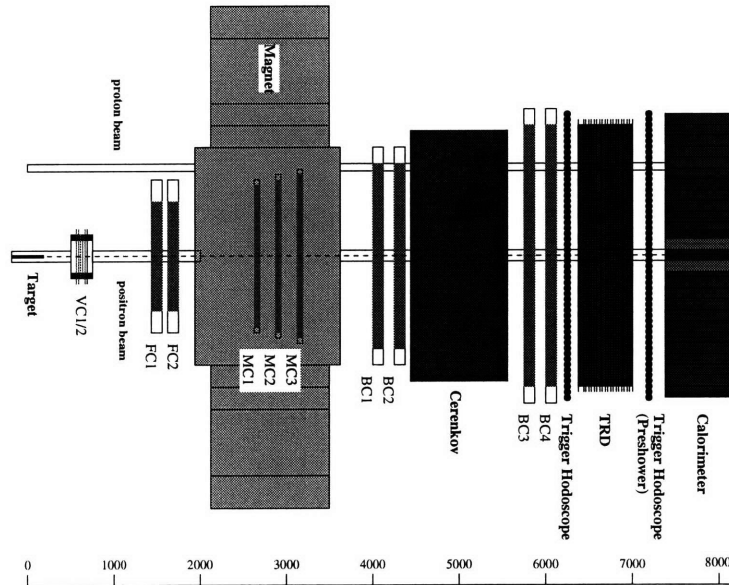


Figure 2-7: Schematic view of the tracking chambers in the HERMES detector

all three projections before combining them. This allows for a more robust and faster reconstruction algorithm.

A reconstructed event highlighting the use of all detectors is shown in figure 2-8. This event is not very typical since it is a high multiplicity event. The average multiplicity is only 1.3 tracks per event. In figure 2-9 the transverse and longitudinal coordinates of the reconstructed vertex are shown. It is clear from those plots that no scattering from the cell walls or the collimators interferes with the measurement.

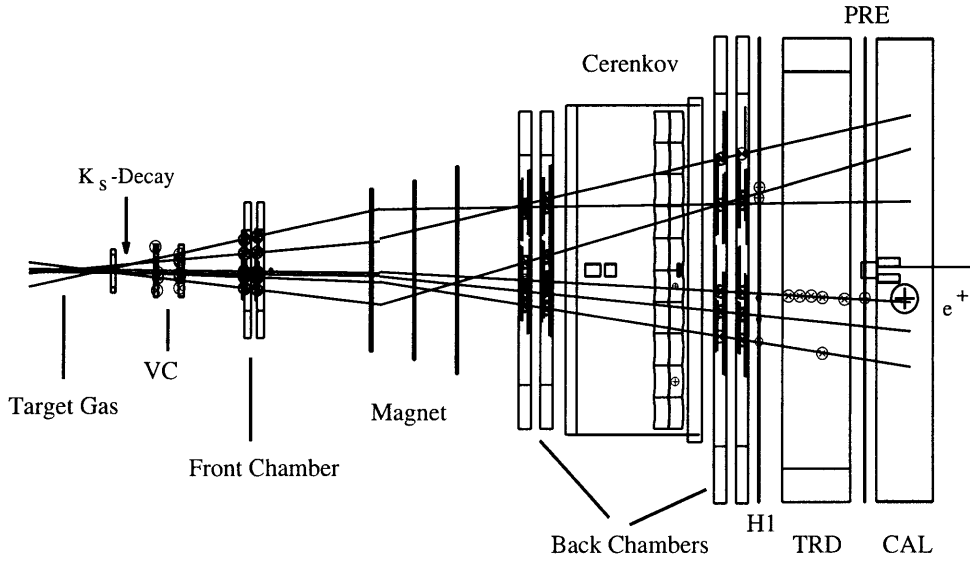


Figure 2-8: Reconstructed high multiplicity event containing a decaying K_s

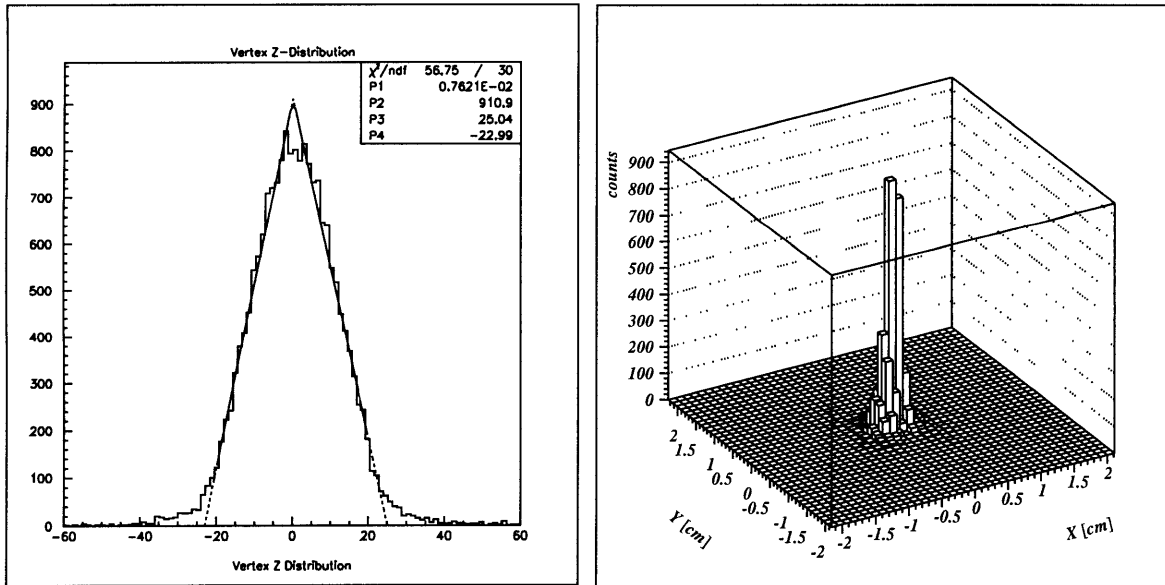


Figure 2-9: The distributions of the reconstructed vertices

2.2.2.1 The vertex chambers

The vertex chambers have to sustain very large background rates and provide enough precision to determine the vertices accurately. HERMES used micro-strip gas chambers for this purpose. Each chamber consists of two modules, with each one plane for the u-, v- and x-direction. Each plane consists of a planar cathode foil and an anode plane. The cathode foil provides a 5 kV/cm drift field over the 3 mm volume between the foil and the substrate. The gas in this volume is a mixture of 60% DME and 40% CO₂. The anode plane consists of a 300 μm thick glass substrate covered with 1 μm thick aluminum anode and cathode strips. The anode strips are 7 μm wide and 193 μm apart, giving a cell size of 0.2 mm. The anodes are interlaced with 90 μm wide cathode strips.

This design has about three times the gain level of silicon detectors of the same thickness. A spatial resolution of 45 μm per module was obtained, translating in a 200 μrad angular resolution for the chamber. This is comparable to the uncertainty due to multiple scattering in the exit window.

During the 1995 data taking the vertex chambers did not function properly. Sustained oscillations in the electronics reduced their efficiency to a level at which they could not be used for standard tracking. Using the VC's for tracking we did construct a smaller data set with which other tracking methods could be checked for systematic biases. The read-out electronics were redesigned and new chips were installed for the 1996 data taking period.

2.2.2.2 The forward chambers

The second set of tracking chambers in the forward region is a drift chamber with a conventional horizontal drift configuration. Each plane is a layer of drift cells consisting of a wire plane of alternating anode and cathode wires between a pair of cathode foils. Each chamber consists of 6 planes, two for each coordinate u, v and x. The second plane for each coordinate is staggered with respect to the first to resolve left-right ambiguities. The gas mixture consists of 90% Argon, 5% CF₄ and 5% CO₂.

The drift cell size of only 7 mm was chosen to reduce the influence of the background. The resolution was expected to be 150 μm , but pick-up from the target RF discharge reduced the observed resolution to $\sim 400 \mu\text{m}$.

2.2.2.3 The back chambers

The back region tracking is done with two sets of drift chambers BC1/2 and BC3/4, positioned respectively at 3.95 and 5.70 meter downstream of the interaction point. They use the same horizontal drift configuration as the forward chambers but with a cell size of 15 mm. The gas mixture was common to both chambers, simplifying the operation of the tracking chambers. Despite their larger cell size a resolution of 150 μm was expected. This is due to the high drift velocity in the Ar/CF₄/CO₂ gas. Indeed, even in the larger cell the maximum drift time is 150 nsec, which compares favorably with the HERA bunch crossing time of 96 nsec. This means very few mixing of hits from different bunches will occur. However, the realistic resolution obtained during the 1995 data run was $\sim 400 \mu\text{m}$.

Each chamber consists of two modules containing 6 planes. This means that BC1/2 and BC3/4 each contains 24 planes, 12 above and 12 below the beam plane, for a total of 48 planes in each detector half.

2.2.2.4 The magnet chambers

The magnet chambers were added to make the matching of front and back tracks easier in case of high multiplicity events. The presence of the strong magnetic field and the low requirement on the resolution directed the choice of the proportional chamber technology for these chambers. The anode wires are separated by 2 mm, resulting in a resolution of 577 μm . Three chambers are present, each containing three planes (u, v and x). The gas used is a mixture of 65% Argon, 5% CF₄ and 30% CO₂.

An unexpected sensitivity of the backplane electronics to the magnetic field resulted in serious damage to the readout electronics early in the year. The limited accessibility of the chambers (inside the magnet) made it impractical to perform repairs. For the 1995 data the magnet chambers were therefore not used, except for specific studies of small-momentum particles, in particular for rare decays.

2.2.3 The particle identification detectors

For the study of inclusive reactions a good hadron-positron separation is necessary. The semi-inclusive processes require further identification of the hadrons. To accomplish these tasks HERMES uses the combination of several particle identification detectors. All are located in the back region of the detector.

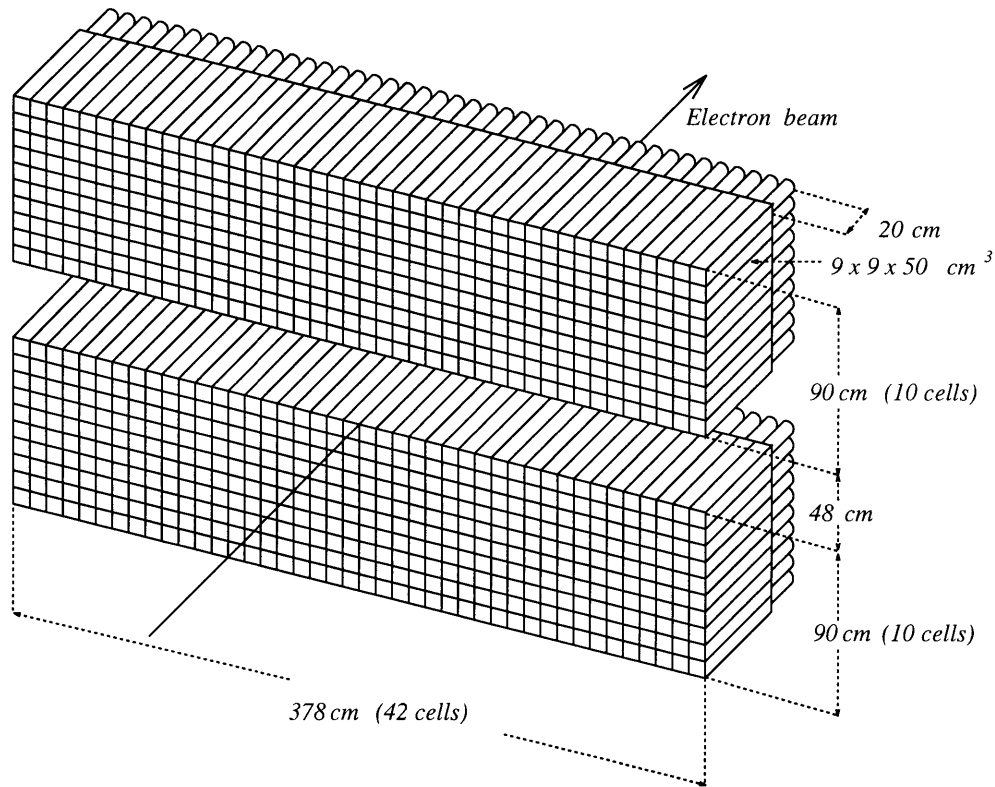


Figure 2-10: Isometric view of the HERMES calorimeter.

2.2.3.1 The calorimeter

The calorimeter is built in two halves (like every other HERMES detector), with each half containing 42×10 radiation resistant lead glass (F101) blocks. Each block has a surface of $9 \times 9 \text{ cm}^2$ and is 50 cm long. This corresponds to 18 radiation lengths. At the back of each block a photo-multiplier tube is mounted to measure the energy deposited in the form of electromagnetic radiation in the block. The violent impact of the scattered positron causes electromagnetic showers. The energy is usually deposited within a cluster of 3×3 adjoining blocks. The spatial resolution of the calorimeter can then be improved over the size of the blocks by analyzing the shape of the energy cluster. The resolution that can be achieved in this manner is about .5 cm.

Pions and other hadrons cause hadronic showers. These particles will usually travel further in the blocks while just losing energy by ionization, since the nuclear reaction length is much larger than the radiation length. The reaction is also much more violent, and the energy is spread wider, covering more

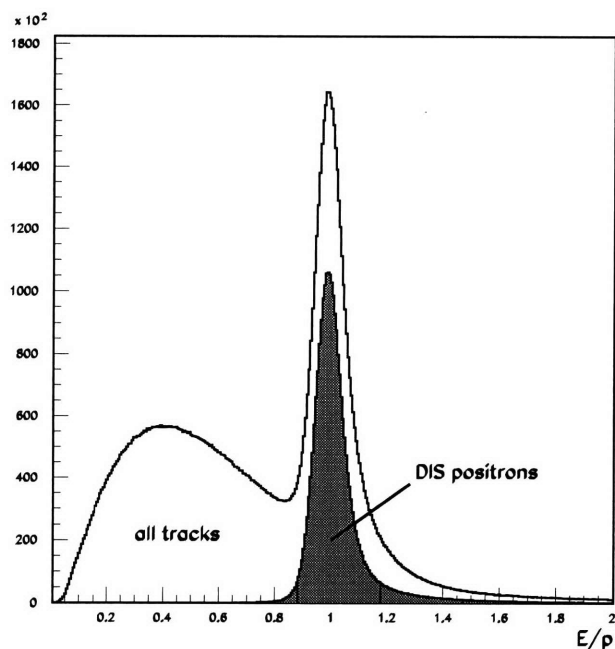


Figure 2-11: Ratio of energy deposited in calorimeter to momentum determined by magnet bending radius

calorimeter blocks. A simple comparison of the energy deposited in the calorimeter with the energy determined by track bending in the magnet provides a way to distinguish hadrons and positrons.

The rejection factor is limited by the presence of the charge exchange reaction that transforms the charged pions into neutral pions that decay into two photons, leading to two electromagnetic showers that cannot be distinguished from a normal positron shower. The charge exchange cross section makes up about 1% of the total inelastic cross section for πN reactions. The rejection factor (disregarding the relative fluxes) for pions is therefore about 100:1 for energies in the 1-10 GeV range. As shown in figure 2-11 there is a fairly large number of events with $E/p < 1$. This is due to pre-magnet brehmstrahlung and attenuation effects in the lead glass. The former effect is easy to understand: the energy lost in the brehmstrahlung is not measured for p, but the brehmstrahlung photon is very likely to end up in the positron impact cluster and will hence be counted towards E. The latter effect is somewhat more subtle and is caused by the preponderance of electromagnetic showers that are started in the preshower. These showers will develop at the start of the calorimeter block. Positrons that do not shower in the preshower

will start showering later in the calorimeter block, which means closer to the phototubes. Hence the light from these showers is less attenuated, and as long as all the energy is deposited in the calorimeter, the signal will be higher. The calorimeter is calibrated to give the right average answer, and is therefore biased towards the showers that start in the preshower.

To reduce the possibility of radiation damage, the calorimeter is moved away from the beam pipe during beam injection and ramp-up as well as beam dumps. It is moved in when the stored beam is stable. To continuously monitor the radiation damage as well as other fluctuations affecting the gain of the calorimeter blocks an extensive gain monitoring system was developed and installed.

The energy resolution of the calorimeter is energy dependent:

$$\frac{\sigma(E)}{E} = 1.47\% + \frac{5.14\%}{\sqrt{E/GeV}} \quad (2.7)$$

2.2.3.2 The preshower detector

The preshower detector consists of an 11 mm thick lead sheet followed by an array of 42 plastic scintillator paddles identical to the H1 hodoscope (figure 2-13). Each paddle covers one vertical column of lead glass blocks in the calorimeter. The lead sheet corresponds to 2 radiation lengths, but only 6.4% of a nuclear interaction length. This will increase the difference in the hadronic and electromagnetic showers, as explained in section 2.2.3.1 and hence improve the hadron-positron differentiation in the detector.

The signal from a hadron passing through the preshower is typically close to that of a minimum ionizing particle. On the other hand, positrons usually start showering, and the energy deposited is much larger. Increasing the thresholds for preshower “hits” would increase the rejection factor of the detector. However, in the test beam at CERN it was found that this would induce a large instability due to gain shifts. The thresholds were therefore set below the minimum ionizing peak.

The preshower-calorimeter combination improves the rejection factor of the calorimeter alone by a factor of 50 for an electron efficiency of 95% per block.

2.2.3.3 The Čerenkov detector

The straightforward separation in β for hadrons from positrons is used in the Čerenkov detector. This detector is a threshold counter, relying on the choice of the radiator gas to determine the threshold at

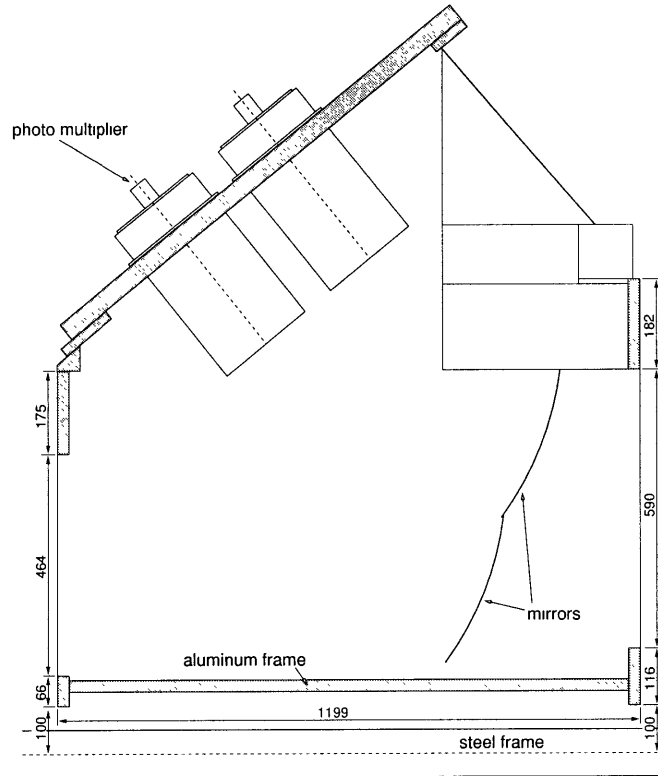


Figure 2-12: Sideview of the HERMES Čerenkov detector.

which a particle will radiate:

$$\beta_{threshold} = \frac{1}{n_{radiator}} \quad (2.8)$$

where $n_{radiator}$ is the index of refraction. The choice of gas determines the window in which the detector will provide particle identification. For 1995 the radiator was nitrogen gas, which results in a pion threshold around 5.5 GeV, a kaon threshold of 19 GeV and a proton threshold of 38 GeV. The pions can be identified cleanly for energies between 5.5 and 19 GeV by the fact that they are the only hadrons radiating at that energy.

The Čerenkov detector consists of a gas radiator and a set of 20 mirrors and PMT's to detect the radiated photons. The total thickness of the detector is only 3.5% of a radiation length, making it possible to insert the detector between the two back region tracking chambers without compromising the momentum measurement.

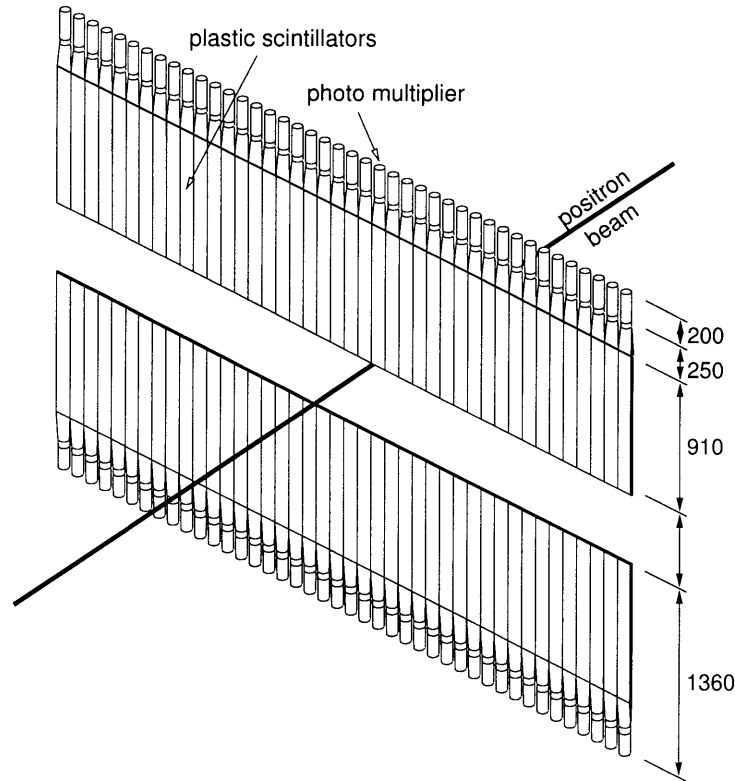


Figure 2-13: Isometric view of the HERMES hodoscope.

2.2.3.4 The hodoscope H1

The hodoscope consists of 42 plastic scintillator paddles with a size of $9.3 \times 91 \times 1 \text{ cm}^3$, each matching a vertical column of calorimeter blocks. No acceptance holes are present since the paddles overlap by 1.5 mm. The H1 hodoscope's main function is in the first-level trigger, but it is also used for low-energy time-of-flight particle identification. As a part of the first-level trigger its short radiation length (2.3%) provides a photon rejection factor of 50 to 1. This is useful to remove triggers by high energy photons (for example coming from π_0 decay). As a time-of-flight particle identification detector it can be used for energies up to 2 GeV.

2.2.3.5 The transition radiation detector

A lesser known relative of the Čerenkov radiation, transition radiation (TR) is generated at the boundary between two media with different refractive indices. The easiest way to think of TR is however as a

phenomenon complementary to brehmstrahlung. Brehmstrahlung is the emission of photons by a particle of rapidly varying velocity in a medium of constant refractive index. TR is the emission of photons by a particle of constant velocity going through a medium of rapidly varying refractive index. There are several treatises describing transition radiation in detail, such as references [42] , [43] and [44]. The crucial step in creating a working detector is to make the particles go through many transitions. For the HERMES TRD the radiator consists of loosely packed propylene fibers with diameters between 17 and 20 μm . Although the ideal radiators are thin foils, the fibers are much easier to manage in the mechanical construction of the detector. Since the performance of the fibers is fairly close to that of the foils the mechanical design considerations were allowed to prevail.

There are 6 consecutive modules of 6.5 cm thick radiator followed by an X-ray detector consisting of a planar proportional wire chamber with 0.5 cm wide cells. The gas in the X-ray detector is a mixture of xenon (90%) and methane (10%). Since the object is the detection of several keV X-rays, the high Z noble gases xenon and krypton are the natural candidates for the wire chamber gas. The decision to use xenon was based on the superior total absorption of X-rays for this gas. Indeed, krypton has a smaller absorption length for energies over 10 keV, but the secondary X-rays it emits can escape fairly easily (mainly the K shell lines). The secondaries emitted after capture by xenon are easily absorbed (absorption is 80% for the L lines within 1 cm) and further converted. The methane is added as a quenchgas to allow larger gains without causing continuous discharges in the proportional chamber. It is important to keep oxygen out of the chambers since it would severely impact the gains. Since it is very hard to guarantee a tight closure for a chamber this size, the wire chambers were protected by flush gaps on either side. Nitrogen was circulated through these gaps to eliminate the chance that oxygen would find its way into the chamber.

In each module the hadrons will deposit energy of the usual ionization type, while positrons will produce 1-2 TR photons. The energy deposited is about 15 keV for hadrons, with a peak at 12 keV, and about 35 keV for positrons. The six modules are combined in a “truncated mean”, which is a mean of the six responses after removing the largest response. This significantly reduces the tail in the distributions, enhancing the separation between the hadron and positrons peaks. The final performance figure is the pion rejection factor. This figure will change with the energy of the particles because of saturation effects in the TRD modules. The pion rejection factor for 90% positron efficiency is about 50 at low momentum and rises to about 200 at high momentum. A significant improvement in the rejection factor can be achieved by a full probability analysis of the 6 module responses. A preliminary analysis indicates the pion rejection factor could exceed 1400.

2.2.4 The luminosity monitor

To monitor the luminosity a set of two small calorimeters was installed close to the beam pipe at a distance of 7.2 meters behind the target. This allows the measurement of the Möller or Bhabha scattering from the target gas. This provides the density-current product. This is very important considering the rapid and large change in this quantity over the course of a fill.

To withstand the intense radiation the calorimeter blocks are $\text{NaBi}(\text{WO}_4)_2$ crystals of size $22 \times 22 \times 200$ mm³. As is the case with the calorimeter, the luminosity monitor can be moved away from the beam for the injection and dumping of the beams. This significantly reduces the radiation dose received.

2.2.5 The trigger

The goal of the HERMES trigger is to select deep inelastic scattered events with scattered lepton energies above 3.5 GeV. Positrons with lower energy cannot fulfill the y-cut imposed to keep radiative corrections in check. A multilevel trigger system was designed with this goal in mind. The first level trigger consisted of a coincidence of the trigger hodoscope H1, the preshower H2 and the calorimeter CAL. It starts the conversion for the DAQ modules and needs to make a decision within a few hundred nanoseconds. A second level trigger initiates the readout of the DAQ by the online computers. At this level the processing speed is about 100 μsec . The third level trigger controls the tape writing and has an average processing speed of 10 msec.

The first level trigger adds each column of calorimeter blocks and makes the sum of each two adjoining columns. One of those two-column sums has to be above a threshold which corresponds to an energy deposit of 3.5 GeV. This eliminates scattered positrons that would be cut by the y-cut anyway and reduces false triggers by pions. It requires a threshold signal in the preshower, suppressing the amount of false triggers by hadrons. The coincidence requirement with the H1 hodoscope then suppresses triggering by photons. The three requirements have to be fulfilled within a short time window which is defined by the time when an electron bunch passes through the target. This time window is derived from the ring-wide HERA clock. This timing requirement reduces triggering by proton background from the proton ring.

The background events that do pass the trigger tests are the following:

1. A high energy charged pion that undergoes a nuclear reaction in the calorimeter, depositing most of its energy and that had an unusually large energy deposit in the preshower.

-
2. A high energy photon triggers the calorimeter while at the same time a charged hadron (from the same event) triggers the hodoscope H1.
 3. A shower from the proton beam coming from a satellite bunch. Satellite bunches are formed by protons leaving their RF buckets. They arrive off-time with the proton bunch signal, and within the time window for the positron beam bunch. In principle they were suppressed by a veto signal from scintillators installed behind the calorimeter.

Currently second and third level triggers are unnecessary since the DAQ can easily handle the rates.

Chapter 3

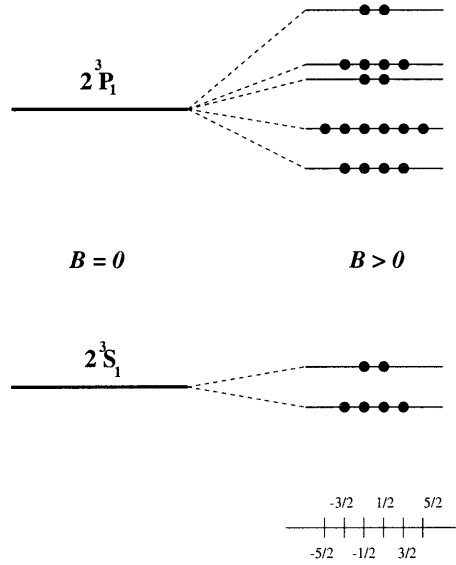
The polarized ^3He internal target

3.1 Principles of the optically pumped metastability exchange polarized target

The metastability exchange technique for optically polarizing helium was developed in the early sixties (references [45], [46], [47] and [48]) culminating in the first use of a polarized ^3He gas target in the nuclear experiment described in [49]. Large progress was made after the LNA laser became commercially available. The high power and polarizability of the laser light allowed much larger polarizations and much faster pump-up times. Descriptions of the target technique to complement the discussion in this section can be found in references [50], [51], [52] and [53]. An excellent overview of the different types of optically pumped targets is given in an article by Chupp, Holt and Milner [54].

3.1.1 The optical pumping mechanism

When an RF field is applied to a low pressure ^3He gas, electrons can be accelerated to speeds where a collision with an atom can produce another electron. This causes a sustainable avalanche. A collision can also excite the atom. Their deexcitation will produce electromagnetic radiation with frequencies corresponding to the energy differences between the different states of the atom. The impact excitation can reach levels that cannot easily decay by emitting electromagnetic radiation. These levels have comparatively long lifetimes and are called metastable. Sustaining a weak discharge in a low pressure helium gas will bring a small fraction of the atoms ($\approx 10^{-6}$) in the long-lived 2^3S_1 metastable state (figure 3-1). This state is essential for the optical pumping mechanism used in the MIT-HERMES target.

Figure 3-1: The energy spectrum of ${}^3\text{He}$

Circularly polarized light incident upon the sample along the axis of a weak magnetic field can cause transitions between the 3S_1 and 3P_0 states. Angular momentum is thus transferred from the pumping light to the metastable atoms, and the metastable atoms become polarized. Transfer of the nuclear polarization to the ground-state atoms is achieved through metastability exchange collisions. We now consider the different aspects of the process in more detail.

3.1.1.1 The atomic level structure of ${}^3\text{He}$

The ground state of the ${}^3\text{He}$ atom splits into two sublevels in a magnetic field, according to the orientation of the nuclear spin: the two 1S_0 states with $m_I = \pm 1/2$. The populations of the states determine the nuclear polarization P of the ground state.

$$n_+ = \frac{1+P}{2} \quad ; \quad n_- = \frac{1-P}{2} \quad ; \quad -1 < P < 1 \quad (3.1)$$

The metastable excited state 2^3S_1 is similarly split into two levels ($F=3/2$ and $F=1/2$). Since the electron spin is no longer zero, however, these levels contain more sublevels, 4 for the $F=3/2$ level and 2 for the $F=1/2$ level.

P_0	0.0
P_x	-27.39
P_1	-28.13
P_y	-32.64
P_2	-34.41
$2^3S_1 ; F = 1/2$	0.0
$2^3S_1 ; F = 3/2$	-6.74

Table 3.1: The hyperfine splitting in the helium spectrum (in GHz)

The third level of consequence for the process is the 2^3P level. This level consists of 5 levels (P_0, P_x, P_1, P_y, P_2) that contain 18 hyperfine levels. The energy difference between the different P_0 level and the $2^3S_1 ; F = 1/2$ corresponds to a wavelength of $1.0834 \mu\text{m}$. The hyperfine splitting of the spectrum is shown in table 3.1, expressed in GHz.

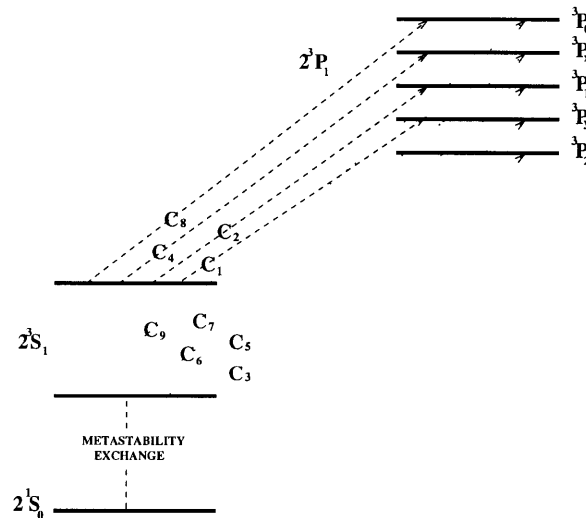


Figure 3-2: Dipole transitions relevant for optical pumping. The energy levels are NOT to scale.

The optical pumping occurs from the metastable level to this set of levels. The strong resonances will be dipole transitions, which are subject to the normal selection rules $\Delta L = \pm 1$ and $\Delta m = 0, \pm 1$. It is important to realize that a dipole transition only changes the orbital angular momentum variables. Neither the electron spin nor the nuclear spin are changed by the transition. Figure 3-2 shows the 9 allowed dipole transitions that are possible between the two sets of states. The transitions are numbered in order of the corresponding energy difference, between the states. The transition with the smallest energy difference is called C_1 , the largest one is called C_9 . The relative energy differences between the

resonances are shown in table 3.2. The relative oscillator strengths for the different transitions can be obtained by the calculation of the transition matrix elements (see [50]) :

$$\langle A_i | \mathbf{e}_\lambda \cdot \mathbf{R} | B_j \rangle \quad (3.2)$$

Transition	E-E _{C₁} (GHz)
C ₁	0.00
C ₂	4.51
C ₃	4.97
C ₄	5.25
C ₅	6.74
C ₆	11.25
C ₇	11.99
C ₈	32.64
C ₉	39.38

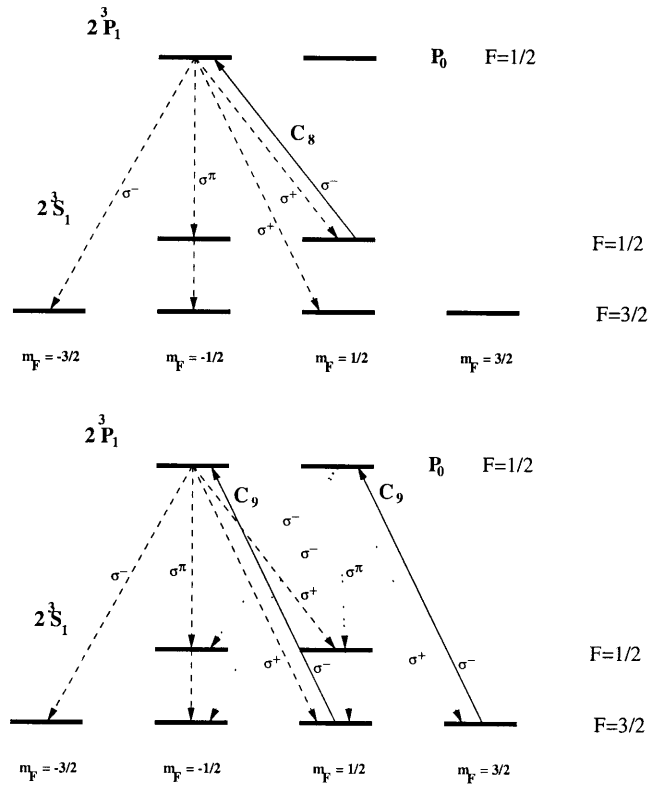
Table 3.2: The relative energy of the dipole resonances

The absorption of the laser beam does not directly change the nuclear polarization. The transitions *can* select lower m_F states (for a left handed polarized beam i.e. $\Delta m = -1$). When the excited state decays, it will emit a photon with no polarization. This means that the m_F value will change by +1, 0 or -1 with equal probability, depending on the direction in which the deexciting photon is emitted. This means the new state will have the same or lower m_F value as the state we started from. The nuclear spin must therefore have changed, although this cannot be due to the dipolar transitions that took place in the absorption and decay. It is the assumption of equal probability in the decay direction that gives rise to this effect. It requires that the atom stays long enough in the ²P state to “forget” the nuclear and electron spin directions of the state it came from. The hyperfine interaction will mix the two spins, allowing the decay to be unpolarized and hence the nuclear spin direction to be changed.

The calculations in [50] as well as experimental tests have shown that the most efficient polarization is achieved by tuning the laser to the C₈ and C₉ resonances. The pumping process for both of these resonances is shown in figure 3-3.

3.1.1.2 The metastability exchange process

The optical pumping will lead to polarization of the metastable population. The final goal is the polarization of the majority of the gas, which means the polarization needs to be transferred to the

Figure 3-3: The full story for C_8 and C_9 pumping

ground state atoms. Since the deexcitation of the metastable state to the ground state is not dipolar it can change the nuclear spins. The transfer of polarization to the ground state can therefore be done most efficiently by relying on the metastability exchange process. This process is based on the exchange of the electron clouds between two atoms during an atomic collision. During this process neither the electron spin nor the nuclear spin of both nuclei are changed. This way the nuclear polarization of the metastable population is transferred to the ground state atoms. Due to the fact that the metastable population is only of the order of 10^{-6} the reverse process (depolarizing the ground state) is negligible. The cross section for the metastability exchange process is about $7.6 \times 10^{-16} \text{cm}^2$ ([55]).

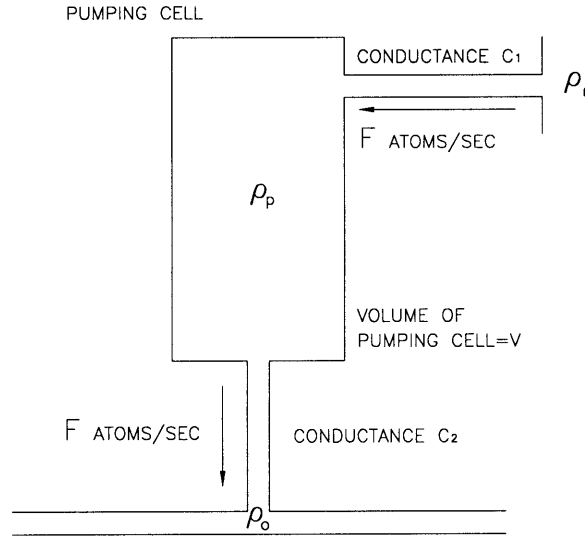


Figure 3-4: Schematic of pumping cell flow system.

3.1.2 The flow-through pumping cell

In order to create an internal target, ^3He gas is flowed through the pumping cell and into the storage cell, which is located inside the storage ring. A schematic diagram of the target is shown in figure 3-4. The ^3He atoms flow through a glass pumping cell of volume V at a rate of F atoms/sec. As shown, the ^3He gas has an input density of ρ_i and traverses an input conductance C_1 . The gas in the pumping cell has an average density of ρ_p and exits through a conductance C_2 to the storage cell. The average residence time of an atom in the pumping cell, t_r , is given by

$$t_r = \frac{\rho_p V}{F} \quad (3.3)$$

For equilibrium flow with $\rho_0 \approx 0$, one has

$$F = C_1(\rho_i - \rho_p) \approx \rho_p C_2 \quad (3.4)$$

and so

$$t_r \approx \frac{V}{C_2} \quad (3.5)$$

Thus, to a very good approximation the average residence time of an atom in the pumping cell depends only on the quantities V and C_2 .

We can also deduce the following relation:

$$\frac{\rho_p}{\rho_i} = \frac{C_1}{C_1 + C_2} \quad (3.6)$$

and so a measurement of ρ_p as a function of ρ_i measures the ratio of conductances C_1 and C_2 . Note that in the intermediate flow region C_1 and C_2 become functions of ρ_p and ρ_i . For the usual pressure range this is not a problem for C_2 , but it needs to be taken into account for C_1 design calculations.

In the pumping cell the atoms are polarized by absorption of angular momentum from the laser pumping light at the $1.083 \mu\text{m}$ transition as described in section 3.1.1. Consider a sample of ^3He atoms in a sealed cell, i.e. a pumping cell where there is no flow and the sample of ^3He atoms is static. In the approximation that the polarization rate does not depend upon polarization, the ^3He atoms will be polarized to an equilibrium polarization P_0^v with a pump-up time-constant of t_p^v given by

$$P(t) = P_0^v(1 - e^{-\frac{t}{t_p^v}}) \quad (3.7)$$

Consider now the atoms in an identical pumping cell but flowing at a constant rate of F atoms/sec. We can treat the flow as a depolarizing effect, taking away polarized atoms at a rate F times P and replacing them with unpolarized ones. Hence we have:

$$\frac{dP}{dt} = -1/t_p^v \times P - 1/t_r \times P. \quad (3.8)$$

The gas in the cell will be polarized to an equilibrium polarization P_0^f with a pump-up time constant t_p^f where

$$\frac{1}{t_p^f} = \frac{1}{t_r} + \frac{1}{t_p^v} \quad (3.9)$$

The equilibrium polarization obtained with a flowing system, P_0^f , and the equilibrium polarization obtained on a sealed copy of the pumping cell, P_0^v , are related by

$$P_0^f = P_0^v \frac{t_r}{t_r + t_p^v} \quad (3.10)$$

where the difference between sealed and flowing systems is the presence of a polarization relaxation with time constant t_r due to unpolarized atoms entering the pumping cell through C_1 . t_r is equal to the residence time of the atoms in the pumping cell.

From this equation we see that for high polarization in the flowing system we require that $t_r \gg t_p^v, t_p^f$, i.e. the pump-up time must be much shorter than the residence time in the pumping cell.

To study the operation of the flowing system it is convenient to define two quantities. First, we define the polarization rate of a sample of ^3He , R , to be

$$R = \frac{NP_0}{t_p} \quad (3.11)$$

where the sample contains N ^3He atoms which are polarized to an equilibrium polarization P_0 with a pump-up time constant t_p . Secondly, the ^3He atoms are polarized by means of a discharge whose intensity is characterized by τ_d , which is the time constant associated with the polarization decay in the absence of optical pumping and in the presence of the discharge. As we shall see below, the performance of the polarized ^3He internal target is strongly dependent on R and τ_d .

3.1.3 Previous experiments with the MIT target

Similar targets have been operated by our group as an internal target for the IUCF ring in the CE-25 experiment [53, 56] and as an external target for the BATES accelerator in the 88-25 experiment [57] and for the PELLETRON accelerator in the HERMES target test experiment [58].

3.2 Design parameters for the HERMES target

Internal gas targets are used in conjunction with storage rings, where they can take advantage of the high beam currents without adversely affecting the beam storage time. They allow for a variety of polarized and unpolarized atomic species to be used as targets for nuclear and particle physics experiments. In an internal gas target, the gas molecules are injected into a T-shaped storage cell, where the beam interacts with the target gas. The gas is confined by the storage cell to the region close to the beam axis, resulting in an increase of the areal target density by two orders of magnitude over a free jet.

The environment in which the internal target operates obviously imposes some very different requirements than those usually encountered in external targets. The following considerations were important for the design of the HERMES internal target:

1. To limit the effect of the target gas on the beam the target thickness needs to be low. As a corollary to this it follows that the gas, when it exits the storage cell, needs to be pumped away as fast as possible. The differential pumping system that accomplishes this will be presented later.

2. A particular problem related to the gas load on the storage ring is posed by the ballistic flow of the target gas. It will be shown to be advantageous to run at lower temperatures to reduce the absolute flow rate of the target gas.
3. The presence of large amounts of synchrotron radiation eliminates some commonly used materials for use inside the shielding (example: Teflon). It could also introduce large backgrounds in the detector. This forced us to construct a collimator system.
4. The possibility of wakefield generation in the target region was a serious design constraint. The main problem is not the energy loss in the beam, which is small compared to the synchrotron radiation, but the heating of the cryogenic target and the interference of the wakefields with the detector. It is crucial to eliminate resonant wakefield generation and minimize non-resonant components.
5. Throughout the design and construction of the internal target the ultra-high vacuum nature of the storage ring was a constant influence, limiting the materials and techniques available.
6. Access to the experiment is very limited. Aside from scheduled monthly accesses it is practically impossible. This required the presence of more diagnostic instrumentation, and in general a more robust design. The inherently delicate components of the target had to be brought outside of the shielding, most notably the laser system.

Aside from these additional requirements there are the usual ones for the efficient operation of a metastability exchange optically pumped helium 3 target:

1. As polarized ^3He is susceptible to depolarization due to inhomogeneous magnetic fields, magnetic materials were minimized in the region around the target. The design of the target's holding field coils was also a major effort since space constraints prohibited the use of Helmholtz coils.
2. The laser beam transport system was complicated due to the requirement that the laser had to be outside the shielding.
3. RF cleaning had to be limited in power due to pick-up in the gas alarm circuits.

Under these constraints we tried to maximize the advantages of the internal target.

1. The thin gas targets do not require high pressures, and the presence of a stored beam prohibits the use of exit windows. It is therefore possible to reduce the material in the acceptance of the detector to an absolute minimum. This reduces the amount of radiative corrections.

2. The short time target atoms spend in the storage cell implies we can reverse the polarization fast by just changing the polarization of the atoms flowing into the cell. Fast polarization reversal is imperative to reduce the influence of systematic errors.

The acceptance of the HERMES detector covers a rectangular region from 40 to 140 mrad in the vertical plane and ± 170 mrad in the horizontal plane over the entire target length. This far-forward looking geometry made the minimization of the materials in the acceptance especially important. However, to avoid the complication of vertex-dependent corrections due to differences in the material seen by the exiting particles, it is important to keep the amount and nature of the material constant over the entire target. To this end the storage cell was extended in the downstream direction. This was a non-trivial effort, requiring the incorporation of pump-out holes in the target storage cell itself.

Last but not least there was the requirement that the entire HERMES experiment, including the target, had to be removable within 24 hours. To this end the detector and target were built on a movable platform as explained in the previous chapter. All data acquisition instruments were built on a “trailer”, which was rigidly connected to the detector platform. This situation complicated the design in many ways.

3.3 The target region

Apart from the significant changes in the beamline (as discussed above), the influence of HERMES on the operation of the HERA storage ring is mainly through the reduction of the stored beam lifetime through atomic bremsstrahlung from the target gas atoms. The lifetime due to this type of beam loss is in general given by the following semi-empirical formula [59]:

$$T_{target}(Z) = T_0 \frac{1}{\ln \left[\frac{183}{Z^{\frac{1}{3}}} \right]} \frac{1}{Z(Z+1)} \frac{8.1 \times 10^{25} \text{atoms/cm}^2}{n} \quad (3.12)$$

where T_0 is the revolution time around the ring (21 μs for HERA) and n is the target thickness. This lifetime reduction has to be compared with other beam loss mechanisms, mainly the beam-beam interaction at the collider points.

The nominal target operating density is therefore determined by balancing the density versus reduction in beam lifetime. In our case, two other experiments (H1 and ZEUS) also use the beam so the lifetime T_{target} was kept above 45 hours. This corresponds with a ^3He target thickness of 1.0×10^{15} nucleons/cm².

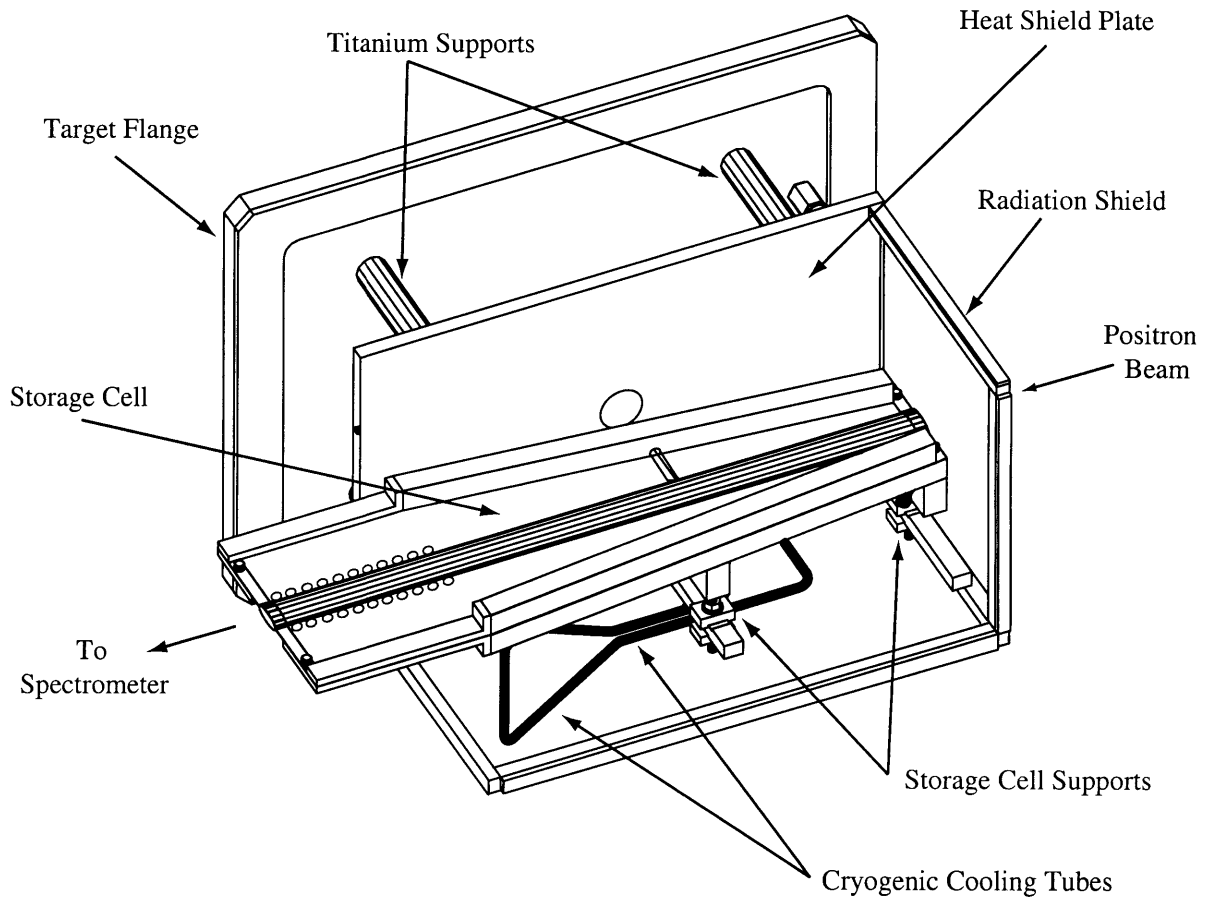


Figure 3-5: The HERMES cryogenic target cell

3.3.1 The storage cell and vacuum chamber

Optimizing the storage cell size includes minimizing the storage cell size to maximize the target density while keeping it large enough so that the beam does not interact with it. This interaction includes the absorption of synchrotron radiation as well as scattering of beam halo positrons into the detector. A related issue is that the collimator system that shields the cell and the detector from this radiation has to have an aperture that allows for some beam steering. The cell has to be in the shadow of this collimator system. Due to the extraordinary large amount of synchrotron light present in the ring, it was necessary to design the collimator system so that only doubly scattered synchrotron light could end up in the detector (see section 3.3.4).

The storage cell was a long elliptical cylinder with its central axis positioned along the beam axis. The axes were 29.0 and 9.8 mm long and the length of the cell was 550 mm. The effective target length was only the first 400 mm of the storage cell. The remaining 150 mm downstream of this was included to insure that particles coming from the end of the storage cell passed through a uniform thickness of storage cell, which simplifies the analysis of the data. The elliptical shape of the cell mirrors the beam shape, and the size corresponds to a 20σ clearance for the beam during injection.

To increase the target density the cell was designed to run at cryogenic temperatures down to 15 K. As discussed below, the cooling system was designed to remove up to 10 Watt at that temperature, while keeping the cell at a uniform temperature with deviations less than 3 K. This requirement forced us to use ultra-pure Al for the target cell material instead of the copper we used for previous targets. Indeed, ultra-pure Al (99.9999%) has an excellent thermal conductivity at cryogenic temperatures, being more than 30 times as conductive as commercially pure Al (99.%) in the working temperature range. Its low atomic number minimizes showering from exiting particles as well as beam halo. The storage cell was fabricated from two 200 mm by 550 mm sheets of 125 μm thick ultra-pure aluminum which were formed into half ellipses between two molds. A feed tube along one side was formed to allow injection of the polarized ^3He atoms. The two foils were then spot welded together along the sides of the ellipse, along the outer edges of the aluminum sheet and along the sides of the feed tube. To allow the removal of the gas outside the active target region, holes were made in the sides of the 150 mm extension at the downstream end of the cell. These holes were outside the acceptance of the detector.

The storage cell was clamped to the mounting assembly that incorporated the cryogenics and the temperature sensors and allows for a three-point alignment. The mounting assembly is shown in figure 3-5. The mounts are thermally isolating as discussed in section 3.3.3.1 and includes a heat shield to minimize the radiative thermal load on the cell.

The vacuum chamber was constructed from a single piece of 6061-T6 aluminum. The use of aluminum was necessary because of its non-magnetic properties, but this did complicate the manufacturing and handling procedures. To prevent vacuum leaks in aluminum welds, the chamber was constructed from a single piece, which was checked with ultrasound to insure there were no voids in the material. The aluminum was machined without cutting oil (only using water or isopropyl alcohol for cooling) to allow for operation in UHV conditions. To make this easier the aluminum block was left in 6061-T0 condition until the rough machining was completed. Then the block was treated to bring it up to T6 surface hardness. To avoid magnetization of the surface, grinding was done using only aluminum oxide abrasives. Welding was done using the tig process. The tolerance on the crucial dimensions was 0.025 mm. After production these dimensions were checked at a second machine shop on a five axis CNC machine and found to be within the specifications.

Five ports were made in the chamber: two circular ports along the beam axis to allow for connection to the storage ring, two rectangular ports on the chamber sides for installation of the internal components, and one circular port in the bottom for attaching a vacuum pump (for test setups only). The latter was a welded aluminum conflat flange, all others were sealed using helicoflex seals. The helicoflex seals on the beam axis ports were essential because they allowed for high precision location of the target chamber. The rectangular helicoflex seals on the side ports were used because they were the only rectangular UHV seals available. The use of helicoflex seals required low tolerance precision machining and careful handling after the machining process.

The design for the target chamber centered around the ability to mount all of the internal target components on one large flange to expedite and simplify assembly and disassembly. This flange was located on the larger side port. The opposite port allowed for access after the mounting of the main flange.

To allow the particles to exit from the target vacuum, a thin exit window was constructed covering the entire detector acceptance. The thickness of this stainless steel window is 0.3 mm. In the center a tube of the same thickness, also of stainless steel and with a diameter of 30 mm, was welded to this window. This tube provided the connection with the downstream wakefield suppressor and with the ring downstream.

3.3.2 The differential pumping system

The target gas reduces the stored beam's lifetime through atomic bremsstrahlung scattering. Further, when the gas exits the target storage cell, it still reduces the lifetime of the beam, creates background events and if it depolarizes and scatters back into the target cell it can reduce the effective polarization of the target. Hence the gas needs to be removed quickly to avoid these effects. Moreover, the ion pumps that are used in the HERA storage ring cannot efficiently pump away the helium. This means that the gas needs to be removed in the HERMES section of the ring.

To this end a set of five turbomolecular pump systems was employed, as shown in figure 3-6. A pumping chamber was attached directly downstream of the target chamber. Attached to this chamber were two Balzers TPU 2200 turbomolecular pumps (nominal He pumping speed: 3200 l/s). Upstream of the target were two additional pumps, both Balzers TPU 1600, (nominal He pumping speed: 1500 l/s). The two upstream pumps were separated from each other by the C1 collimator and from the target by the C2 collimator, which served as conductance limiters. The final pumping system was located in the detector, 5 meters downstream of the target and was equipped with a Balzers TPU 1600 turbomolecular

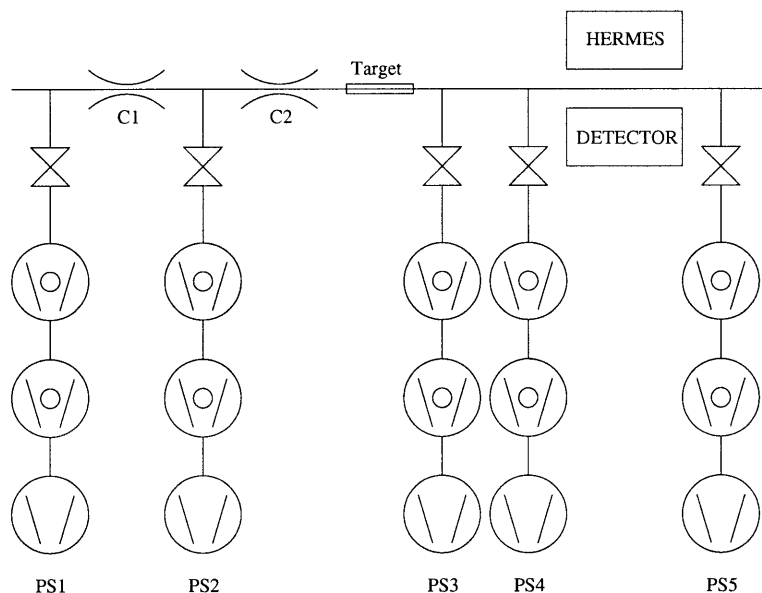


Figure 3-6: The HERMES vacuum system

pump. All of the pumps were operated in compound mode, i.e. backed by a second turbomolecular pump. The secondary pump was Balzers TPH 062 (nominal He pumping speed: 52 l/s). A standard mechanical roughing pump completed the turbo stations. All pump stations had identical secondary pumps and roughing pumps.

When operating the ^3He target at the design flow of 7.5×10^{-3} mbar.liter/sec the pressure distribution can be calculated from the physical dimensions of the beam pipes and apertures as well as the pumping power of the 5 stations. The main conductance limiters are the collimators C1 and C2 for the upstream region and the long beam pipe through the detector on the downstream pipe. The results for the loads are shown in table 3.3.

Special consideration has to be given to the ballistic flow of the target gas. This flow is important because the target cell acts as an atomic beam source, collimating the gas. At the design temperature of 15 K, the forward flow intensity (calculated from standard engineering formula [60]) is almost a constant. This means that the deposition of the ballistic flow is simply proportional to the reduction in solid angle of the beam pipe aperture as seen from the exit of the target cell.

The gas loads were calculated for the target chamber (where pump stations 3 and 4 are located), the three smaller pump stations (PS1, PS2 and PS5) and inside the wakefield meshes upstream and

downstream of the target cell. The meshes limit the pumping power on the exits of the cell, making it harder to remove the gas. The pressure was calculated separately inside this mesh since it can affect the background for the experiment.

The results of the calculations as integrated loads in each pumping station are shown in table 3.3.

location	ballistic flow load mbar.l/s	conductive load mbar.l/s	pressure mbar
upstream mesh	$3.6 \cdot 10^{-3}$	n/a	$8 \cdot 10^{-6}$
PS2	$5.4 \cdot 10^{-5}$	$3.4 \cdot 10^{-6}$	$6 \cdot 10^{-8}$
PS1	$4 \cdot 10^{-8}$ (*)	$7.9 \cdot 10^{-8}$	$1 \cdot 10^{-10}$
downstream mesh	$3.6 \cdot 10^{-3}$	n/a	$3 \cdot 10^{-6}$
PS5	$5.4 \cdot 10^{-5}$	$3.4 \cdot 10^{-6}$	$6 \cdot 10^{-8}$
target chamber	$7.5 \cdot 10^{-3}$	n/a	$3 \cdot 10^{-6}$

Table 3.3: The gas loads and pressures in the HERMES pump stations. (*) Calculated by estimating that 58% of the deposit between the two C1 collimators will be pumped out by PS1, the remainder by PS2.

Typical HERA vacuums are 10^{-9} Torr. It is clear that in the upstream endstation PS1 the pressure is low enough for the interface to the ring. In the downstream region the pressure is slightly too high, but the gas load on the ring is very small in either direction and can easily be dealt with. The ballistic flow into the ring upstream from C1 is 2.3×10^{-8} mbar.l/s. The flow downstream past the luminosity monitor is 2×10^{-7} mbar.l/s. The actual pressures measured were $\sim 3 \times 10^{-7}$ mbar in the target chamber for nominal flow rates of ^3He , and $\sim 8 \times 10^{-9}$ mbar in PS5 and PS1.

3.3.3 The cryogenic cooling system

The storage cell was cryogenically cooled to increase the target density without increasing the gas load to the storage ring. This was accomplished by flowing cryogenic helium gas through the storage cell support rails. The system was designed to be able to cool the cell to approximately 15 K with a cooling capacity of about 10 Watts. An earlier design for this system is described in reference [61]. By operating at 15 K, the target density was increased by a factor of 4.5 over a room temperature storage cell. Below this temperature, ^3He wall-depolarization effects may become non-negligible, as discussed in section 3.4.6.5. An investigation of temperature dependent wall-depolarization from aluminum was reported in reference [58].

3.3.3.1 Thermal properties of the target cell and its support system

To make the temperature of the target cell more uniform, the storage cell was fabricated from ultra-pure (99.999%) aluminum stock, which is over thirty times more thermally conducting than commercial pure (99%) aluminum at our operating temperatures. The storage cell support system is shown in figure 3-5. It supported the cell with two sets of aluminum rails, clamping the cell along its edge. A set of eight titanium fasteners were used for each rail to ensure good thermal contact between the rails and target. These rails were supported by two U-shaped aluminum brackets, which were attached to a set of cantilevered titanium beams. The brackets were thermally isolated from the beams via a set of nickel-flashed ceramic isolators. The beams were attached to an aluminum plate that also supported the radiation shield that encapsulated the storage cell as much as possible. This shield plate was mounted to the vacuum flange with a set of four thin-walled titanium posts. The storage cell alignment was adjusted with a three-point support system utilizing threaded rods and slotted holes on the support beams. The target cell support system was positioned outside the limits of the detector acceptance. The downstream face of the radiation shield was therefore missing. Titanium and aluminum were used throughout the support system because of their non-magnetic properties. For the mounting posts it was also important that titanium has a small thermal contraction, minimizing the movement of the target cell during cooldown. The strength of titanium also allowed the posts to be very thin, reducing the conductive heat load on the radiation shield.

3.3.3.2 The cryogenic cooling circuit

The cooling loop consisted of gun-drilled aluminum support parts connected by 1/4 inch aluminum tubing segments welded onto them. The cooling loop began at the entrance to the vacuum chamber with a bayonet fitting with 1/4 inch aluminum tubing. The tubing passed through the bottom of the radiation shield plate and was welded to the gun-drilled aluminum support rails. A short segment of aluminum tubing attached the first rail to the second. After leaving the second rail, the aluminum tubing passed through the shield plate again and was welded to the gun-drilled radiation shield plate. This allowed the cooling exhaust from the cell support to cool the radiation shield, eliminating the necessity for a separate radiation shield cooling loop. Several gun-drilled holes in the shield plate produced an effective U-shaped cooling loop in the plate. Aluminum tubing welded to the shield plate led to the exhaust bayonet. Two stainless steel 1/4 inch Cajon VCR fittings were attached between the aluminum tubing and feed-through bayonets to allow for disassembly. The aluminum tubing was attached to the VCR fittings by welding the tubing to Bi-Braze stainless-steel/aluminum transition joints. The complete system was mounted on one flange to allow for easy assembly and disassembly on the vacuum chamber.

The cryogenic helium gas was supplied by a dewar located near the target chamber. This dewar was fed by the DESY HERA storage ring cryogenic supply and refilled between data taking periods. The helium flow was controlled by pumping on the exhaust of the storage cell cooling. A set of 4 Compton Compressors (model 0/416-6/10) 100 liter/min diaphragm pumps were attached to a pumping manifold and could be operated singly or in combination to attain the necessary flow capacity. The typical flow rate was between 40 and 60 standard liters per minute, which could easily be sustained with a single pump. The exhaust of the pumps was returned to the DESY HERA recovery system.

3.3.3.3 Target temperature measurement and control

The temperature was monitored by a set of three sensors attached to the storage cell rails. As these sensors were not located directly on the storage cell, they did not provide a measurement of the storage cell temperature. They did provide a measure of the temperature stability of the system. The sensors were Lake Shore Cryotronics rhodium-iron temperature sensors (model RF-100T-AA). To mount the sensors inside the vacuum chamber and maintain UHV, they were placed inside 90 cm long, 4 mm OD, 0.175 mm thick beryllium-copper tubes. Beryllium-copper tubing was chosen due to its low thermal conductivity and non-magnetic properties. To ensure good thermal contact between the sensor and support rail, a copper end cap was attached to the beryllium-copper tubing to improve the contact between the tube and the rail. Also a low-pressure helium gas atmosphere was maintained inside the tubing to improve the thermal contact of the sensor with the tube. The sensors were read out in four-lead sense mode using a Lake Shore Cryotronics 91CA temperature controller.

Coarse temperature control was achieved by changing the flow rate of the helium gas. A feedback loop for the input cryogenic helium temperature was built to provide finer control. It consisted of regulated heater mounted in the helium supply line and another rhodium-iron sensor downstream of the heater. The sensor was read out by another 91 CA temperature controller that also controlled the power output from the heater.

3.3.3.4 Heat load on the storage cell

The heat load on the storage cell comes from thermal conduction through the support system and the wakefield suppressors, thermal radiation and beam-induced heating. The thermal conduction was minimized through the use of thin titanium posts and thin beryllium-copper fingers for the wakefield suppressors. The heat load through the posts was estimated to be less than 4 Watts, the heat load through the wakefield suppressors less than 2 Watts. The heat load on the target cell from the walls -

where the cell was exposed to them - and the heat shield - where the shield protected the cell from the walls - was estimated to be less than 2 Watts. Beam-induced heating was not observed, except during the injection of the positron beam. As discussed in section 3.3.5 this is due to the excitation of transient wakefields. Since the system could be run in a stable manner at temperatures down to 9 Kelvin, we concluded that the heat loads were well within the expected range.

3.3.4 The collimator system

The potentially most harmful background source of the HERMES experiment is synchrotron radiation. Without a special collimator system about 100 W of synchrotron energy would be incident upon the storage cell and about $10^{13} - 10^{14}$ Hz of soft synchrotron photons would be Compton scattered into the acceptance of the detector, basically making the operation of the wire chambers impossible. To protect the storage cell and the detector from this unacceptably high background flux a system of two collimators was installed in front of the experiment. C1 is placed about 2 m upstream of the target and shields the storage cell from direct radiation. This collimator is movable. Since it is such a restrictive aperture it is moved out during the injection of the beam, and is moved into its nominal narrow setting ($15\sigma + 0.5$ mm) before the acceleration of the beam. For practical construction reasons and to attain greater flexibility the collimator was split in two parts, one providing horizontal collimation (C1H) and one providing vertical collimation (C1V), separated by about 0.5 m. When closed, the horizontal aperture of the collimators is 6.5 mm while the vertical aperture is 2.6 mm.

The second collimator C2 is mounted on the target vacuum chamber, ending about 5 cm upstream of the storage cell. It is slightly bigger than C1 in order not to be hit by direct radiation. Instead C2 protects the cell from photons that scattered from the edge of the C1 collimator. With this arrangement only double scattered radiation can hit the storage cell and the detector. The collimator C2 as well as the cell can not be opened during injection. Therefore the elliptical opening of C2 (8.6×2.9 mm²) exceeded the scaled arc aperture of the HERA electron ring by 0.5 mm.

3.3.5 The wakefield suppressors

Beam bunches traveling around the storage ring induce a corresponding image charge in the beam pipe which follows the bunch around the ring. If this image charge encounters any discontinuities in the beam pipe, wake fields may be generated. These wake fields can cause energy loss in the beam which translates into heating of the offending components. It can also change the momentum and emittance of the beam, and therefore has to be avoided throughout the accelerator ring. Non-resonant excitations due

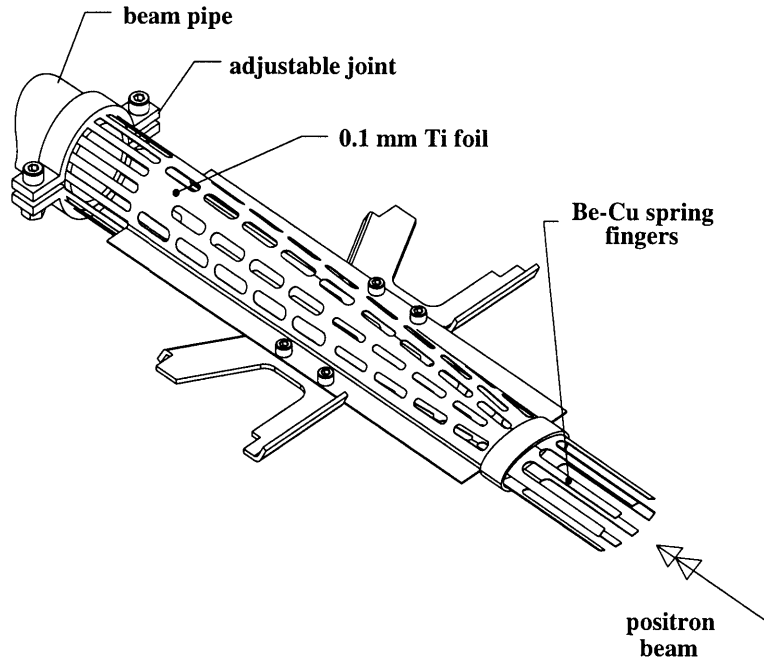


Figure 3-7: The downstream wakefield suppressor

to rapid changes in cross section acting on the same bunch (short-range wake fields) result in *transient* power losses. Excitations of electromagnetic eigenmodes in elements acting as a cavity (like the target chamber) lead to *resonant* power losses acting on the whole beam (long-range wake fields). The power losses can be arbitrarily high in this case. For a more detailed description of wake fields see References [62] and [63].

To minimize these effects, the cross section of the beamline is kept constant as much as possible. Where it needs to be varied, it is done smoothly and the transition pieces are cooled. Applying this to the storage cell presents a difficult design challenge, especially since the cryogenic cooling of the storage cell requires that the thermal load be minimal. Since removal of the target gas requires an open geometry, one cannot use solid surfaces to make the transition between the cell and the ring. The system also has to allow for movement of the storage cell during thermal cycling, requiring the connection to be flexible. The design is not facilitated by the fragile nature of the storage cell and the requirement that the material inside the vacuum (and especially within the detector acceptance) be kept at an absolute minimum.

All this was achieved by using so-called *wake field suppressors*: a thin-walled titanium mesh (figure 3-7) connecting to the target cell with beryllium copper fingers. The meshes are 50% transparent to allow

for the removal of the target gas. Similar meshes are used in the different pump stations to avoid generating wakefields at the pump-out ports. The thin meshes can also provide smooth transitions between different cross sections. The downstream wake field suppressor was a 30 cm long, 100 μm thick titanium tube with longitudinal slots which allowed for the target gas to be pumped out. The slots in the meshes were designed to be small enough to make it appear solid to the electromagnetic field generated by the passing bunches. The suppressor was supported from the sides of the chamber and was attached to the storage cell with a set of thin beryllium copper *fingers*. The upstream wake field suppressor consisted only of these beryllium-copper fingers attached to the C2 collimator, located about 5 cm upstream from the storage cell. Beryllium-copper was used for its low thermal conductivity, non-magnetic properties and especially its high flexibility.

These fingers provided electrical contact between the storage cell and the rest of the beamline while creating a thermal break at the end of the storage cell. They also allowed for movement of the storage cell during thermal cycling. The fingers were spot welded to the titanium and hand formed to match the storage cell cross section. For the upstream suppressor the fingers were welded to a titanium ring that was mounted on the collimator. The ends of the storage cell were strengthened with 10 mm \times 1.25 mm aluminum strips, spot welded to the storage cell. The wake field suppressors fingers contacted the storage cell at these strips, preventing damage to the thin storage cell walls. The strips also added to the mechanical stability of the storage cell.

Using such wakefield suppressors the remaining power losses are given by the finite conductivity of the meshes and the storage cell. Detailed calculations using the MAFIA code predicted the deposition of several kWatt in the target chamber without the wake field suppressors, mainly due to excitation of cavity resonances, while the estimates for the final geometry gave $P \leq 1$ W for the full beam current of 58 mA [64].

Temperature increases in the storage cell of up to 11 K at 40 mA injected current were observed at injection energy. After the beam is ramped up to the full energy the cell temperature drops dramatically and stabilizes to the pre-injection temperature. The heating of the cell during injection is probably due to non-resonant excitations of the short range wake fields, which are stronger at injection than at full beam energy as the bunch length of the stored positron beam is inversely proportional to the beam energy and thus decreases roughly by a factor 2 during ramping. In addition offsets of the beam from the nominal axis are likely during injection. Such offsets lead to additional losses through the generation of transverse wakefields. These losses are proportional to the square of the offset. It is unlikely that the heating would be caused by synchrotron radiation, since the synchrotron radiation increases with beam energy, while the temperature of the cell is observed to decrease during the energy ramp-up. Furthermore, closing of

the movable C1 collimators at 19 GeV, which significantly improves the shielding of the target against synchrotron radiation, does not result in a faster cooldown of the cell.

The total power loss through wakefield generation is expected to increase quadratically with the beam current. The exact power deposition in the cell can not be measured. However one can compare the results with the temperature rises measured with a prototype cell as described in [61]. One has to keep in mind that the prototype cell discussed in that paper was not connected to wakefield suppressors as in the real target. The quoted numbers in the paper are $\Delta P/\Delta T \approx 0.9\text{W/K}$ at a cell temperature of 16 K. Comparing with the fitted data, the deposited power is $\Delta P \approx 0.0063 \cdot I^2$, e.g. $P = 10\text{ W}$ at 40 mA stored current. This indicates very little heating over and above the radiative and conductive heating. The results at full beam energy are therefore well in agreement with MAFIA calculations and show that the carefully chosen design of the target region by using thin metallic meshes works as expected. The heating of the target during injection by a few degrees is easily tolerable and can be compensated for by the cooling system of the cell.

3.4 The helium target

3.4.1 The pumping cell

The quartz pumping cell assembly was developed in close collaboration with the scientific glassware company Finkenbeiner Inc. The entrance capillary C1 (see figure 3-4) is necessary to bring the pressure before the pumping cell up into a more easily regulated range and to provide a low-conductance connection from inside the cell to the metal parts of the gasfeedsystem. The latter is necessary to avoid wall depolarization on the metal. A bypass valve was added to increase the conductance from the inside of the cell during cleaning procedures (section 3.4.1.2). This valve is made out of quartz, with sealing provided by a set of O-rings (KONTES 826450-0004). The C1 capillary is 2.96 inch long and has an ID of 0.017 inch.

The exit capillary C2 to the target cell determines the actual flow rate of the system (given that the optimal pressure for polarization is around .5 Torr). Its length was chosen to be 4.1 inch for an ID of 0.045 inch. The outer diameter was also specified to $6.5 \pm 1/1000\text{ mm}$ to allow a tight fit to the sliding thin aluminum tube that provides the final connection to the target cell. Both capillaries were obtained from Wilmad.

The pumping cell was constructed as a cube, to allow for two different polarization directions. Its inner side length was 3.5 inch, the largest that was achievable given the strength of quartz and the

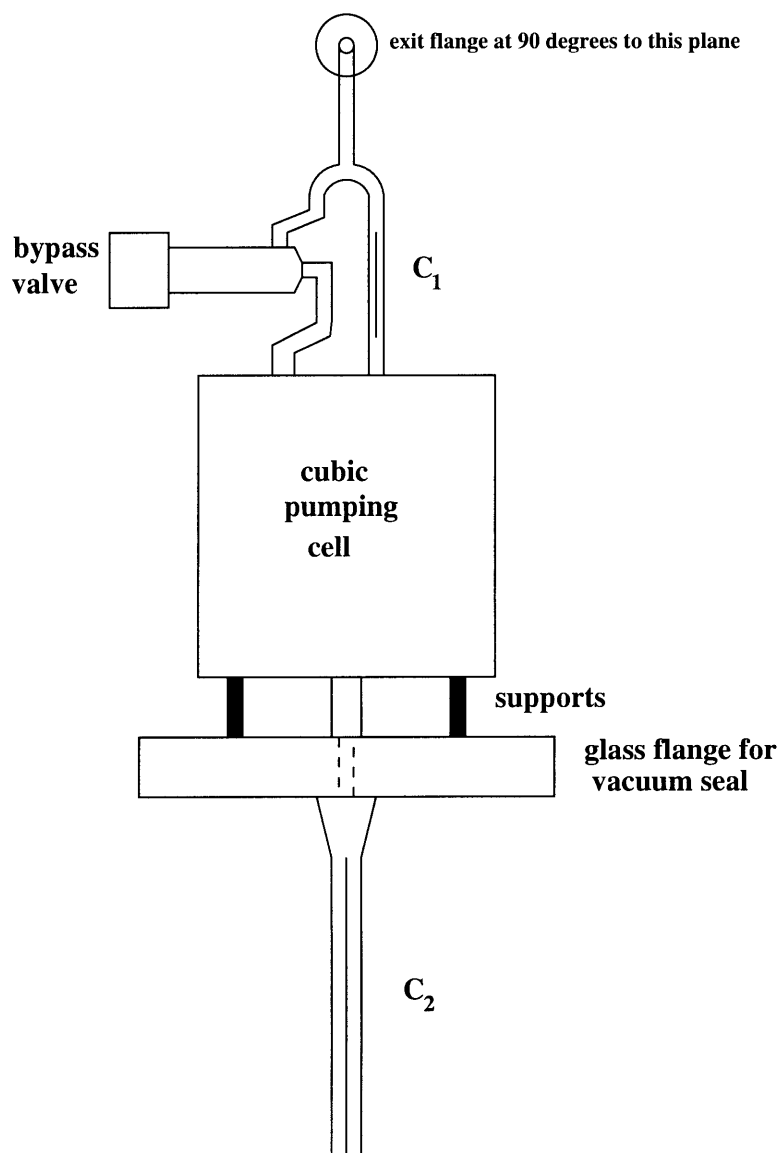


Figure 3-8: A sketch of the quartz cubic pumping cell

difficulty of working with it. The thickness of the glass windows was 0.25 inch. The windows were carefully annealed to minimize birefringent effects. Maximization of the cubic cell volume was essential to maximize the residence time in the cell, and hence minimize its influence on the polarization. While it is easy to adapt the laser beam diameter to the size of the pumping cell, the laser beam is generally circular or elliptical with a small eccentricity. It is therefore impossible to completely fill the cell without losing laser power. This introduces a dead volume that contributes to the discharge-induced relaxation time without contributing to the optical pumping. As an alternative design we tried a crossed cylinder cell. The dead volume in this cell is however similar to the cubic cell. Extensive tests at Caltech showed that both cells performed very similarly. We decided to go with the cubic cell because it is much easier to obtain a uniform discharge in it.

The actual assembly is shown in figure 3-8. The pumping cell and the C2 capillary are mounted on opposite sides of the quartz baseplate. This baseplate is a 0.5 inch thick, circular plate with a 6 inch diameter and is mounted on the side of the vacuum chamber as shown in figure 3-9. The helicoflex seal sandwiched between the large, optically flat quartz baseplate and the side of the target chamber provides a UHV compatible seal. A second helicoflex seal was used to transmit the pressure from a mounting bracket to the glass plate.

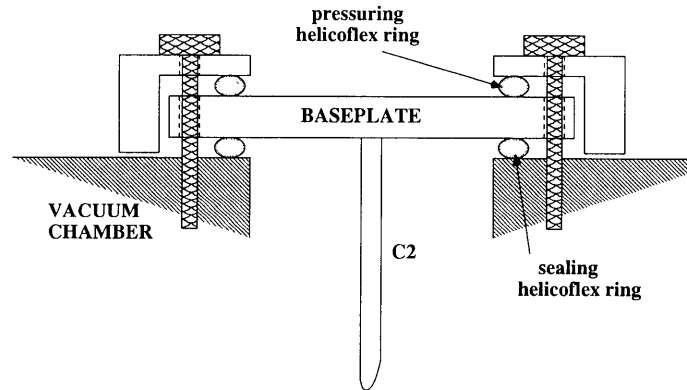


Figure 3-9: The UHV vacuum seal for the glass cell

The entrance tube was bent at 90° because of the tight space constraints in the target region. The graded quartz-to-pyrex transition starts shortly after the bend. The transition is necessary to connect to the metal bellows. The bellows don't suffice to take up all the thermal stresses that can occur, since it can only bend sideways. A pull along this bellows directly stresses the corner of the entrance tube. To provide compressibility a stress-free connection was made.

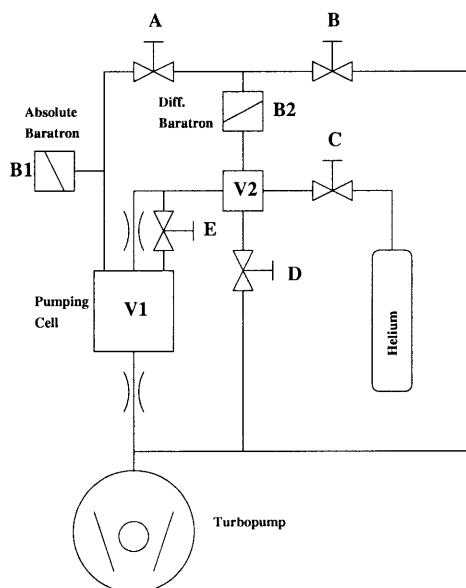


Figure 3-10: The calibration setup.

For use in the calibration procedures a temporary connection was added directly to the cube. After the calibrations this connection was sealed to eliminate the metal surface from the cell.

3.4.1.1 Calibrations

Because of the unavoidable changes in both the diameter (at the ends) and the length of the capillaries in connecting them to the rest of the assembly, the final system needs to be recalibrated. The most important relation is between the pressure in the pumping cell and the pressure before the entrance tube, since the pressure in the pumping cell cannot be measured directly during normal operation. The presence of the temporary connection allows for a direct measure of this relationship.

As a cross-check as well as a calibration of the absolute flow rate (necessary to calculate the target density) we also conducted several pressure decay calibrations. The arrangement is shown in figure 3-10. The following measurements were then performed.

1. Valves A,D closed, B,E open

Open valve C to fill V_1+V_2 , then close C and measure pressure decay. Fit the decay to $\exp(-\frac{C^2(p)}{V_1+V_2} \times t)$.

2. Valves D,E closed, A,B open

Open valve C to fill V_2 , then close and measure pressure decay with B2. Fit the decay to $\exp(-\frac{C1(p)}{V_2} \times t)$.

3. Valves A,E closed, B open

Close D, open C to fill V_1 . Close C, open D. Measure pressure decay with B1. Fit the decay to $\exp(-\frac{C1(p)+C2(p)}{V_1} \times t)$.

All conductances were assumed to have a molecular as well as a viscous term. The exponential decay formula is a good approximation as long as the viscous term is not dominating. This is the case in the pressure range we work in. The volumes in the formulae were both calculated and measured by filling the volume with water and then weighing it. The excellent agreement (see figure 3-11) between the different calibrations and calculated conductances allowed us to determine the flow rate to about 5%.

3.4.1.2 Cleaning

One of the main requirements for the operation of a metastability exchange ^3He target is a very clean system. This was one of the reasons why quartz was used instead of pyrex for the cell. The quartz cannot introduce any contaminations into the gas since it is pure silicate. It also allows higher bakeout temperatures. Quartz was also chosen since it is very radiation resistant. Due to the high synchrotron radiation flux in the target region all optical components (including the optically flat pumping cell walls) were made of quartz. To clean it we baked the whole assembly for several hours at well over 100 degrees C, while pumping on it with the bypass valve open. This was done several times in alternation with hot discharge cleaning as described in [53].

3.4.2 The gasfeedsystem

The attachment of the glass pumping cell to the storage cell provided an interesting experimental challenge:

1. It has to be essentially leak tight to minimize loss of the flowing atoms.
2. Stress between the glass capillary and the connection has to be minimized to prevent glass breakage.
3. It has to allow for the thermal contraction of the cryogenic storage cell support structure.

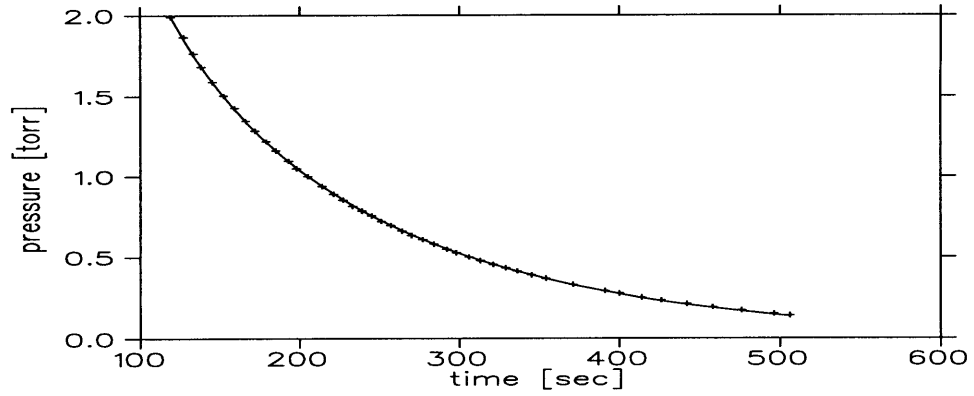
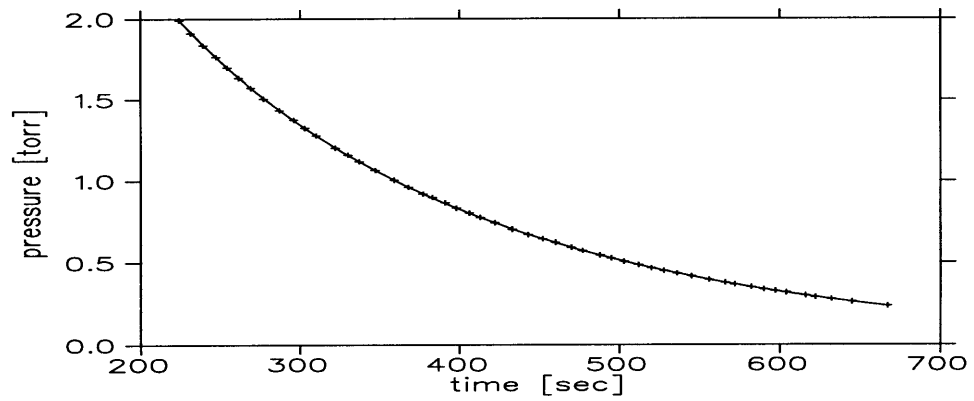
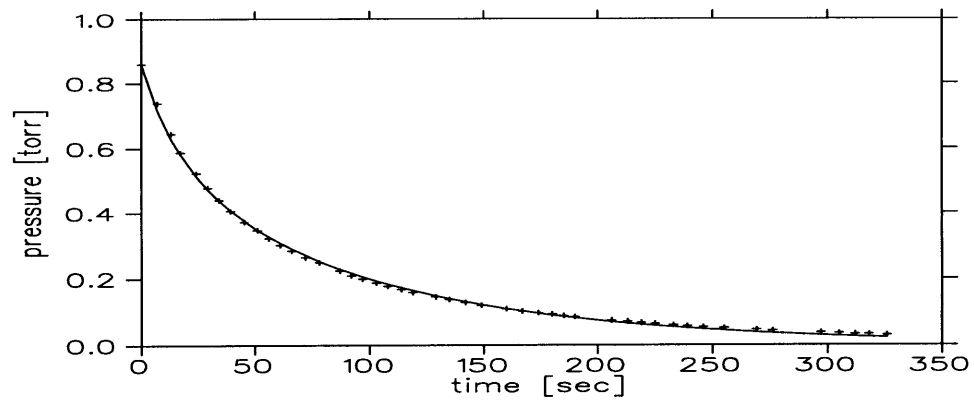
(a) First measurement yields C_2 (b) Second measurement yields C_1 (c) Third measurement yields $C_1 + C_2$

Figure 3-11: Results from the gasflow system calibrations

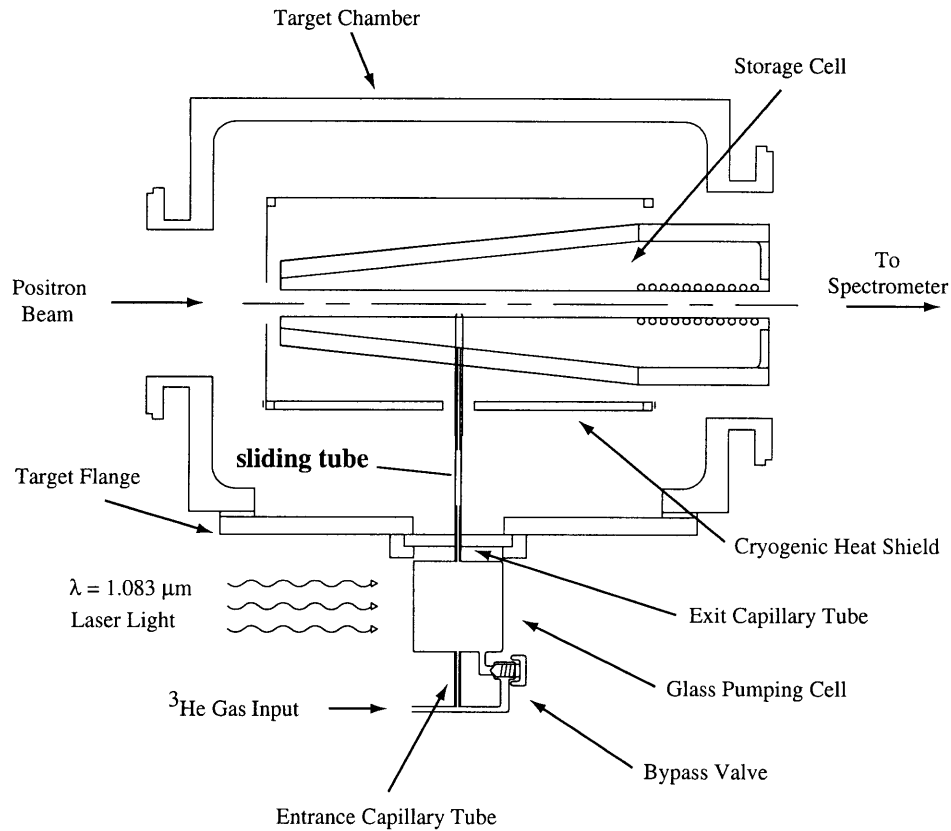


Figure 3-12: The connection of the pumping cell to the storage cell using a sliding tube

4. It has to auto-align with the glass capillary, as the storage cell was permanently attached inside the chamber and the only access was through the pumping cell flange.
5. It has to be non-magnetic, since the polarized ^3He atoms passed through the connection and are susceptible to the depolarization.
6. It has to be UHV compatible.

The solution was to use a very thin ($25\ \mu\text{m}$) aluminum tube that just fits over the glass capillary extending from the pumping cell, with a $5\ \mu\text{m}$ clearance (see figure 3-12). The tube slid onto a mating aluminum tube that was clamped into the storage cell feed tube and held rigid by the support rails. The sealing was provided by the large overlap between the tubes which was more than 2 inches. The glass capillary was laser-aligned to be normal to the quartz baseplate to less than 0.5° . To allow for small misalignments between the storage cell tube and the capillary, the free length between the two was kept

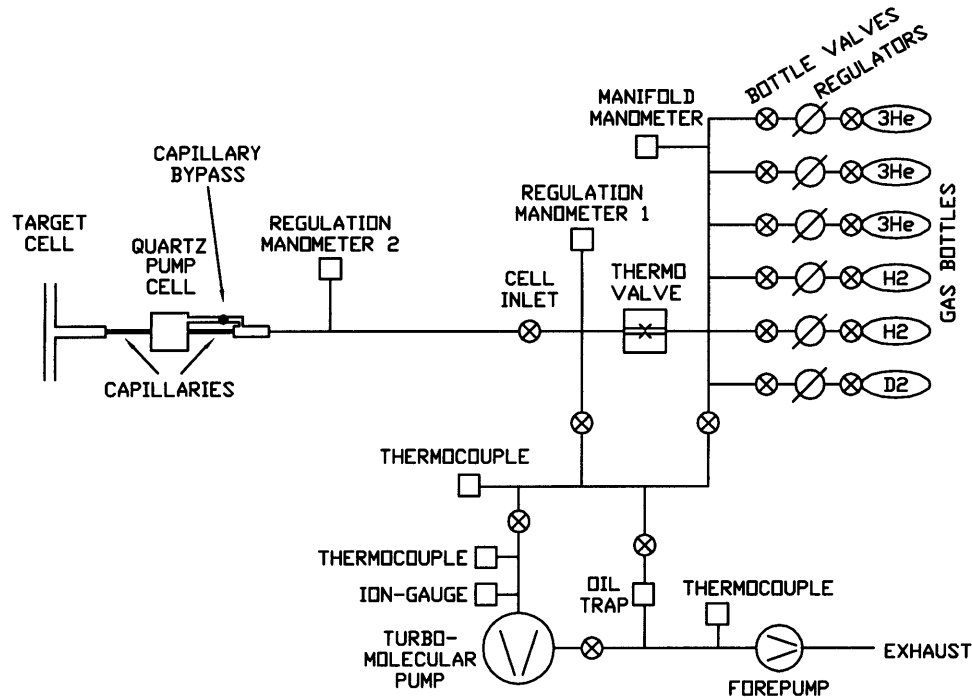


Figure 3-13: Schematic diagram of the gas feed system.

long enough so that the natural flexibility of the thin aluminum tube could take up the slack. Since the tube slid freely over the capillary and the storage cell tube, thermal contraction during the cooldown of the target cell does not stress the connection. The large overlap also means that the contraction does not significantly change the sealing properties.

The principal job of the gas feed system was to allow pure ^3He gas to flow at a constant rate into the pumping cell where the gas would be polarized and flow on to the target cell. The system also needed to be able to introduce unpolarized H_2 and D_2 gas into the target cell for the purposes of data-taking with those gases. The control and fault diagnosis of the system had to be possible remotely.

Figure 3-13 shows the configuration of the final gas feed system. Bottles of ^3He , H_2 , and D_2 were each connected to a manifold through a regulator and a remote controlled valve. The pressures in each bottle were limited to 10 bar due to safety regulations – the entire gas feed system was located in the enclosed shielded radiation area. The regulators were set to approximately 500 mbar. In order to avoid mixing the gases in the different bottles, an interlock system prevented more than one of the bottle manifold valves from being open at the same time. The pressures in the manifold and in the feedline to the pumping cell entrance were measured with manometers. The temperature controlled needle valve

(*thermovalve*) standing between the manifold and the feedline to the pumping cell regulated the flow rate into the cell by using the pressure in the feedline to the pumping cell (as measured by one of the two *regulation manometers*) as a reference. The two regulation manometers had different ranges of sensitivity, allowing the regulation of a wide range of gas flows. This was important since the mass flow of H_2 and D_2 needed for scattering measurements with those gases was very different than that needed for polarized ^3He . Other valves and lines were present to permit pumping the gas out of the manifold and pumping cell when the gas species is changed – a small turbomolecular pump system provided pumping for such work. All the valves in this system (except the glass bypass valve on the pumping cell) were controlled by a programmable interlock system built at MIT. This interlock system could receive commands from the target data-acquisition system, and could also be operated manually.

The cleanliness of the gas that flows into the pumping cell is a major factor in obtaining good polarization, and so the gas feed system is constructed from all stainless steel parts and joined with all metal seals, allowing extensive baking to drive out any contaminants.

3.4.3 The laser system

An infrared laser system was used as the source for the $1.083\ \mu\text{m}$ photons. A cylindrical crystal with dimensions $4\ \text{mm} \times 79\ \text{mm}$ of $\text{La}_{85}\text{Nd}_{15}\text{MgAl}_{11}\text{O}_{19}$ (Nd:LNA) was used as the lasing rod in a standard Lasermetrics 9550 Nd:YAG cavity. The output mirror has a reflectivity of 92.5%, the back mirror has maximal reflectivity. The Nd:LNA gain curve has peaks at 1.054 and $1.084\ \mu\text{m}$. Two uncoated etalons, one $0.3\ \text{mm}$ and the other $1.0\ \text{mm}$ thick, were placed inside the cavity to select the desired frequency. Both etalons were mounted in rotatable, temperature-controlled *ovens* to stabilize the tune. To facilitate the tuning process a *tuning cell* was installed behind the back mirror of the cavity. The laser light leaking through this highly reflecting mirror passes through a small cell filled with $0.5\ \text{Torr}$ of pure ^3He gas. A small discharge creates a metastable population in the same way as it does in the pumping cell. The scattering cross section for the laser light will increase dramatically when its frequency corresponds to the energy difference between the metastable 2^3S_1 and one of the 2^3P levels. By observing the laser light with a simple photomultiplier tube at 90° the increase in the scattering cross section is translated into an easily detectable signal. This signal can be monitored while rotating the etalons to scan through the different resonances. With some experience one can distinguish the different resonances fairly easily. To make the signal easier to observe the leaked laser light is chopped and the resulting periodic signal is displayed on a standard oscilloscope. The average signal is measured and displayed in the control room to provide a continuous measure of the laser tune.

The tuning process is a two-step process. One first installs the thin etalon. This etalon has a low resolution but large spectral width. It allows the elimination of the 1.054 gain peak and a rough

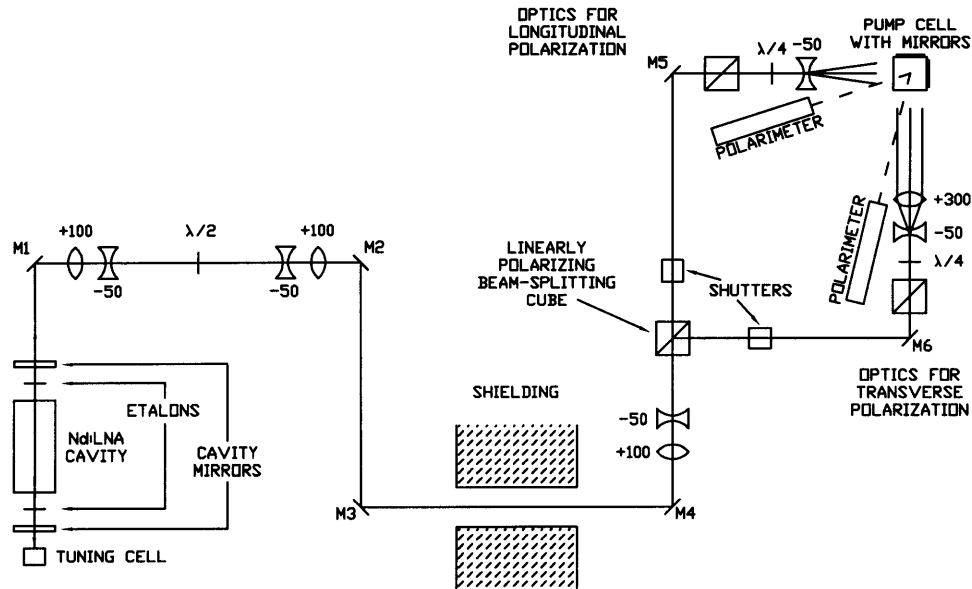


Figure 3-14: Schematic diagram of the laser transport optics system. The lenses are labelled with their focal length in mm. Retardation plates are labelled as “ $\lambda/2$ ” (half-wave) or as “ $\lambda/4$ ” (quarter-wave). The figure is not to scale. The total pathlength from laser to pumping cell is about 10 meters.

selection between the C1-C5 resonance group and the C8-C9 resonances. Then the 1.0 mm etalon can be inserted to further narrow the gain curve of the cavity so that all available power is fully at the C8 or C9 frequency. The resulting gain curve’s width closely matches the Doppler width of the helium gas at room temperature. Up to 7 Watts can be extracted at 16 Amps. At higher currents the beam shape becomes quite distorted and sometimes unstable, although the power output increases until about 21 Amps.. The power available at the optical transition was between 2 and 3 Watts during the 1995 running period. The laser ran smoothly and re-tuning was only necessary about once a week.

The optics for transporting the laser beam made use of the fact that the dispersion of the beam is roughly inversely proportional to the beam waist. Hence, in order to transport the beam a long distance (about 15 m) with little change in the beam diameter during transport, the beam was first expanded to about 2 cm full-width-at-tenth-maximum (FWTM). Nearer the target, the beam was contracted to about 1 cm FWTM for passage through polarizing optics, and finally expanded to fill the volume of the pumping cell. Figure 3-14 shows a schematic view of the laser transport optics. To increase the optical pumping efficiency, a mirror attached to the opposite side of the pumping cell reflected the laser light back through it. All mirrors used had commercially dielectric coatings set for the Nd:YAG wavelength of 1064 nm — typically, there is little change in the functioning of these coatings at 1083 nm. The polarizing optics (beam splitting cubes and zero-order retardation plates) were also stock 1064 nm

items, and behave similarly at 1083 nm. All lenses used in the region near the target were made from fused silica, in order to have the highest radiation hardness.

The light from the laser is originally linearly polarized. Circular polarization of the laser light was established using a linearly polarizing cube followed by a zero-order quarter-wave plate. The linearly polarizing cube was set to most closely align to the linear polarization of the incident beam, thus maximizing transmission of power while also eliminating any elliptical polarization components that might have been introduced during reflections from the various mirrors. The fast axis of the following quarter-wave plate was rotated 45° with respect to the axis of the linear polarization in order to give the highest degree of circular polarization. The angle of the quarter-wave plate was carefully adjusted to give measured values of circular polarization in excess of 99%.

To reverse the polarization of the target, we reversed the sense of the circular polarization (or equivalently, the helicity) of the laser light. We mounted, in fact, two quarter-wave plates on an air-driven rotary actuator downstream of the linearly polarizing cube. Each wave plate was set to give one of the two possible helicities. The actuator state was controlled by the target data acquisition system and was switched every 10 minutes automatically. The state of the sign of the polarization was maintained in a CAMAC register which was read by the HERMES data acquisition at every triggered event.

The actual helicity of the laser light for each actuator state was determined from the properties of the optical components. The direction of the polarization of the target is the same as the direction of the helicity of the laser light. The TOM can independently determine the direction of the target polarization in the case that the target is longitudinally polarized (see section 3.4.6.4) and these two determinations are in agreement.

As the target system was designed to be able to deliver either longitudinal or transverse target polarization, a system for directing the laser beam along one of two final optics paths was needed. A half-wave plate near the laser and a polarizing cube near the pumping cell were employed for this purpose. When the half-wave plate *was not* in the laser beam path, the linear polarization of the light was such that it was *transmitted* through the first polarizing cube and the light then traveled through the optics for longitudinal target polarization. When the half-wave plate *was* in the laser beam path, the axis of linear polarization of the light was rotated by 90° , so that the light was *reflected* at the first polarizing cube and the light traveled through the optics for transverse polarization. Shutters along either of these paths were available to block any light from traveling along the path not in current use.

Since the entire laser system was in a clean, air-conditioned room, access to it was reduced as much as possible. The thermal stability of the system and the remote sensing equipment made this possible. The laser power at the cavity was monitored by putting a small etalon at 45° in the laser beam on the

laser table and measuring the power in the scattered beam. The tune was continuously observed by measuring the height of the chopped signal in the tuning cell PMT.

3.4.4 The target holding field

A holding field is required to determine the quantization axis of polarization, and the strength and uniformity of that field play a role in obtaining good polarization. Gradients in the transverse components of the holding field (*i.e.* transverse to the quantization axis) contribute a relaxation time τ_{GRAD} to the total relaxation time of the polarization. Taking into account the velocity, mean free path, and diffusion time in the pumping cell, one can show [65] that $\frac{1}{\tau_{GRAD}} \simeq \frac{1}{3} \frac{|\vec{\nabla} B_{\perp}|^2}{|B|^2}$ for ^3He at room temperature and at 0.5 Torr pressure. The residence time in the pumping cell is about 125 seconds, so in the design we aimed for $\tau_{GRAD} \geq 300$ sec so that the gradients would not be the determining factor in the ultimate polarization. This implies that the gradient-to-field ratio above should be less than 0.1 m^{-1} , or about 10 mGauss/cm for a 10 Gauss field. Such conditions are easily achieved using holding coils in a Helmholtz pair configuration, but severe spatial constraints in the HERMES target region prevented the use of such coils and a different design was undertaken, using the MAFIA code[66] to calculate the fields for a given coil geometry. As shown in figure 3-15 the longitudinal coils were a pair of rectangular coils of dimensions 1560 mm by 1200 mm, separated by 640 mm. For the transverse coils, a set of four “rectangular” coils were built; two outer coils of 1440 mm by 520 mm, separated by 1040 mm, and two inner coils of 1440 mm by 720 mm, separated by 360 mm. Each coil has a cross section of $40 \times 60 \text{ mm}^2$ and 48 turns of water-cooled copper conductor. The curved sections of the inner transverse coils are necessary to avoid the vacuum flanges of the scattering chamber. Despite this odd design, the field calculated at the pumping and target cells is quite uniform enough for our purposes.

After construction, the coils were mapped using a computer-controlled motion table which moved a probe arm carrying three uniaxial field probes. A personal computer controlled the motion of the probe arm and read the field probes in uniform spatial intervals. In this way, all three components of the field were measured in an efficient and systematic way. A similar system was used to map the HERMES spectrometer magnet. The mapping covered three regions of interest to the experiment; (1) the region around the pumping cell, (2) the region around the target cell, and (3) the region downstream of the target cell.

Figures 3-16 and 3-17 compare the field calculated from MAFIA and that measured in the map. The longitudinal and transverse coils were mapped separately, each at a current of 50 amperes. We found that the calculated field exceeded the mapped value by about 2.6% for both the longitudinal and transverse coils. This disagreement is too large to be attributed to a misalignment of the probe arm.

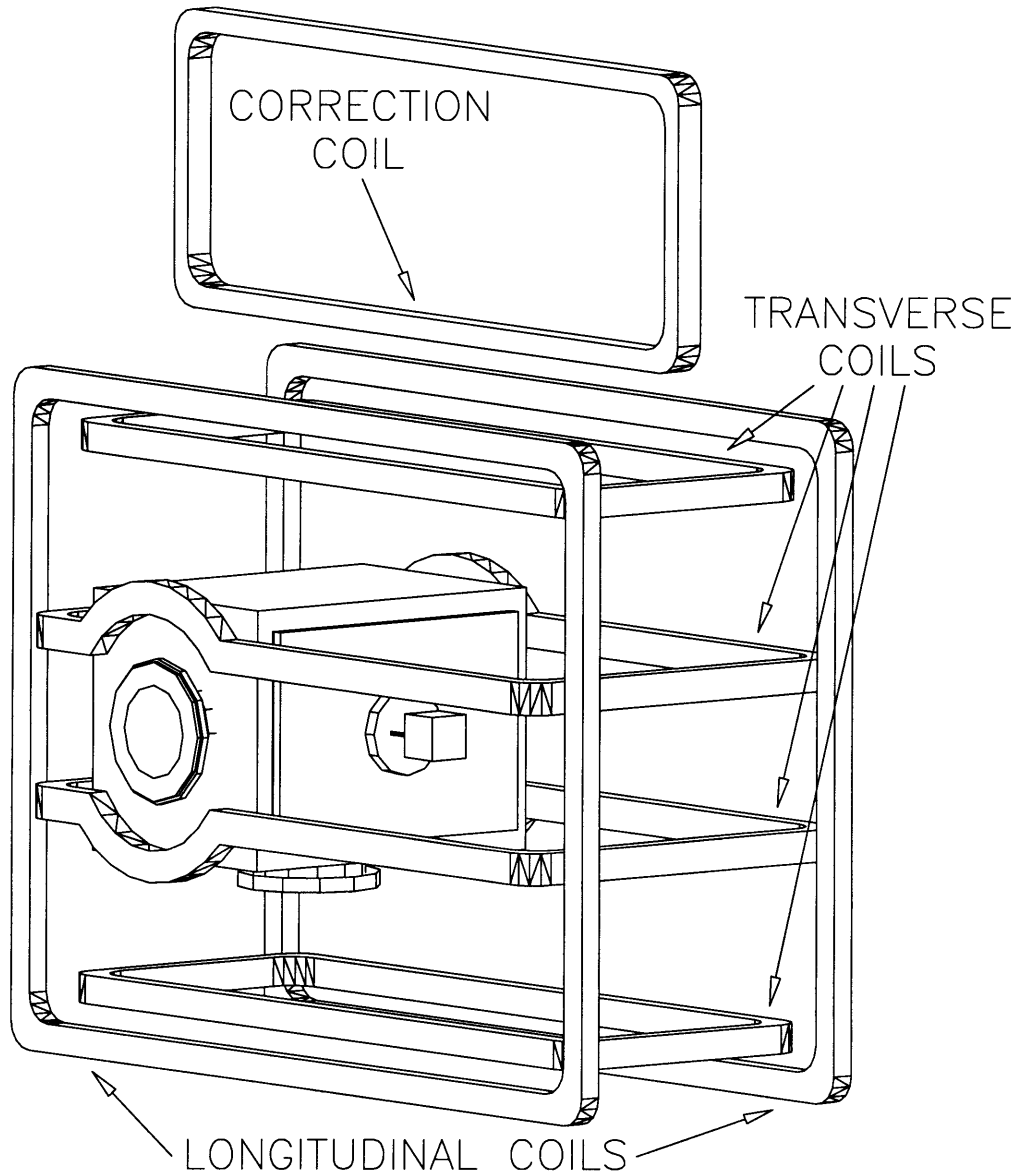


Figure 3-15: Final design of the transverse and longitudinal holding field coils. Also shown is the correction coil, which removed a large gradient produced by the HERMES spectrometer magnet. The scattering chamber and pumping cell are shown inside the coils. The curved parts of the inner transverse coils avoid the vacuum flanges of the scattering chamber.

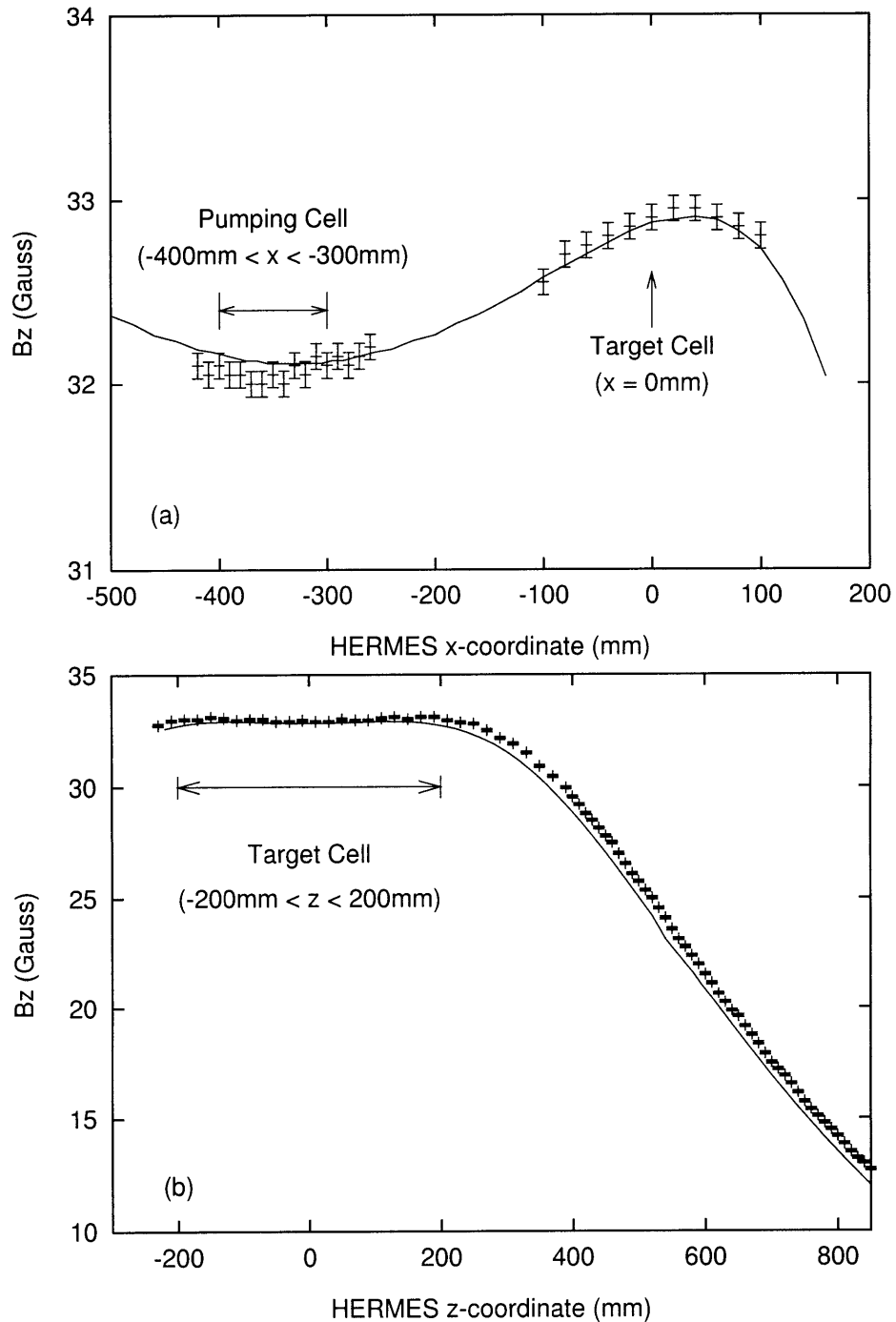


Figure 3-16: Longitudinal holding field: (a) B_z vs. x for $y = z = 0$, (b) B_z vs. z for $x = y = 0$. The data points are from the mapping measurement, the line is from the MAFIA calculation. The calculation has been scaled to fit the data.

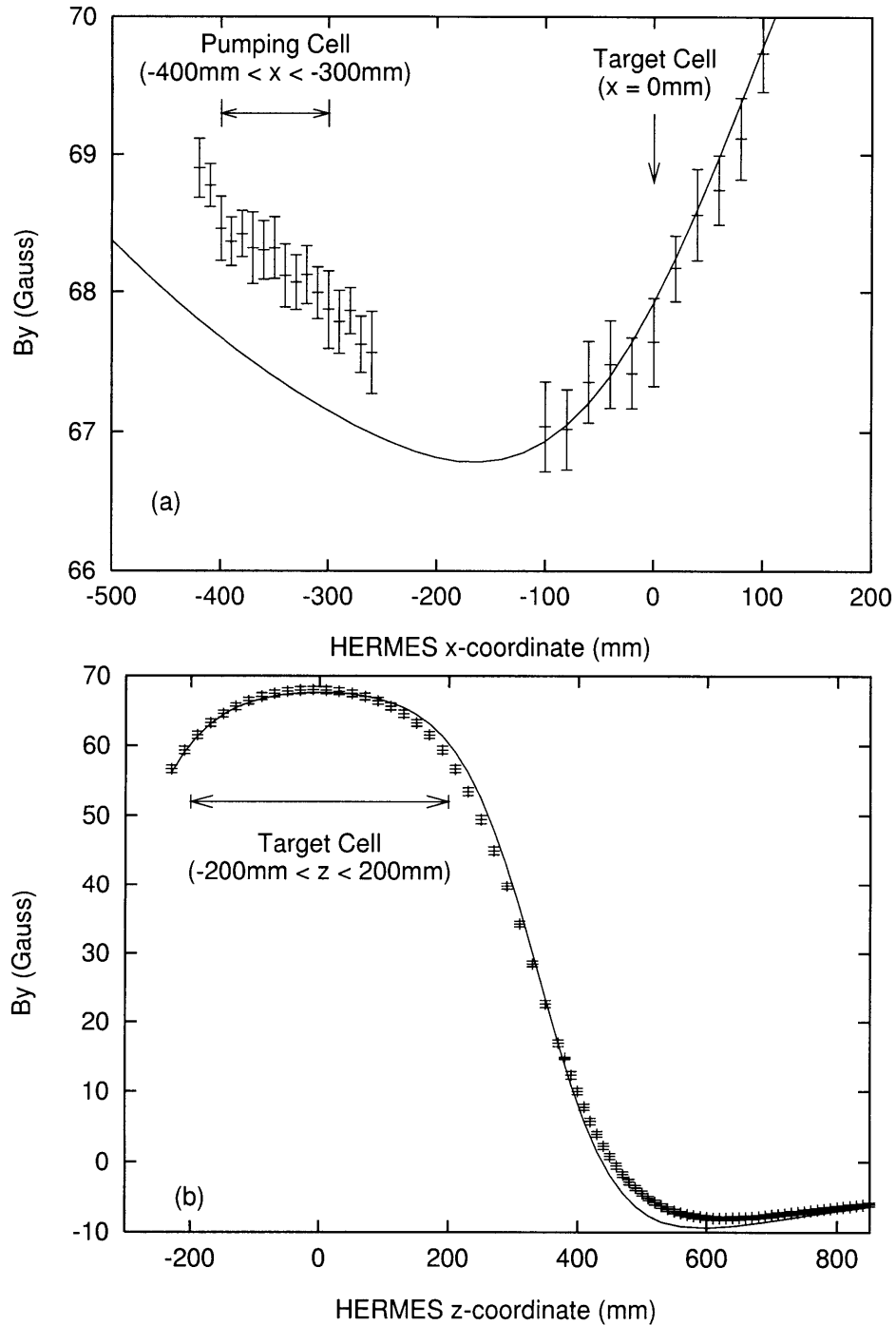


Figure 3-17: Transverse holding field: (a) B_y vs. x for $y = z = 0$, (b) B_y vs. z for $x = y = 0$. The data points are from the mapping measurement, the line is from the MAFIA calculation. The calculation has been scaled to fit the data.

(An alignment error of about 12° would be needed to produce such a discrepancy.) Since two different field probes were involved, we rejected the possibility that both probes were in error in exactly the same way. We attributed the error to the only common feature of the two measurements, which was the power supply used to energize the coils for these tests (which was not the supply used in the final experimental arrangement). Specifically, the current indication of this supply must not have been in correct calibration. Other small differences in the shapes of the measured and calculated field profiles we attribute to small differences in the positioning of the coils between the design and the realization.

The stray field of the HERMES spectrometer magnet in the region of the target, while only a few Gauss in magnitude, has a significant gradient $dB_y/dz \simeq 200$ mGauss/cm. In order to cancel this gradient, a correction coil (of the same construction as one of the outer transverse holding coils) was mounted 860 mm above the target cell, with its principal field axis pointed parallel to the beam axis. The field produced by this coil at the pumping cell exactly cancels the gradient mentioned above. In tests with sealed cells of ^3He , the maximum polarization achieved with the HERMES magnet and this correction coil on was 94% of that seen with both the magnet and this coil off, compared to about 50% with the correction coil unused.

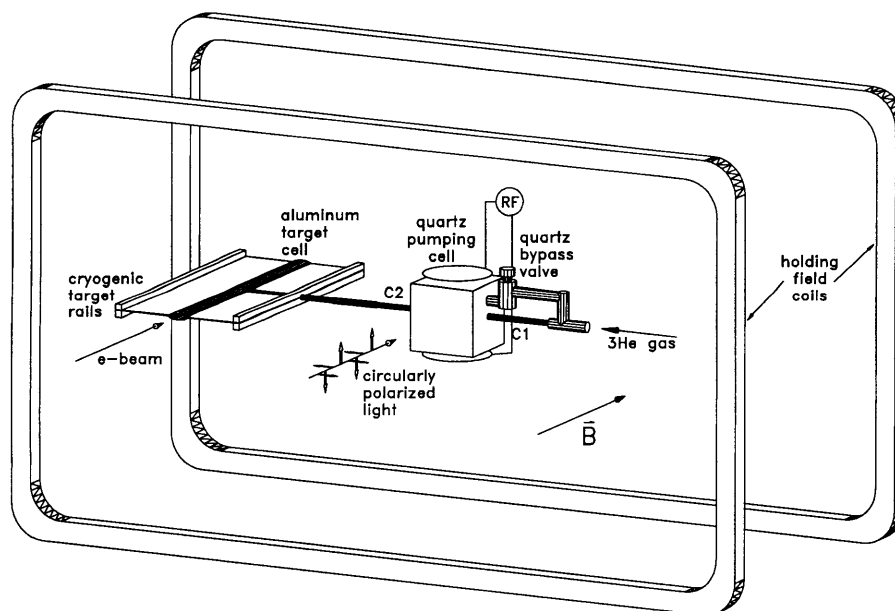


Figure 3-18: An overview of the internal target (vacuum chamber not drawn) showing the position of the RF electrodes

3.4.5 The RF system

As described in section 3.1 the creation of a metastable population is fundamental to the polarization process. To this end we used an RF discharge at low intensity in the pumping cell. Since the discharge is a depolarizing factor itself, it is crucial to obtain a uniform discharge over the region illuminated by the laser. This was obtained by using two square electrodes on the two sides of the sides that weren't used to let the laser light in (see figure 3-18). A 15 MHz RF source constructed at Caltech was used to provide the discharge. Since the RF source was not strong enough to break down the gas to start the discharge, an MIT-built RF source with a frequency of 200 kHz was used to start the discharge. This procedure was automated.

3.4.6 Target polarimetry

The polarization of the target needs to be measured accurately to minimize the error on the extracted asymmetry. To this end there are two polarimeters that continuously measure the polarization in the pumping cell *and* in the storage cell. Both measurements use the circular polarization of the light emitted during deexcitation of electronic states created in the discharge. This technique was developed by Pavlovic and Laloë [67].

3.4.6.1 The principle of optical polarimetry for ^3He

The principle and operation of the optical polarimeter has been described in references [53] and [68]. The optical method for ^3He polarimetry relies on the hyperfine interaction to transfer nuclear polarization to the electrons. Since there is no electron spin in the ground state, we will again need an excited state. This is easy in the pumping cell since the discharge excites several atomic states. The polarization of the electron will be transferred to the photon emitted when the state deexcites.

Several excited states can be used. The pumping cell polarimeter (PCP) uses the 3^1D_2 level. The excitation to this level through a collision with a discharge electron leaves the nuclear spin unchanged. The lifetime of this level is about 15 nsec, enough to allow some transfer of the nuclear polarization to the electron polarization through the hyperfine interaction. The photon emitted in the deexcitation to the 2^1P_1 level will show be somewhat circularly polarized. The wavelength of this transition is 667 nm. The relation of the circular polarization of this photon to the nuclear polarization of the gas has been determined experimentally using NMR ([68]).

The calibration of this nuclear polarization measurement has to be performed at several gas pressures. Indeed, the hyperfine interaction mixing of the spins can be interrupted by atomic collisions. Those collisions randomize the spin of the electron cloud, destroying the polarization. It is clear that an increasing pressure implies that the emitted photons will be less polarized. This pressure dependence has been studied in detail by Pinard and Van Der Linde ([69] and [70]). A short overview will be presented here.

Define P to be the degree of circular polarization of the emitted light and P_n the nuclear polarization of the gas. For a $J = 2 \rightarrow J = 1$ transition they obtain the following pressure dependence:

$$\frac{P}{P_n} = \frac{3a^2 \frac{\Gamma + \gamma_2}{2}}{(\Gamma + \gamma_2)(\Gamma + \gamma_1)^2 + \frac{6a^2}{\Gamma}(\Gamma + \gamma_1)(\Gamma + \frac{2\gamma_2}{3}) + \frac{a^2}{4}(\Gamma - \gamma_1 + 2\gamma_2)} \quad (3.13)$$

with Γ the spontaneous emission rate for the transition and γ_1 and γ_2 the disorientation and disalignment rates. The constant a is defined by the hyperfine Hamiltonian $a\hbar\vec{I}\vec{J}$, with \vec{I} the nuclear spin angular momentum and \vec{J} the total electronic angular momentum.

The disorientation and disalignment rates are related to the cross sections for these processes:

$$\gamma_i = n\sigma_i v_r \quad (3.14)$$

where n is the density of the (ground state) atoms and v_r is the mean relative velocity of the two colliding atoms. These quantities will cause the temperature and pressure dependence in this model. To account for other collisions that can disturb the 3^1D_2 state Γ is replaced by $\Gamma' = \Gamma + n\sigma_0 v_r$. The cross section σ_0 is the total for all those processes.

All three cross sections are adjusted to reproduce the measured variation of $\frac{P}{P_n}$. An interesting case is the zero pressure limit. In that case $\gamma_i = 0$ and the relation of the polarizations is:

$$\frac{P}{P_n} = \frac{0.24}{1 + \frac{\Gamma^2}{\Omega^2}} \quad (3.15)$$

For the 3^1D_2 level $\Gamma = 6.58 \times 10^7 s^{-1}$ [71] and $\Omega = 8.74 \times 10^8 s^{-1}$ [72], so we expect a polarization ratio of 0.239. This has been found inconsistent with experimental determinations of this limit. It has been speculated that this is due to cascading effects from higher levels. These would contribute significantly for pressures above about 0.15 Torr. A constant normalization factor parameter Z was introduced to account for this. After that addition the fit to the experimental data is quite satisfactory.

The measurement of the circular polarization of the emitted light was done using a rotating quarter wave plate (QWP) (see figure 3-19). This will convert the circular polarized component into a rotating

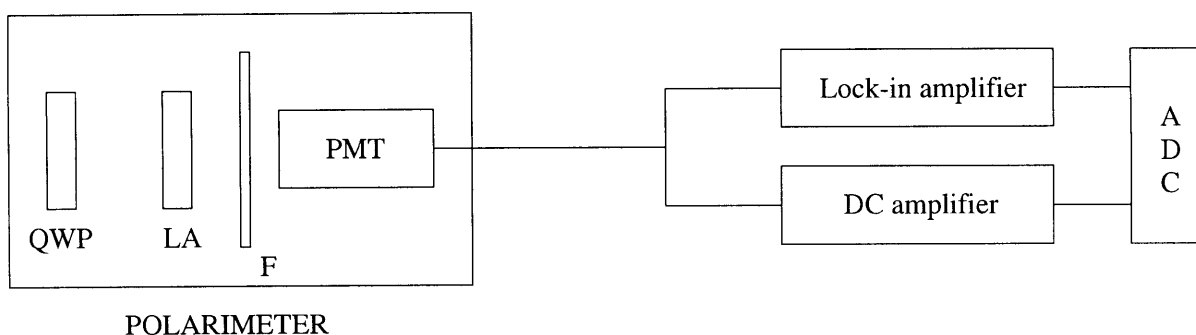


Figure 3-19: The optical polarimeter. QWP: rotating quarter wave plate ; LA: fixed linear analyzer ; F: 667 nm filter ; PMT: photo-multiplier tube

linear polarized one. Analogously the linear polarization is transformed in a circular polarization. Using a linear analyzer between this QWP and the photomultiplier tube (PMT) turns the rotating linear polarization into an oscillating signal, with a frequency twice the rotation frequency of the QWP. The circular polarized component on the other hand will transmit through the analyzer with a constant intensity. This turns the problem of measuring circular polarization into the measurement of the oscillating component of the PMT signal. This can easily be accomplished by sending the output of the PMT to a lock-in amplifier and a DC amplifier. The rotating QWP can be used to lock the signal to.

The measured degree of circular polarization of the light is given by

$$P_m = K \frac{A - A_o}{D - D_o} \quad (3.16)$$

Where A and D are the output of the lock-in and dc amplifiers respectively, and A_o and D_o are the respective outputs in absence of any polarization. K is a calibration factor taking in account the difference in the two amplification factors. The “real” circular polarization of the light can be found from this measurement by correcting for the small magnetic field dependence and the not-so-small angular dependence. The angular dependence follows from the dipolar nature of the emission (see for example [68]):

$$P = M(B) \frac{P_m}{\cos\theta} \quad (3.17)$$

The magnetic field dependence has been calibrated and can be parametrized for fields below 50 Gauss as follows:

$$M(B) = 1 + 4.08710^{-4} \cdot B + 5.58610^{-6} \cdot B^2 \quad (3.18)$$

3.4.6.2 The pumping cell polarimeter (PCP)

The easiest way to measure the polarization is to use the light coming from the same discharge that creates the metastable population used for the optical pumping process. A polarimeter was mounted 350 mm from the pumping cell, at an angle of 16.6° with respect to the laser beam. The polarimeter was housed in a magnetically shielded container. The output from the PMT was fed to two amplifiers, one amplifying only the dc part of the signal, the other amplifying the signal without any change in gain for frequencies up to several kHz. The output of the first amplifier is the dc-signal from the PMT and was directly read by a CAMAC ADC-module. The output of the second amplifier was fed into a lock-in amplifier using the rotation frequency of the QWP of the polarimeter as a reference. This allows the extraction of the small ac part of the signal.

The polarimeter was found to be sensitive to the 15 MHz discharge frequency. This appeared as a *dc offset* depending on the discharge intensity. This offset was measured at every spin reversal and subtracted from the dc signal. The procedure at spin reversal went as follows:

1. Turn off 15 MHz discharge.
2. Reverse laser beam polarization.
3. Turn on 15 MHz discharge. This does *not* start the discharge since the 15 MHz RF signal is not strong enough to break down the gas.
4. Measure the dc signal. This is the offset.
5. A short, strong 200 kHz pulse is applied to the gas. This breaks down the gas and starts the discharge. The 15 MHz RF source then maintains the discharge.

3.4.6.3 Systematic error of the target polarization measurement

The measurement of the target polarization starts with the measurement of the ac and dc components of the PMT signal. The different sources of errors in these measurements are shown in table 3.4. The error in the ac measurement is dominated by the uncertainty in the amplifier offset. This was usually negligible, but sometimes offsets in the order of 1.0% occurred. The dc offset is less than one third of the total signal, hence the error in the dc level is dominated by the error in dc_{meas} , the measured dc voltage. This is in turn dominated by the errors in the amplifier gains.

Measurement of the AC component of the PMT signal		
Variable	source of error	error
$lockin\ signal = li_{adc} \cdot li_{scale}$		
li_{adc}	CAMAC adc measurement (from manual)	0.1%
li_{scale}	factory calibration of lock-in amplifier (from manual)	0.1%
additional lock-in amplifier errors		
	lock-in amplifier phase offset (4)	0.4%
	lock-in amplifier offset (5)	1.0%
TOTAL		1.1%
Measurement of the DC component of the PMT signal		
$dc\ signal = dc_{meas} - dc_{offset}$		
$dc_{meas/offset} = dc_{adc} \cdot dc_{scale}/dc_{gain}$		
dc_{adc}	CAMAC adc measurement (from manual)	0.2%
dc_{scale}	adc scale factors (factory calibration)	0.1%
dc_{gain}	dc gain - all amplifier gains (1)	1.0%
TOTAL		1.0%

Table 3.4: Errors in the measurement of the PMT signal

The PMT signal is related to the nuclear polarization by the pressure factor. The error in the pressure factor is due to the error in the cell pressure measurement and the absolute calibration accuracy. The sources of the errors are itemized in table 3.5. The errors in the capillary conductance are due to the measurement of the pumping cell volume and therefore the errors in both C_1 capillaries are completely correlated. The dependence of the pressure factor on the pressure is roughly linear with a tangent of about 3 and the ratio of their values is around 23 to 1. The error of 7.0% on the pressure therefore translates to an error of about 1% on the pressure factor.

Measurement of the pumping cell pressure		
Variable	source of error	error
$p_{input\ pressure} = (p_{dvm} + p_{dvm\ offset}) \cdot p_{dvm\ calibration}$		
p_{dvm}	dvm reading	0.05%
$p_{dvm\ offset}$	dvm reading offset	0.1%
$p_{calibration}$	factory calibration of baratron(from manual)	0.2%
$p_{cell} = \frac{C_{1m} + C_{1v} \cdot p_{input\ pressure}}{C_{2m}} \cdot p_{input\ pressure}$		
C_{1m}	input capillary molecular conductance calibration	5.0%
C_{1v}	input capillary viscous conductance calibration	5.0%
C_{2m}	output capillary molecular conductance calibration	5.0%
TOTAL		7.0%

Table 3.5: Errors in the measurement of the pumping cell pressure

The magnetic field dependence of the pressure factor was measured by Lorenzon et al. (see reference [68]). In table 3.6 the sources of the error in the magnetic field measurement are estimated. The offset in the magnetic field (due to the stray field of the spectrometer magnet and the target correction coil) is about 1/3 of the total field, opposite the target holding field. Its absolute error is therefore about 1/4th of that of the holding field. Hence the error in the magnetic field is completely dominated by the error in $b_{calibration}$. This implies an error of 1%. This translates in an error of less than .1% in the magnetic field correction factor.

Measurement of the magnetic field		
Variable	source of error	error
$I_{coil} = (b_{dvm} + b_{dvm\ offset}) \cdot b_{dvm\ calibration}$		
b_{dvm}	dvm reading	0.05%
$b_{dvm\ offset}$	dvm reading offset	0.1%
$b_{dvm\ calibration}$	factory calibration of supply (from manual)	0.1%
$b_{field} = (I_{coil} \cdot b_{calibration}) + b_{offset}$		
$b_{calibration}$	fit to field map	1.0%
b_{offset}	fit to field map	1.0%
TOTAL		1.0%

Table 3.6: Errors in the measurement of the magnetic field

The influence of the measurement errors in the correction factors is summarized in table 3.7. The error due to the error in the measurement of the polarimeter angle was added. The angular dependence of the circular polarization is a simple $\cos(\theta)$ form [68]. Hence an error of 1° corresponds to a 0.5% error in the angular correction factor.

Errors in the correction factors		
Variable	source of error	error
pressure factor	pressure dependence	1.0%
pressure factor	calibration accuracy [68]	1.9%
magnetic field correction	magnetic field dependence	0.1%
θ	measurement of angle of polarimeter	0.5%
TOTAL		2.2%

Table 3.7: Summary of the errors in the correction factors

The combination of all the above errors into the error in the polarization is shown in table 3.8.

Apart from the systematic error discussed above, there are two other sources of measurement errors. The first is caused by the strong RF pulse starting the discharge. This pulse causes a strong light flux into the PMT, increasing its dark current. This in turn increases the dc signal. The dc signals for a

Propagation of the errors into the polarization	
$P_{target} = \sqrt{2} \cdot (\text{pressure correction}) \cdot (\text{lockin signal}) / (\text{dc signal})$	
correction factors	2.2%
ac signal	1.1%
dc signal	1.0%
	TOTAL 2.7%

Table 3.8: Error propagation for the polarization

typical sequence of spin flips is shown in figure 3-20. The dark current increase after the spin slip is shown clearly. This effect causes an error of about 1% right after the discharge is lit. By the time the polarization has built up the error is reduced considerably. The average polarization measurement suffers even less, since this effect only persists for the first few bursts after the spin flip (there are 60 bursts between spin flips). An upper estimate of the error is .1%.

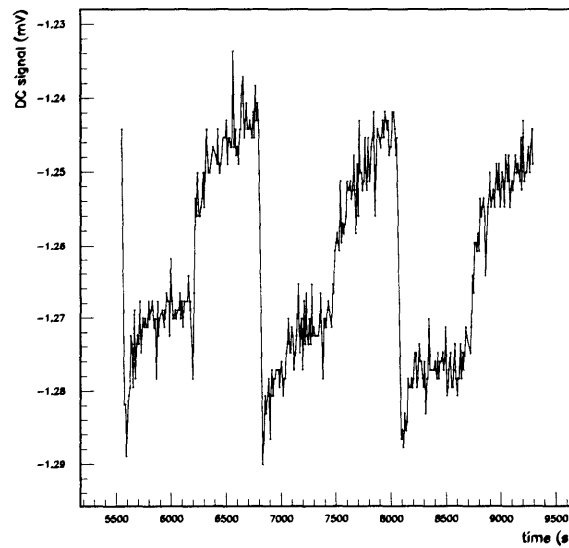


Figure 3-20: The dc component of the polarimeter signal

A second source of error is caused by an unexplained correlation between the dc level of the discharge and the target polarization state. This is obvious from figure 3-20. This effect was studied and the following conclusions were drawn:

- The difference is not caused by the laser light. Shuttering the laser beam did not cause instant changes in the dc nor the ac signal.
- The difference is not caused by a systematic difference in the discharge properties. This is clear because the discharge properties could only accidentally correlate with the target state. The correlation was however very stable and reproducible over several months.
- Reversing the target holding field switched the position of the dc level, that is the state that used to have the lowest dc level now had the highest dc level and vice versa.

The conclusion was that the effect was real. The dc level of the discharge light is correlated to the polarization of the gas. We have not been able to explain the effect. It seems to be caused by a higher multipole component of the emitted light. It has been treated as a systematic error for the current analysis of the data. Further studies of this effect will be undertaken in 1997. The difference between the dc levels is about 2.5%. To determine the total error in the polarization it seems prudent to add this error linearly to the error coming from other sources, giving an error of 5.2%. The error introduced by the increased dark current after a spin flip should probably also be added linearly to this error, since its sign is constant. The final estimate for the error in the polarization measurement is therefore 5.3%.

3.4.6.4 The target optical polarimeter (TOM)

A second polarimeter was used to measure the polarization inside the target cell directly. The main difference between this polarimeter and the PCP lies in the excitation mechanism generating the light. Whereas the PCP uses the light coming from the RF discharge, the *target optical monitor* (TOM) uses the light coming from the recombination of excited states created by Coulomb excitation from the positron beam. The photon flux is of course much smaller, necessitating the use of photon counting techniques. Aside from the technological complications it is also clear that the statistical errors will be much larger. An example of the simultaneous polarization measurements with the PCP and TOM is shown in figure 3-22. In this plot each datapoint represents the average polarization over 100 seconds of data. The statistical error on the TOM polarization is about 30% in this case. A full description of the technical details of the TOM can be found in reference [73]. Here we just look at the main points.

A schematic diagram of the TOM is shown in figure 3-21. The photons coming from the target cell are collected by a polished aluminum mirror placed upstream. The center of the mirror has an elliptical hole in it to accommodate the passage of the positron beam. The photons reflecting on the mirror leave the vacuum through a quartz vacuum window. A second mirror reflects them into the polarimeter. This second mirror is constructed identically to the first one, but rotated by 90° . This cancels the phase

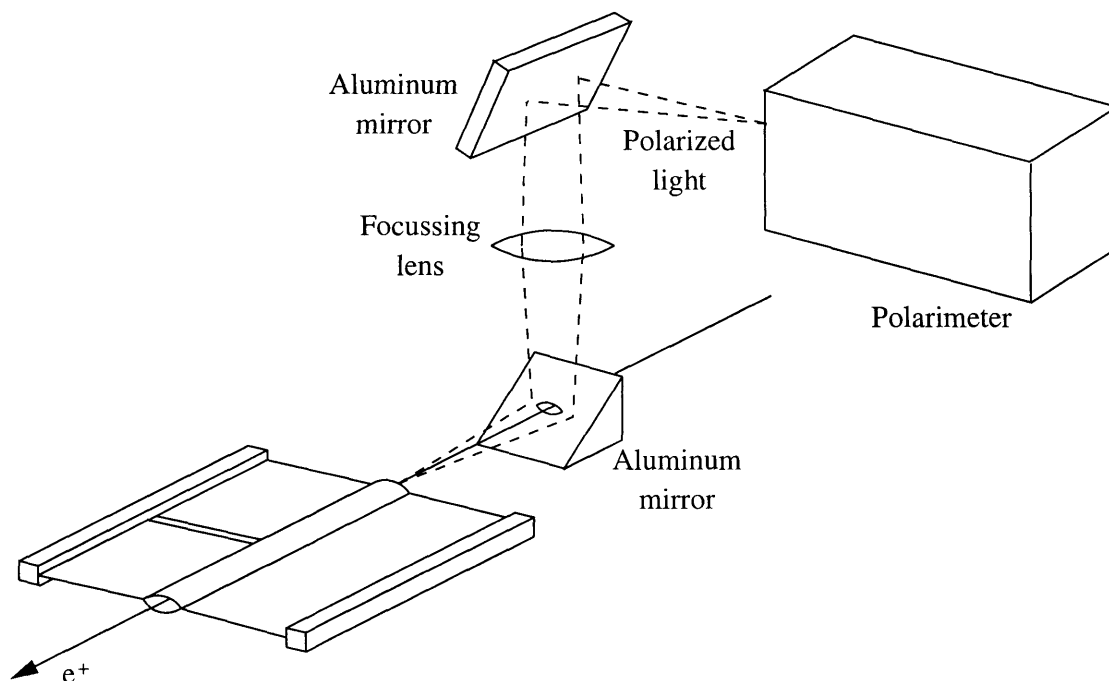


Figure 3-21: The Target Optical Monitor (TOM)

shifts introduced by the first mirror to a large degree, an essential point since the phase shifts change the polarization state of the photons.

Whereas the PCP looks at the light coming from a pure gas discharge, with clearly separated transition lines, the TOM has large continuous backgrounds coming from synchrotron radiation and thermal radiation. This background makes it imperative to use a more sophisticated interference filter (3 nm bandwidth). Since the synchrotron background is in time with the positron bursts, it can be reduced by using a gated measurement. This does not affect the signal too much. With this gating scheme the signal-to-background ratio is typically about 1:2. The backgrounds were measured every fill for a short period (with no gas in the target). The changes in the background were monitored continuously by splitting off a small fraction of the light with a beam splitter. This light was then passed through a different interference filter centered around a wavelength where there are no ^3He transitions. A second PMT monitored this background signal.

The optical transition monitored by the TOM is the 4^1D to 2^1P transition (492.2 nm). This is different from the one used by the PCP, and the reason for this is the longer lifetime 37 ns of this transition. This is long compared to the hyperfine mixing time constant for this level (1.5 ns), but still

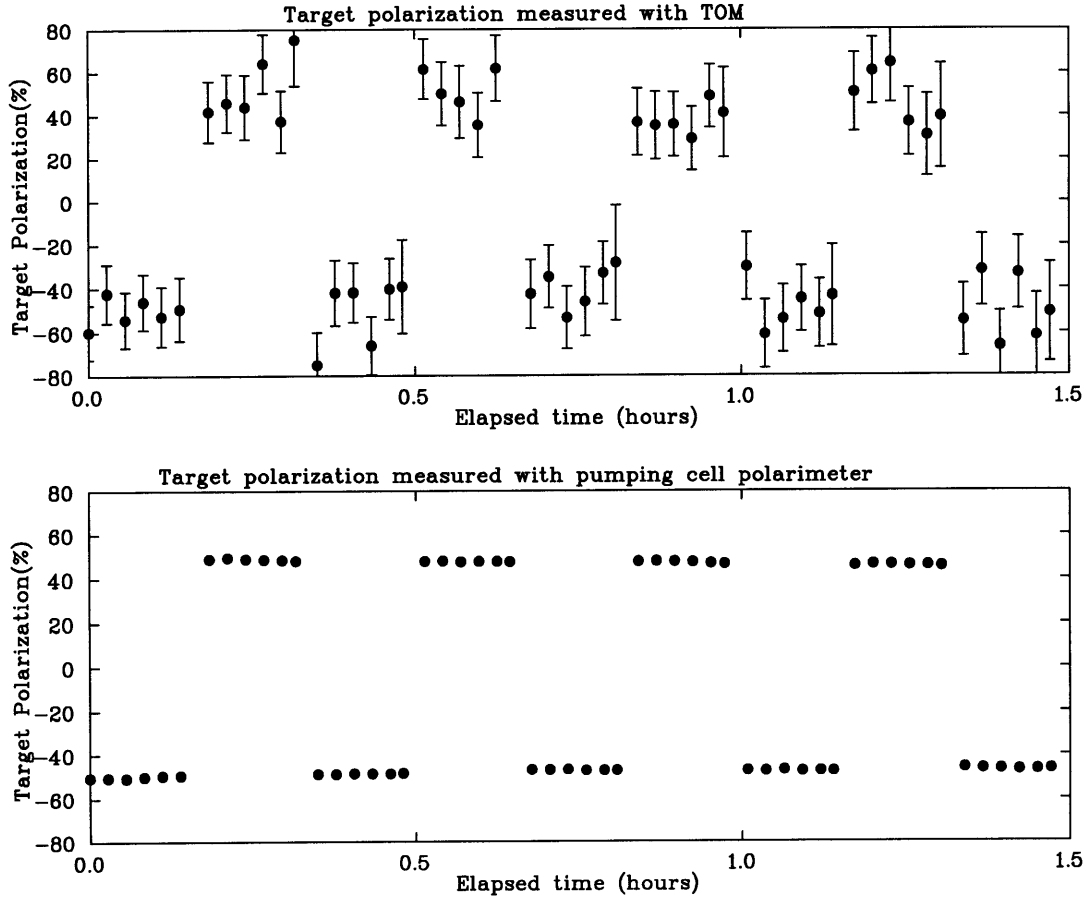


Figure 3-22: TOM and PCP polarizations measurements for 100 second intervals

much shorter than the length between HERA positron bursts (96 ns). Hence the circular polarization will be large and the entire signal can be integrated with a straightforward gate.

3.4.6.5 Depolarization studies

The main use of the TOM is not in the absolute measurement of the polarization, but as a monitor of the relative polarization. As such it is extremely useful to study beam depolarization as well as temperature dependent wall depolarization effects.

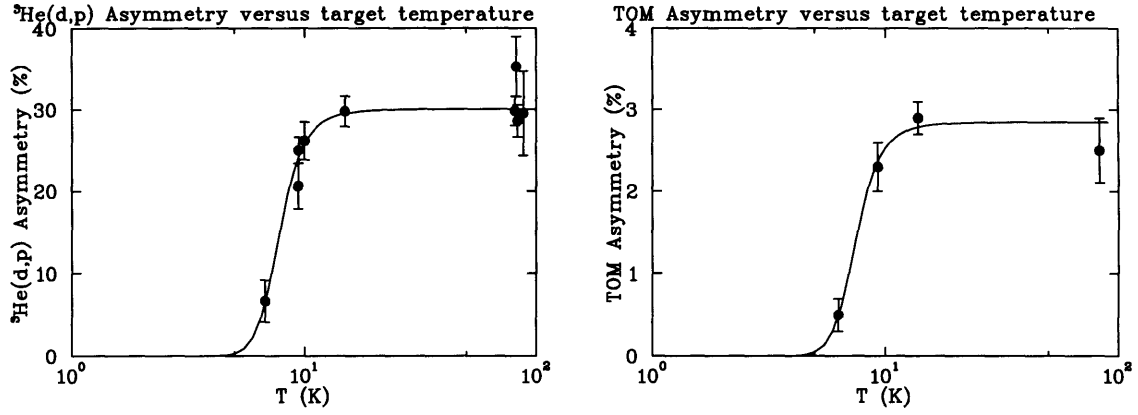


Figure 3-23: Results from the Caltech test experiment for the temperature-dependent wall depolarization

This was demonstrated in the tests performed at Caltech using the low energy proton and deuterium beams from the PELLETRON accelerator as described in [58]. These tests used a target very similar to the HERMES target. The polarization in the target cell was measured with a TOM as well as with the left-right proton analyzing power of the $^3\text{He(d,p)}$ reaction. The correlation between the two measurements was very good, both indicating no substantial depolarization for temperatures over 8 Kelvin. The drop in polarization for lower temperatures is caused by the increased sticking time of the atoms to the wall. From the observed $P(T)$ relation the adsorption energy of ^3He on the aluminum surface can be derived. The results from this experiment are shown in figure 3-23.

The temperature in the HERMES target cell was always safely above 18 K. Figure 3-24 shows the ratio of TOM and PCP measurements of the polarization for various internal target temperatures. Over the entire measured range (18-60 K) the ratio changes less than 5% at the 1σ confidence level.

Although helium has a closed electron shell configuration, the presence of ions in the target allows for the possibility of beam-induced depolarization. This has been shown experimentally for the high-density external targets (see [74] and [75]). For the HERMES target the gas only spends a very short time inside the storage cell, after which it is pumped away. This means there is very little time for an atom to become ionized, depolarized and DIS-scattered from. Hence we do not expect a significant beam-induced depolarization. This was tested by measuring the TOM to PCP ratio as a function of positron beam current. The result (shown in figure 3-25) does not indicate any decrease of the polarization in the target cell with increasing beam current. The relative change in polarization from 12 to 29 mA is less 7% at the 1σ confidence level.

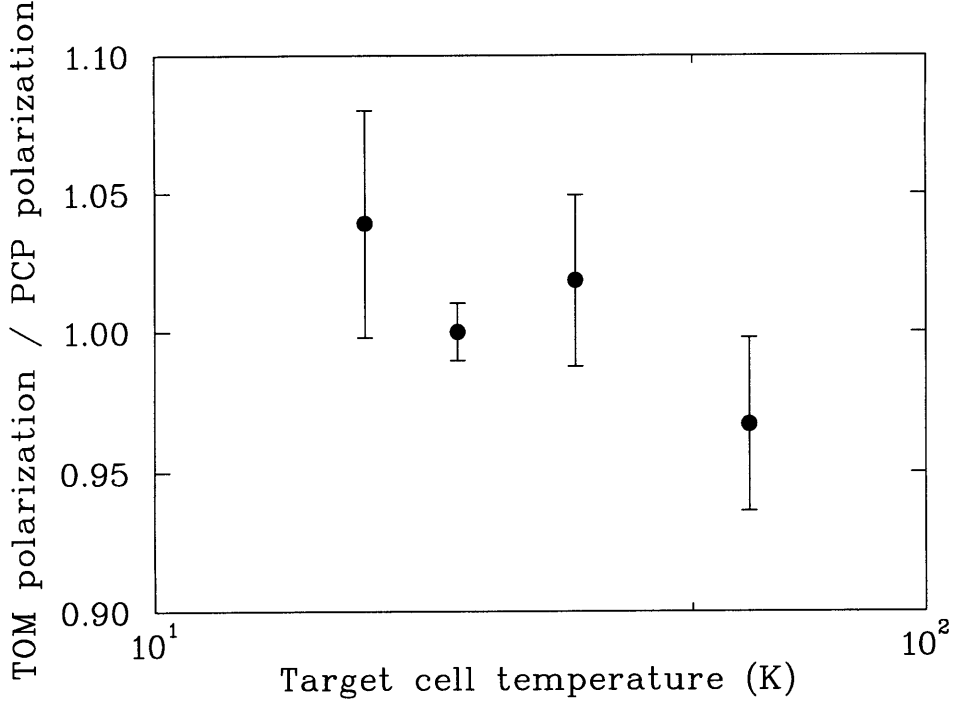


Figure 3-24: Ratio of TOM to PCP polarizations for different temperatures ranging from 18 to 60 Kelvin

3.5 Target performance

The maximum polarization reached on small tuning cells was 81%, with a laser power of 3.2 W, in a Helmholtz field. The preliminary tests using sealed cells were done with a 3 inch ID cubic cell (volume .44 liter) and a crossed cylinder cell made of two cylinders of 2.75 inch ID (volume about .7 liter), both filled to .5 Torr. The polarization in the latter cell was optimized with a 3 Watt, 2-etalon laser. We found a maximum polarization of 67%, for a pump-up time of 43 seconds. This corresponds to a polarization rate of $\frac{.67}{43} \times 1.2 \times 10^{19}$ [1/sec] = 1.8×10^{17} [1/sec]. The maximum polarization for the cubic cell was found to be 76%, for a pump-up time of 35 seconds. This corresponds to a polarization rate of 1.7×10^{17} . The polarization that these cells would reach in a flow-through assembly at a nominal flow rate of 10^{17} was estimated from the formula $P_o^{flow} = P_o^{sealed} \times \frac{\tau_{res}}{\tau_p + \tau_{res}}$ where τ_{res} is the residence time of the helium atoms in the pumping cell and τ_p is the pump-up time in the sealed cell. The result gave an optimized polarization of about 61% for the cubic cell, and about 57% for the crossed cylinder cell.

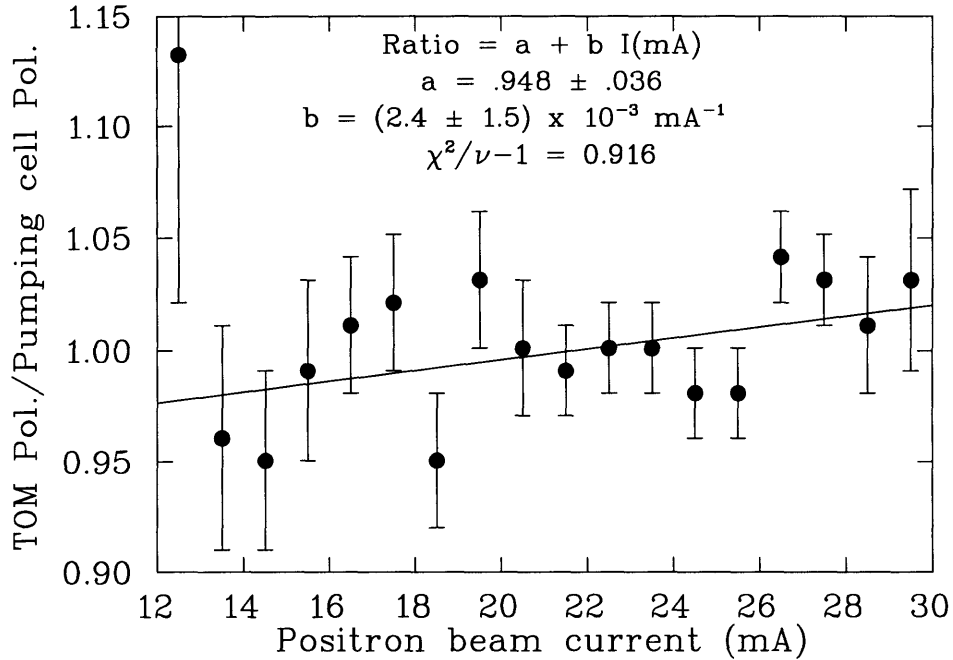


Figure 3-25: Ratio of TOM to PCP polarizations for different current ranging from 12.5 to 29.5 mA

The maximum polarization observed in the target was 54%, but polarizations in excess of 50% were normal. The reason for the somewhat lower than expected polarization is the reduced laser power available on the target platform (typically 1-2 Watts). The averaged polarization over the datataking period was 47%. The polarization was reversed every 10 minutes. During the spin reversal the polarimeter DC offset was measured. Each reversal took about 30 seconds.

For the 1996 and 1997 data taking HERMES will use a hydrogen target. For 1998-1999 the neutron will again be studied. If the helium target is installed again, several improvements can be made. First, the uniformity of the target holding field can be improved by removing the plain steel pump station support for PS2. Second, the gas cleanliness can be improved by longer baking and possibly the use of purifiers just before the glass cell. Third, the cubic cell design can be replaced by the more efficient cylindrical cell. While the latter design only allows one polarization direction, it has less dead volume and will therefore allow an increase in the target polarization.

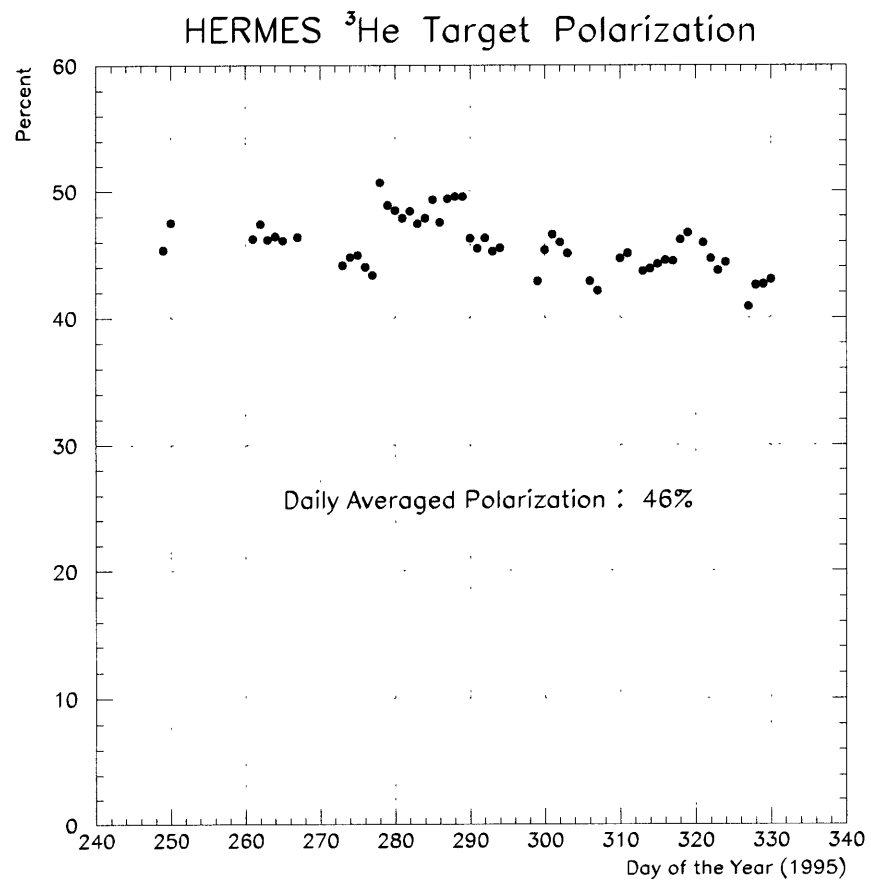


Figure 3-26: The target polarisation during the 1995 HERMES data run. Average of polarization during data taking was 47%

Chapter 4

The data analysis

One of the problems complicating the analysis of the neutron data is that the measured (diluted) asymmetries are relatively small. Their extraction requires stability of all the components in the experiment. The constantly varying luminosity inherent to the storage ring technique makes this an interesting challenge. The fact that 1995 was the first production year meant that the ground was unploughed, and it was necessary to identify the essential cuts and data quality criteria. This has been brought to a fairly satisfactory end, and further analyses can use the extensive body of experience acquired.

Most of the effort of the g_1 analysis was spent in understanding the quality of the data, especially in understanding possible time variations and correlations in the measured asymmetry. The commissioning of the experiment was plagued by the usual problems, and the final result of the analysis contains some residual error that could not be identified. The quantization of this error and the search for its cause took most of the time spent on the analysis. Because of this experience the range of diagnostics available in the data stream was expanded considerably for the next production run.

In this chapter the data quality studies will be described. These studies determined the cuts applied to obtain $A_{||}$.

4.1 The data flow

4.1.1 The data acquisition system

The detector ADC and TDC values were read out with every event trigger as explained in section 2.2.5. Additional information on the status of the detector (voltages, gas flow, etc.) was read out every 10

seconds in a *slow control event*. All events were buffered by the online computers and written to tape as soon as possible.

4.1.2 The analysis chain

The raw HERMES data were written to tape in EPIO format on an event by event basis. The raw data are data register dumps from the FASTBUS and VME crates. These data are processed by the data analysis software to reduce the size of the files by eliminating superfluous information and rationalizing the necessary information. This process is done in three steps. In the first step the data is read in EPIO format by HDC, the Hermes DeCoder. It transfers the raw ADC and TDC values into ADAMO [76] data structures and applies calibration functions to translate the raw values into physical quantities. HDC also translates module numbers to actual detector components. The end result is an ADAMO database containing energies, times and pulse heights for each detector component that fired. In the second step HRC, the *Hermes Reconstruction Code*, reads the ADAMO files and processes them further. Tracks are found and associated with wire hits, pulse heights and timing information. The output consists of ADAMO tables relating this information on a track by track basis in a more accessible format. The slow control information is also added to the tables. In the third step ACE, the *Alignment, Calibration and Efficiency* program, is run on the HRC output to determine wire chamber efficiencies, calibration constants and the like. In principle this step needs to be alternated with the second to improve calibration and alignment. This was done several times - partially because the calibration procedures were continuously improved.

The final files are still fairly large in size, and need to be this way to allow flexibility in the analysis. The size is further reduced for specific analyses by compressing the data in DST (*Data Summary Tapes*) files. These files are constructed by eliminating all information that is irrelevant for the physics analysis at hand. These files also contain the information from the periodic 10 second "slow-control" events (so-called bursts) that are used for quality selection and normalization (e.g. ACE efficiencies, beam and target polarizations, luminosity, ...) and a minimum of track information (e.g. E' , θ , ϕ , PID3, ...) that allows the kinematics of the track to be determined and particle identification to be made. For the g_1 analysis essentially all bursts and their fully reconstructed tracks are transferred to the DST's with the following exceptions:

- Bursts that originate at the start and end of target spin flipping (so-called 1203's) are eliminated.
- Tracks are kept if they correspond to trigger 18 (H1*H2*CAL) and were fully reconstructed (i.e. no partial tracks).

- Only tracks that have $Q^2 > 0.6 \text{ GeV}^2$ and $y < .85$ are transferred.

This keeps the files to a reasonable size and allows hadrons to be included, although the information kept on the hadrons is very limited. A different DST is produced for semi-inclusive studies that does contain all the PID information on the hadrons.

4.1.2.1 The track reconstruction algorithm

The reconstruction of decoded events is done using a tree search algorithm. This algorithm is a very efficient way to select the hits belonging to a track. A full explanation is given in [77], so only a short description will here be given.

All tracking chambers provide three position parameters: u, v and x (see section 2.2.2). The tracks are first reconstructed in each of these 3 projections separately. Every physically possible track can be classified by the pattern of the hits in a *grid* describing the detector. The most detailed grid actually describes each wire in each chamber as a cell, and consequently every track corresponds to only one pattern. By limiting the resolution of the grid more tracks will correspond to the same pattern. The search algorithm will overlay a rough grid over the data and see which patterns are present. Those patterns are then further refined by taking a smaller grid and repeating the process, but only for the subpatterns of the pattern that was determined. This is done several times until the full track has been identified. The final pattern that is found is called a *tree line*. For each projection such a tree line will be found. The number of hits that are allowed to be missing in a tree line is a value that can be optimized to allow for inefficiencies in the chambers without creating too many fake tracks during the search.

This procedure is fast since the patterns can all be enumerated and hierarchically stored in a lookup table. No fitting routines have to be used until all hits belonging to a pattern have been identified.

The finite resolution of the detectors and possible miscalibrations are taken into account by allowing a *road width* in which hits are considered. This means the granularity of the search tree is limited to the road width.

The track search is done independently for the front and back region of the detector. The full tracks are then determined by matching the front and back tracks. The corresponding momentum for the track is deduced from the bend of the track in the magnet using a momentum lookup table.

The low efficiency of the VC's in 1995 restricted the front region reconstruction to the front chambers, since otherwise the statistics would drop unacceptably low. This reduced the accuracy of the

reconstruction considerably. The large dead areas in the MC's also prohibited the use of a Kalman-filter technique to combine front and back region tracks. It was hence necessary to rethink the reconstruction program for the analysis of the 1995 data. The front region tracks were reconstructed using only the front chambers. The partial tracks in front and back region were then connected using the so-called *forced-bridge* technique. This technique relies on the fact that the extrapolation of the back region track to the center of the magnet coincides to within 1.0 cm (for low energetic particles) with the extrapolation of the front region track. This allows to find the corresponding tracks in front and back region. Since the average multiplicity of tracks is very low (1-2), there is very little ambiguity in the association. To make up for the reduced accuracy in the front region tracking, the back region tracks are used to optimize the front track. This method (suggested by P. Galumian) relies on the calculation of the momentum using front and back tracks, which is then used to improve the front track. This can be reiterated and converges in 2 to 3 iterations. The standard tracking technique was used to cross-check this algorithm and showed no detectable biases. Hence we can use it to increase the statistics of the experiment without adding to the systematic error.

4.1.2.2 The particle identification procedure

Each detector reacts differently for positrons and hadrons. When one knows the response function for each particle as well as the total number of particles of each type going through the detector (the flux factor), one can determine the probability that the hit was caused by each type of particle. The basis of the particle identification capacity of each detector has been discussed in chapter 2. One can use the PID detectors as 4 separate detectors, placing cuts on the response of each of them. This method of particle identification is referred to as *hard cuts* PID. This usually is not the optimal procedure to get a maximum efficiency for a minimal contamination, but it is very useful to obtain a clean sample of a certain particle type by applying restrictive cuts.

The optimized PID criterion uses all 4 PID detectors simultaneously. The responses of the calorimeter (CAL), preshower (PRE), Čerenkov (CER) and transition radiation detector (TRD) are combined to calculate a probability that a particle was of a certain type. For this we need to know the *parent distributions*, the response curves for each particle type r , for each detector. The value $D^r(R)$ of the parent distribution is large when the chance that a type r particle produces the response R is large. The parent distributions are normalized, such that the integral over the entire response range is 1. Given those distributions $D_i^r(R_i)$ and the relative frequency with which each particle goes through the detector (the flux factor Φ^r) we calculate the following probabilities that a track with responses R_i for each

detector i was created by a particle of type t :

$$P_{CAL}^t \equiv \frac{D_{CAL}^t(R_{CAL}) \cdot \Phi^t}{\sum_r D_{CAL}^r(R_{CAL}) \cdot \Phi^r} \quad (4.1)$$

$$P_{PRE}^t \equiv \frac{D_{PRE}^t(R_{PRE}) \cdot \Phi^t}{\sum_r D_{PRE}^r(R_{PRE}) \cdot \Phi^r} \quad (4.2)$$

$$P_{CER}^t \equiv \frac{D_{CER}^t(R_{CER}) \cdot \Phi^t}{\sum_r D_{CER}^r(R_{CER}) \cdot \Phi^r} \quad (4.3)$$

$$P_{TRD}^t \equiv \frac{D_{TRD}^t(R_{TRD}) \cdot \Phi^t}{\sum_r D_{TRD}^r(R_{TRD}) \cdot \Phi^r} \quad (4.4)$$

This is a simple application of Bayes' theorem.

For the case of hadron-positron separation there are only two types of "particles", positrons and hadrons. The formulae then simplify to:

$$P_i^e \equiv \frac{D_i^e(R_i) \cdot \Phi^e}{D_i^e(R_i) \cdot \Phi^e + D_i^h(R_i) \cdot \Phi^h} \quad (4.5)$$

Alternatively one can use the ratio of the probability that the particle is a positron to the probability that it is a hadron:

$$P_i^{\frac{e}{h}} \equiv \frac{D_i^e(R_i)}{D_i^h(R_i) \cdot \Phi} \quad (4.6)$$

$$\Phi \equiv \frac{\Phi^h}{\Phi^e} \quad (4.7)$$

To use all available information of the detectors we combine the probabilities in a multiplicative fashion:

$$P^{\frac{e}{h}} \equiv \prod_i P_i^{\frac{e}{h}} \quad (4.8)$$

The product of probabilities is *not* a probability. For example, it will not add up to unity. This is not a full probability analysis of the total detector response. It does however incorporate all information in a straightforward manner. The separation between hadrons and positrons is large and easy to use. It is however hard to understand what quantity we are actually cutting on. This makes it hard to find the contamination and efficiency for this cut.

Since the range of $P^{\frac{e}{h}}$ is very large it is customary to use the logarithm of the ratio, which has been defined as the variable PID3:

$$PID3 \equiv \log_{10} (P^{\frac{e}{h}}) \quad (4.9)$$

x-bin	PID3-TRD cut		PID3 cut		PID2-TRD cut	
	e^+ eff.	h^+ cont.	e^+ eff.	h^+ cont.	e^+ eff.	h^+ cont.
0.023 - 0.040	97.77	1.18	96.21	4.07	98.55	1.58
0.040 - 0.055	98.38	0.81	97.28	2.65	98.96	1.07
0.055 - 0.075	98.78	0.55	97.93	1.71	99.12	0.74
0.075 - 0.100	99.21	0.37	98.64	1.09	99.47	0.47
0.100 - 0.140	99.44	0.22	99.05	0.68	99.57	0.26
0.140 - 0.200	99.64	0.16	99.33	0.43	99.69	0.15
0.200 - 0.300	99.71	0.16	99.44	0.30	99.74	0.15
0.300 - 0.400	99.72	0.16	99.48	0.27	99.77	0.15
0.400 - 0.600	99.72	0.11	99.48	0.26	99.77	0.14

Table 4.1: Positron efficiency and hadron contamination in each x-bin for the three different PID schemes

A linear combination of the TRD response and PID3 is then used to identify positrons and hadrons. It has to be stressed that this analysis is only useful for a two-particle differentiation. To distinguish more particle types one needs to use the full probability analysis.

For runs where the TRD or the Čerenkov were not operational, a simple PID *downshifting* scheme was implemented. If the Čerenkov cannot be used, a cut in the TRD versus PID2 plane is used instead, where PID2 is the logarithmic likelihood generated from the PRE and CAL signals. If the TRD is not usable, a simple cut on PID3 is used. In the rare case that both the TRD and the Čerenkov are unusable the run is discarded for the affected detector half.

The particle ID cuts were:

- Positive charged tracks: $charge = +1$
- Positron identification TRD and CER good: $PID3 + 0.31 \cdot TRD > 5.48$
- Positron identification if TRD bad: $PID3 > 0$
- Positron identification if CER bad: $PID2 + 0.51 \cdot TRD > 9.0$
- Positron with leading momentum in the event: $p = p_{max}$ (all e^+ per event)

The values for the positron efficiency and hadron contamination for all three PID cuts are given in table 4.1. For the down-shifted PID without TRD or without Čerenkov the efficiencies are not much lower than for the full PID, but the hadron contamination can reach up to 4% in the lowest x_{B_j} bin. A thorough discussion of the particle identification procedure at HERMES can be found in reference [78].

4.2 The data quality selection criteria

Since 1995 was the commissioning year for the HERMES detector, there were several periods where the detector or beam conditions were far from ideal. The data quality studies were designed to select the runs where the detector worked reliably. To this end we used mainly the slow control information, using the actual event yields and distributions as a check for stability. Cutting on the data themselves has to be avoided as “bad practice”, liable to bias the data in a subtle but detrimental fashion.

The data selection naturally divides into three levels.

Run Selection: The HERMES runs were about 10 minutes long. The data from four runs fit on one exabyte tape. Using information in the HERMES logbooks and from the beam polarization and target groups, a list of potentially good runs was defined which was the basis for all other investigations. The DST files were written for only these runs. For some of the runs only one half of the detector (top or bottom) was considered good. A flag in the DST indicated the good and bad half.

Burst Selection: The data was naturally divided up in 10 second *bursts*, corresponding to the slow control data events. The slow control information about the detector and target was used to check the performance of the experiment. Only events from good bursts were used in the analysis.

Track Selection: Each event and track had to fulfill certain conditions to be included in the g_1^n analysis. These cuts were mainly kinematic, but also included the requirement that the track came from the target and made it through the entire detector.

A fourth level was the *fill* level. The HERA fills were natural subsets of the data. This was especially clear when one studied the normalized yields (see section 4.5.1). The yields were not very stable across fills, due to the sensitivity of the detector to beam conditions. However, within a fill the yields were stable and could well be used for asymmetry extractions.

4.2.1 Run Selection

Table 4.2 gives an overview of the run selection statistics. 2183 runs out of 4011 remained after selection by logbook, good beam and good target polarization. The logbook information and run summaries identified runs that were potentially useful for the g_1^n analysis. For example runs where there was an unpolarized target, the spectrometer was off, or significant parts of the detector were not operating

critterion	runs cut	remaining runs
all runs 1995		4011
logbook cut	965	3046
beam pol. bad	720	2326
target pol. bad	143	2183
RUNS on μ -DST		2180
Čerenkov bad top	114	2069
Čerenkov bad bottom	98	2085
TRD bad top	218	1851
TRD bad bottom	74	2011

Table 4.2: Statistics of the run quality selection.

were removed. Also runs where the polarimeter and target groups have indicated that the polarization information was unreliable and uncorrectable have been removed. Runs where the individual particle ID detectors were unusable have been determined by the detector groups and the gain monitoring system (GMS) information.

4.2.2 Burst Selection

The burst selection was done separately for the top and the bottom detector. A flag which is assigned to every burst indicated if the burst is good or bad and which of the criteria fail. The following sections describe the burst cuts in more detail. A summary of the effects of the burst level cuts is shown here in table 4.3. Starting with 125196 bursts which are on the μ -DST, the table shows how many bursts were cut out by each of the selection criteria and how many were cut in addition to the previous cuts.

4.2.2.1 Target Polarization

To be usable the target must to be in a well-defined polarization state. When the target is switching its polarization direction the polarization state is undefined and the whole burst is cut.

As described in section 3.4.6, the target polarization was measured by the pumping cell polarimeter (PCP) and by the target optical monitor (TOM). The measured values should be in a reasonable range. As the statistical error of the TOM measurement is large, fill-averaged values were used when using the TOM measurement was used. The target polarization cuts required:

- Target polarization in a well defined state

$$\text{TargetBit} = \{3,5\}$$

	Total		Incremental	
	top	bot	top	bot
target polarization	12128 (9.7%)	12128 (9.7%)	12128 (9.7%)	12128 (9.7%)
beam polarization	4611 (3.7%)	4611 (3.7%)	4234 (3.4%)	4234 (3.4%)
first bursts	6473 (5.2%)	6473 (5.2%)	5766 (4.6%)	5766 (4.6%)
last burst	2155 (1.7%)	2155 (1.7%)	1831 (1.5%)	1831 (1.5%)
live time	4021 (3.2%)	4021 (3.2%)	645 (0.5%)	645 (0.5%)
burst length	627 (0.5%)	627 (0.5%)	0 (0.0%)	0 (0.0%)
beam current	781 (0.6%)	781 (0.6%)	635 (0.5%)	635 (0.5%)
target density	1730 (1.4%)	1730 (1.4%)	813 (0.6%)	813 (0.6%)
lumi rate	880 (0.7%)	880 (0.7%)	86 (0.1%)	86 (0.1%)
lumi/(I*dens)	2533 (2.0%)	2533 (2.0%)	913 (0.7%)	913 (0.7%)
tracking efficiency	16144 (12.9%)	12713 (10.2%)	12315 (9.8%)	9598 (7.7%)
GMS calo	718 (0.6%)	2262 (1.8%)	545 (0.4%)	1837 (1.5%)
GMS preshower	759 (0.6%)	422 (0.3%)	271 (0.2%)	15 (0.0%)
bad H1 scaler	872 (0.7%)	52 (0.0%)	764 (0.6%)	43 (0.0%)
bad PRE scaler	11 (0.0%)	4 (0.0%)	2 (0.0%)	0 (0.0%)
CER and TRD bad	9302 (7.4%)	1562 (1.2%)	3894 (3.1%)	777 (0.6%)
gap/badburst cut	34551 (27.6%)	28715 (22.9%)	5659 (4.5%)	6033 (4.8%)
good fill	20197 (16.1%)	19426 (15.5%)	1533 (1.2%)	1737 (1.4%)
skip due to previous bad	22916 (18.3%)	20068 (16.0%)	1818 (1.5%)	1836 (1.5%)
TOTAL NUMBER OF BAD BURSTS:			53852 (43.0%)	48927 (39.1%)
TOTAL NUMBER OF GOOD BURSTS:			71344 (57.0%)	76269 (60.9%)
TOTAL NUMBER OF BURSTS:			125196 (100.0%)	125196 (100.0%)

Table 4.3: The table shows the total and incremental statistics of burst cuts. The left columns show the total number of bursts that were identified as “bad” due to that cut; the right columns show how many of those “bad” bursts were not cut out by the previous cuts.

- Target polarization PCP: $30\% < P_T < 60\%$
- Target polarization TOM (if PCP unavailable): $30\% < P_{T(ave/full)} < 60\%$

This eliminated some low polarization values where the pump-up time was large enough that the target polarization was not at its final value when the target state was considered stable. In principle there is nothing wrong with these bursts, but they do not contribute significantly to the asymmetry measurement.

In figure 4-1 the distribution of the target polarization is shown (together with those of other cut quantities). The period where the TOM was used instead of the PCP is clearly visible as a high peak. The periods where the target was unpolarized or where the polarization was not measured do not appear on the plot since those periods are not included in the good-run list.

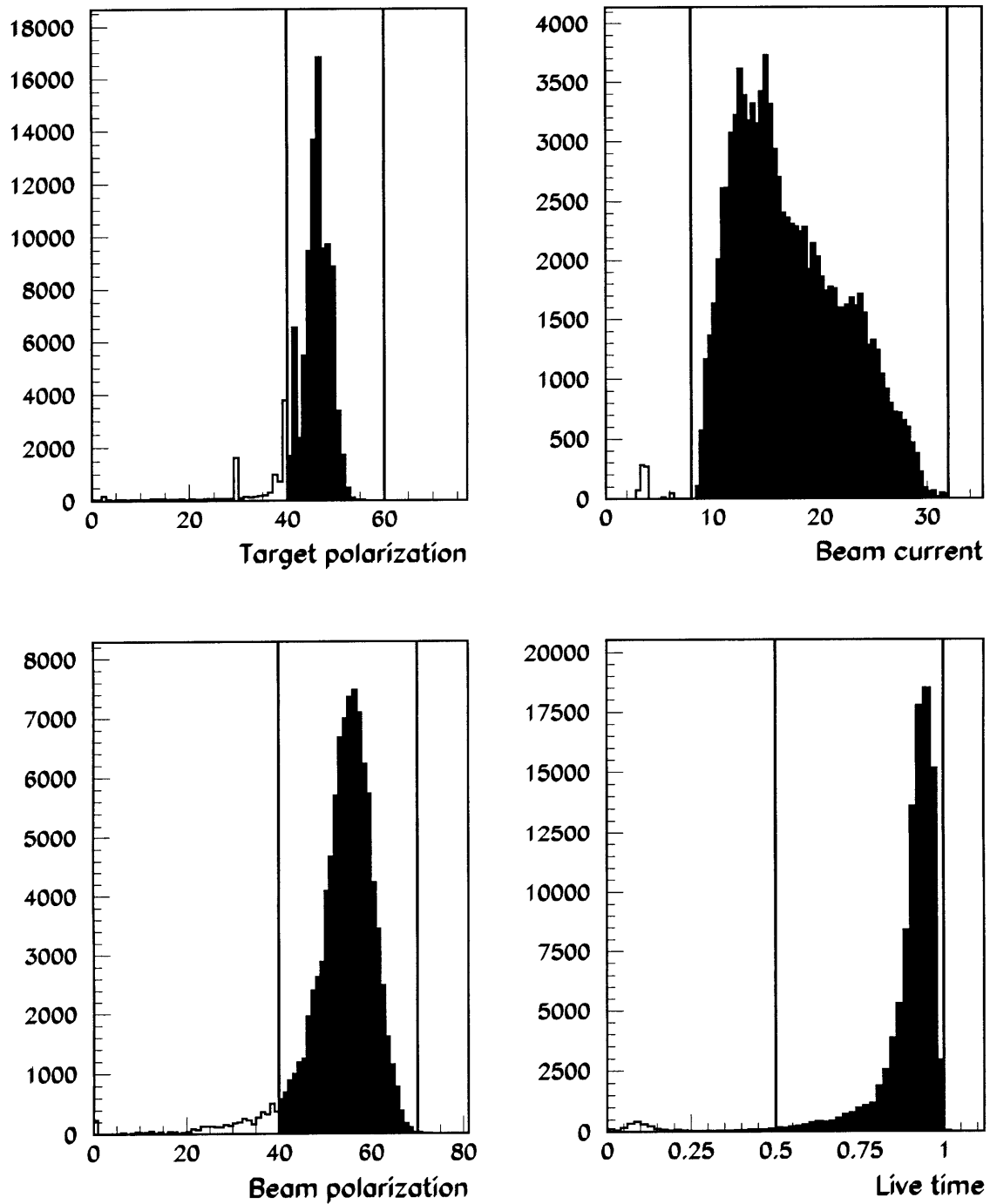


Figure 4-1: The distributions of the basic quantities

4.2.2.2 Beam Polarization

The beam polarization is required to be reasonably large, as low values do not contribute significantly to the asymmetry measurement. The polarimeter has to have reasonable measurements with acceptable errors. The minute by minute measurements are smoothed to remove unphysical jumps and large statistical fluctuations. The smoothed values are also used to fill small gaps in the measurement caused by temporary malfunctions in the polarimeter. However, any period longer than 30 minutes without a polarization measurement was removed from the data set. Each fill was fit separately and checked visually. Periods with unreliable polarization measurements (unknown calibration or large statistical or systematic uncertainties) were flagged by a fitted value of $P_{B(ft)} = 0$ and were not used in the analysis. The beam polarization cut was:

- Beam polarization: $40\% < P_{B(ft)} < 70\%$

4.2.2.3 DAQ

For 1995, the data acquisition system had periods where the dead-time was very large and where the burst length was different from the nominal value of 10 seconds. As this burst length is used to obtain the luminosity normalization, it is important that this information be reliable. To remove these periods, the following DAQ cuts are applied:

- Reject in each run: first 3 bursts
- Reject in each run: last burst
- Live time: $50\% < T_{live} < 100\%$
- Burst length: $9 \text{ sec} \leq T_{burst} \leq 11 \text{ sec}$

4.2.2.4 Luminosity

The luminosity measurement is of great importance for the asymmetry measurement because of the changing beam current and the relatively long time between polarization reversals (typically 10 minutes). To cross-check the performance of the luminosity monitor, the rate is compared to the product of beam current and target density. To ensure that the results are meaningful, all quantities are cut at reasonable boundaries. Bursts with spikes in the luminosity rates are rejected as they indicate problems with the beam, usually partial beam losses. The luminosity cuts are:

- Beam current (machine data module (MDM) current): $8 \text{ mA} < I < 32 \text{ mA}$
- Target density [in nucleons/cm²]: $0.85 \cdot 10^{15} < n < 1.4 \cdot 10^{15}$
- Luminosity monitor rate: $40 \text{ Hz} < \dot{N}_{lumi} < 210 \text{ Hz}$
- Ratio of luminosity/(density \times current) [in cm²s/mA nucleons]: $5 \cdot 10^{-15} < \frac{\dot{N}_{lumi}}{nI} < 7.2 \cdot 10^{-15}$

4.2.2.5 Tracking Efficiency

The quality of the tracking chambers is controlled by cuts on the tracking efficiencies as calculated from the plane efficiencies from the ACE program at the burst level. Since in 1995 the HV information was not written to tape, this is the only way we can identify chamber trips. Since this cannot be expected to be immediately effective we also cut the burst before the efficiency drops under the threshold. The cuts are applied separately for the top and bottom detector.

- Tracking efficiency for forward partial tracks: $80\% < \epsilon_{front} < 100\%$
- Tracking efficiency for backward partial tracks: $94\% < \epsilon_{back} < 100\%$
- If burst fails any of the above cuts: delete previous burst

The rather high number of bursts in table 4.3 which are cut by the back efficiency criteria correspond mainly to a block of runs where the BC threshold voltage was set incorrectly due to a hardware failure which was not recognized by the slow control system. The BC efficiency was increased at the end of the data taking period by a change of the high voltage. In figure 4-2 a trip is shown in the top front detector. The detection drops to zero very fast. There are a few bursts in which the detection efficiency is non-zero, this is due to a very few tracks that were found despite the trip. This is not a problem since these bursts will be eliminated because there are only a few tracks.

4.2.2.6 PID and Trigger Quality:

The performance of the Hodoscope H1, the Preshower (PRE) and the Calorimeter (CAL) effect the trigger efficiency and particle identification (PID). The PID is also affected by the performance of the Čerenkov (CER) and the Transition Radiation Detector (TRD). It is therefore crucial to monitor the performance of these detectors.

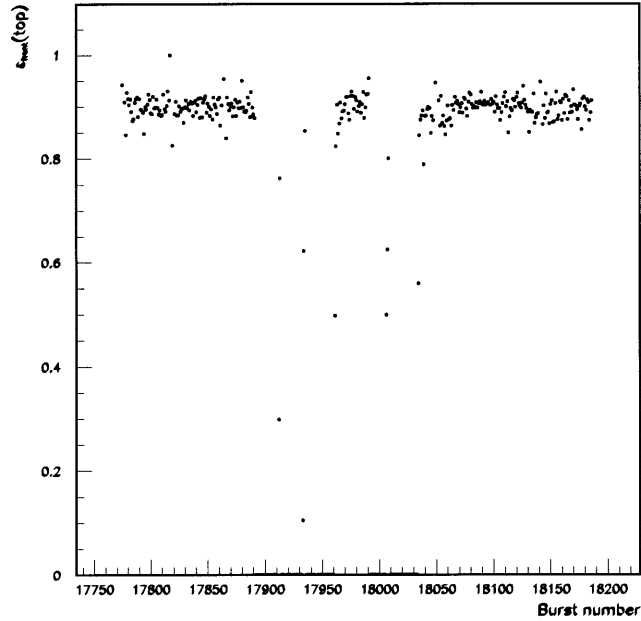


Figure 4-2: Example of trip detection using the tracking efficiency.

For PRE and CAL, GMS information is available on a run-by-run basis since the frequency of the GMS events is too low to calculate the gains at burst level. This data was used to determine the number of bad modules from a comparison of the average gain of the module compared to its nominal value. A cut is applied separately for the inner and outer region of the detector since the inner region is much more critical due to the very forward nature of the scattering. We define the inner region as the central 30 columns of the calorimeter. For the calorimeter the gain must be within 10% and for the preshower it must be within 20% of the nominal value. For H1, the number of scaler counts per burst for each channel of H1 is used. A non-zero value of scaler counts indicates that the HV was on for that channel.

To check the Čerenkov performance an efficiency is calculated from the number of tracks recognized in the Čerenkov detector divided by the total number of good electron tracks. The sample of good electron tracks is defined by PRE and CAL. Because of low statistics, this is available only at the run level as well.

For the same reason the TRD quality is given per run as well. The criteria for the TRD quality include checks if the TRD was on and operating at the proper voltage, trip detection and linearity checks. They are assembled into the TRD run quality bit by the TRD group, separately for top and bottom, and available in the DST's.

The PID performance cuts are:

- number of GMS-bad blocks in top inner calorimeter: $N_i^t \leq 3$
- number of GMS-bad blocks in bottom inner calorimeter: $N_i^b \leq 4$
- number of GMS-bad blocks in outer calorimeter: $N_o \leq 8$
- number of GMS-bad channels in inner preshower: $N_i \leq 1$
- number of GMS-bad channels in outer preshower: $N_o \leq 5$
- number of bad channels in top H1: $N^t \leq 1$
- number of bad channels in bottom H1: $N^b = 0$
- number of bad channels in top PRE: $N^t = 0$
- number of bad channels in bottom PRE: $N^b = 0$
- Čerenkov efficiency $\epsilon_{CER} > 92\%$
- TRD usable: TRD-bit = 1
- If TRD and Čerenkov are unusable top or bottom (T/B): reject run (T/B)

4.2.2.7 Overall Stability

Data periods where the performance of the experiment is unstable should be rejected from the analysis. Runs where the burst quality criteria indicate only a small fraction of good bursts remain or where there are frequent changes from a good to bad state should be rejected (“swiss cheese” cut). These gaps between good periods are quantified as the number of times the burst quality changes from good to bad. The basic time unit for overall detector stability is the HERA fill. To remove possible systematics in the time dependence the spin asymmetry is calculated separately for each HERA fill. Thus there should be enough events in each spin state to make a useful asymmetry measurement. The stability cuts are:

- maximum fraction of gaps: $\frac{n_{gaps}}{n_{bursts}} < 0.10$ (per run)
- minimum fraction of good bursts $\frac{n_{goodbursts}}{n_{bursts}} > .40$ (per run)
- good fill criteria (top and bottom separately):
 - $n_{goodbursts}^+ \geq 100$ (per fill)
 - $n_{goodbursts}^- \geq 100$ (per fill)

4.2.3 Track Selection

The track selection defines the positron sample which enters the g_1^n analysis. We did not use the VC chambers for the reconstruction of the tracks. This provides the maximum amount of data, due to the low efficiency of the VC detector for the 1995 run. The VC's are still used to study possible biases introduced by the *forced-bridge* tracking method as explained in section 4.1.2.1.

Ghost tracks, poorly identified tracks, background tracks, tracks which do not come from the target gas, secondary tracks and hadron tracks have to be removed from the data sample. Fiducial cuts ensure that all tracks have proper particle identification and tracking at the edges of the detectors. The high y cut ensures that positrons near the trigger threshold are cut and also removes events with large radiative corrections. The low y cut deletes events with large smearing corrections. The Q^2 and W^2 cuts select DIS events.

- The vertex is in the target gas: $-30 < z_{vertex} < 30$ cm
- Vertex quality (transverse offset): $r_{vertex} < 0.75$ cm
- Horiz. Fiducial cut at CALO: $|x| < 175$ cm
- Vert. Fiducial cut at CALO: $|y| > 30$ cm
- Fiducial cut septum plate: $|\theta_y| > 0.040$
- DIS kinematic cut (scaling region): $Q^2 > 1$ GeV
This requirement can be relaxed (see appendix B).
- DIS kinematic cut: (non-resonance region) $W^2 > 4$ GeV
- DIS kinematic cut (radiative corrections) and trigger threshold: $y < 0.85$

The kinematic variables are calculated using the momentum and scattering angle as given on the DST. The beam energy and proton mass of

$$E_B = 27.52 \text{ GeV} \quad (4.10)$$

$$m_p = 0.93827 \text{ GeV}/c^2 \quad (4.11)$$

are used to calculate the kinematic variables.

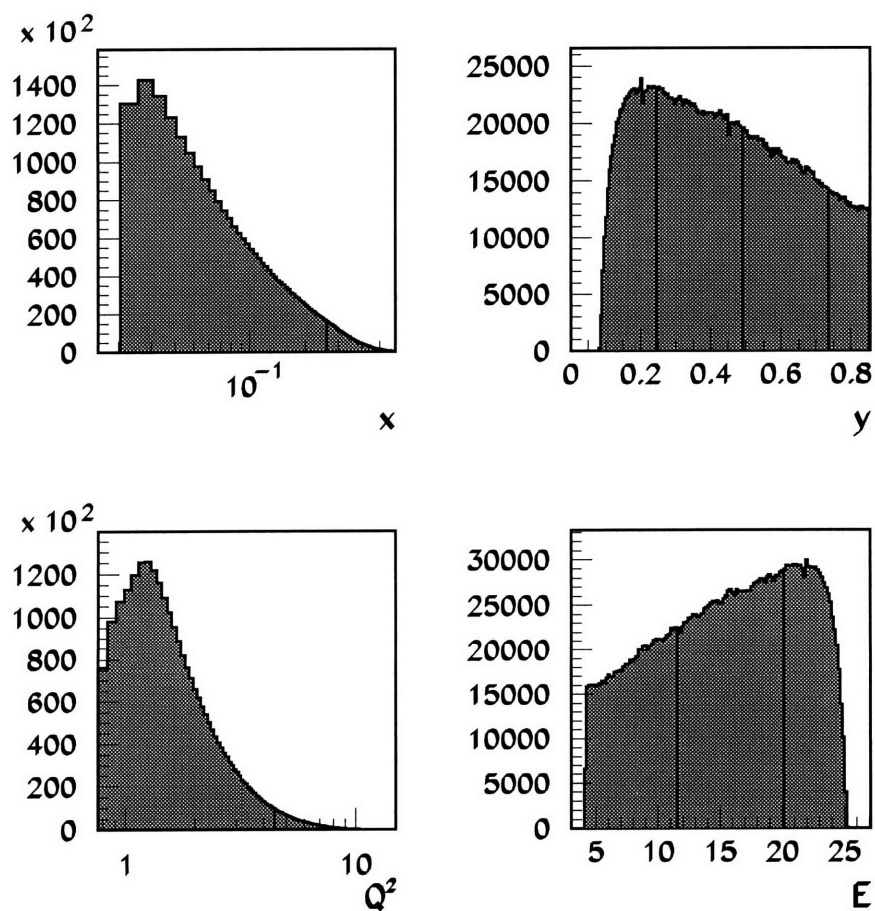


Figure 4-3: The kinematic quantities for all positrons that pass the track cuts

4.3 Extracting the inclusive asymmetries

The count rates for the two spin states are given according to the following formulae:

$$\begin{aligned} N^+ &= \int_+ \mathcal{A}(t, x, Q^2) \mathcal{E}(t, x, Q^2) \sigma^{(unpol)}(x, Q^2) \left(\mathcal{L}(t) - A_1^{3\text{He}}(x, Q^2) \mathcal{L}(t) D(x, Q^2) p_B(t) p_T(t) \right) dt \\ N^- &= \int_- \mathcal{A}(t, x, Q^2) \mathcal{E}(t, x, Q^2) \sigma^{(unpol)}(x, Q^2) \left(\mathcal{L}(t) + A_1^{3\text{He}}(x, Q^2) \mathcal{L}(t) D(x, Q^2) p_B(t) p_T(t) \right) dt \end{aligned}$$

Here \mathcal{A} is the acceptance and \mathcal{E} the overall efficiency of the detector. Assuming the \mathcal{A} and \mathcal{E} are approximately time independent during one measurement and assuming that the data are binned in x and y , the following formulae can be derived:

$$\begin{aligned} N^+ &= \mathcal{A} \mathcal{E} \sigma^{(unpol)}(x, Q^2) \left(\int_+ \mathcal{L}(t) dt - A_1^{3\text{He}}(x, y) \langle D(y) \rangle \int_+ \mathcal{L}(t) p_B(t) p_T(t) dt \right) \\ N^- &= \mathcal{A} \mathcal{E} \sigma^{(unpol)}(x, Q^2) \left(\int_- \mathcal{L}(t) dt + A_1^{3\text{He}}(x, y) \langle D(y) \rangle \int_- \mathcal{L}(t) p_B(t) p_T(t) dt \right) \end{aligned}$$

Assuming that the polarization $p_B(t)$ and $p_T(t)$ is constant over a burst i , the number of events n_i in a burst with positive (negative) polarization is given as

$$n_i^\pm = \mathcal{A} \mathcal{E} \sigma^{(unpol)}(x, Q^2) \left(L_i - (\pm) A_1^{3\text{He}}(x, y) \langle D \rangle L_i (p_B p_T)_i \right). \quad (4.12)$$

Here L_i is the integrated luminosity of the burst. The mean depolarization factor $\langle D \rangle$ will not differ from burst to burst. Using the notation:

$$N^\pm = \sum_{i^\pm} n_i \quad (4.13)$$

$$L^\pm = \sum_{i^\pm} L_i \quad (4.14)$$

$$P^\pm = \sum_{i^\pm} |L_i p_B p_T| \quad (4.15)$$

where \sum_{i^+} (\sum_{i^-}) denotes the sum over all positive (negative) bursts. Then the asymmetry can be calculated as:

$$A_1^{3\text{He}}(x, y) = \frac{1}{\langle D \rangle} \frac{N^- L^+ - N^+ L^-}{N^- P^+ + N^+ P^-} \quad (4.16)$$

and the statistical error is given according to:

$$(\delta A_1^{3\text{He}})^2 = \frac{1}{\langle D \rangle^2} \left(\left(\frac{\partial A_1}{\partial N^+} \delta N^+ \right)^2 + \left(\frac{\partial A_1}{\partial N^-} \delta N^- \right)^2 \right) \quad (4.17)$$

$$= \frac{1}{\langle D \rangle^2} \left(\left(\frac{N^- (L^+ P^- + L^- P^+)}{(N^- P^+ + N^+ P^-)^2} \right)^2 (\delta N^+)^2 \right. \quad (4.18)$$

$$\left. + \left(\frac{N^+ (L^+ P^- + L^- P^+)}{(N^- P^+ + N^+ P^-)^2} \right)^2 (\delta N^-)^2 \right) \quad (4.19)$$

$$\delta A_1^{3\text{He}} = \frac{1}{\langle D \rangle} \frac{L^+ P^- + L^- P^+}{(N^- P^+ + N^+ P^-)^2} \sqrt{(N^-)^2 N^+ + (N^+)^2 N^-} \quad (4.20)$$

The asymmetry for each x -bin is obtained by a weighted average of the asymmetry of the three corresponding y bins. To improve the particle identification and to facilitate the final determination of the contaminations we only use data where we can use all PID detectors.

4.3.1 The kinematic plane

The kinematic plane is shown in figure 4-4. The distribution of the events in x is shown in figure 4-3. There are few events below $x = 0.023$ or above $x = 0.6$, and those values are taken as the low and high boundaries for the data. The bin boundaries are chosen such that the statistics are approximately equally divided. At large x an additional bin with smaller statistics is included. The bin boundaries in x for approximately equally distributed statistics are:

$$0.023 - 0.04 - 0.055 - 0.075 - 0.1 - 0.14 - 0.2 - 0.3 - 0.4 - 0.6 \quad (4.21)$$

It has been checked that all bins are larger than the x resolution for each bin.

For the calculation of A_1 , the virtual photon depolarization factor

$$D = \frac{y(2-y)}{y^2 + 2(1-y)(1+R)} \quad (4.22)$$

is needed to correct the measured raw asymmetry, as well as the polarizations of the beam and target. One way is to weight every event with the (average) polarization of the photon:

$$w = P_T \cdot P_B \cdot D(y). \quad (4.23)$$

x	low y range	middle y range	high y range
.023-.040	0.0-0.68	0.68-0.78	0.78-0.85
.040-.055	0.0-0.53	0.53-0.67	0.67-0.85
.055-.075	0.0-0.42	0.42-0.58	0.58-0.85
.075-.100	0.0-0.34	0.34-0.49	0.49-0.85
.100-.140	0.0-0.27	0.27-0.42	0.42-0.85
.140-.200	0.0-0.22	0.22-0.34	0.34-0.85
.200-.300	0.0-0.17	0.17-0.26	0.26-0.85
.300-.400	0.0-0.14	0.14-0.23	0.23-0.85
.400-.600	0.0-0.15	0.15-0.22	0.22-0.85

Table 4.4: Bin boundaries for each bin

A simpler (and more straightforward) method is to bin the events in y as well as x , which amounts to an effective binning in $D(y)$. As the spread of $P_T P_B$ is not very large in our experiment, a single bin in these quantities is sufficient. Because of the evaluation of the asymmetry for each fill a large number of y values is not possible. Therefore only three bins in y are chosen such that the number of events are divided equally. Table 4.3.1 shows the y bin boundaries for all x bins. All kinematic functions were calculated for each event and averaged over each bin.

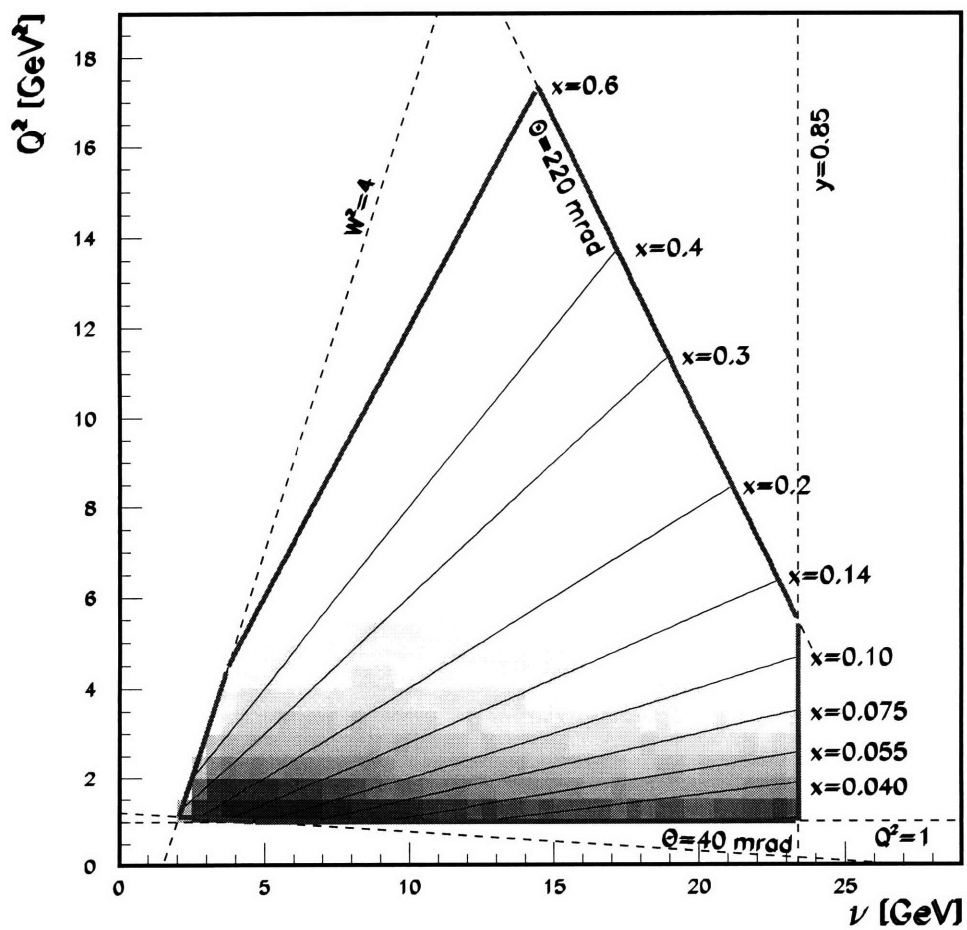


Figure 4-4: The kinematic plane for the HERMES detector

x-bin	low y	middle y	high y
1	.03571	.03249	.03070
2	.04858	.04689	.04676
3	.06589	.06419	.06395
4	.08819	.08659	.08622
5	0.12104	0.11815	0.11740
6	0.17066	0.16669	0.16569
7	0.24860	0.24222	0.24055
8	0.34116	0.34275	0.34128
9	0.45093	0.47155	0.46660

Table 4.5: Average x

x-bin	low y	middle y	high y
1	0.084206	0.079943	0.077591
2	0.102175	0.099816	0.099877
3	0.128962	0.126467	0.126761
4	0.166694	0.164531	0.165478
5	0.222852	0.219606	0.222558
6	0.294490	0.293843	0.301375
7	0.363750	0.368870	0.381416
8	0.402515	0.416330	0.432733
9	0.424363	0.436900	0.449957

Table 4.9: Average of A_p^1

x-bin	low y	middle y	high y
1	1.12250	1.22834	1.29443
2	1.15941	1.44433	1.83063
3	1.21599	1.63708	2.31480
4	1.29061	1.82768	2.81452
5	1.38515	2.05607	3.42741
6	1.53224	2.35295	4.12931
7	1.68014	2.63170	4.87724
8	2.02219	3.16822	6.08875
9	3.01354	4.40160	7.59779

Table 4.6: Average q2

x-bin	low y	middle y	high y
1	0.31354	0.31809	0.32063
2	0.31904	0.33171	0.34524
3	0.32508	0.34002	0.35622
4	0.33144	0.34599	0.36158
5	0.33784	0.34996	0.36259
6	0.34063	0.34860	0.35475
7	0.32310	0.32721	0.32543
8	0.27697	0.27136	0.26122
9	0.20236	0.17897	0.16765

Table 4.10: Average of F_p^2

x-bin	low y	middle y	high y
1	0.59935	0.74070	0.83422
2	0.43302	0.58460	0.77262
3	0.32141	0.46999	0.71250
4	0.24784	0.37925	0.64059
5	0.19006	0.30747	0.57701
6	0.14777	0.24801	0.49918
7	0.11114	0.19114	0.40991
8	0.09869	0.16616	0.36571
9	0.11713	0.17446	0.33711

Table 4.7: Average depolarization factor

x-bin	low y	middle y	high y
1	0.29930	0.30402	0.30668
2	0.30327	0.31548	0.32834
3	0.30685	0.32089	0.33583
4	0.30935	0.32254	0.33627
5	0.30948	0.32001	0.33026
6	0.30352	0.30958	0.31320
7	0.27820	0.27978	0.27575
8	0.23064	0.22257	0.21121
9	0.16069	0.13949	0.12919

Table 4.11: Average of F_d^2

x-bin	low y	middle y	high y
1	0.31252	0.31309	0.31345
2	0.31063	0.31086	0.31085
3	0.30745	0.30737	0.30690
4	0.30235	0.30180	0.30071
5	0.29384	0.29301	0.29119
6	0.28111	0.27953	0.27679
7	0.26507	0.26171	0.25741
8	0.24927	0.24209	0.23523
9	0.22577	0.21594	0.21063

Table 4.8: Average of the dilution factor

x-bin	low y	middle y	high y
1	0.33925	0.33977	0.33943
2	0.33544	0.33410	0.32714
3	0.32892	0.32462	0.31093
4	0.31988	0.31190	0.28897
5	0.30767	0.29323	0.25080
6	0.29084	0.26251	0.20048
7	0.26649	0.22372	0.15560
8	0.23235	0.18028	0.11632
9	0.17567	0.13331	0.09058

Table 4.12: Average of R_{1990}

4.3.2 The raw asymmetries

The asymmetry formulae assume identical acceptance and efficiency of the detector for the two spin states. As the two spin states are not measured simultaneously but sequentially in time, any variation in those quantities is a potential systematic error. To minimize these effect we split the data into periods which are stable, determine the asymmetry for each of the stable periods and perform a weighted average. The method itself could lead to systematic effects if, for example, the time periods are so short that the number of events per bin is small (≤ 10) and the statistics become non-Gaussian. A natural time period for the data taking is the HERA fill boundary. There are many quantities that change between fills such as positron beam current, position and polarization, as well as proton backgrounds and the like. The fills usually provide enough data to keep the statistics Gaussian. The asymmetry is calculated per fill and the resulting asymmetries are combined using their statistical significance.

Top detector only:

x-bin	$\langle A_{ } \rangle$ for low y	$\langle A_{ } \rangle$ for middle y	$\langle A_{ } \rangle$ for high y
1	-0.03858	-0.06430	-0.02251
2	-0.00566	-0.01564	-0.06510
3	0.01641	-0.01412	-0.01814
4	0.01673	-0.00963	-0.02271
5	0.00386	-0.04215	0.00223
6	0.00513	0.00203	-0.02981
7	0.00573	-0.02805	-0.01955
8	-0.00115	0.01960	-0.00293
9	-0.02069	0.02345	0.00377

x-bin	$\delta \langle A_{ } \rangle$ for low y	$\delta \langle A_{ } \rangle$ for middle y	$\delta \langle A_{ } \rangle$ for high y
1	0.02073	0.02022	0.02070
2	0.01902	0.01941	0.01933
3	0.01801	0.01767	0.01777
4	0.01808	0.01800	0.01752
5	0.01687	0.01608	0.01641
6	0.01581	0.01691	0.01638
7	0.01617	0.01855	0.01647
8	0.02706	0.02610	0.02579
9	0.04321	0.03935	0.03588

The cuts presented in the previous section can be used in two different ways. The first possibility is to consider top and bottom detector halves as totally independent experiments. This means bursts are accepted when one of the detector halves is working. To improve the data stability only fills were used where at least 1500 positrons were found in each target state for the detector half in question. This ensures that the number of positrons in a bin does not drop low enough to make the use of Gaussian statistics problematic.

Bottom detector only:

x-bin	$\langle A_{ } \rangle$ for low y	$\langle A_{ } \rangle$ for middle y	$\langle A_{ } \rangle$ for high y
1	0.01110	-0.03201	0.02091
2	0.02446	-0.01654	0.01720
3	-0.01039	-0.00136	-0.03110
4	-0.00129	-0.03149	0.00243
5	-0.01877	-0.00082	-0.02362
6	0.01803	-0.04610	-0.01903
7	0.00705	-0.00993	0.00434
8	0.01156	0.03543	-0.00196
9	-0.06738	0.00592	-0.00955

x-bin	$\delta \langle A_{ } \rangle$ for low y	$\delta \langle A_{ } \rangle$ for middle y	$\delta \langle A_{ } \rangle$ for high y
1	0.02046	0.01989	0.02053
2	0.01873	0.01919	0.01914
3	0.01786	0.01740	0.01747
4	0.01802	0.01771	0.01722
5	0.01681	0.01578	0.01612
6	0.01576	0.01672	0.01609
7	0.01580	0.01824	0.01614
8	0.02545	0.02504	0.02517
9	0.03990	0.03692	0.03492

The second option is using the fact that if one of the detector halves is not working correctly, chances are that the experimental conditions were not optimal. This means we should only accept bursts where both detector halves function reliably. In this case we require the fills to have at least 3000 positrons in each target state.

Requiring both detector halves:

x-bin	$\langle A_{ } \rangle$ for low y	$\langle A_{ } \rangle$ for middle y	$\langle A_{ } \rangle$ for high y
1	-0.01678	-0.05715	-0.00635
2	0.01433	-0.01095	-0.01821
3	0.00056	-0.00207	-0.02088
4	0.00616	-0.02324	-0.01395
5	-0.00618	-0.02212	-0.01199
6	0.00808	-0.01663	-0.02533
7	0.00963	-0.02562	-0.00717
8	0.01384	0.02926	-0.00187
9	-0.04563	0.00152	0.00091

x-bin	$\delta \langle A_{ } \rangle$ for low y	$\delta \langle A_{ } \rangle$ for middle y	$\delta \langle A_{ } \rangle$ for high y
1	0.01523	0.01484	0.01526
2	0.01396	0.01427	0.01424
3	0.01326	0.01297	0.01303
4	0.01334	0.01321	0.01286
5	0.01245	0.01180	0.01203
6	0.01167	0.01244	0.01202
7	0.01182	0.01361	0.01206
8	0.01941	0.01893	0.01885
9	0.03071	0.02821	0.02623

4.4 Corrections to the measured asymmetry

The measured asymmetry is not entirely due to DIS scattering of positrons. The most obvious problem arises due to misidentified hadrons. A second problem is created by charge symmetric processes. In this section the data are used to extract the influence of those two processes on the measured asymmetry.

4.4.1 Hadron contamination

Although the particle identification is very good, some contamination is unavoidable. The influence of this contamination on the measured asymmetry is given by:

$$A_{||}^{3He}{}_{measured} = \frac{N_{e^+} \cdot A_{||}^{3He} + N_{h^+} \cdot A_{h^+}^{3He}}{N_{e^+} + N_{h^+}} \quad (4.24)$$

This can be rewritten in terms of the hadron contaminations as follows:

$$A_{||}^{3He}{}_{measured} = (1 - c_{h^+}) \cdot A_{||}^{3He} + c_{h^+} \cdot A_{h^+}^{3He} \quad (4.25)$$

where the contamination c_{h^+} is defined as $\frac{N_{h^+}}{N_{e^+} + N_{h^+}}$.

To correct for this background we need the contaminations as well as the hadron asymmetries. The corrected asymmetry can then be calculated from:

$$A_{||}^{3He}{}_{corrected} = \frac{A_{||}^{3He}{}_{measured}}{1 - c_{h^+}} - \frac{c_{h^+} \cdot A_{h^+}^{3He}}{1 - c_{h^+}} \quad (4.26)$$

Since the hadron asymmetries are of the same order of magnitude as the inclusive asymmetries, and the contaminations are very small, we can neglect the second term. The correction then reduces to:

$$A_{||}^{3He}{}_{corrected} = \frac{A_{||}^{3He}{}_{measured}}{1 - c_{h^+}} \quad (4.27)$$

The contaminations have been determined for each x-y bin by the PID group and are listed in the following table:

x-bin	low y	middle y	high y
1	0.0074 ± 0.0038	0.0121 ± 0.0062	0.0136 ± 0.0070
2	0.0034 ± 0.0017	0.0069 ± 0.0035	0.0131 ± 0.0067
3	0.0021 ± 0.0011	0.0035 ± 0.0018	0.0106 ± 0.0054
4	0.0013 ± 0.0007	0.0019 ± 0.0010	0.0076 ± 0.0039
5	0.0013 ± 0.0009	0.0014 ± 0.0007	0.0049 ± 0.0025
6	0.0012 ± 0.0009	0.0011 ± 0.0007	0.0027 ± 0.0014
7	0.0010 ± 0.0010	0.0011 ± 0.0008	0.0018 ± 0.0009
8	0.0010 ± 0.0010	0.0010 ± 0.0010	0.0012 ± 0.0006
9	0.0010 ± 0.0010	0.0010 ± 0.0010	0.0012 ± 0.0006

Table 4.13: Hadronic contamination c_{h+} for each x-bin

4.4.2 Charge symmetric background

The charge symmetric background results from pair production processes whose positrons end up in the detector. To account for them it is easiest to take all positrons that enter the detector, without trying to select the actual scattered positron by taking only the leading positron. This allows for easy correction since we can then just determine the quantity and asymmetry of the electrons in the detector. This will be an accurate measurement of the pair-produced positrons.

The charge symmetric background can then be calculated in an identical manner as the hadron contamination:

$$A_{||corrected}^{3He} = \frac{A_{||measured}^{3He}}{1 - c_{e-}} - \frac{c_{e-} \cdot A_{e-}^{3He}}{1 - c_{e-}} \quad (4.28)$$

with the contamination c_{e-} is defined as $\frac{N_{e-}}{N_{e+} + N_{e-}}$. However, the asymmetry from pair production has to be zero, so the formula reduces to:

$$A_{||corrected}^{3He} = \frac{A_{||measured}^{3He}}{1 - c_{e-}} \quad (4.29)$$

The pair production contaminations are listed in the following table:

x-bin	low y	middle y	high y
1	0.0124	0.0489	0.1273
2	0.0024	0.0105	0.0755
3	$5.7 \cdot 10^{-4}$	0.0030	0.0419
4	$3.0 \cdot 10^{-4}$	0.0011	0.0210
5	$1.1 \cdot 10^{-4}$	$3.9 \cdot 10^{-4}$	0.0080
6	$1.4 \cdot 10^{-4}$	$1.2 \cdot 10^{-4}$	0.0021
7	$2.2 \cdot 10^{-5}$	$3.8 \cdot 10^{-5}$	$5.8 \cdot 10^{-4}$
8	$1.0 \cdot 10^{-4}$	$1.1 \cdot 10^{-4}$	$2.2 \cdot 10^{-4}$
9	$1.0 \cdot 10^{-4}$	$4.2 \cdot 10^{-5}$	$3.6 \cdot 10^{-5}$

Table 4.14: Charge symmetric contamination c_{e-} for each x-bin as deduced from electron counts

4.4.3 The corrected asymmetry

Since both asymmetry corrections are very small, we can just apply them consecutively. The corrected asymmetry is then:

$$A_{||}^{3He \text{ corrected}} = \frac{A_{||}^{3He \text{ measured}}}{(1 - c_{e-})(1 - c_{h+})} \quad (4.30)$$

Since this correction is multiplicative it can be applied before or after applying the depolarization factor.

4.5 Estimating the systematic error on the result

To quantify the residual systematic errors many tests were done on the data set. In the end the most useful studies were the following:

- **Yield fluctuations** The nature of the experiment requires an extremely stable detector. A direct quantification of the stability of the detector is the stability of the normalized yields. Small discrepancies on the time scale of the target spin flip between the expected spread in measured yields and the observed spread translate in a systematic error on the asymmetry.
- **Asymmetry fluctuation studies** Similar to the previous method, and even more direct. Since the asymmetries are very small, the low statistics do affect this method much stronger.
- **Time dependence studies** One of the most worrisome type of studies was centered on a possible systematic difference between the early and late period of the experiment. This type of study was usually based on the asymmetries.

4.5.1 Yield fluctuation studies

The normalized yields are very useful in the study of detector stability. They can be determined quite accurately on the time scale of a run (10 minutes), which is also the time scale for spin flips. Confronting the fluctuations in the measured yields with the fluctuation one expect from the statistics (DIS scattering in the detector and Bhabha scattering into the luminosity monitor) gives an accurate measure of the non-statistical fluctuations in this basic quantity. Since the Bhabha scattering rate is much higher than the DIS scattering rate, the corresponding error can be ignored.

The spread in the run-based yields was 23% higher than expected from statistics, with no correlation to the spin state. If we attribute the entire excess spread to a systematic error, we can either increase the statistical error bar by 23% or we can add a systematic error of 51% of the statistical error.

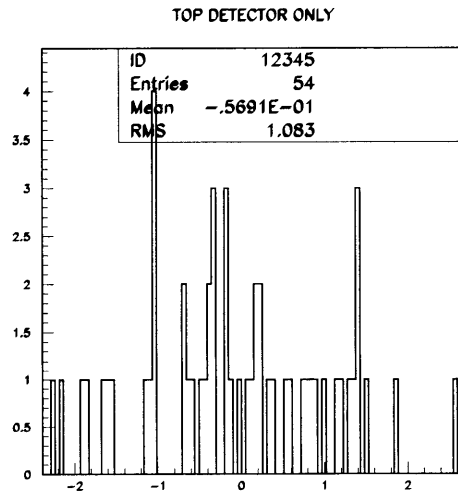


Figure 4-5: Normalised deviation of the asymmetry per fill (top detector)

4.5.2 Asymmetry fluctuation studies

A very rough measure of the systematic error can be obtained from the spread in the raw total asymmetry calculated per fill. Normalizing the difference of the asymmetry in the fill and the average asymmetry for the experiment by the square root sum of the statistical errors on those two quantities should give

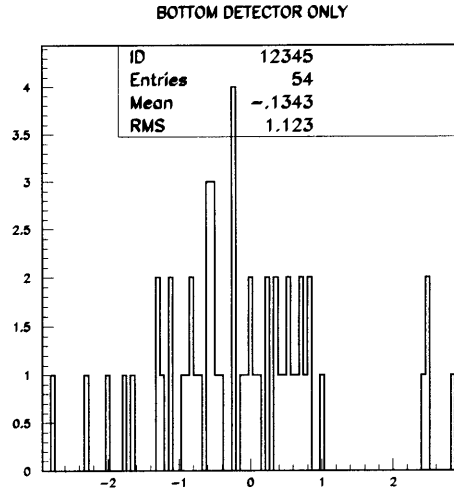


Figure 4-6: Normalised deviation of the asymmetry per fill (bottom detector)

a Gaussian distribution with a spread of 1. The excess spread can be interpreted as a measure of the systematic error in the data set. The distribution of the normalized deviations of the fill asymmetries with respect to the average asymmetry is shown in figure 4-7. The spread in the asymmetries is between 8% and 28% higher than expected from statistical variations. If attributed entirely to a systematic error, we would assign a systematic error of 17% to 64% of the statistical error. This is comparable to the excess spread in the yields.

It is at first sight strange to see the RMS value of the distribution is smaller for the top and bottom detectors separately than when one requires the full detector to be on. In principle the data should be better in the latter case. This indicates that the systematic errors are really located in a few fills, and appear in top and bottom simultaneously. Since there are more fills when we require only half the detector to be on, these bad fills have less influence. There are 50 fills in the analysis when we require both detectors to be on, and a minimum of 3000 positrons in each target state. There are 54 fills when we only consider the top detector, and require 1500 positrons in each target state, and 54 fills when we consider the bottom detector under the same circumstance. Further support for the hypothesis that the bad data is concentrated in a few fills will be shown in the next section.

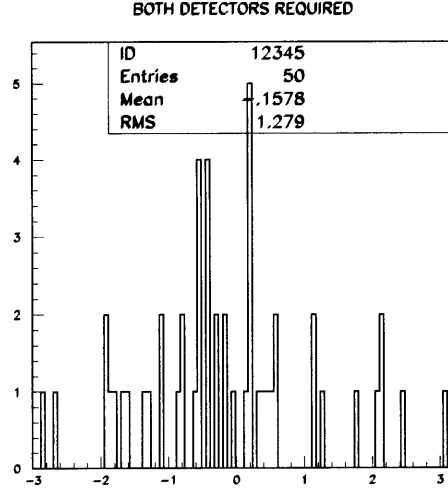


Figure 4-7: Normalised deviation of the asymmetry per fill (both detectors)

4.5.3 Time dependence studies

During the data quality studies it was observed that the data sample from before fill 95 has a significantly different asymmetry than the data after this fill. We quantify the difference the following way:

$$\Delta = \frac{A^{late} - A^{early}}{\sqrt{\sigma_{late}^2 + \sigma_{early}^2}} \quad (4.31)$$

The asymmetry used is the total raw asymmetry of the data. This quantity is dimensionless and can be interpreted as the difference between the early and late data set in units of σ . Δ is 3.125 for the total data set, requiring both detectors to be on. For the separate detector halves this value is 2.923 (top) and 0.650 (bottom).

The difference in the asymmetry between the first and second half of the data-taking period caused a lot of concern. The previous two studies already indicated the presence of some systematic error remaining in the data set. The essential question is whether the observed difference in the measured asymmetry is due to a change in the experimental conditions halfway through the year or whether the observed systematic fluctuations in some fills just happen to conspire to cause this effect.

The two hypotheses under study are then:

1. The experimental conditions changed during the experiment, causing a time dependence in the results.
2. The systematic errors observed are more prominent in some fills than in others. The time dependence was a statistical fluctuation, caused by the spread of those bad fills.

The easy way to determine which of those two hypotheses is the more likely is to eliminate the worst fills and see how the “early-late” difference changes. If hypothesis 1 is true, removal of the outliers should not change this difference much. If hypothesis 2 is true, the difference should fall drastically with the removal of a few fills. The presence of systematic errors will clearly limit the χ^2 for the fits. The result of progressive removal of outliers on Δ is shown in figure 4-10.

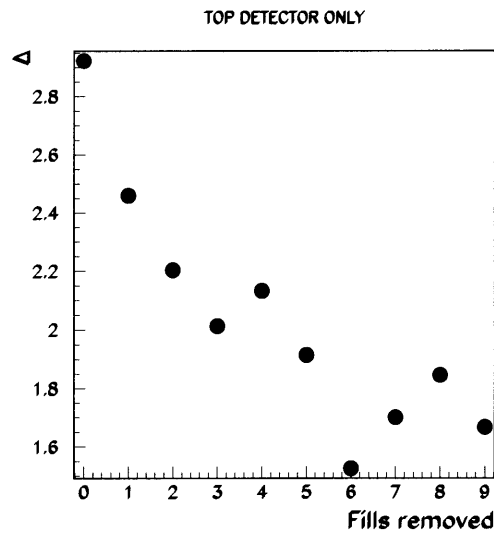


Figure 4-8: Influence of the removal of outliers on the early-late difference (top detector)

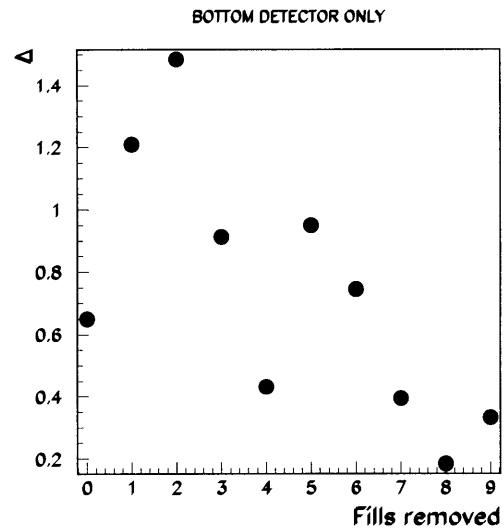


Figure 4-9: Influence of the removal of outliers on the early-late difference (bottom detector)

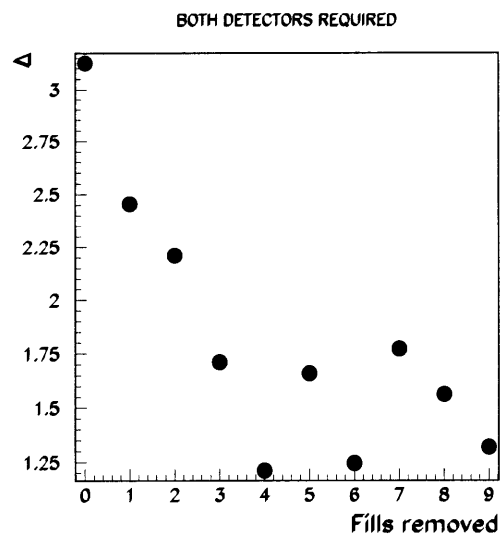


Figure 4-10: Influence of the removal of outliers on the early-late difference (both detectors)

The sudden drop in the difference between the early and the late period after removal of only a few fills indicates that hypothesis 2 is correct. There are a few fills in the data set where the statistical deviation and the systematic errors conspire to create an exceptionally large or small asymmetry. These few fills are unfortunately spread over the data set in such a way that the net asymmetry for the first period is significantly different from that of the next period.

4.5.4 Smearing effects

In contrast to the previous studies, which center around systematic errors created by the presence of some undetectable variations in the experimental conditions, this study addresses a fundamental limitation to the accuracy of the HERMES experiment due to the detector resolution. The effect of the finite momentum and angular resolution of the HERMES spectrometer on the the experimental asymmetry was studied on a big sample of Monte Carlo (MC) events. The events were generated with HMC, the Hermes Monte Carlo, where only the scattered positron was tracked through the detector. The events were reconstructed, and stored in μ -DSTs in the same format as the data, with an additional table for the true (generated) kinematics of each event. The MC events were generated with weights according to the DIS cross section. This weight also included a theoretical asymmetry, derived from existing parameterizations of the polarized parton distributions. The asymmetry A_1 and the structure function g_1 were computed with the same program that is used for the data analysis in three different ways:

MC-kinematic Use the true kinematic variables for all generated events. This should give the asymmetry that was used as an input and is just a check on the procedure.

MCRC-kinematic Use the true kinematics of the reconstructed events only. This will show the effect of the acceptance only, assuming a perfect detector.

RC-kinematic Use the reconstructed kinematic variables. This will show all detector effects, not just from the acceptance but also from smearing.

The comparison was done using three different asymmetries as input, with different x-dependence and different magnitude (see figures 4-11 and 4-12). In all cases the observed differences between the true and the reconstructed kinematics were of the size of the statistical precision of the MC-sample itself. Since the statistical error on the MC event sample was much smaller than in the data, these studies show, that kinematic smearing has no systematic effect on the extracted asymmetry.

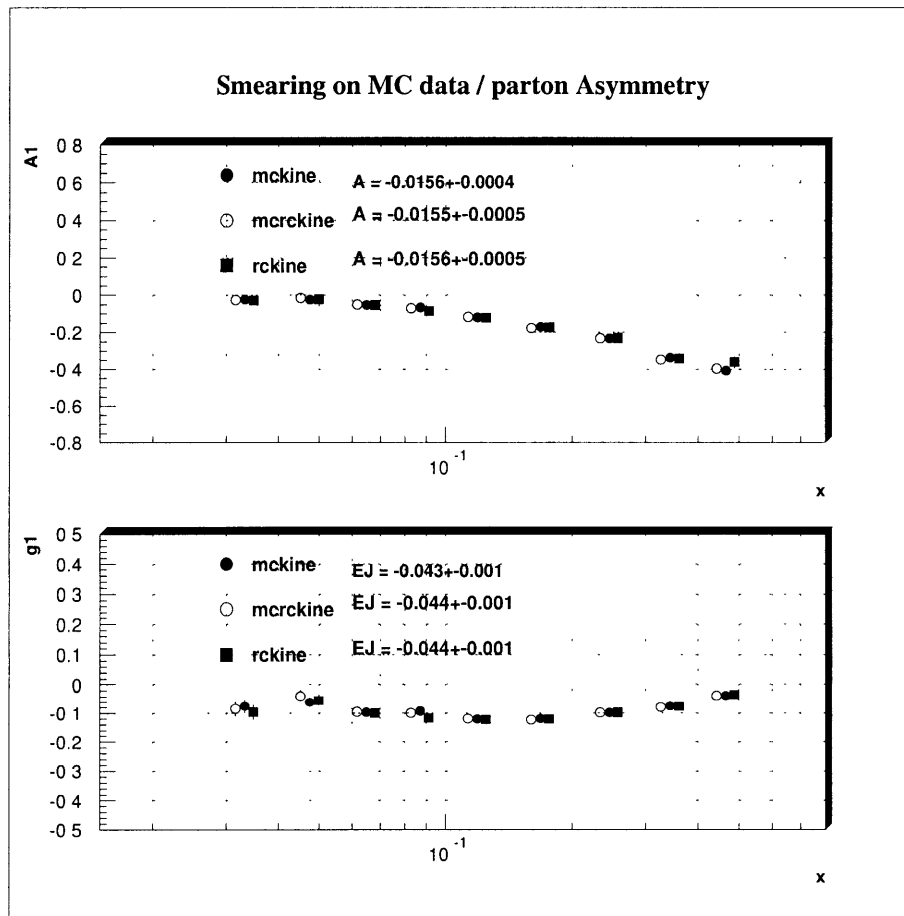


Figure 4-11: A_1 and g_1 derived from the true kinematics (mckine), the true kinematics of reconstructed events (mcrcine) and from the reconstructed kinematics (rckine) for a MC-asymmetry

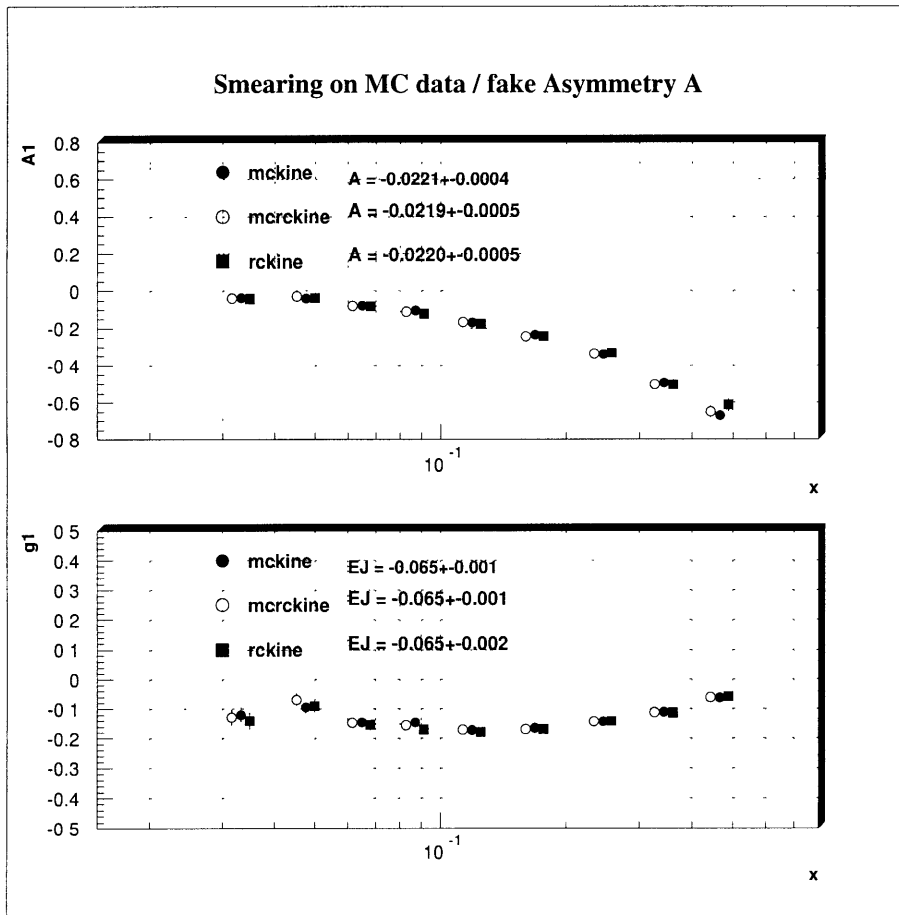


Figure 4-12: A_1 and g_1 derived from the true kinematics (mckine), the true kinematics of reconstructed events (mcrcine) and from the reconstructed kinematics (rckine) for a faked asymmetry, which is large at high x

4.5.5 Conclusion

From the time dependence analysis it is clear that some fills contain tainted data. It is clear that the bad fills cannot be removed from the data set based on this study alone. There are some indications from the logbook that the data taken during those fills was not optimal. However, nothing indicates serious problems, and no criterion can be found to eliminate those fills other than the fact that the asymmetry is far from the average. This is not sufficient and we have to leave these fills in. It is possible that the fluctuations are always present and they just show up more prominently in some fills.

The inclusion of data with larger than normal fluctuations needs to be accounted for by assigning a systematic error. It seems reasonable to assign an error of *50% of the statistical error*. This is based on the yield analysis, and agrees with the estimates based on the asymmetry spread.

Chapter 5

The physics results

Several steps are involved in extracting $g_1^n(x)$ from the measured $A_{||}^{3\text{He}}$. The application of the depolarization factor has already been discussed, as has been the correction for the hadron and pair produced positrons. Next radiative corrections and nuclear corrections (which account for scattering from the unpolarized protons in ^3He and for the small number of polarized protons present in the ground state of ^3He) need to be applied. Kinematic and structure function factors then take A_1^n to g_1^n . With some assumptions about the Q^2 dependence of A_1^n , g_1^n can be evaluated at a fixed value of Q^2 . The structure function integrals can then be extracted. These procedures are now discussed in more detail.

5.1 Extraction of A_1^n

The starting point of the calculation is the corrected $A_1^{3\text{He}}$ shown in table 5.1. The corrections that have already been applied are the depolarization factor, the hadron contaminations and the pair production background. All quantities are calculated for the three separate cases discussed in section 4.3.2:

1. **both together** The data is only used when both detector halves were functioning completely. There are 2111563 positrons in this data set.
2. **top only** The data for the top tracks is used when the top detector is functioning, regardless of whether the bottom detector is. There are 1175355 positrons in this data set.
3. **bottom only** The data for the bottom tracks is used when the bottom detector is functioning, regardless of whether the top detector is. There are 1131955 positrons in this data set.

The data sets “top only” and “bottom only” will be combined later on into the “standard” data set containing 2.3 million events.

x-bin	both together				top only				bottom only			
	$A_{ }^m$	$\delta A_{ }^m$	A_1^{3He}	δA_1^{3He}	$A_{ }^m$	$\delta A_{ }^m$	A_1^{3He}	δA_1^{3He}	$A_{ }^m$	$\delta A_{ }^m$	A_1^{3He}	δA_1^{3He}
1	-0.027	0.009	-0.041	0.013	-0.042	0.012	-0.063	0.018	-0.001	0.012	-0.002	0.017
2	-0.005	0.008	-0.012	0.014	-0.029	0.011	-0.056	0.019	0.009	0.011	0.013	0.019
3	-0.008	0.008	-0.019	0.015	-0.006	0.010	-0.018	0.020	-0.014	0.010	-0.032	0.020
4	-0.011	0.008	-0.027	0.017	-0.006	0.010	-0.024	0.023	-0.010	0.010	-0.017	0.023
5	-0.014	0.007	-0.033	0.018	-0.013	0.009	-0.025	0.024	-0.014	0.009	-0.037	0.024
6	-0.011	0.007	-0.046	0.021	-0.007	0.009	-0.041	0.029	-0.014	0.009	-0.053	0.028
7	-0.006	0.007	-0.027	0.026	-0.013	0.010	-0.055	0.036	0.001	0.010	0.005	0.035
8	0.014	0.011	0.032	0.046	0.005	0.015	0.012	0.063	0.015	0.015	0.037	0.061
9	-0.012	0.016	-0.022	0.068	0.004	0.023	0.020	0.093	-0.021	0.021	-0.055	0.090

Table 5.1: Measured (m) and corrected asymmetries and errors averaged over the three y bins

5.1.1 Nuclear Corrections

To obtain A_1^n , the dilution of the asymmetry by the presence of the other nucleons has to be taken into account, as well as the asymmetry introduced by the small polarization of the protons (see section 1.2.3, formula 1.59):

$$A_1^n = \frac{A_1^{3He} (2F_2^d + F_2^p)}{P_n^{3He} (2F_2^d - F_2^p)} - 2 \frac{F_2^p}{(2F_2^d - F_2^p)} \frac{P_p^{3He}}{P_n^{3He}} A_1^p$$

where P_n^{3He} and P_p^{3He} are taken to be 0.86 and -0.028 respectively ([18],[19]). The average values of F_2^p , F_2^d , A_1^p and R as well as the dilution factor (defined as the multiplicative factor of the helium asymmetry in the above equation) are shown in appendix A.1. They were calculated for each event and then averaged per bin. The calculation used the parameterizations from reference [13]. The resulting A_1^n is shown in table 5.2.

x-bin	both detectors		top only		bottom only	
	A_1^n	δA_1^n	A_1^n	δA_1^n	A_1^n	δA_1^n
1	-0.15	0.05	-0.23	0.07	0.00	0.06
2	-0.04	0.05	-0.20	0.07	0.06	0.07
3	-0.06	0.06	-0.06	0.08	-0.11	0.08
4	-0.09	0.07	-0.08	0.09	-0.05	0.09
5	-0.11	0.07	-0.08	0.10	-0.13	0.09
6	-0.17	0.09	-0.15	0.12	-0.20	0.12
7	-0.09	0.12	-0.21	0.16	0.06	0.16
8	0.20	0.22	0.10	0.30	0.22	0.29
9	-0.07	0.36	0.16	0.50	-0.25	0.48

Table 5.2: A_1^n per x-bin for the three analyses

5.1.2 Radiative Corrections

The radiative corrections were calculated with the POLRAD [14] code. There are currently two versions of the POLRAD code available. The first requires A_1^n as an input, the second works from A_1^{3He} . Both are in principle identical since they do or do not apply the nuclear corrections mentioned in section 5.1.1. The code uses an iterative procedure to correct the measured data. A parameterization of the Schäfer model for $A_1(x)$ is fitted to the data, and then “radiated”. The radiative corrections thus obtained are applied to the data as follows: $A_{1,rc}^n = A_1^n - \Delta_{RC}$ where $\Delta_{RC} = A_{radiated} - A_{Born}$. The procedure is then repeated using the corrected data. Four iterations were performed on the HERMES data to yield the final values for the radiative corrections.

Convergence is usually quick as can be seen from the tables in appendix A.2. After the second iteration convergence has been achieved, except in the case of the “top only” data, where the data were too positive at high x for POLRAD to obtain a good enough precision for the inelastic tail calculation in any iteration. Although the corrected data still look reasonable even for that case, it is not safe to use the results. It is better to combine the “top only” and “bottom only” data set at this point and then radiatively correct those. The result is shown in table 5.3. Since this data set is the largest data set that passes all standard data quality criteria, it can be considered our standard data set:

4. **standard** The combination of the independent data sets “top only” and “bottom only”.

x-bin	raw A_1^n	corrected A_1^n			
		1 st it.	2 nd it.	3 ^d it.	4 th it.
1	-0.112	-0.125	-0.128	-0.129	-0.129
2	-0.072	-0.085	-0.087	-0.087	-0.087
3	-0.085	-0.099	-0.101	-0.101	-0.101
4	-0.066	-0.080	-0.082	-0.082	-0.082
5	-0.107	-0.122	-0.123	-0.124	-0.124
6	-0.172	-0.189	-0.190	-0.190	-0.190
7	-0.075	-0.096	-0.096	-0.096	-0.096
8	0.162	0.137	0.137	0.136	0.136
9	-0.050	-0.073	-0.075	-0.074	-0.074

Table 5.3: Radiatively corrected data determined by POLRAD using the combined “top only” and “bottom only” data set, i.e. the “standard” data set

5.2 Extraction of g_1^n

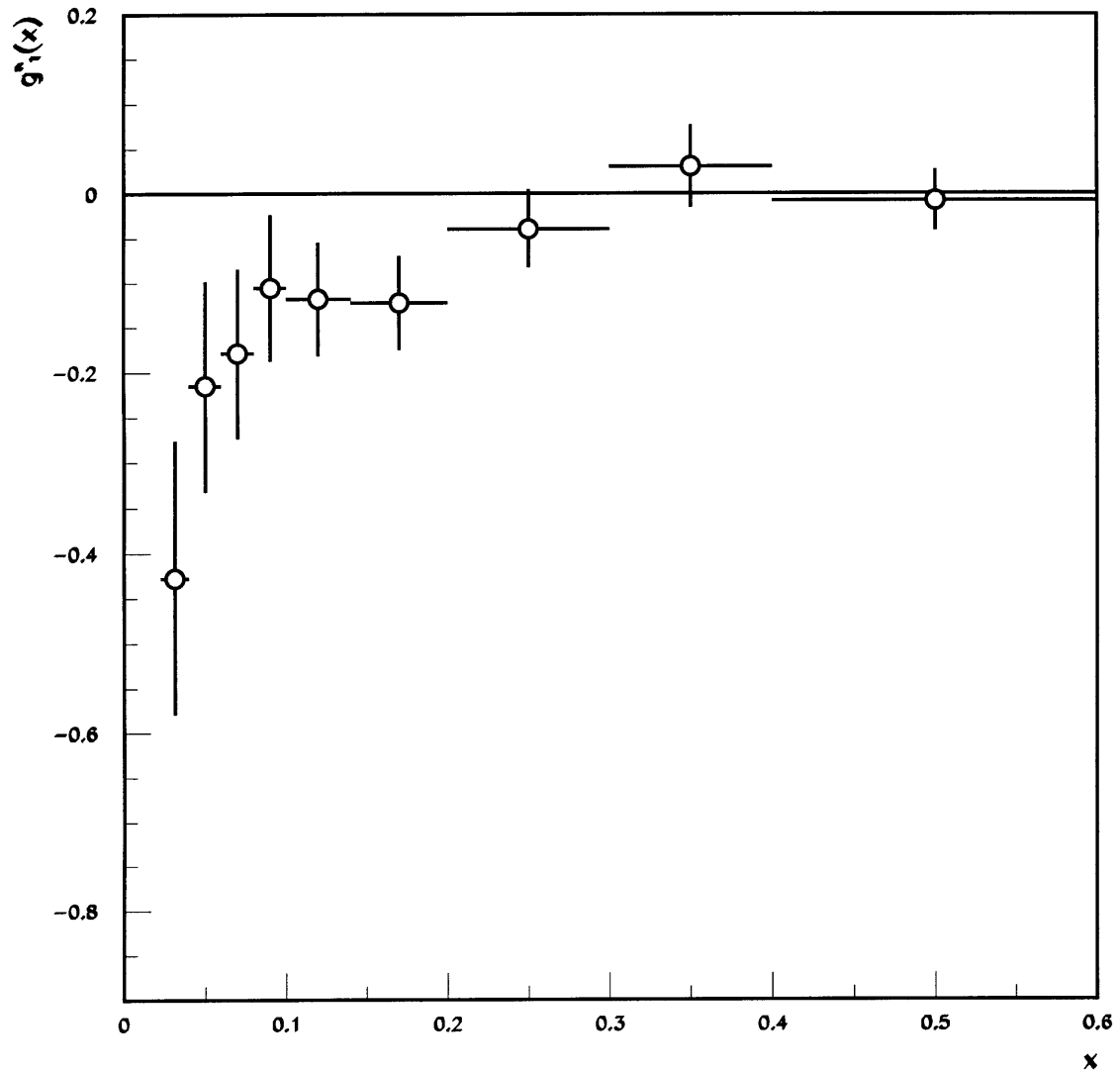
We obtain g_1^n from A_1^n by the following:

$$g_1^n = A_1^n \times \frac{F_2^n}{2x(1+R)} \quad (5.1)$$

assuming both A_2 and g_2 are assumed equal to zero. The resulting g_1^n at the measured Q^2 is shown in figure 5.2 for the two remaining data sets.

x-bin	“standard data” set	“both together” data set
1	-0.43 ± 0.15	-0.52 ± 0.15
2	-0.22 ± 0.12	-0.13 ± 0.12
3	-0.18 ± 0.09	-0.14 ± 0.10
4	-0.11 ± 0.08	-0.14 ± 0.09
5	-0.12 ± 0.06	-0.13 ± 0.07
6	-0.12 ± 0.05	-0.12 ± 0.06
7	-0.04 ± 0.04	-0.04 ± 0.05
8	0.03 ± 0.05	0.04 ± 0.05
9	-0.01 ± 0.03	-0.01 ± 0.04

Table 5.4: Result for g_1^n at measured Q^2

Figure 5-1: g_1^n at measured Q^2 for "standard" data set

5.3 Evaluation of the Ellis-Jaffe Sum of the Neutron

5.3.1 Evolution to Constant Q^2

Evolving the data to a fixed value of Q^2 is necessary to perform a consistent evaluation of the integral $\int_0^1 g_1^n dx$. The average value of Q^2 for HERMES is 2.3 GeV². As the statistical uncertainty does not strongly depend on the value of Q^2 for the evolution we choose $Q^2 = 2.5$ GeV².

Assuming that A_1^n is independent of Q^2 is not entirely consistent with the recently available Next-to-Leading-Order QCD calculations of the evolution for g_1^n . As discussed in section 1.2.4 this is not important for the extraction of Γ_1^n , and consequently we will evolve our results using the following:

$$\frac{g_1^n(x, Q_0^2)}{g_1^n(x, Q^2)} = \frac{F_2^n(x, Q_0^2) \cdot (1 + R(x, Q^2))}{F_2^n(x, Q^2) \cdot (1 + R(x, Q_0^2))} \equiv f(x, Q_0^2, Q^2) \quad (5.2)$$

The ratios f are tabulated for a few frequently used momentum scales in table A.7.

bin	g_1^n (at measured Q^2)	at $Q_0^2 = 2.0\text{GeV}^2$	at $Q_0^2 = 2.5\text{GeV}^2$	at $Q_0^2 = 3.0\text{GeV}^2$	at $Q_0^2 = 5.0\text{GeV}^2$
1	-0.43 ± 0.15	-0.48 ± 0.17	-0.50 ± 0.18	-0.52 ± 0.18	-0.58 ± 0.20
2	-0.22 ± 0.12	-0.23 ± 0.13	-0.24 ± 0.13	-0.25 ± 0.13	-0.27 ± 0.15
3	-0.18 ± 0.09	-0.18 ± 0.10	-0.19 ± 0.10	-0.20 ± 0.10	-0.21 ± 0.11
4	-0.11 ± 0.08	-0.11 ± 0.08	-0.11 ± 0.09	-0.11 ± 0.09	-0.12 ± 0.09
5	-0.12 ± 0.06	-0.12 ± 0.06	-0.12 ± 0.06	-0.12 ± 0.07	-0.13 ± 0.07
6	-0.12 ± 0.05	-0.12 ± 0.05	-0.12 ± 0.05	-0.12 ± 0.05	-0.13 ± 0.06
7	-0.04 ± 0.04	-0.04 ± 0.04	-0.04 ± 0.04	-0.04 ± 0.04	-0.04 ± 0.04
8	0.03 ± 0.05	0.03 ± 0.05	0.03 ± 0.05	0.03 ± 0.05	0.03 ± 0.04
9	-0.01 ± 0.03	-0.01 ± 0.04	-0.01 ± 0.04	-0.01 ± 0.04	-0.01 ± 0.03

Table 5.5: Evolved g_1^n for the “standard” data set

A comparison of the result for g_1^n with that obtained by the E142 experiment is shown in figure 5.3.1 for the values evolved to $Q^2 = 2.0$ GeV².

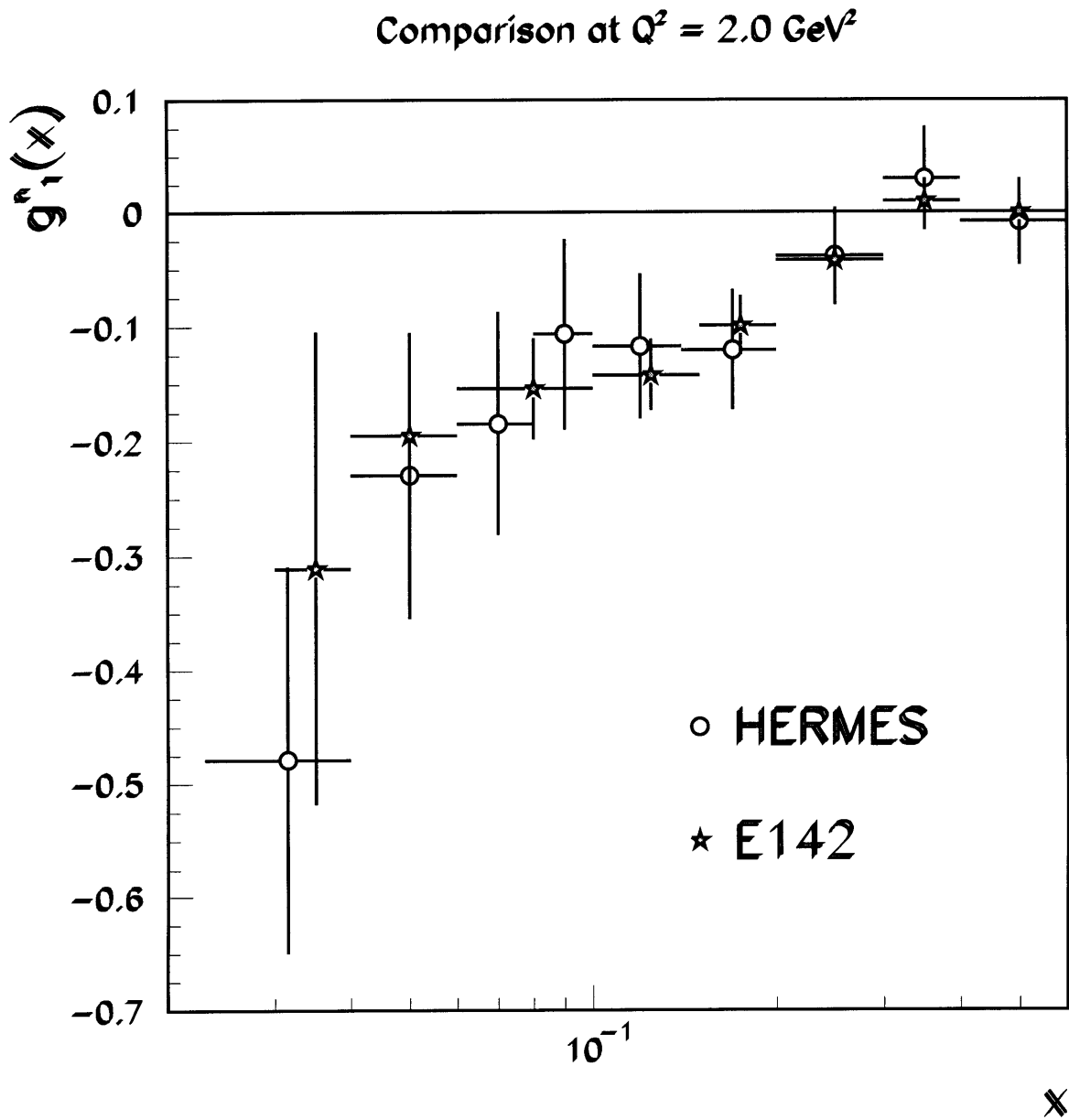


Figure 5-2: Comparison of g_1^n at $Q^2 = 2.0 \text{ GeV}^2$ for “standard” data set with data obtained by the E142 experiment. Statistical errors only.

The integral over the measured region at different Q^2 is shown in table 5.3.1. The equivalent results on the “both together” data set are tabulated in appendix A.4.

Q^2	$\int_{x=0.023}^{x=0.6} dx g_1^n(x)$
$\langle Q^2 \rangle$	-0.031 ± 0.011
2.00	-0.032 ± 0.012
2.50	-0.033 ± 0.011
3.00	-0.034 ± 0.011
5.00	-0.037 ± 0.011

Table 5.6: Integral over the measured region at measured and several fixed Q^2 for the data combining the separate detector halves. Statistical uncertainties only are shown.

5.3.2 Extrapolation

We used several different approaches to extrapolate the data to low x . A first approach was to fit $g_1^n(x)$ with a Regge form $g_1^n \propto x^{-\alpha_1}$, where α_1 is expected to be in the interval $[-0.5,0]$. This fit resulted in $\alpha_1 \approx 0$. This is in agreement with previous experiments (E143,E143,SMC). The Regge form is expected to hold for x up to 0.1 for low Q^2 . The Regge fit is a constant which we determined from the N lowest x -bins. N was varied from 1 through 4. It is however clear that the data is not well described by a constant for low x . Recent NLO fits suggest that $g_1^n(x)$ may actually become more negative as $x \rightarrow 0$. Based on Pomeron exchange models [79] logarithmic behavior has been suggested. The following functions can be used, with little more motivation than that they describe the data very well:

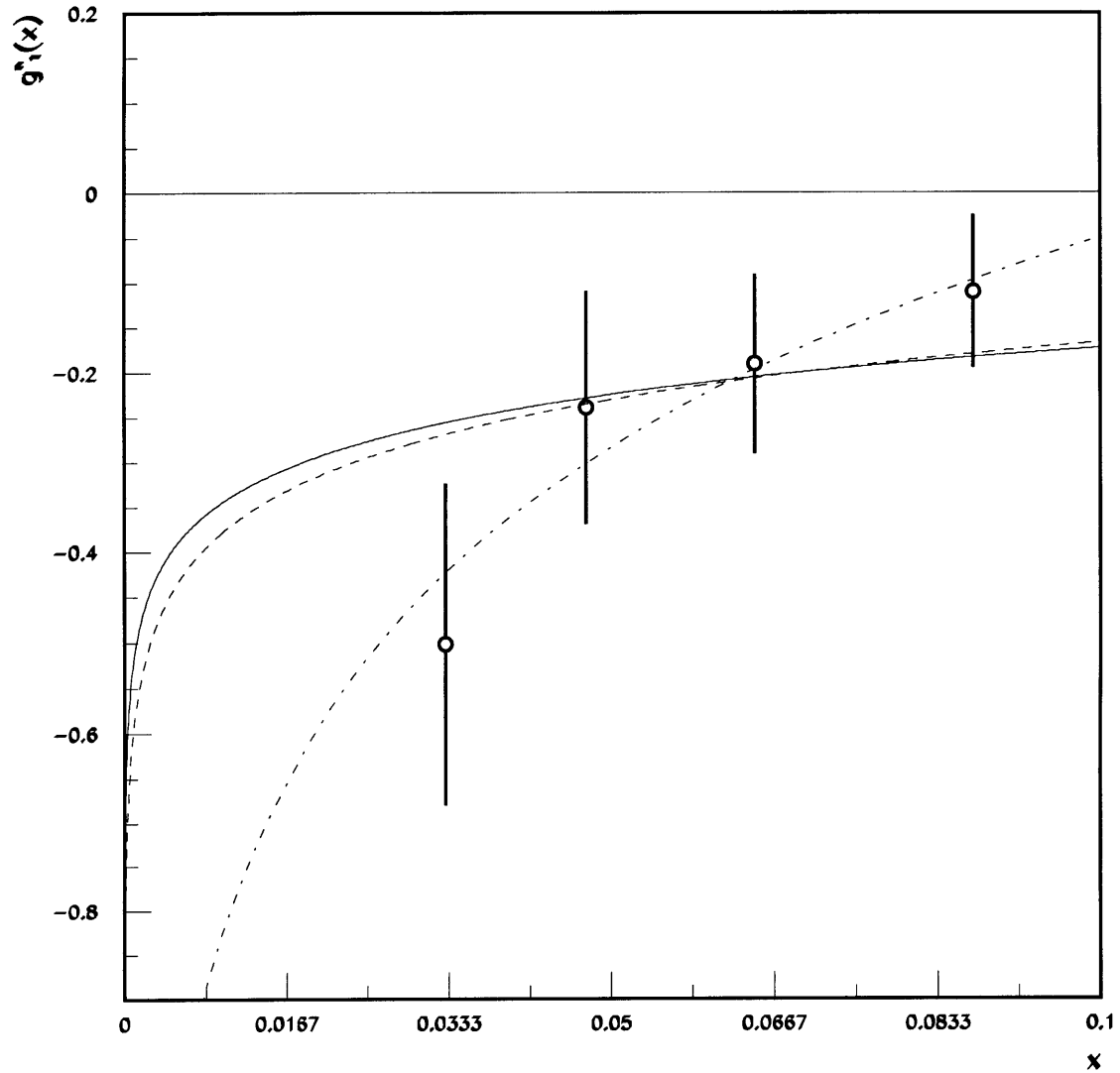
$$g_1^n \propto A \cdot \ln(x) \quad (5.3)$$

$$g_1^n \propto A \cdot \ln(x) + B \quad (5.4)$$

$$g_1^n \propto A \cdot (1 + 2\ln(x)) \quad (5.5)$$

The fits are shown in figure 5.3.2.

A simple way to extrapolate the integral is by a linear fit to the *running integral*. This is the integral formed by integrating the N highest bins, with N going from 1 to 9. This is shown in figure 5.3.2 for $Q^2=2.5 \text{ GeV}^2$. Fits were performed using the first 2, 3 and 4 data points.

Figure 5-3: Logarithmic fits to g_1^n at $Q^2 = 2.5 \text{ GeV}^2$ for “standard” data set

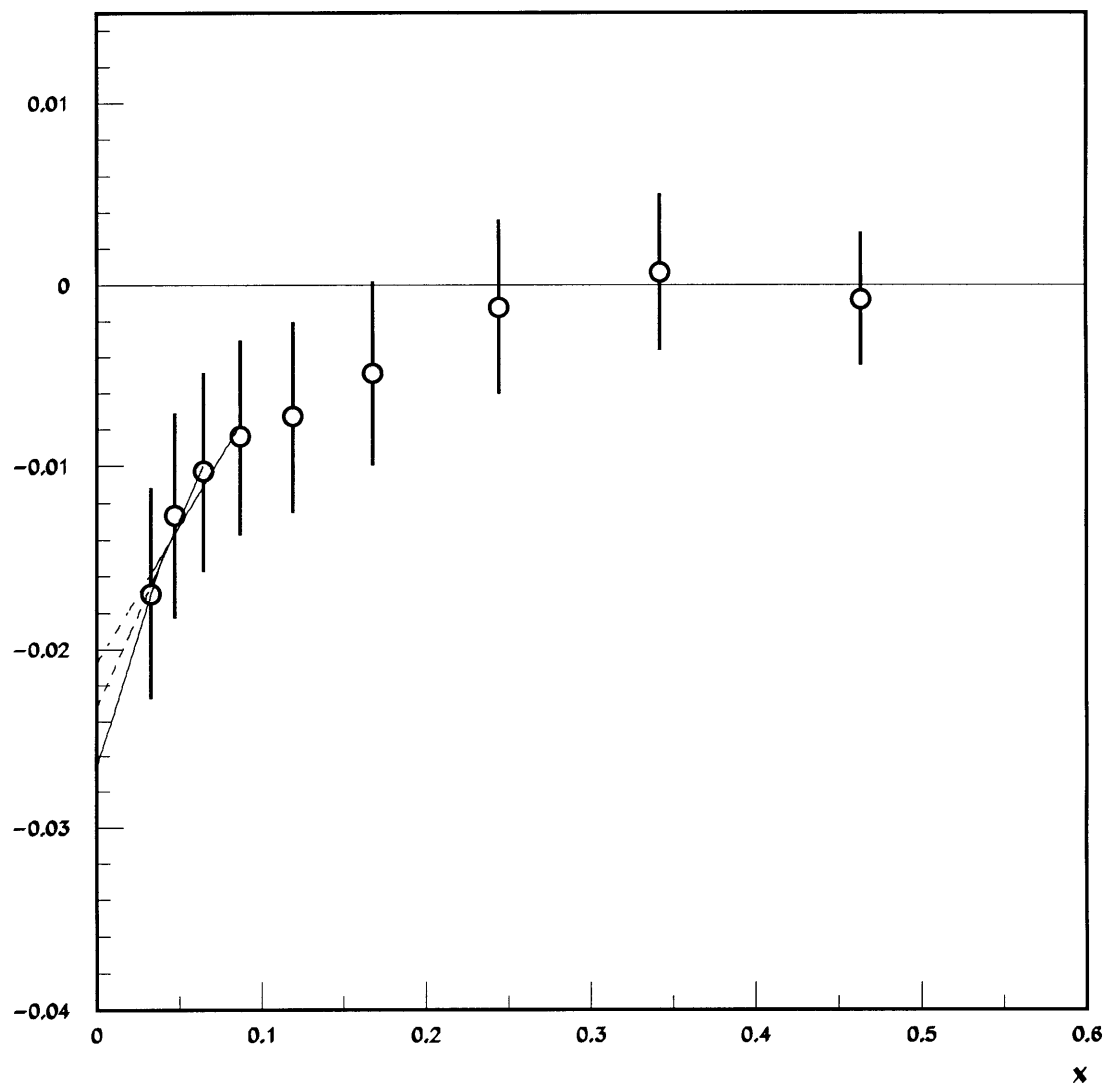


Figure 5-4: Running integral over g_1^n at $Q^2 = 2.5 \text{ GeV}^2$ for "standard" data set

In table 5.7 the resulting integrals for the low x extrapolation are shown for the different methods.

Q^2	Regge type fit (constant g_1^n)				Running integral linear fit			Logarithmic fits		
	1 bin	2 bins	3 bins	4 bins	2 bins	3 bins	4 bins	form. 5.3	form. 5.5	form. 5.4
2.0	-.0110	-.0073	-.0057	-.0044	-.0093	-.0061	-.0037	-.0080	-.0088	-.0194
2.5	-.0116	-.0076	-.0059	-.0045	-.0097	-.0063	-.0038	-.0082	-.0091	-.0203
3.0	-.0120	-.0078	-.0061	-.0046	-.0101	-.0065	-.0039	-.0084	-.0093	-.0210
5.0	-.0132	-.0086	-.0067	-.0050	-.0111	-.0072	-.0043	-.0092	-.0101	-.0232

Table 5.7: Integral over the low x region ($\int_{x=0}^{x=0.023} dx g_1^n(x)$) at several fixed Q^2 for the data combining the separate detector halves

The extrapolation to $x = 1$ is done assuming $g_1^n(x) \propto (1-x)^3$. Since we only have one measurement in the region where the counting rules are supposed to hold, the fit is : $g_1^n(x) = g_1^n(x_0) \frac{(1-x)^3}{(1-x_0)^3}$. The fit was also done using the second highest x -bin. This changes the sign of the correction, but it stays very small. The resulting integrals are shown in table 5.8.

Q^2	2 bins	1 bin
2.0	.0004	-.0003
2.5	.0004	-.0003
3.0	.0004	-.0003
5.0	.0003	-.0003

Table 5.8: Integral over the high x region ($\int_{x=0}^{x=1} dx g_1^n(x)$) at several fixed Q^2 for the “standard” data set

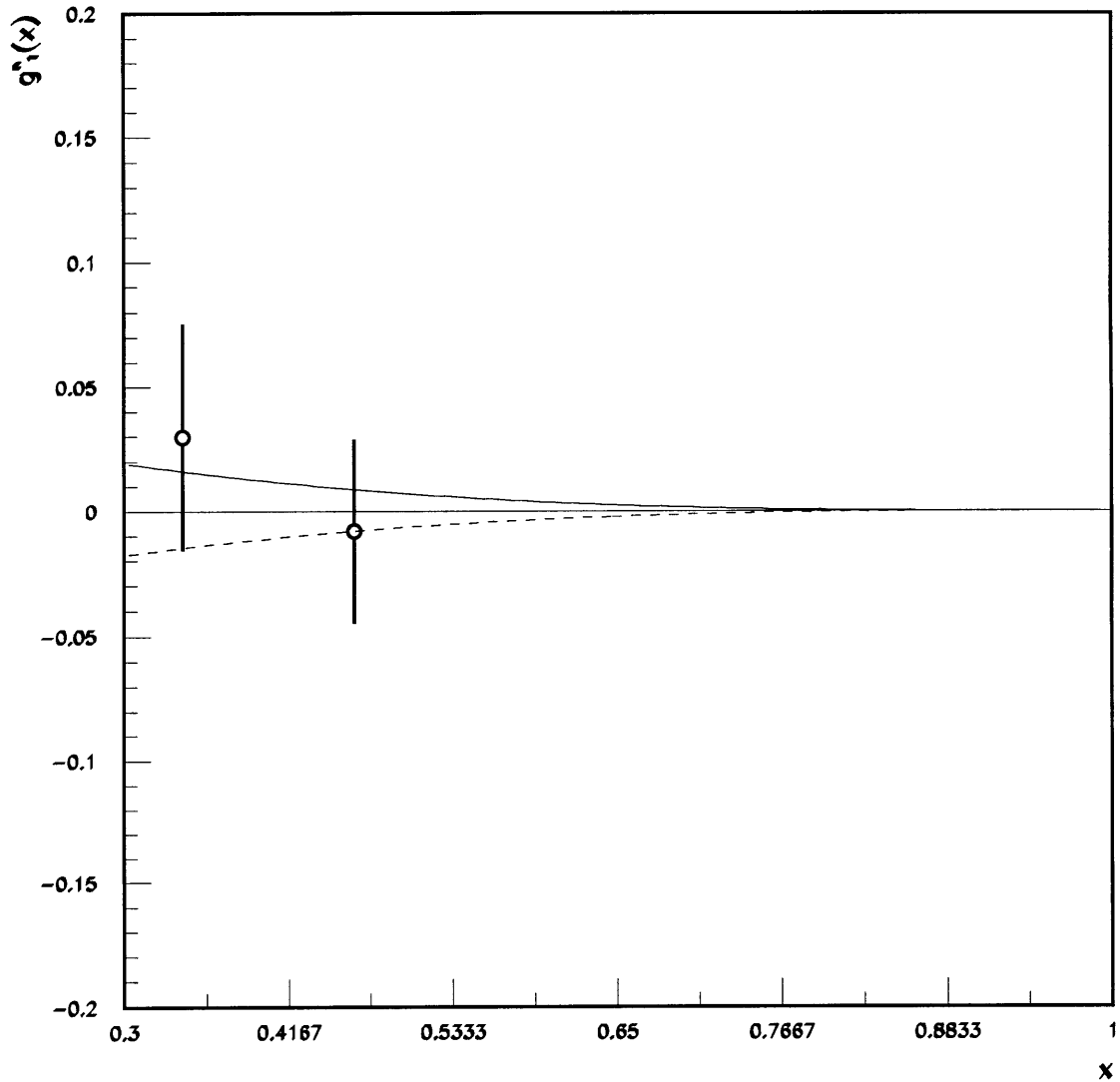


Figure 5-5: Counting rule fits to g_1^n at $Q^2 = 2.5 \text{ GeV}^2$ for “standard” data set

5.3.3 Result

The final result for the integral of the g_1^n structure function is shown in table 5.9. The high x extrapolation

Q^2	low x	measured region	high x	Γ_1^n
2.0	-0.008 ± 0.004	-0.032 ± 0.012	0.0 ± 0.0004	-0.040
2.5	-0.008 ± 0.004	-0.033 ± 0.011	0.0 ± 0.0004	-0.041
3.0	-0.008 ± 0.004	-0.034 ± 0.011	0.0 ± 0.0004	-0.042
5.0	-0.009 ± 0.005	-0.037 ± 0.011	0.0 ± 0.0003	-0.046

Table 5.9: Final results for Γ_1 for “standard” data set. Statistical uncertainty only for measured region, estimated error for extrapolation on low and high x integrals.

is very small, and since the value changes sign by taking in the second highest point, it seems reasonable to *take the integral to be zero, with the error being the largest of the two integrals*. This implies an error of 0.0004 at $Q^2 = 2.5 \text{ GeV}^2$.

The low x extrapolation is not negligible, and varies from -0.020 to -0.004 at $Q^2 = 2.5 \text{ GeV}^2$. It seems reasonable to assign a value at that momentum scale of **-0.008±0.004**. This covers all the Regge fits and the running integral fits as well as two of the three logarithmic fits. The fit based on formula 5.4 always gives a much more negative contribution than the other fits. This deviates from the assigned value by about 3σ . Similar estimates are given for all Q^2 in the table 5.9 *by eliminating the highest (absolute) value of the integral and covering the range of the remaining ones*.

5.3.3.1 Systematic errors

The systematic errors in the derivation of the structure function integral have several different sources:

1. The systematic error on the asymmetry originating from the systematic error on the measured polarizations. This relative error on the beam polarization was determined to be 5.5% and on the target polarization 5.3%.
2. The systematic error on the asymmetry originating from more than random fluctuations on the luminosity monitor. This error is estimated to be 50% of the statistical error on the asymmetry.
3. The error on the radiative corrections. The error is difficult to estimate, but extensive studies have shown that the error is less than 50% of the correction in every x -bin. We will take 50% of the correction as the systematic error on the asymmetry.

4. The error on the functions used to derive the structure function from the measured asymmetry. These are derived from the world's data and the estimate for the resulting errors is shown in table 5.11.
5. The error on the extrapolations at low and high x . This was estimated in the previous section to be $\sqrt{0.004^2 + 0.00030} \approx 0.004$ for $Q^2 = 2.5 \text{ GeV}^2$.

Parameter	x-bin									Integral
	1	2	3	4	5	6	7	8	9	
P_b	0.0216	0.0153	0.0091	0.0096	0.0073	0.0057	0.0014	0.0014	0.0006	0.0021
P_t	0.0196	0.0140	0.0083	0.0087	0.0067	0.0052	0.0012	0.0013	0.0006	0.0019
Δ_{Rc}	0.0351	0.0120	0.0044	0.0012	0.0025	0.0028	0.0025	0.0019	0.0010	0.0018
A_1^P	0.0018	0.0018	0.0018	0.0017	0.0017	0.0016	0.0014	0.0011	0.0007	0.0007
p_n	0.0127	0.0069	0.0052	0.0050	0.0036	0.0041	0.0015	0.0011	0.0006	0.0013
p_p	0.0026	0.0025	0.0025	0.0025	0.0024	0.0023	0.0021	0.0016	0.0010	0.0010
F_2^n/F_2^P	0.0073	0.0039	0.0028	0.0027	0.0020	0.0023	0.0010	0.0007	0.0003	0.0008
F_2^n	0.0053	0.0044	0.0034	0.0025	0.0017	0.0019	0.0005	0.0005	0.0004	0.0006
\tilde{R}	0.0131	0.0072	0.0038	0.0025	0.0019	0.0012	0.0005	0.0004	0.0002	0.0008
A_2^n	0.0052	0.0041	0.0034	0.0027	0.0021	0.0015	0.0015	0.0021	0.0017	0.0012
total	0.0520	0.0278	0.0162	0.0155	0.0122	0.0104	0.0048	0.0046	0.0027	0.0046

Table 5.10: Contributions to the systematic error on g_1^n at the measured values of Q^2

Parameter	x-bin									Integral
	1	2	3	4	5	6	7	8	9	
P_b	0.0248	0.0169	0.0097	0.0097	0.0073	0.0057	0.0014	0.0016	0.0008	0.0022
P_t	0.0226	0.0154	0.0089	0.0088	0.0067	0.0052	0.0013	0.0015	0.0008	0.0020
Δ_{Rc}	0.0404	0.0130	0.0046	0.0012	0.0025	0.0029	0.0026	0.0021	0.0013	0.0020
A_1^P	0.0021	0.0019	0.0018	0.0018	0.0017	0.0016	0.0015	0.0012	0.0009	0.0008
p_n	0.0146	0.0075	0.0054	0.0049	0.0036	0.0041	0.0016	0.0012	0.0008	0.0014
p_p	0.0030	0.0027	0.0026	0.0025	0.0024	0.0023	0.0021	0.0017	0.0012	0.0011
F_2^n/F_2^P	0.0084	0.0042	0.0030	0.0026	0.0020	0.0023	0.0010	0.0009	0.0004	0.0008
F_2^n	0.0093	0.0058	0.0037	0.0025	0.0017	0.0019	0.0005	0.0007	0.0008	0.0008
\tilde{R}	0.0150	0.0079	0.0039	0.0026	0.0019	0.0012	0.0005	0.0004	0.0003	0.0008
A_2^n	0.0060	0.0044	0.0035	0.0028	0.0021	0.0015	0.0016	0.0023	0.0021	0.0013
total	0.0605	0.0307	0.0172	0.0156	0.0121	0.0104	0.0050	0.0051	0.0036	0.0051

Table 5.11: Contributions to the systematic error on g_1^n at $Q^2 = 2.5 \text{ (GeV/c)}^2$

An additional error on the integral can come from the Q^2 -evolution, but as discussed in section 1.2.5 this should be negligible compared to the errors from the functional parameterizations.

The integrated error from all sources except the low and high x extrapolation and the yield fluctuations is shown for $Q^2 = 2.5 \text{ GeV}^2$ in table 5.11. The total error was determined by adding the integrated errors in quadrature. This can be justified since all errors are unrelated and adding them linearly will likely overestimate the total error.

5.3.3.2 Conclusion

We have obtained the following measurement for Γ_1^n from the 2.3 million events detected in the commissioning year of the HERMES experiment :

$$\Gamma_1^n(Q^2 = 2.5) = -0.041 \pm 0.011 \text{ (statistical)} \pm 0.005 \text{ (systematic)} \pm 0.006 \text{ (yield fluctuations)} \pm 0.004 \text{ (extrapolation)} \quad (5.6)$$

All non-statistical errors can be added in quadrature, giving the final result:

$$\Gamma_1^n(Q^2 = 2.5) = -0.041 \pm 0.011 \text{ (statistical)} \pm 0.009 \text{ (total systematic)} = -0.041 \pm 0.014 \quad (5.7)$$

This result is in good agreement with the world data. A comparison with the Ellis-Jaffe sum rule is shown in figure 5.3.3.2 for the different Q^2 to which the result was evolved (table 5.9). For $Q^2 = 2.5$ the Ellis-Jaffe prediction for Γ_1^n is -0.0133 ± 0.0052 , so the disagreement is 1.8σ . The difference between the result derived in this thesis and the result published by the HERMES collaboration [80] is due to minor differences in the analysis. In this thesis a stricter PID requirement was imposed. The HERMES particle identification detectors are redundant if the only goal is the separation of hadrons and positrons. Hence it is possible to use the data when one of the detectors is not functioning correctly. In this work this was not done: if any of the PID detectors was not functioning, the data was not used. This inspires greater confidence in the hadron contaminations that were calculated and in general leads to a cleaner data sample. The data sample was only reduced from 2.6 million to 2.3 million events. The low x extrapolation was also treated somewhat differently, accounting for about half the difference in the two results. Finally the systematic error caused by yield fluctuations was added in quadrature to the statistical error in the publication, whereas it was added to the systematic error in this thesis.

It was shown in figure 5.3.1 that the structure function determined from our data is in good agreement with the E142 result, but it tends to be more negative. This leads to a more negative integral and a clear violation of the Ellis-Jaffe prediction. The E142 data were originally interpreted to indicate the validity of the Ellis-Jaffe sum rule. From our data we clearly determine that this sum rule is violated. We therefore expect the strange quark contribution to the nucleon spin, Δs , to be nonzero. We will now use the formulae derived in section 1.1.5 to check this.

We use the measured values for F and D [13]:

$$\begin{aligned} F &= 0.461 \pm 0.014 \\ D &= 0.798 \pm 0.013 \end{aligned} \quad (5.8)$$

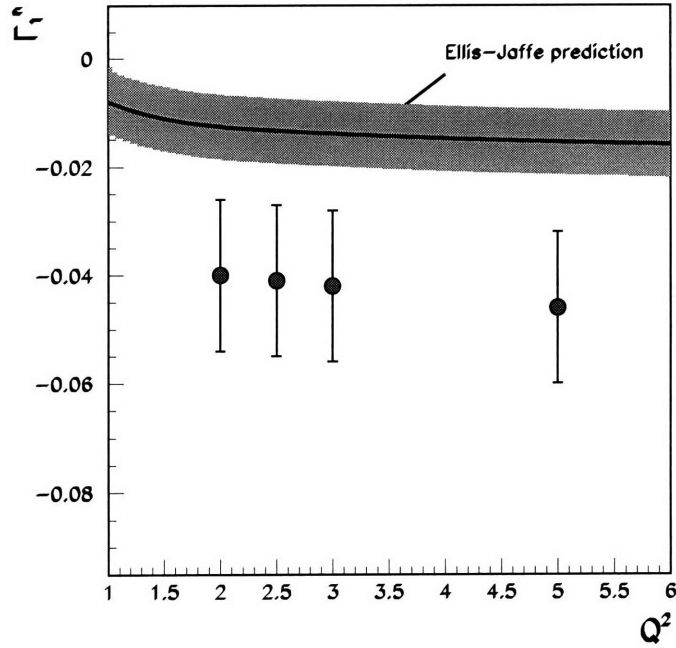


Figure 5-6: Ellis-Jaffe prediction for Γ_1^n versus Q^2 and results from HERMES at different evolved Q^2 as determined in this thesis.

and the interpolated value from the Particle Data Group tables for α_s :

$$\alpha_s(Q^2 = 2.5) = 0.27 \pm 0.02 \Rightarrow \begin{cases} C_0(Q^2 = 2.5) = 0.967 \pm 0.002 \\ C_1(Q^2 = 2.5) = 0.875 \pm 0.013 \end{cases} \quad (5.9)$$

The contributions to the spin from the u, d and s quarks using the formulae 1.49 is then:

$$\begin{aligned} \Delta\Sigma &= 0.34 \pm 0.09 \\ \Delta u &= 0.84 \pm 0.05 \\ \Delta d &= -0.42 \pm 0.05 \\ \Delta s &= -0.08 \pm 0.05 \end{aligned} \quad (5.10)$$

The error on $\Delta\Sigma$ is completely dominated by the error on Γ_1^n . The errors on C_i , F and D are negligible. For the contributions of each flavor, the errors on F and D do contribute significantly (40% of the total error bar for u and d, 25% for s).

In 1995 the HERMES experiment was installed and commissioned and the first data were taken on a polarized ^3He target. In this thesis the results from the analysis of the inclusive data are presented. These results are in good agreement with previous experiments, proving that the experiment works as proposed. Additional data taken over the next years will provide an accurate measurement of the spin dependent structure function of both the proton and the neutron. A very exciting aspect of the HERMES experiment is the possibility to study semi-inclusive reactions as well. The study of the inclusive scattering is now almost as complete as the current accelerators allow for. The persistence of the low x extrapolation problem makes it difficult to extract physical results from the data with any confidence. It is therefore necessary to consider the additional information accessible through the semi-inclusive asymmetries. The first semi-inclusive results from the HERMES experiment will be released in the summer of 1997. At the end of 1997 a RICH detector will be installed to further improve the hadron identification. This will allow HERMES to extract such interesting quantities as the kaon production asymmetry.

Appendix A

Additional tables

A.1 Tables of averaged kinematic functions per bin

In the following table the parameterization for R_{1990} has been taken from reference [13], as are all other parameterizations. The parameterization of R uses the weighted average of the fit to the SLAC data from [81] and two other fits. It is however clear from figure 2 in reference [81] that the other fits do not describe the data very well at low Q^2 . For the calculations in this thesis we therefore used the fit from the SLAC data only.

x-bin	x	q^2	dilution	F_2^p	F_2^d	R_{1990}	A_1^p
1	0.03296	1.21522	0.31302	0.31743	0.30334	0.33949	0.08057
2	0.04743	1.47366	0.31078	0.33181	0.31552	0.33227	0.10065
3	0.06466	1.72803	0.30724	0.34061	0.32135	0.32142	0.12738
4	0.08698	1.99754	0.30160	0.34672	0.32306	0.30650	0.16556
5	0.11880	2.30703	0.29266	0.35041	0.32016	0.28348	0.22162
6	0.16776	2.65678	0.27917	0.34784	0.30865	0.25179	0.29659
7	0.24398	3.07388	0.26143	0.32506	0.27778	0.21544	0.37141
8	0.34174	3.79340	0.24207	0.26971	0.22130	0.17527	0.41747
9	0.46386	5.24630	0.21664	0.18116	0.14146	0.12869	0.43843

Table A.1: The averages of the kinematic functions for each x-bin for the entire y-range for the “both together” data set

x-bin	x	q^2	dilution	F_2^p	F_2^d	R_{1990}	A_1^p
1	0.03298	1.21644	0.31302	0.31749	0.30340	0.33947	0.08060
2	0.04742	1.47416	0.31078	0.33183	0.31554	0.33226	0.10064
3	0.06467	1.72600	0.30724	0.34055	0.32130	0.32145	0.12739
4	0.08695	1.99385	0.30161	0.34663	0.32298	0.30658	0.16551
5	0.11877	2.29994	0.29268	0.35032	0.32009	0.28369	0.22153
6	0.16777	2.64927	0.27919	0.34778	0.30861	0.25203	0.29657
7	0.24379	3.07209	0.26146	0.32514	0.27786	0.21549	0.37129
8	0.34159	3.81703	0.24200	0.26971	0.22127	0.17459	0.41762
9	0.46378	5.29683	0.21653	0.18095	0.14126	0.12782	0.43869

Table A.2: The averages of the kinematic functions for each x-bin for the entire y-range, “top only” data set

x-bin	x	q^2	dilution	F_2^p	F_2^d	R_{1990}	A_1^p
1	0.03294	1.21399	0.31302	0.31736	0.30328	0.33951	0.08054
2	0.04744	1.47361	0.31077	0.33181	0.31552	0.33227	0.10066
3	0.06465	1.73018	0.30724	0.34068	0.32142	0.32139	0.12735
4	0.08699	2.00287	0.30159	0.34683	0.32315	0.30639	0.16559
5	0.11883	2.31339	0.29264	0.35049	0.32022	0.28331	0.22168
6	0.16773	2.66497	0.27916	0.34791	0.30870	0.25152	0.29660
7	0.24412	3.07488	0.26140	0.32502	0.27772	0.21539	0.37150
8	0.34185	3.76813	0.24213	0.26975	0.22136	0.17594	0.41731
9	0.46395	5.20471	0.21673	0.18132	0.14161	0.12943	0.43820

Table A.3: The averages of the kinematic functions for each x-bin for the entire y-range, “bottom only” data set

A.2 Convergence of the radiative corrections

x-bin	uncorrected A_1^n	corrected A_1^n			
		1 st iter.	2 nd iter.	3 ^d iter.	4 th iter.
1	-0.14699	-0.16061	-0.16349	-0.16407	-0.16420
2	-0.03934	-0.05259	-0.05484	-0.05529	-0.05539
3	-0.06338	-0.07726	-0.07915	-0.07955	-0.07963
4	-0.09122	-0.10548	-0.10701	-0.10736	-0.10744
5	-0.11311	-0.12853	-0.12973	-0.13005	-0.13012
6	-0.16817	-0.18566	-0.18645	-0.18674	-0.18679
7	-0.08656	-0.10781	-0.10824	-0.10847	-0.10852
8	0.19574	0.17073	0.17021	0.17008	0.17005
9	-0.06964	-0.09240	-0.09366	-0.09362	-0.09361

Table A.4: Radiative corrections determined by POLRAD for the “both together” data set

x-bin	uncorrected A_1^n	corrected A_1^n			
		1 st iter.	2 nd iter.	3 ^d iter.	4 th iter.
1	-0.22693	-0.27146	-0.28326	-0.28572	-0.28622
2	-0.20390	-0.23789	-0.24540	-0.24701	-0.24734
3	-0.05790	-0.08761	-0.09296	-0.09413	-0.09437
4	-0.07859	-0.10510	-0.10884	-0.10967	-0.10985
5	-0.08294	-0.10777	-0.11037	-0.11096	-0.11108
6	-0.14704	-0.17107	-0.17270	-0.17309	-0.17317
7	-0.21241	-0.23629	-0.23731	-0.23753	-0.23758
8	0.09965	0.07683	0.07621	0.07607	0.07604
9	0.15955	0.14413	0.14377	0.14370	0.14368

Table A.5: Radiative corrections determined by POLRAD for the “top only” data set (NOTE: POLRAD error code 3 = no satisfactory accuracy is obtained for the inelastic tail)

x-bin	uncorrected A_1^n	corrected A_1^n			
		1 st iter.	2 nd iter.	3 ^d iter.	4 th iter.
1	-0.00004	-0.00392	-0.00443	-0.00443	-0.00443
2	0.05748	0.05235	0.05207	0.05207	0.05207
3	-0.11202	-0.11832	-0.11847	-0.11847	-0.11848
4	-0.05434	-0.06165	-0.06165	-0.06165	-0.06166
5	-0.13053	-0.13941	-0.13926	-0.13926	-0.13927
6	-0.19538	-0.20689	-0.20655	-0.20655	-0.20655
7	0.05772	0.04141	0.04194	0.04194	0.04193
8	0.22064	0.19838	0.19863	0.19864	0.19863
9	-0.24542	-0.26876	-0.26990	-0.26990	-0.26990

Table A.6: Radiative corrections determined by POLRAD for the “bottom only” data set

A.3 Helpful factors for Q^2 evolution

bin	$\frac{F_2^n}{2x(1+R)}$ (at measured Q^2)	f at 2.0 GeV ²	f at 2.5 GeV ²	f at 3.0 GeV ²	f at 5.0 GeV ²
1	0.21570	1.12068	1.17455	1.21734	1.34618
2	0.22403	1.06642	1.11003	1.14462	1.25599
3	0.22863	1.03066	1.06648	1.09535	1.19477
4	0.22865	1.0105	1.03989	1.06468	1.15377
5	0.22501	0.995422	1.01938	1.04129	1.11688
6	0.21542	0.981385	1.00028	1.0182	1.07144
7	0.19211	0.976055	0.986414	0.995732	1.01687
8	0.14933	1.0004	0.994777	0.990491	0.973214
9	0.09070	1.13153	1.08423	1.0505	0.966814

Table A.7: Kinematical factor used to obtain g_1^n from A_1^n at measured Q^2 and factor f for evolution to different Q_0^2 as defined in formula 5.2

A.4 Evolved g_1^n and integral for “both together” data set

bin	g_1^n (at measured Q^2)	at $Q_0^2 = 2.0\text{GeV}^2$	at $Q_0^2 = 2.5\text{GeV}^2$	at $Q_0^2 = 3.0\text{GeV}^2$	at $Q_0^2 = 5.0\text{GeV}^2$
1	-0.522 ± 0.154	-0.597 ± 0.176	-0.633 ± 0.186	-0.663 ± 0.195	-0.746 ± 0.220
2	-0.128 ± 0.122	-0.139 ± 0.132	-0.146 ± 0.139	-0.152 ± 0.145	-0.169 ± 0.161
3	-0.139 ± 0.098	-0.145 ± 0.102	-0.152 ± 0.107	-0.157 ± 0.111	-0.172 ± 0.121
4	-0.142 ± 0.086	-0.143 ± 0.087	-0.149 ± 0.090	-0.154 ± 0.093	-0.166 ± 0.101
5	-0.125 ± 0.068	-0.124 ± 0.067	-0.128 ± 0.070	-0.131 ± 0.071	-0.140 ± 0.076
6	-0.122 ± 0.057	-0.119 ± 0.056	-0.122 ± 0.057	-0.124 ± 0.058	-0.130 ± 0.061
7	-0.043 ± 0.047	-0.042 ± 0.045	-0.043 ± 0.046	-0.043 ± 0.046	-0.044 ± 0.047
8	0.037 ± 0.048	0.037 ± 0.048	0.037 ± 0.048	0.037 ± 0.048	0.036 ± 0.047
9	-0.009 ± 0.036	-0.010 ± 0.040	-0.010 ± 0.038	-0.010 ± 0.037	-0.009 ± 0.034

Table A.8: Evolved g_1^n for the “both together” data set

Q^2	$\int_{x=0.023}^{x=0.6} dx g_1^n(x)$
$\langle Q^2 \rangle$	-0.032 ± 0.012
2.00	-0.033 ± 0.012
2.50	-0.035 ± 0.012
3.00	-0.036 ± 0.012
5.00	-0.039 ± 0.012

Table A.9: Integral over the measured region at measured and several fixed Q^2 for the data requiring both detectors working at the same time. Statistical error only.

A.5 Extrapolations for “both together” data set

Q^2	Regge type fit (constant g_1^n)				Running integral linear fit			Logarithmic fits		
	1 bin	2 bins	3 bins	4 bins	2 bins	3 bins	4 bins	$A \ln(x)$	$A(1 + 2 \ln(x))$	$A \ln(x) + B$
2.0	-0.1373	-0.00699	-0.00510	-0.00435	-0.1156	-0.00570	-0.00279	-0.00792	-0.00872	-0.01874
2.5	-0.1456	-0.00737	-0.00536	-0.00454	-0.1226	-0.00601	-0.00291	-0.00829	-0.00913	-0.01981
3.0	-0.1525	-0.00768	-0.00555	-0.00469	-0.1284	-0.00626	-0.00300	-0.00858	-0.00946	-0.02068
5.0	-0.1716	-0.00852	-0.00607	-0.00509	-0.1444	-0.00696	-0.00325	-0.00934	-0.01031	-0.02311

Table A.10: Integral over the low x region ($\int_{x=0}^{x=0.023} dx g_1^n(x)$) at several fixed Q^2 for the data requiring both detectors working at the same time

Q^2	2 bins	1 bin
2.0	.0005	-.0004
2.5	.0004	-.0004
3.0	.0004	-.0004
5.0	.0004	-.0004

Table A.11: Integral over the high x region ($\int_{x=0.6}^{x=1} dx g_1^n(x)$) at several fixed Q^2 for the “both together” data set

Appendix B

The influence of the lower Q^2 limit on the result

Recent progress in the understanding of structure functions [?] indicate that the DIS scattering formalism does not require that Q^2 be greater than 1.0 GeV². Rather it seems that this requirement can be relaxed to $Q^2 \geq 0.3$ GeV². Applying this looser requirement to the extraction of g_n^1 translates in higher counts for the low x . The DST's currently hold only data down to $Q^2 = 0.6$ GeV², to limit the size of the files. In figure B-1 the resulting g_1^n for a minimum Q^2 of 0.6, 0.7, 0.8, 0.9 and the standard 1.0 GeV² are shown. The data set used was “both together”, requiring both detector halves to be fully operational. It can be seen clearly that the effect on the value of the structure function is not big and no “trend” can be distinguished. It seems reasonable to conclude that one could use the lower the Q^2 -threshold to gain counts in the lowest x bin.

In figure B-2 the error on g_1^n for the first and second x bin is shown for the different Q^2 -thresholds. This result needs to be qualified by the remark that the lower boundary of the lowest x bin was not changed. Since the lower x boundary is mainly determined by the geometric acceptance of the spectrometer, this is not expected to make much difference.

In conclusion, it has been shown that lowering the Q^2 -threshold for the DIS events increases the statistics in the lowest x -bin. There is no indication of a systematic trend in the resulting g_1^n . The error on the integral over the measured range is not affected by the reduction in the error in this bin.

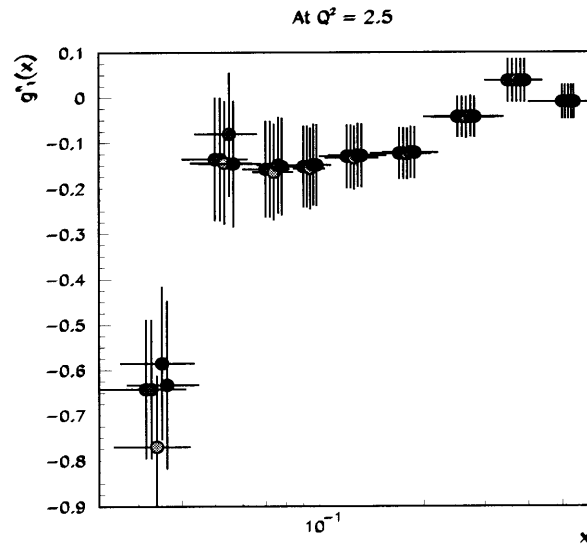


Figure B-1: g_1^n evolved to 2.5 GeV^2 for different Q^2 -thresholds

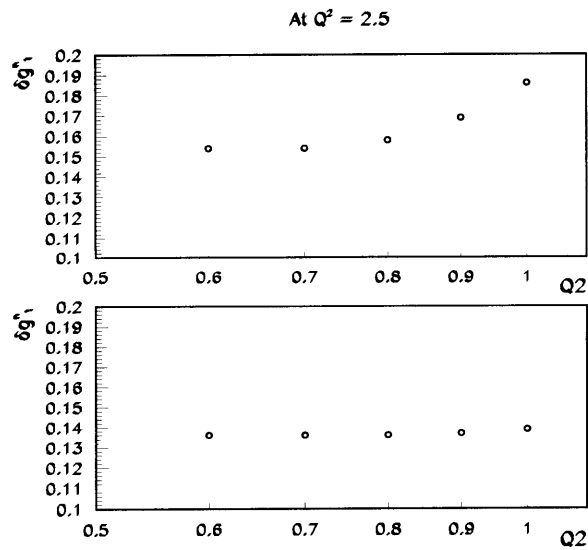


Figure B-2: The error bar on g_1^n (evolved to 2.5 GeV^2) for the first x bin (top) and the second x bin (bottom) as a function of the Q^2 -threshold

Bibliography

- [1] F. Halzen and A. D. Martin. *Quarks and leptons: an introductory course in modern particle physics*. John Wiley and sons, New York, 1984.
- [2] F. Mandl and G. Shaw. *Quantum Field Theory*. John Wiley and Sons, New York, 1984.
- [3] I. J. R. Aitchison and A. J. G. Hey. *Gauge theories in particle physics: a practical introduction*. Adam Hilger, Bristol and Philadelphia, 1989.
- [4] R. Feynman *Phys. Rev. Lett.*, **23**, 1415 (1969).
- [5] J. Bjorken and E. Paschos *Phys. Rev.*, **185**, 1975 (1969).
- [6] M. Gell-Mann *Phys. Lett.*, **8**, 214 (1964).
- [7] G. Zweig. CERN-TH-412. Technical report, CERN, 1964.
- [8] D. Soper and J. Collins. Issues in the determination of parton distribution functions. hep-ph/9411214, 1994.
- [9] G. A. Ladinsky. A collection of polarized parton densities. preprint hep-ph/9601287, 1996.
- [10] H. L. Lai et al. Global QCD analysis and the CTEQ parton distributions. preprint hep-ph/9410404, 1994.
- [11] G. Altarelli and G. Parisi *Nucl. Phys. B*, **126**, 298 (1977).
- [12] W. Greiner and B. Mueller. *Quantenmechanik, Teil 2: Symmetrien*. Verlag Harri Deutsch, Frankfurt am Main, Germany, 1990.
- [13] T. Pussieux and R. Windmolders. A collection of formulas for spin dependent deep inelastic scattering. In *Symposium on the Internal Spin Structure of the Nucleon*, page 212. 1994.
- [14] I. Akusevich and N. Shumeiko *J. Phys. G*, **20**, 513 (1994).
- [15] A. Schaefer. “Spin-dependent structure functions for the proton and neutron,” *Phys. Lett. B*, **208**(2), 175 (1988).

- [16] B. Blankleider and R. Woloshyn *Phys. Rev. C*, **29**, 538 (1984).
- [17] R. Schulze and P. Sauer *Phys. Rev. C*, **48**, 38 (1990).
- [18] J. Friar et al. *Phys. Rev. C*, **42**, 2310 (1990).
- [19] E. P. C. Ciofi degli Atti and G. Salme *Phys. Rev. C*, **46**, 1591 (1992).
- [20] G. Altarelli et al. Determination of the Bjorken sum and strong coupling from polarized structure functions. preprint hep-ph/9701289, 1997.
- [21] R. D. Ball et al. *Nucl. Phys. B*, **444**, 287 (1995).
- [22] R. D. Ball et al. *Phys. Lett. B*, **378**, 255 (1996).
- [23] S. J. Brodsky et al. *Nucl. Phys. B*, **441**, 197–214 (1995).
- [24] L. Osborn. An oscillator model for hadronization. Technical report, M.I.T., 1994.
- [25] M. Niczyporuk and E. Bruins. Flavor tagging at HERMES. Technical report, HERMES, 1996.
- [26] L. Mankiewicz et al. In *Proceedings of the workshop 'Physics at HERA'*, volume 3, october 1991.
- [27] M. Strikman. Probing polarised nucleon structure in semi-inclusive deep inelastic processes. In *Symposium on the Internal Spin Structure of the Nucleon*, page 153. 1994.
- [28] Sloan et al. *Phys. Reports*, **161**, 46 (1988).
- [29] R. Jaffe. Polarized Λ 's in the current fragmentation region. To be published in *Phys. Rev. D*, Rapid Communications, May 1996.
- [30] P. Anthony et al. "Deep inelastic scattering of polarized electrons by polarized ^3He and the study of the neutron spin structure," *Phys.Rev. D*, **54**(6620-6650) (1996). SLAC-PUB-7103.
- [31] K. Abe et al. "Precision measurement of the deuteron spin structure function g_1^d ," *Phys.Rev.Lett.*, **76**, 587 (1996). SLAC-PUB-95-6734.
- [32] K. Abe et al. Precision determination of the neutron spin structure function g_1^n . hep-ex/9705012, 1997.
- [33] D. Adams et al. The spin-dependent structure function $g_1(x)$ of the deuteron from polarized deep-inelastic muon scattering. CERN-PPE/97-08, submitted to *Phys. Lett. B*, 1997.
- [34] A. Sokolov and I. Ternov *Sov. Phys. Doklady*, **8**, 1203 (1964).
- [35] V. Baier et al. *Sov. Phys. JETP*, **31**, 908 (1970).

- [36] B. Montague *Phys. Rep.*, **113**, 1 (1984).
- [37] L. Thomas *Philos. Mag.*, **3**, 1 (1927).
- [38] V. Bargmann et al. *Phys. Rev. Letters*, **2**, 435 (1959).
- [39] J. Buon and K. Steffen *Nucl. Instr. and Meth. A*, **245**, 248 (1986).
- [40] J. Kewisch et al. *Phys. Rev. Lett.*, **62**, 419 (1989).
- [41] M. Boege. *Analysis of Spin Depolarizing Effects in Electron Storage Rings*. PhD thesis, University of Hamburg, 1994.
- [42] B. Dolgoshein. "Transition Radiation Detectors," *Nucl. Instr. and Meth. A*, **326**, 434 (1993).
- [43] X. Artru et al. "Practical theory of the Multilayered Transition Radiation Detector," *Phys. Rep. D*, **12**(5), 1289 (1975).
- [44] W. Allison and P. Wright. The Physics of Charged Particle Identification: dE/dx , Čerenkov and Transition Radiation. In T. Ferbel, editor, *Experimental Techniques in High Energy Physics*. Addison-Wesley, 1987.
- [45] F. Colegrove and P. Franken. "Optical pumping of helium in the 3S_1 metastable state," *Physical Review*, **119**(2), 680–690 (1960).
- [46] G. Walters et al. "Nuclear polarization of He^3 gas by metastability exchange with optically pumped metastable He^3 atoms," *Phys. Rev. Lett.*, **8**(11), 439–442 june 1962.
- [47] L. Schearer et al. "Large 3 nuclear polarization," *Phys. Rev. Lett.*, **10**(3), 108–110 february 1963.
- [48] F. Colegrove et al. "Polarization of He^3 gas by optical pumping," *Physical Review*, **132**(6), 2561–2572 december 1963.
- [49] G. Phillips et al. "Demonstration of a polarized He^3 target for nuclear reactions," *Phys. Rev. Lett.*, **9**(12), 502–504 december 1962.
- [50] P. Nacher and M. Leduc. "Optical pumping in 3He with a laser," *Journal de Physique*, **46**(12), 2057–2073 (1985).
- [51] J. Daniels et al. "Polarizing 3He nuclei with neodymium $La_{1-x}Nd_xMgAl_{11}O_{19}$," *Journal of the Optical Society of America*, **4**, 1133–1135 july 1987.
- [52] R. Milner et al. "A polarized 3He target for nuclear physics," *Nucl. Instr. and Meth. A*, **274**, 56–63 (1989).

- [53] K. Lee et al. "A laser optically pumped polarized ^3He target for storage rings," *Nucl. Instr. and Meth. A*, **333**, 294 (1993).
- [54] T. Chupp et al. "Optically pumped polarized gaseous H,D and ^3He gas targets," *Annual Reviews of Nuclear and Particle Science*, **44**, 373-411 (1994).
- [55] J. Dupont-Roc et al. "New value for the metastability exchange cross section in helium," *Phys. Rev. Lett.*, **27**, 467 (1971).
- [56] M. Miller et al. "Measurement of quasielastic $^3\text{He}(p,pN)$ scattering from polarized ^3He and the three body ground state spin structure," *Phys. Rev. Lett.*, **70**, 738 (1993).
- [57] J. Hansen et al. "The transverse-longitudinal asymmetry in the quasielastic $^3\vec{\text{He}}(e,e')$ reaction," (19).
- [58] W. Korsch et al. *Nucl Instr. and Meth. A*, **354**, 437 (1995).
- [59] Spencer et al. -, -, - (-).
- [60] Giormaine and Wang *Journal of Applied Physics*, **31**(3) (1960).
- [61] L. Kramer et al. *Nucl. Instr. and Meth. A*, **365**, 49 (1995).
- [62] T. Weiland and R. Wanzenberg. Wake Fields and Impedances. Technical Report DESY M-91-06, DESY, 1991.
- [63] K. Bane and M. S. DESY. Wakefields of Very Short Bunches in an Accelerating Cavity. Technical Report SLAC-PUB-4441, SLAC, 1987.
- [64] HERMES Proposal to DESY, DESY-PRC-90-01, Unpublished 1990.
- [65] C. E. Jones. *A Measurement of the Spin-Dependent Asymmetry in Quasielastic Scattering of Polarized Electrons from Polarized ^3He* . PhD thesis, 1992.
- [66] MAFIA computer code, ©Prof. Dr.-Ing. T. Weiland, Ohlystrasse 69, D-64285 Darmstadt, Germany.
- [67] M. Pavlovic and F. Laloe *J. Phys.*, **31**, 173 (1970).
- [68] W. Lorenzon et al. "NMR calibration of optical measurement of nuclear polarization in ^3He ," *Phys. Rev. A*, **47**, 468 (1993).
- [69] M. Pinard and J. V. D. Linde *Can. J. Phys.*, **52**, 1615 (1974).
- [70] M. Pinard. PhD thesis, Universite de Paris, France, 1973.
- [71] H. Bukow et al. *J. Phys. B*, **10**, 2347 (1977).

- [72] R. Brooks et al. *Nucl. Instr. and Meth.*, **202**, 113 (1982).
- [73] M. L. Pitt. In H. Paetz, editor, *Int. Workshop on Polarized Beams and Polarized Gas Targets*, pages 413–417. World Scientific, 1996.
- [74] R. Milner et al. “Study of spin relaxation by a charged particle beam in a polarized ^3He gas target,” *Nucl. Instr. and Meth. A*, **257**, 286–290 (1987).
- [75] K. Bonin et al. *Phys. Rev. A*, **37**, 3270 (1988).
- [76] ECP. *ADAMO - Entity-relationship programming system, version 3.3*. CERN, 1994.
- [77] W. Wander. *Rekonstruktion hochenergetischer Streueignisse im HERMES Experiment*. PhD thesis, Friedrich-Alexander-Univ. Erlangen-Nuernberg, 1996.
- [78] R. Kaiser. Particle Identification at HERMES. Technical report, HERMES, 1997.
- [79] F. Close and R. Roberts *Phys. Lett. B*, **336**, 257 (1994).
- [80] K. Ackerstaff et al. Measurement of the neutron spin structure function g_1^n with a polarized ^3He internal target. To be published in *Phys. Lett.*, 1997.
- [81] L. Whitlow et al. “A precise extraction of $R = \sigma_L/\sigma_T$ from a global analysis of the SLAC deep inelastic e-p and e-d scattering cross sections,” *Phys. Lett. B*, **250**, 193 (1990).

List of Figures

1-1	The basic deep inelastic scattering diagram	14
1-2	Visualising the hadronisation process	15
1-3	The Breit reference frame	16
1-4	Visualising partons	17
1-5	The consequences of the simple QPM	18
1-6	General OPA diagram	20
1-7	A simple QPM explanation of the sensitivity of polarized DIS to the polarized distributions	23
1-8	Ellis-Jaffe prediction for Γ_1^n versus Q^2	31
1-9	Components of the ground state wave function of ${}^3\text{He}$. (a) S-wave, protons paired off. (b) D-wave. (c) S'-wave, neutron pairs with one of the protons.	35
1-10	Ellis-Jaffe prediction for Γ_1^n versus Q^2 and experimental results.	45
2-1	The HERA ring with the HERMES spin rotators	49
2-2	The polarization build-up in the HERA positron ring.	50
2-3	Layout of the transverse beam polarimeter	51
2-4	Internal structure of the beam polarimeter's calorimeter	51
2-5	An overview of the HERMES detector.	53
2-6	Distributions for the DIS positrons in the HERMES detector	54
2-7	Schematic view of the tracking chambers in the HERMES detector	56
2-8	Reconstructed high multiplicity event containing a decaying K_s	57
2-9	The distributions of the reconstructed vertices	57
2-10	Isometric view of the HERMES calorimeter.	60
2-11	Ratio of energy deposited in calorimeter to momentum determined by magnet bending radius	61
2-12	Sideview of the HERMES Čerenkov detector.	63
2-13	Isometric view of the HERMES hodoscope.	64
3-1	The energy spectrum of ${}^3\text{He}$	69
3-2	Dipole transitions relevant for optical pumping. The energy levels are NOT to scale. . . .	70
3-3	The full story for C_8 and C_9 pumping	72

3-4	Schematic of pumping cell flow system.	73
3-5	The HERMES cryogenic target cell	78
3-6	The HERMES vacuum system	81
3-7	The downstream wakefield suppressor	86
3-8	A sketch of the quartz cubic pumping cell	89
3-9	The UHV vacuum seal for the glass cell	90
3-10	The calibration setup.	91
3-11	Results from the gasflow system calibrations	93
3-12	The connection of the pumping cell to the storage cell using a sliding tube	94
3-13	Gas Feed System.	95
3-14	Schematic diagram of the laser transport optics system. The lenses are labelled with their focal length in mm. Retardation plates are labelled as “ $\lambda/2$ ” (half-wave) or as “ $\lambda/4$ ” (quarter-wave). The figure is not to scale. The total pathlength from laser to pumping cell is about 10 meters.	97
3-15	Final design of the transverse and longitudinal holding field coils. Also shown is the correction coil, which removed a large gradient produced by the HERMES spectrometer magnet. The scattering chamber and pumping cell are shown inside the coils. The curved parts of the inner transverse coils avoid the vacuum flanges of the scattering chamber. . .	100
3-16	Longitudinal holding field: (a) B_z vs. x for $y = z = 0$, (b) B_z vs. z for $x = y = 0$. The data points are from the mapping measurement, the line is from the MAFIA calculation. The calculation has been scaled to fit the data.	101
3-17	Transverse holding field: (a) B_y vs. x for $y = z = 0$, (b) B_y vs. z for $x = y = 0$. The data points are from the mapping measurement, the line is from the MAFIA calculation. The calculation has been scaled to fit the data.	102
3-18	An overview of the internal target (vacuum chamber not drawn) showing the position of the RF electrodes	103
3-19	The optical polarimeter. QWP: rotating quarter wave plate ; LA: fixed linear analyzer ; F: 667 nm filter ; PMT: photo-multiplier tube	106
3-20	The dc component of the polarimeter signal	110
3-21	The Target Optical Monitor (TOM)	112
3-22	TOM and PCP polarizations measurements for 100 second intervals	113
3-23	Results from the Caltech test experiment for the temperature-dependent wall depolarization	114
3-24	Ratio of TOM to PCP polarizations for different temperatures ranging from 18 to 60 Kelvin	115
3-25	Ratio of TOM to PCP polarizations for different current ranging from 12.5 to 29.5 mA .	116
3-26	The target polarisation during the 1995 HERMES data run. Average of polarization during data taking was 47%	117

4-1	The distributions of the basic quantities	127
4-2	Example of trip detection using the tracking efficiency.	130
4-3	The kinematic quantities for all positrons that pass the track cuts	133
4-4	The kinematic plane for the HERMES detector	137
4-5	Normalised deviation of the asymmetry per fill (top detector)	144
4-6	Normalised deviation of the asymmetry per fill (bottom detector)	145
4-7	Normalised deviation of the asymmetry per fill (both detectors)	146
4-8	Influence of the removal of outliers on the early-late difference (top detector)	147
4-9	Influence of the removal of outliers on the early-late difference (bottom detector)	148
4-10	Influence of the removal of outliers on the early-late difference (both detectors)	148
4-11	A_1 and g_1 derived from the true kinematics (mckine), the true kinematics of reconstructed events (mcrckine) and from the reconstructed kinematics (rckine) for a MC-asymmetry	150
4-12	A_1 and g_1 derived from the true kinematics (mckine), the true kinematics of reconstructed events (mcrckine) and from the reconstructed kinematics (rckine) for a faked asymmetry, which is large at high x	151
5-1	g_1^n at measured Q^2 for “standard” data set	157
5-2	Comparison of g_1^n at $Q^2 = 2.0\text{GeV}^2$ for “standard” data set with data obtained by the E142 experiment. Statistical errors only.	159
5-3	Logarithmic fits to g_1^n at $Q^2 = 2.5\text{ GeV}^2$ for “standard” data set	161
5-4	Running integral over g_1^n at $Q^2 = 2.5\text{ GeV}^2$ for “standard” data set	162
5-5	Counting rule fits to g_1^n at $Q^2 = 2.5\text{ GeV}^2$ for “standard” data set	164
5-6	Ellis-Jaffe prediction for Γ_1^n versus Q^2 and results from HERMES at different evolved Q^2 as determined in this thesis.	168
B-1	g_1^n evolved to 2.5 GeV^2 for different Q^2 -thresholds	177
B-2	The error bar on g_1^n (evolved to 2.5 GeV^2) for the first x bin (top) and the second x bin (bottom) as a function of the Q^2 -threshold	177

List of Tables

1.3	Quark purity matrix for $x = 0.1$, integrated for $z > 0.4$ as calculated from a PEPSI simulation under fairly simplistic assumptions	39
1.4	Experimental data for Γ_1^n	45
3.1	The hyperfine splitting in the helium spectrum (in GHz)	70
3.2	The relative energy of the dipole resonances	71
3.3	The gas loads and pressures in the HERMES pump stations. (*) Calculated by estimating that 58% of the deposit between the two C1 collimators will be pumped out by PS1, the remainder by PS2.	82
3.4	Errors in the measurement of the PMT signal	108
3.5	Errors in the measurement of the pumping cell pressure	108
3.6	Errors in the measurement of the magnetic field	109
3.7	Summary of the errors in the correction factors	109
3.8	Error propagation for the polarization	110
4.1	Positron efficiency and hadron contamination in each x-bin for the three different PID schemes	123
4.2	Statistics of the run quality selection.	125
4.3	The table shows the total and incremental statistics of burst cuts. The left columns show the total number of bursts that were identified as “bad” due to that cut; the right columns show how many of those “bad” bursts were not cut out by the previous cuts.	126
4.4	Bin boundaries for each bin	136
4.5	Average x	138
4.6	Average q^2	138
4.7	Average depolarization factor	138
4.8	Average of the dilution factor	138
4.9	Average of A_p^1	138
4.10	Average of F_p^2	138
4.11	Average of F_d^2	138
4.12	Average of R_{1990}	138

4.13	Hadronic contamination c_{h+} for each x-bin	142
4.14	Charge symmetric contamination c_{e-} for each x-bin as deduced from electron counts . . .	143
5.1	Measured (m) and corrected asymmetries and errors averaged over the three y bins	154
5.2	A_n^1 per x-bin for the three analyses	155
5.3	Radiatively corrected data determined by POLRAD using the combined “top only” and “bottom only” data set, i.e. the “standard” data set	156
5.4	Result for g_1^n at measured Q^2	156
5.5	Evolved g_1^n for the “standard” data set	158
5.6	Integral over the measured region at measured and several fixed Q^2 for the data combining the separate detector halves. Statistical uncertainties only are shown.	160
5.7	Integral over the low x region ($\int_{x=0}^{x=0.023} dx g_1^n(x)$) at several fixed Q^2 for the data combining the separate detector halves	163
5.8	Integral over the high x region ($\int_{x=0.6}^{x=1} dx g_1^n(x)$) at several fixed Q^2 for the “standard” data set	163
5.9	Final results for Γ_1 for “standard” data set. Statistical uncertainty only for measured region, estimated error for extrapolation on low and high x integrals.	165
5.10	Contributions to the systematic error on g_1^n at the measured values of Q^2	166
5.11	Contributions to the systematic error on g_1^n at $Q^2 = 2.5$ (GeV/c) ²	166
A.1	The averages of the kinematic functions for each x-bin for the entire y-range for the “both together” data set	172
A.2	The averages of the kinematic functions for each x-bin for the entire y-range, “top only” data set	172
A.3	The averages of the kinematic functions for each x-bin for the entire y-range, “bottom only” data set	172
A.4	Radiative corrections determined by POLRAD for the “both together” data set	173
A.5	Radiative corrections determined by POLRAD for the “top only” data set (NOTE: POL- RAD error code 3 = no satisfactory accuracy is obtained for the inelastic tail)	173
A.6	Radiative corrections determined by POLRAD for the “bottom only” data set	173
A.7	Kinematical factor used to obtain g_1^n from A_1^n at measured Q^2 and factor f for evolution to different Q_0^2 as defined in formula 5.2	174
A.8	Evolved g_1^n for the “both together” data set	174
A.9	Integral over the measured region at measured and several fixed Q^2 for the data requiring both detectors working at the same time. Statistical error only.	174
A.10	Integral over the low x region ($\int_{x=0}^{x=0.023} dx g_1^n(x)$) at several fixed Q^2 for the data requiring both detectors working at the same time	175

A.11 Integral over the high x region ($\int_{x=0}^{x=1} dx g_1^n(x)$) at several fixed Q^2 for the “both together”
data set 175